Summer 2024

Nickel Ferrite as a Model Corrosion Product and its Deposition on Current and Future Nuclear Fuel Cladding Materials

Bhavani Sasank Nagothi
bnagothi@albany.edu

Nickel Ferrite as a Model Corrosion Product and its Deposition on Current and Future Nuclear Fuel Cladding Materials

by

Bhavani Sasank Nagothi

A dissertation

Submitted to the University at Albany – State University of New York

in partial fulfillment of the requirements for the degree of

Doctor of Philosophy

College of Nanotechnology, Science, and Engineering

Department of Nanoscale Science and Engineering

July 2024

Abstract

The primary corrosion products in Light Water Reactors (LWRs) are nickel ferrites (nominal stoichiometry $NiFe_2O_4$) having the spinel crystal structure. These products, commonly called CRUD (Chalk River Unidentified Deposits) are challenging to study *in situ*, yet understanding their properties is key to improving reactor performance and reducing worker's radiological exposure risk. In this thesis, a hydrothermal synthesis technique was used to produce nickel ferrite particles from goethite and nickel nitrate hexahydrate in the presence of NaOH. X-ray diffraction was used for phase identification, with scanning electron microscopy used for particle shape and size analysis. By varying the [Ni]:[Fe] ratio of the precursors and synthesis temperature between 100-250 °C, a phase diagram was developed to determine the stability field in both composition and temperature for obtaining a single phase, non-stoichiometric nickel ferrite products. The compositional boundaries of the single phase region of the diagram are a function of temperature, consistent with the increased solubility and reaction rates at temperatures above 125°C. However, even at the highest temperature studied, the end members ([Ni]:[Fe]=0 and [Ni]:[Fe]=0.5) did not produce a single phase product.

Usually, LWRs operate under either Normal Water Chemistry (NWC) which provides an oxidizing environment or Hydrogen Water Chemistry (HWC) which provides a reducing environment. However, the hydrogen overpressure achievable in the laboratory-scale hydrothermal reactor were insufficient to replicate the HWC. Instead, a chemical reducing agent, Ethylenediamine (EDA), was introduced during hydrothermal synthesis. This provided the needed reduction of Fe ions to synthesize the full range of Ni-poor ferrites that were not achieved in the first study. The iso-

electric (IEP) point of all synthesized particles was found to depend on composition, but the use of EDA changed the nature of the compositional dependence. In particular, Ni-poor particles synthesized with EDA had a lower IEP than particles of the same [Ni]:[Fe] ratio synthesized without EDA, and in the extreme case, particles synthesized with no Ni approached the IEP of magnetite (Fe_3O_4) in the presence of EDA rather than hematite ($Fe_2O_{3)}$. These findings suggest that re-deposition of liberated particles downstream in the coolant loop (and strategies for mitigating same) will need to take water chemistry into account as well as particle composition.

Along with understanding the behavior of corrosion products, the latter part of this thesis focused on the corrosion of current and future fuel cladding materials and the growth of CRUD products on these cladding tubes, motivated by Fukushima disaster wherein an explosion was directly related to steam oxidation of the Zircaloy fuel cladding. Iron–chromium–aluminum (FeCrAl) alloys are one of the leading contenders in this race. Several alloy compositions were corroded in a test loop at General Electric Vernova in Niskayuna, NY over the course of 6 months. The results implied that water chemistry along with alloy chemistry has a profound effect on the corrosion rate of FeCrAl alloys. Finally, CRUD deposition on latest generation of FeCrAl cladding materials, cladding rods were submerged and heated, followed by CRUD ion injection. The resulting oxide and CRUD on FeCrAl claddings was more difficult to remove than those growing on standard Zircaloy, which can be removed by simple ultrasonication. This apparently stronger adhesion between FeCrAl claddings, oxide layers, and CRUD on these cladding rods could prove to be an impediment to the implementation of next-generation accident-tolerant fuel materials.

Keywords: LWR, hydrothermal synthesis, ferrite, FA-SMT (Ferritic Alloy-Sandvik Material Technology); ATF (accident tolerant fuel); PM-C26M; hydrothermal corrosion; FeCrAl.

Acknowledgements

First and foremost, I want to express my deep gratitude to my mentor, Dr. Kathleen Dunn, whose support and expertise have been invaluable to me during my time at SUNY Polytechnic Institute and UAlbany. Not only is she an excellent mentor but beyond that an amazing human. Her assistance has significantly influenced my personal and professional life and I am forever grateful to her. My heartfelt thanks, Dr. Dunn and I always look up to you. I'd also like to thank Dr. Arnason and Dr. Armstrong from NNL for their valuable technical guidance and support for my thesis project. It would have been impossible to finish this project without the support of my group's members, the CRUD group, and the Cu Club. Thank you, Sri, Sarabjot, Eric, Justin, and Anton for your technical assistance. I would also like to thank Dr Schujman, Miguel and the rest of the Metrology department for their support during my research.

Just like Dr. Dunn at UAlbany, I also had a privilege to work under the guidance of another amazing mentor, Dr. Rajnikant Umretiya at GE-Research. Dear RK, words cannot express how grateful I am for all that you've done for me. More importantly I will cherish your friendship during my time at GE-R.

I also want to express my gratitude to Dr.'s Armstrong, Cady, Kaushik and Schujman for agreeing to join my defense committee. I greatly admire you and your contributions. I am honored to have great scientific minds like you on my committee.

To my uncle and aunt, Mallesh and Hima, and my dear Rishi and Ashu, thank you for your love and support throughout the years. Babai and Pinni, all my accomplishments will forever be at your grace. I am forever grateful to you both. To my parents, Rani and Ramesh and my loving sister Priya I would not have accomplished a fraction of what I have today without you. Finally, the one who picked me up when I couldn't, thank you my dear Moira. I will love you all forever and always!

Table of Minerals and their Chemical Formulas

Mineral Name	Chemical Formula	Crystal System
Goethite	α-FeO(OH)	Orthorhombic
Theophrastite	β-$Ni(OH)_2$	Trigonal
Hematite	α-Fe_2O_3	Trigonal
Maghemite	γ-Fe_2O_3	Cubic
Magnetite	$Fe^{2+}Fe^{+3}{}_2O_4$	Cubic inverse spinel
Trevorite (Nickel Ferrite)	$NiFe_2O_4$	Cubic inverse spinel
Franklinite (Zinc Ferrite)	Zn Fe_2O_4	Cubic spinel

List of Acronyms

LWRs	Light Water Reactors
BWRs	Boiling Water Reactors
PWRs	Pressurized water Reactors
SS	Austenitic Stainless Steel
SCC	Stress Corrosion Cracking
IGSCC	Intergranular Stress Corrosion Cracking
CRUD	Chalk River Unidentified Deposits
CILC	Crud Induced Localized Corrosion
AOA	Axial Offset Anomalies
NWC	Normal Water Chemistry
HWC	Hydrogen Water Chemistry
NMCA	Noble Metal Chemical Addition
EDL	Electrical Double Layer
PZC	Point of Zero charge
IEP	Isoelectric Point
ECP	Electro Chemical Potential
SEM	Scanning Electron Microscopy
TEM	Transmission Electron Microscopy
EDS	Energy Dispersive X-ray Spectroscopy
XRD	X-ray diffraction
XPS	X-ray photoelectron Spectroscopy
ICP-OES	Inductively coupled plasma Optical Emission spectroscopy
FTIR	Fourier Transform Infrared Spectroscopy
DLS	Dynamic light scattering
EDA	Ethylenediamine
ATF	Accident Tolerant Fuels

DOE	Department of Energy
UHP	Ultra High Purity
FASMT	Ferritic Alloy-Sandvik Material Technology
PM	Powder Metallurgy
GE	General Electric
EBA	Enriched Boric Acid (EBA
AISI	American Iron and Steel Institute
IHL	Inner Helmholtz layers
OHL	Outer Helmholtz layers
IHP	Inner Helmholtz Plane
OHP	Outer Helmholtz Plane
CVCS	Chemical and Volume Control System
LOCA	Loss Of Coolant Accident
SPP	Secondary Phase Particles
CHF	Critical Heat Flux
SNB	Subcooled nuclear boiling

Table of Contents

List of Tables

List of Figures

1.Introduction

Year by year, as global concern rises over increased greenhouse gas emissions, national and international regulatory parties are issuing policies to drive change in the way electricity is produced. This transition can be made possible with nuclear power technology, which has extremely low carbon emissions [1]. In 2022, approximately 10% of the world's electricity was produced by nuclear energy [2], which has two main problematic aspects for wider adoption: the extremely high costs of building a new power plant, and the production/ regulation of nuclear waste [3]. To address the first issue, the nuclear community is developing new reactor designs, such as small modular reactors and fast neutron reactors. However, these new reactor concepts are far from deployment into commercial use, requiring a minimum of 10 years (if not more) before the technology is mature. Out of 440 commercially operated nuclear power plants, 369 are light water reactors (LWRs) which account for approximately 90% of the total nuclear energy output worldwide [4]. This classification can be broken down further into two types of LWRs, with 308 pressurized water reactors (PWRs) and 61 boiling water reactors (BWRs) [5]. Beyond the existing plants, 57 additional nuclear power plants are currently being constructed around the world, particularly in China, India, Russia and the United Arab Emirates; of these, 51 are LWRs: 49 PWRs and 2 BWRs [6,7].

In general, LWRs face numerous problems like safety and security issues, radiation waste, enrichment of uranium, inefficiencies caused by neutron stealing by water molecules, and many more. The primary problem for aging infrastructure, however, is material degradation, especially

by corrosion of the turbine and condenser, as well as stress corrosion cracking (SCC) of materials in the core region of the nuclear reactor.

CRUD (Chalk River Unidentified Deposit or Corrosion Related Unidentified Deposit) is the term currently used in the nuclear materials community to describe corrosion products transported through the coolant system in LWRs. These products were first observed in late 1950s at the Chalk River Nuclear Laboratory [8]. According to literature, CRUD in PWRs mainly consists of non-stoichiometric nickel ferrites and nickel oxides, whereas in BWRs, CRUD deposits are predominantly non-stoichiometric nickel ferrites and hematite [9]. The issues associated with CRUD deposition to other regions of the reactor rapidly became a reason for concern for several reasons. The deposition of insulating CRUD on fuel rods reduces heat transfer across the fuel-cladding component [10,11], which increases the surface temperature of the cladding, ultimately leading to fuel failure [12,13]. In addition, any Co and Ni accumulated on the surface of the fuel cladding, when exposed to high neutron flux, could become the radioactive nuclei ^{58}Co, ^{60}Co and ^{58}Ni to ^{59}Ni, respectively. If detached from the cladding, these activated radioactive nuclei could be released into the coolant of the primary circuit of the core [13], enhancing the radiation dose in the primary water circuits and potential worker exposures [10,14]. Finally, localized corrosion [15,16] of other structural components can lead to cracking, and increased maintenance time/costs. Together, these effects ultimately lead to reduced power output efficiency of nuclear reactors [10,11,14].

While the above are problems for all LWRs, PWRs in particular are subject to an additional issue due to the use of boron in the primary coolant water for absorbing thermal neutrons and controlling

the chain reaction. Any boron incorporated into the CRUD layer as $NiFeBO_5$ [17] absorbs an anomalous amount of neutrons that otherwise contribute to heating of the surrounding water. The design of the reactor flow means more of this material accumulates at the top of the fuel assembly, causing a shift in power towards the bottom of the core [13,18]. This anomaly is called Axial Offset Assembly (AOA) [19] or CRUD induced power shift (CIPS). Even though AOA was first observed at the German Obrigheim PWR, the most significant impact of AOA was observed during the 9th operational cycle in the late 1990s at Callaway in United States. Currently, if a plant observes a Axial Offset (AO) value of greater than 3%, operators must either reduced the power output or shutdown and refuel [20]. Thus, CRUD is an ongoing issues for the nuclear community worldwide.

1.1 Outline of thesis

This thesis is structured in a format where the literature review is carried out to provide the most up-to-date knowledge in the nuclear field and to highlight the knowledge gaps associated with CRUD deposition under different operating conditions of Light water Reactors (LWRs). Chapter 2 summarizes the current literature and lays out the aims of the dissertation. Chapter 3 includes an overview of the characterization techniques that will be used to address those aims, followed by the synthesis and deposition methods in Chapter 4. The results are presented in Chapters 5 through 8, including previously published material (with appropriate permissions). Chapter 9 concludes the thesis and offers an outlook for plausible future work.

2.Literature Review

The water chemistry of LWRs is discussed in this chapter. Moreover, greater attention is given to oxidation of construction material (stainless steel) at high temperatures to understand the origin and re-deposition of CRUD particles. In this chapter, I also propose different mechanisms of CRUD particle deposition which lead to the research aims of this dissertation.

2.1 Light Water Reactors (LWRs)

Nuclear reactors that use water as both a coolant and a neutron moderator to reduce the speed of fast-moving neutrons are called LWRs. In these reactors, heat is produced by nuclear fission reactions. Fission reactions are initiated when thermal neutrons collide with enriched uranium pellets that are stacked in hollow zirconium (Zr)-based cladding tubes (Figure 1). A certain percentage of uranium nuclei which have captured a neutron will split into two (or more) unstable nuclei, releasing additional neutrons which initiate a chain reaction. The number of neutrons available for further reactions can be controlled using control rods made up of either hafnium, cadmium, graphite, or boron. The heat generated by these reactions is used to heat water, generating steam to spin turbines and yielding carbon-free electricity [21].

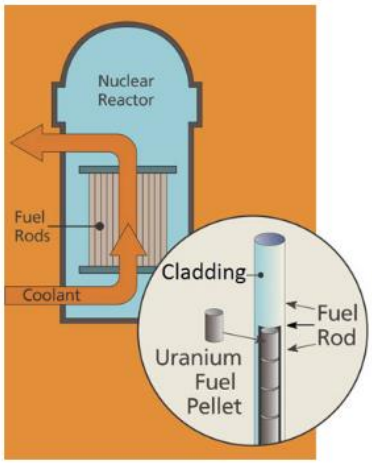

Figure 1. Schematic highlighting the uranium pellets being stacked in hollow zirconium cladding [21].

Depending upon the way in which steam is generated, LWRs are again divided into two sub-types, pressurized water reactors (PWRs) and boiling water reactors (BWRs), which account for the vast majority of the commercial nuclear reactors currently in operation across the world [22]. These sub-types are described next.

2.1.1 Pressurized Water Reactors (PWRs)

A PWR reactor contains two water loops, designated the primary and secondary circuits, as shown in Figure 2. The primary circuit includes the water surrounding the core at high pressure (150 atm), which is heated directly by fission reactions. The heat is then transferred into the secondary circuit. The secondary circuit is usually operated under lower pressure (60 atm) thus transforming the water into steam which in turn is used to produce electricity.

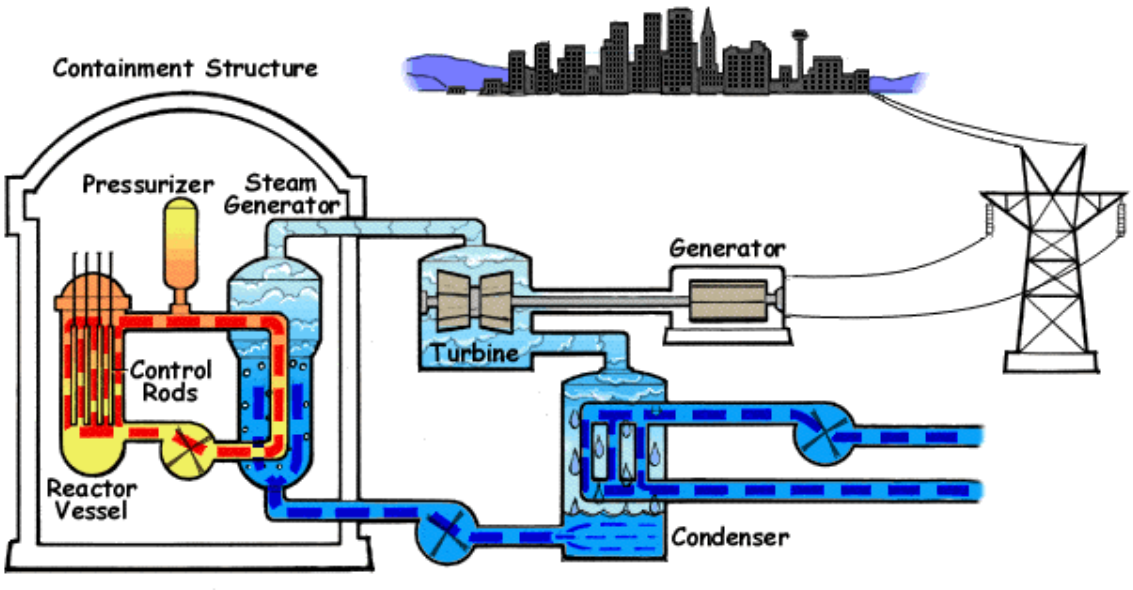

Figure 2. Basic schematic of a Pressurized Water Reactor (PWR) [23].

2.1.2 Boiling Water Reactors (BWRs)

A schematic drawing of a BWR core is shown in Figure 3. In BWRs, the reactor core is usually operated at 75 atmospheres of pressure raising the boiling point of water to 285°C. Inside the core of the reactor at this temperature and pressure, a mixture of water-steam is produced moving upwards through the core. This mixture then is separated, with liquid water being recirculated and steam leaving the top of the core to spin the turbine, producing electricity. The steam is then condensed and fed back into the core.

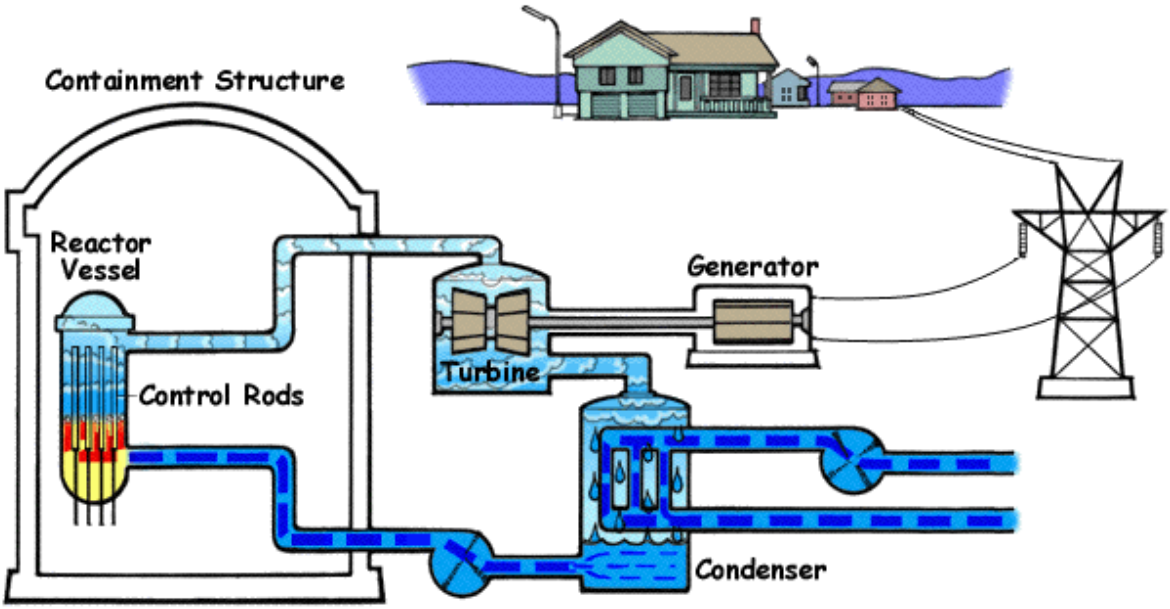

Figure 3. Basic schematic of a Boiling Water Reactor (BWR) [24].

2.2 Corrosion of structural material at operating conditions

The materials used for structural integrity in the nuclear industry are typically austenitic stainless steel, nickel and zirconium alloys, and in lesser quantities titanium alloys [25]. The corrosion resistance of these materials is attributed to the development of protective oxide layers. The passive oxide layer reduces the corrosion potential of the surface, as it has a lower solubility in water than the base metal does. As a real life example, in the steam generator of the secondary circuit of the Beznau Nuclear Power Plant, manufactured from Alloy 690 TT, an annual CRUD accumulation of 10 to 12 kg/year was measured, corresponding to an annual average CRUD coverage of 3.2 g/m^2. Because fluctuations in pH, temperature, and chemical composition in the coolant may all influence the corrosion resistance of the oxides, constant monitoring and optimization of the water chemistry in both primary and secondary reactor loop is necessary.

2.2.1 Corrosion under PWR Conditions

The corrosion in the primary circuit of a PWR is characterized by the presence of Fe, Ni, Cr and Zn, with the most observed corrosion products being nickel ferrite ($NiFe_2O_4$), magnetite (Fe_3O_4), and Nickel oxide/Nickel) (NiO/Ni). Nickel ferrite and magnetite are inverse spinels with A^{+2} on octahedral sites, and B^{+3} divided between tetrahedral & octahedral sites as shown in Figure 4. Mixed oxide spinels can occur as well, described generally by $Ni_xFe_{(1-x)}Cr_yFe_{3-x-y}O_4$, where $0<x<1$ and $y<0.1$ [26]. Furthermore, if cobalt is present in the structural materials (i.e. stellite, a cobalt alloy), Co is often incorporated into nickel ferrite, resulting in the formation of nickel cobalt ferrite ($Ni_{1-x}Co_{(x)}Fe_2O_4$). When the accumulation of CRUD on a Zr cladding specimen during the initial two cycles of domestic PWR and BWR lifecycles was evaluated, it was observed that the morphology of CRUD was not homogeneous across the oxide layer, with a porous CRUD composed of nickel oxide needles, and a relatively compact outer CRUD oxide. In the secondary circuits of PWRs, corrosion products (also called fouling) are mainly composed of nickel ferrite deposits and are usually seen on the tube bundles [27].

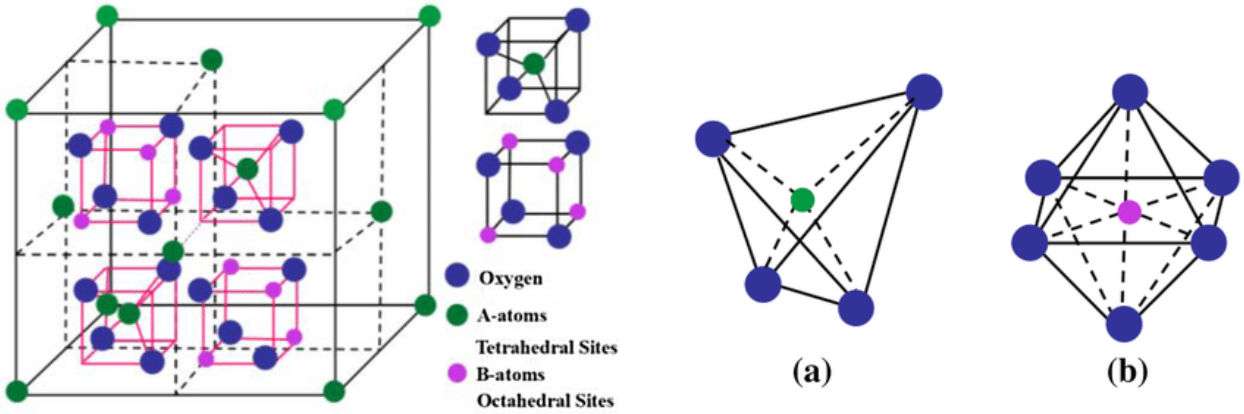

Figure 4. Schematic of Inverse spinel Nickel Ferrites [28].

2.2.2 Corrosion under BWR Conditions

In Boiling Water Reactors, high purity water is used as the primary coolant and neutron moderator in the generation of steam. Due to the radiolysis of water, the coolant of the reactor contains varying amounts of oxygen, hydrogen, hydrogen peroxide, and other oxidants. In normal water chemistry conditions, the overall oxidant concentration (O_2, H_2O_2) is approximately 200 parts per billion, as measured in recirculating water. This is considered Normal Water Chemistry (NWC) conditions, where the coolant content is oxidizing to the point where material corrosion is possible.

Hydrogen Water Chemistry (HWC) has been found to be highly effective in reducing the oxidant concentration due to water radiolysis thus lowering the ECP of the reactor. However, it has a significant side-effect of producing more unstable N-16 species and amplifying radiation fields in primary coolant circuit. To address the shortcomings of HWC, NobleChem, a technology based on the injection of small amounts of noble metals such as Pt and Rh, has been developed. This process has been found to significantly reduce the ECP of the material, with only minimal hydrogen addition required. All coolant chemistry modifications and additives have had a significant impact on the transport behavior of corrosion products, both on fuel cladding surfaces and on surfaces of out-core materials. Corrosion products as impurities in the BWR coolant may exist in ionic, colloidal and insoluble oxide forms (CRUD).

Under NWC conditions, the majority of corrosion products are subject to oxidation to their highest oxidation states due to the increased oxidizing potential of dissolved oxygen and hydrogen in the

water. However, in HWC conditions, certain products may be reduced. An example of this is iron oxide, which exists under NWC conditions α-Fe_2O_3 and γ-Fe_2O_3 and can be converted to Fe_3O_4 to a certain extent under reducing water conditions [29].

2.2.3 Stress Corrosion Cracking in LWRs

Stress corrosion cracking is a major material degradation that can occur in major components of both PWRs and BWRs [30]. The majority of the cracking was found in the heat affected zones of welds where small diameter austenite steel piping and associated parts in light water reactors are joined. In early 1970s-1980s, hundreds of BWRs were shutdown resulting in loss of over $240,000 per day due to pipe cracking. A brief history of SCC is shown in Figure 5.

In the presence of corrosive agents and under high tensile stresses austenitic stainless steel may be susceptible to the entry of oxidizing species via grain boundaries thus resulting in Intergranular Stress Corrosion (IGSCC). IGSCC was mainly reported as the major mechanism behind the cracking in LWRs (Figure 6).

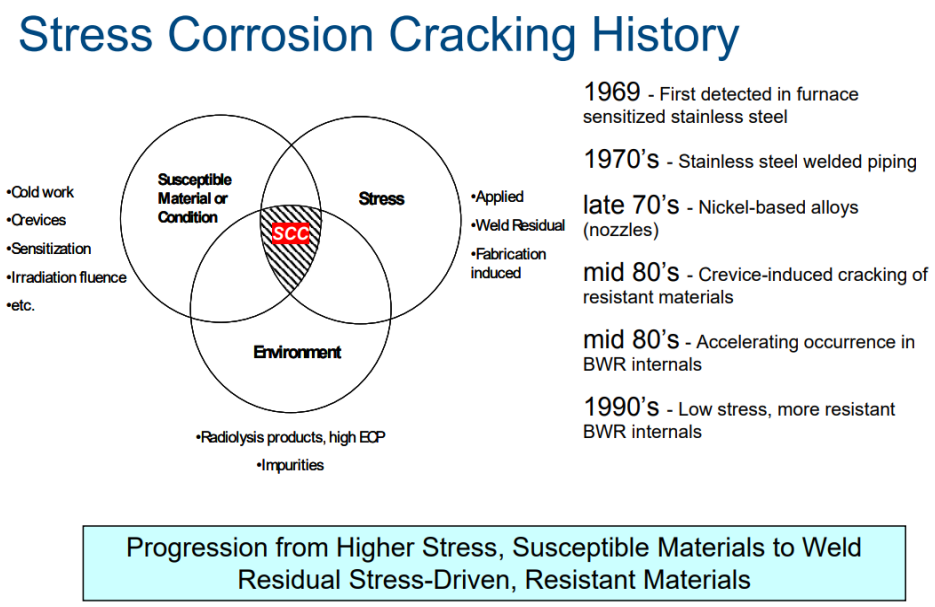

Figure 5. SCC history in BWRs showcasing the higher stresses and weld joints being the major culprits resulting in IGSCC [31].

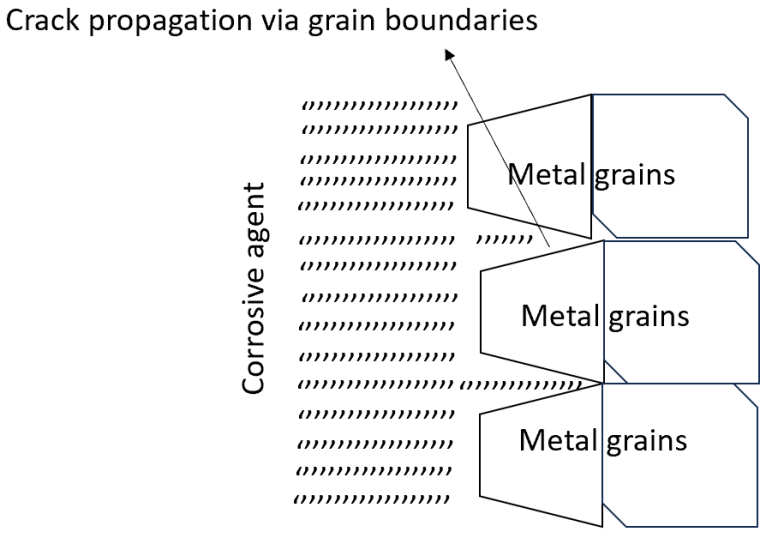

Figure 6. A schematic of oxidizing species entering the grain boundaries of stainless steel resulting in IGSCC [31].

Thus, the prevention of IGSCC relies on the control of the water chemistry in LWRs. Hence Hydrogen Water Chemistry (HWC) was introduced in LWRs. (Figure 7) shows the overall electrochemical reduction of reactor core in BWR-HWC range due to the injection of hydrogen in reactor core.

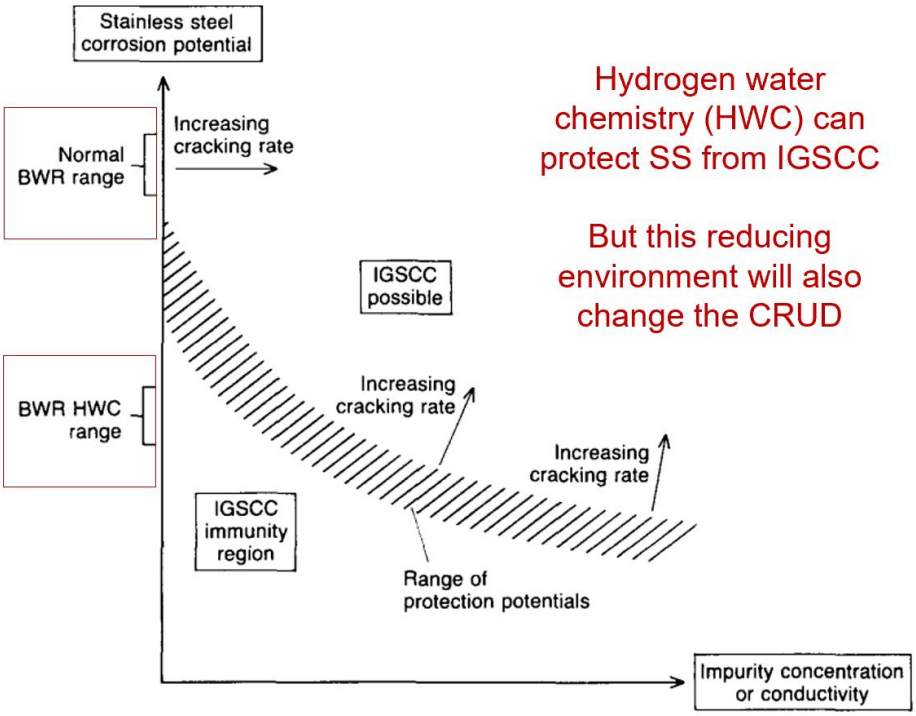

Figure 7. Introduction of hydrogen results in the switch of Electrochemical potential of the reactor thus preventing IGSCC [31].

2.2.4 Chemistry of the coolant water in LWRs

In LWRs, the deposition of CRUD onto fuel cladding material is a complex process that is dictated by the presence of soluble ions, active corrosion, precipitation, and transportation of particulate corrosion products within the coolant water. Since the balance of dissolution and deposition is dependent on the aqueous conditions, water chemistry plays a vital role in dictating CRUD build up on the cladding tubes. Water chemistry in LWRs is optimized by swiftly controlling the pH of the reactor along with the addition of chemical additives that are responsible for maintaining the structural integrity of material throughout the water loops, along with limiting the water radiolysis in the core of the reactor. Hence the addition of these chemical agents in the core of the reactor needs to be monitored very carefully. The operating conditions are summarized below Table 1.

Table 1. Operating Conditions of LWRs [32,33]

	PWR Primary circuit	PWR Secondary circuit	BWR
Pressure (atm)	160	60	60
Temperature (°C)	200-325	20-285	200-288
Oxygen (ppb)	< 0.01		1-300
Conductivity (µS/cm)	1-40		
H_2 (ppm)	2-3.5		0-0.3
LiOH (ppm)	0.1-3.5		
H_3BO_3 (ppm)	0-2300		
Chloride (ppb)	<10		
Fluoride (ppb)	<10		
pH 25°C	9.0-11.5	8.8-9.5	7

2.2.4.1 Hydrogen

To suppress water radiolysis and decrease the concentration of oxidizing species (O_2 and H_2O_2) in the coolant water, hydrogen is introduced to create a reducing environment in the LWRs [34–36]. Hydrogen environment lowers the electrochemical potential (ECP) of metals, and slows the corrosion of the construction materials. When the concentration of oxidizing species decreases, crack initiation and propagation in the stainless steel was minimized, thus decreasing the incidence of Stress Corrosion Cracking (SCC) [37–39].

The Evans diagrams in Figure 8 plot the potential and current for the relevant oxidation and reduction reactions. Assuming no current flows into or from the system, all the electrons released from the oxidation reaction must be accepted by the reduction reaction. These reactions can corrode only at the potential where the currents are the same. From Figure 8 (a) the equilibrium ECP value can be determined as the intersection point of the reactions for oxidation of water and reduction of oxygen. Figure 8 (b), the introduction of hydrogen creates a mixed potential as other reactions can also occur, and the intersection of the reaction lines for oxidation of hydrogen and reduction occurs at a lower equilibrium ECP value. Hence addition of hydrogen is crucial to decrease the dissociation of water molecules by radiolysis.

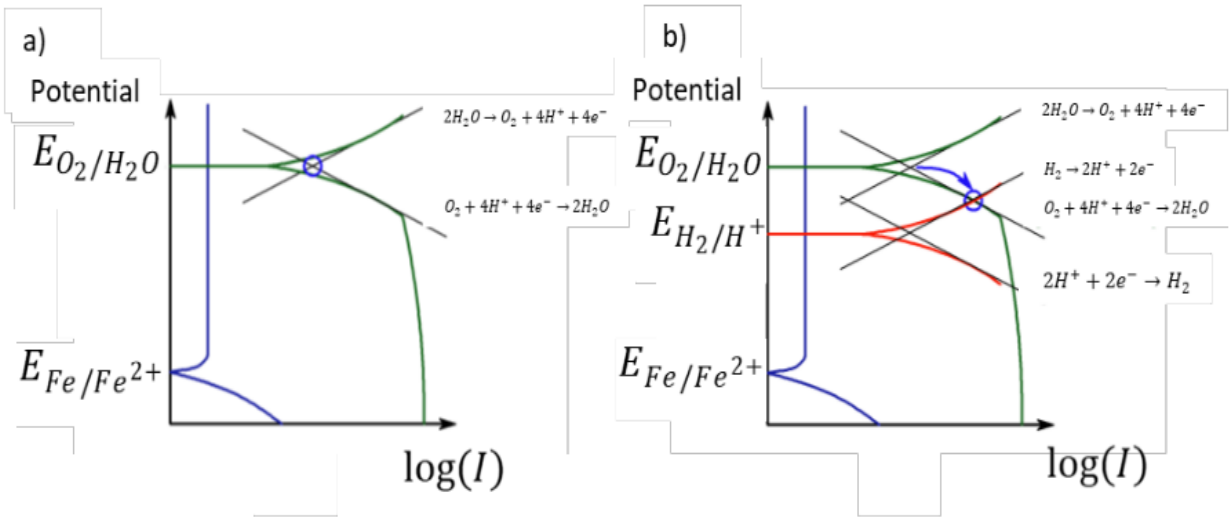

Figure 8. Evans diagrams representative of the influence of H_2 on the Electrochemical Corrosion Potential (ECP), a) without hydrogen addition b) with hydrogen injection. Overall, H_2 lowers the ECP creating a reducing environment [40].

2.2.4.2 Noble Metal Chemical Addition (NMCA)

In BWRs, even with the injection of H_2, oxidants exceed reductants due to the non-volatility of H_2O_2 oxidizing species and the partitioning of H_2 into vapor. This oxidizing environment can lead to higher ECP, increasing the susceptibility to SCC. Consequently, to overcome the oxidizing

environments in BWRs, noble metal injection in addition to H_2 was proposed in 1991 [40] to act as a catalyst for reducing O_2 in the presence of injected H_2 gas. This was subsequently commercialized by General Electric (GE-Research) [41].

2.2.4.3 Boron

In nuclear reactors, boron acts as a moderator for controlling the fission chain reaction by absorbing neutrons that might otherwise be captured by fuel nuclides. In PWRs, this boron is injected in the form of boric acid in concentrations ranging from 1200 pm to 1800 ppm[42]. To maintain the optimal power output, boric acid is carefully monitored and controlled. As boron is a weak Brønsted–Lowry acid it does not significantly impact the pH of the reactor. Moreover, in the reactor during irradiation it exists in two isotopic forms, Boron-10 and Boron-11. During the normal operating conditions of a reactor, the Boron-10 isotope acts as a good moderator due to its high neutron absorption [12]. Hence Enriched Boric Acid (EBA) is proposed to be used at the beginning of the cycle to attain the desired pH_T to enhance the metal passivation. On the downside, EBA is expensive.

2.2.4.4 Lithium

Lithium is usually added in PWRs to optimize the pH range in the reactor, by shifting the operating range to slightly alkaline [43]. Usually, lithium is added in a concentration of 2-5 ppm. When nickel ferrites [27] were detected as a prominent CRUD deposit, 3.5 ppm of lithium was coordinated with boron to achieve a pH_T 7.4 to mitigate the CRUD build-up. This strategy resulted in almost 50% reduction of CRUD build-up, but this elevated chemistry was terminated due to the

a potential risk of increase in SCC [44] for nuclear alloys. Later, a modified chemistry was introduced where a maximum of 2.2 ppm of lithium was coordinated with boron reaching a pH_T between 7.2-7.4 [27]. Tight control of pH is one of the important key parameters to reduce the CRUD build-up in LWRs without negatively impacting other performance parameters.

2.2.4.5 Zinc

Zinc injection was first carried out in PWRs in 1994. The feedback from the injection showed a reduction of radioactive dose and a decrease in SCC, especially for Alloy 600. In later years the Zn injection strategy was adopted at over 100 PWRs. During long term injections, Zn^{+2} can reduce the radiation fields along with corrosion in the reactors. Zn^{+2} ions have a greater affinity for the tetrahedral sites in the spinel oxide when compared to Co^{+2} and Ni^{+2} thus resulting in a more protective oxide layer [45–47]. However, higher concentrations of Zn injection could lead to SCC. Hence for the reactors with high duty core, the best practice is to start with minimal concentration and increase gradually by the end of the cycle.

2.2.5 Material Selection in LWRs and Oxide Layer Formation

2.2.5.1 Iron Alloys

Iron alloys are standardized by the American Iron and Steel Institute(AISI). AISI 304 & 316 are widely used stainless steel (SS) alloys in nuclear power plants. AISI 304 is a manufacturing material used in making reactor vessel. Table 2 summarizes the compositions of the alloys SS 316 and SS 304. SS 316 contains slightly less chromium (16% vs. 18%) but slightly more nickel (10%

vs. 18%). SS316 also contains about 2% molybdenum. This makes SS316 resistant to chloride-induced SCC as well as localized corrosion [48].

Table 2. Nominal compositions of Austenitic Stainless Steel grades AISI 304 and 316 (wt%) [29].

AISI Type	C	Mn	Si	P	S	Cr	Ni	Mo	Fe
304	0.08	2.0	1.0	0.05	0.03	18.0-20.0	8.0-10.5	-	Balance
304 L	0.03	2.0	1.0	0.05	0.03	18.0-20.0	8.0-12.0	-	Balance
316	0.08	2.0	1.0	0.05	0.03	16.0-18.0	10.0-14.0	2.0-3.0	Balance
316L	0.03	2.0	1.0	0.05	0.03	16.0-18.0	10.0-14.0	2.0-3.0	Balance

The corrosion resistance of stainless steel results from the formation of oxide layers. The structure of the oxide layer is dependent on the temperature and environmental conditions in which the material is used. For example, when the material is exposed to high temperature gases (> 600°C), the inner layer of oxide is composed of chromium oxide, and the outer layer is composed of magnetite, Fe_3O_4 [49]. Cr has a sufficiently high outward diffusion at this temperature and can be oxidized selectively to produce chromia and disperse it throughout the outer layer. In the similar way, under LWRs conditions, stainless steel is primarily formed as a double-layer structure by solid state diffusion. The inner layer consists primarily of a protective internal spinel oxide, and a non-protective outer layer (Figure 9). The inner layer is made up of Cr_2O_3 which is formed by the direct oxidation of the chromium from the base metal. The outer layer, on the other hand, follows an out-diffusion mechanism and precipitation. Metal cations diffuse through the inner layer to reprecipitate on the surface, forming the outer layer. The outer layer does not follow a uniform distribution along the surface and is highly sensitive to local hydrodynamics, particularly flow rate

and dissolved element concentration in coolant. As a result, the outer surface layer is porous and contains high concentrations of magnetite Fe_3O_4 and $Ni_xFe_{(1-x)}Fe_2O_4$ but is not protective.

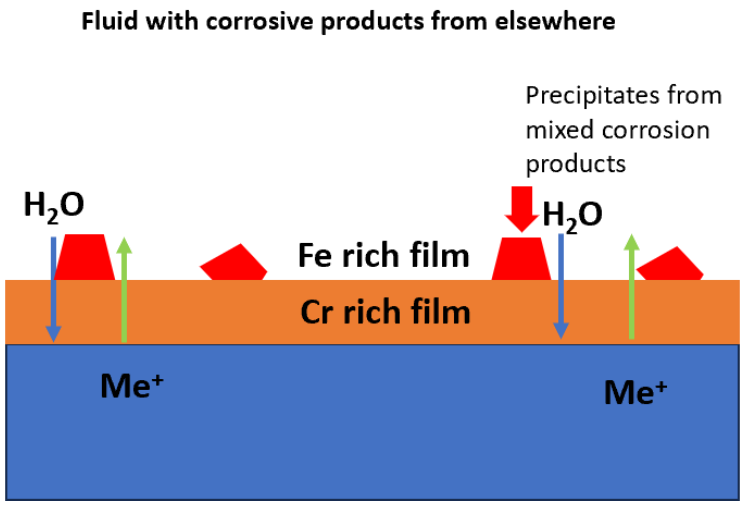

Figure 9. Structure of the protective oxide layers on stainless steel under PWR operating conditions[50].

2.2.5.2 Nickel Alloys

Nickel-based alloys like Alloy 690 are often used to make LWRs steam generators. Alloy 690 is the most used alloy in nuclear power plants due to its higher resistance to stress corrosion cracking [51]. The internal surface area of these alloys accounts for 65% to 70% of the overall reactor surface area, so corrosion of these alloys has the greatest effect on the chemical makeup of CRUD deposited in the reactor [52]. Table 3 summarizes the compositions of the two most common nickel-based alloys, known as Alloy 600 and Alloy 690.

Table 3. Nominal compositions of Alloy 600 and 690 (wt%).

Alloy	C	Mn	Si	P	S	Cr	Ni	Fe	Cu	Al	Ti
600	0.07	0.25	0.29	0.007	< 0.001	15.54	75.4	7.76	0.11	0.17	0.35
690	0.026	0.29	0.01	0.001	0.0005	29.54	59.8	8.25	0.01	0.31	0.32

The oxide structure of nickel base alloys is expected to have a double oxide layer structure (inner oxide layer and outer oxide layer) [53] like the oxide formation on SS. The outer oxide layer of nickel base alloy is not protective and is mainly composed of nickel ferrite crystals. On the other hand, the inner oxide layer is a protective chrome spinel enriched in nickel, with the potential for Cr_2O_3 to form at the metal/oxide interface. Because the nickel content of Alloy 690 is higher than that of SS 304/316, the nickel content in the inner and outer oxide layer is usually higher than the nickel content in oxides found on SS.

2.2.5.3 Zirconium Alloys

Zirconium (Zr) alloys were first used as a nuclear fuel cladding material in the U.S. Navy in the 1950s [54]. Today, zirconium is still being used as a cladding material and for the containment of the uranium dioxide (UO_2) pellet nuclear fuel because of the low neutron cross-section absorption of zirconium. The rods are tube-shaped (4 m in length, 1 cm in diameter, 0.6 mm in thickness). Typical Zirconium alloys in PWRs include ZIRLO and Zircaloy-4. In BWRs, Zircaloy-2 is the most widely used alloys. Zircaloy-4, ZIRLO and Zircaloy-2 chemical compositions are shown in Table 4.

Table 4. Nominal compositions of Zirconium Alloys (wt%)

Element	Sn (%)	Fe (%)	Cr (%)	Ni (%)	O (%)	Hf	Zr	Nb (%)
Zircaloy-2	1.2-1.7	0.07-0.20	0.05-0.15	0.03-0.08	0.12	<100 ppm	bal.	-
Zircaloy-4	1.2-1.7	0.18-0.24	0.07-0.13	-	0.12	<100 ppm	bal.	-
Zirlo®	0-0.99	0.11	-	-	0.11	40 ppm	bal.	0.98

Zirlo® is a trade-mark from Westinghouse Electric Company. – Not specified.

The corrosion reaction of Zirconium metal in LWRs [55] is shown in Equation 2.1 below.

$$Zr\ (s) + 2H_2O(l) \rightarrow ZrO_2(s) + 2\ H_2(g) \qquad 2.1$$

The oxidation process of Zircaloy can be conceptually broken down into several steps as shown in Figure 10 (numbers refer to the steps labelled in this figure). 1. Oxygen dissociates from a water molecule and adsorbs onto the native oxide layer surface at the oxygen vacancy site. 2. Due to the defect concentration and the electrical potential across the oxide and the space charge inside the oxide, oxygen anions diffuse through the bulk oxide or along oxide grain boundaries via solid-state diffusion. 3. Oxygen anions react with zirconium cations to form ZrO_x. 4. The formation of the ZrO_x releases electrons which migrate through the oxide via a hopping mechanism. 5. The cathodic site (where hydrogen ions are reduced) is usually at the oxide/electrolyte interface. Some of the hydrogen ions generated via dissociation of water will not recombine with the electrons. Instead, they are absorbed into the oxide layer and migrate into the metal. This phenomenon is called hydrogen pick up. These migrated hydrogen atoms are either dissolved in the α-Zr matrix forming a solid solution, or, when the concentration of hydrogen exceeds the solubility limit, they end up as hydride precipitates which eventually affect the integrity of the Zr cladding.

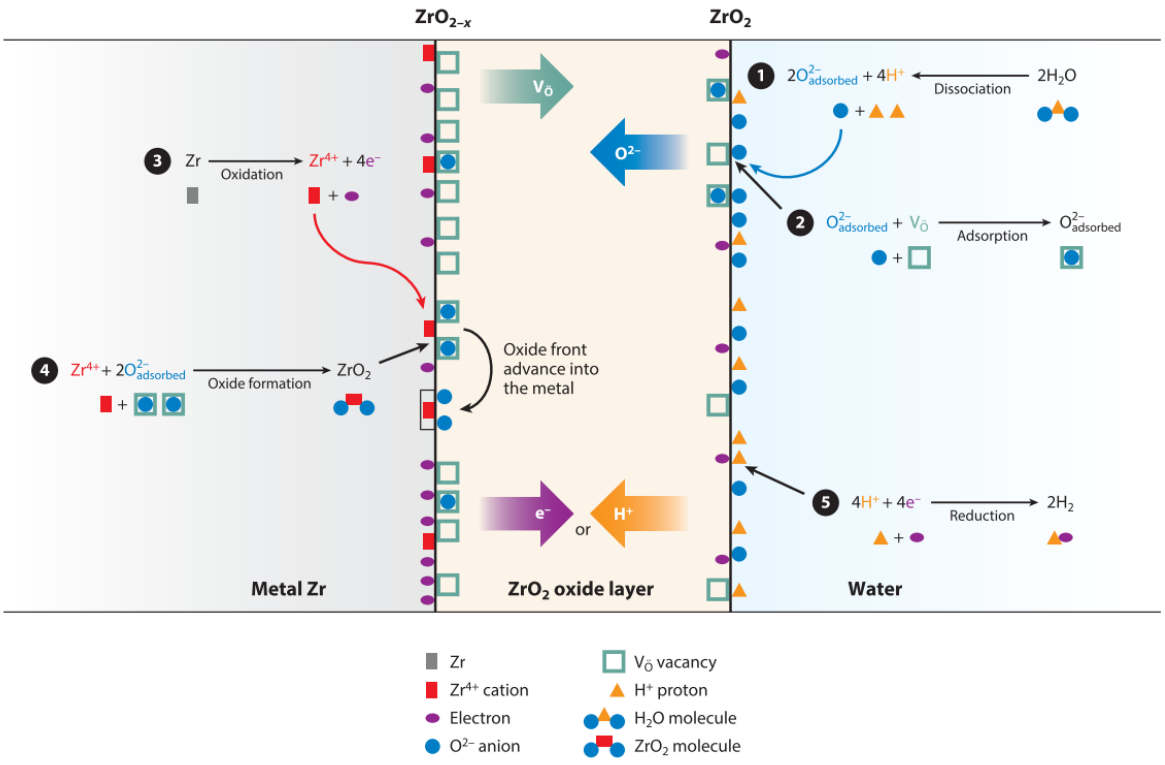

Figure 10. Schematic of the corrosion process in zirconium alloys. Surface reactions 1–5 occur in series, but the rate-limiting steps are the transport of oxidizing species (oxygen, electrons, and hydrogen) in the oxide layers, as indicated by the thick arrows [56].

2.2.6 High Temperature Corrosion, Metal oxide solubility and Pourbaix Diagrams.

The release of corrosion products into the coolant occurs during the deposition of the oxide layers results in a tenacious layer and a loose layer (Figure 11), which are primarily composed of magnetite (Fe_3O_4), non-stoichiometric nickel ferrite ($Ni_xFe_xO_4$) [56], and nickel oxides (NiO_x). Therefore, the solubility of these oxides at high temperatures plays an important role in the deposition of CRUD on other surfaces. Discussed below is the structure of CRUD particles that are seen in LWRs.

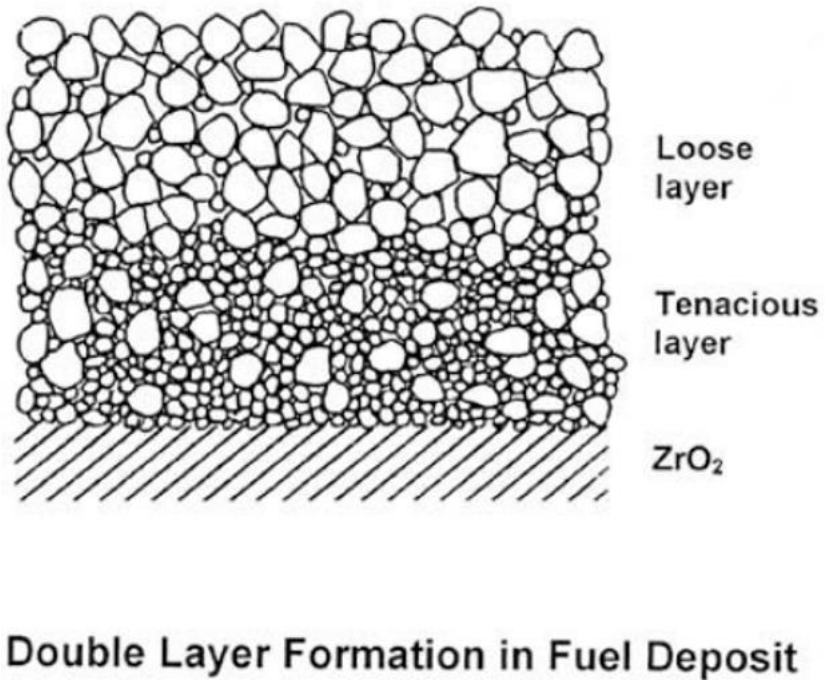

Figure 11. Schematic of corrosion product deposition on fuel cladding surface.

As mentioned earlier, the main crystal form of the nickel ferrite CRUD is a spinel. That structure is described in more detail here. There are two main types of spinels [57]: normal and inverse (Figure 12). In both types, the anions form a close-packed face-centered cubic sublattice, with cations occupying voids in this sublattice which are formed either by 4 neighboring anions (a tetrahedral site), or 6 neighboring anions (an octahedral site). One eighth of the tetrahedral voids are filled, and half of the octahedral voids are filled. The difference between normal and inverse spinels is the distribution of the cations between these two types of sites. In a normal spinel, X^{2+} divalent ions occupy tetrahedral sites and X^{3+} trivalent cations occupy octahedral sites. In an inverse spinel, the tetrahedral sites are occupied by half of the X^{3+} ions, while the remaining X^{3+} ions and all of the divalent X^{2+} ions occupy octahedral sites. The most thermodynamically stable CRUD particles that are seen under the operation condition of LWRs are characterized by inverse spinel structures mainly consisting of magnetite and nickel ferrites.

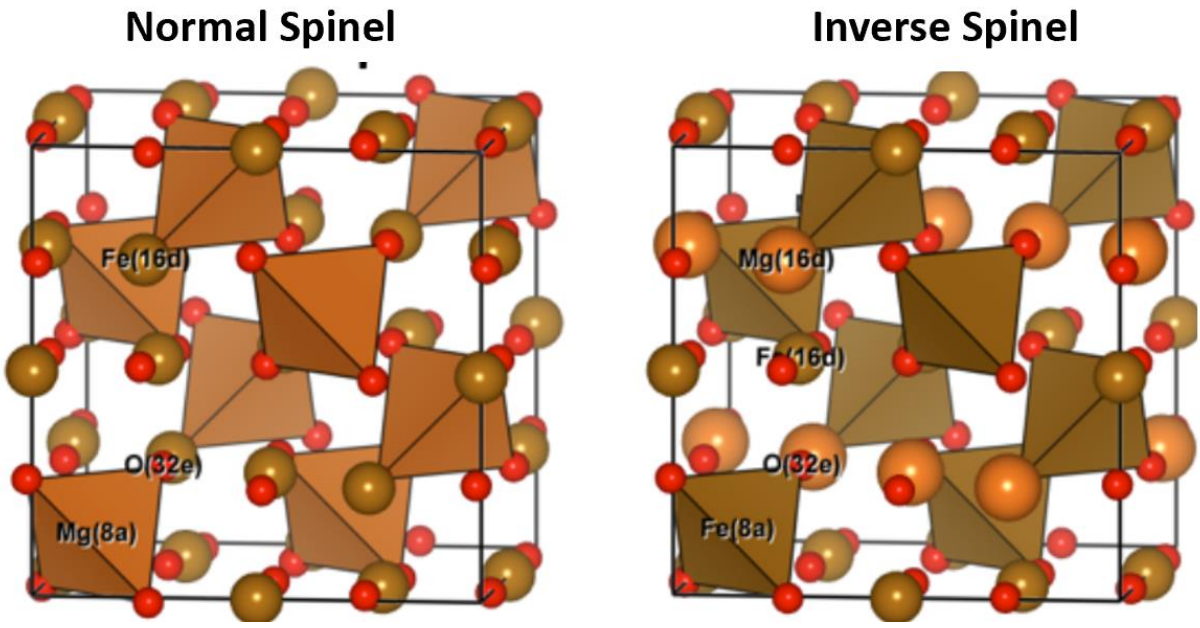

Figure 12. Structure of normal and inverse spinels [58].

The solubility of the CRUD particles in LWRs is believed to be a function of reactor environment including the pH at which the reactor operates. Figure 13 shows the solubility of magnetite as a function of temperature and pH, in the presence of 1.57ppm H_2. At 300°C, the pH range of 9.5 to 10.5 showed the lowest Fe_3O_4 solubility [59–61]. The highest solubility of magnetite is measured at 120°C at $pH_{25\,°C} = 7$. On the other hand, at $pH_{25\,°C} = 10$, the solubility of magnetite approaches a plateau between 100°C and 190°C, and then increases rapidly (up to 1.1 ppb) around 300°C.

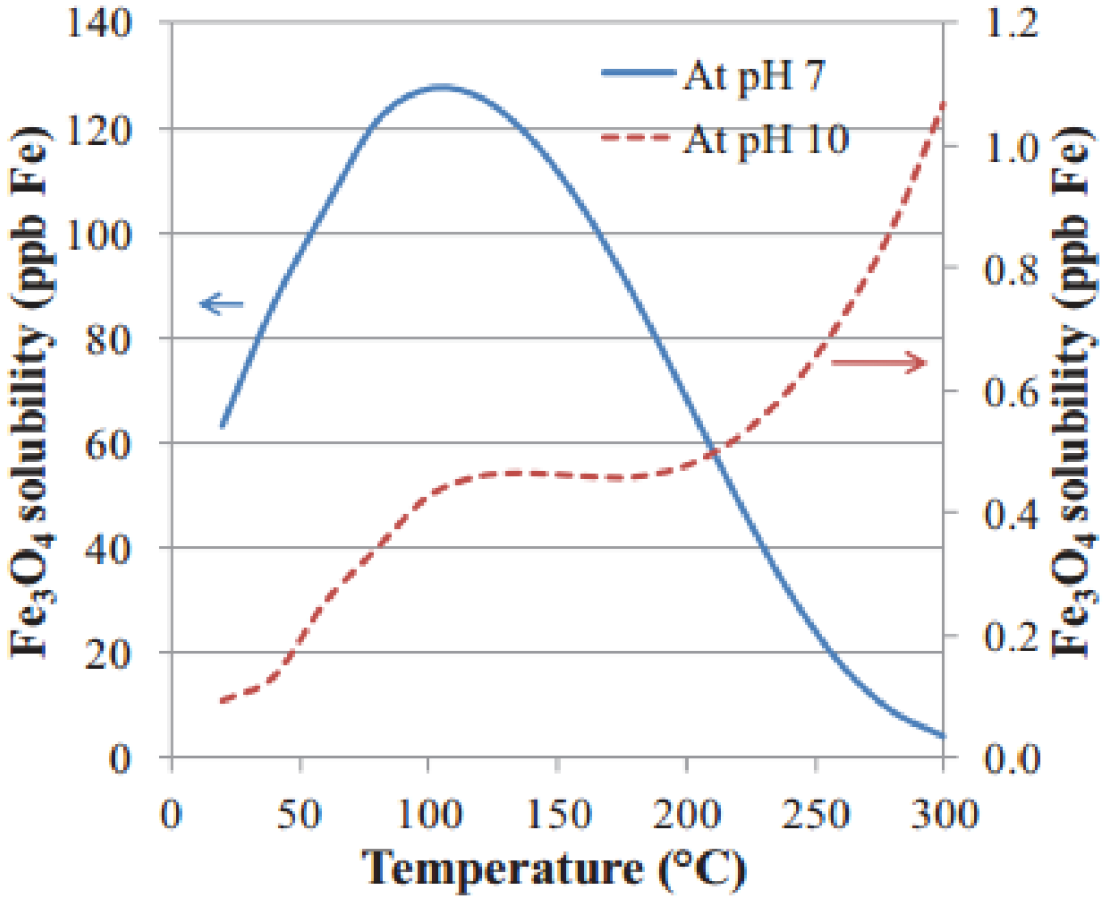

Figure 13. Dependence of magnetite solubility (µg/kg or ppb) on temperature (0 to 300°C) and on the solution's pH25°C (7 and 10) [32].

As nickel-base alloys are used to make the steam generators, Ni and NiO are also commonly seen as CRUD constituents. NiO develops preferentially in low hydrogenated water chemistry and on fuel rods with subcooled nucleate boiling conditions. Under these circumstances, the development of a porous oxide facilitates boron incorporation and results in CIPS [62]. The equation below states that the presence of hydrogen accelerates the transition from NiO (Ni^{2+}) to metallic nickel.

$$NiO + H_2 \rightarrow Ni + H_2O \qquad 2.5.1$$

Furthermore, it is anticipated that the Ni/NiO transition can initiate SCC. Temperature-dependent changes along with critical concentration of H_2 are necessary to maintain metallic Ni as a stable phase. Thus, for a given hydrogen level, NiO can develop if the temperature on the fuel rods rises.

Pourbaix diagrams, also known as potential-pH diagrams, show the areas of stability of metallic species with water. They are particularly useful for corrosion scientists because they show the areas of potential and pH where oxides of a metal are stable, and thus the regions where an oxide layer can form on a metal, protecting it from corrosion.

To generate a Pourbaix diagram, the change in Gibbs free energy for an electrochemical reaction involving the species of interest is evaluated. Generally, this is expressed as a potential over a reference half reaction, for example: $2H^{+}+2e^{-} \rightarrow H_2$, by the equation.

$$\Delta G = (-nFE) \qquad 2.5.2$$

where ΔG is Gibbs energy change, (n is number of electrons), F is a Faraday's constant, and E is the reaction potential. Boundaries are drawn where the activities of the species on either side of the line are equal; away from the line, one form of the species will predominate. The equilibrium lines are combined to create convex polygons, indicating the predominant field of each compound and species. Table 5 shows the most common species that are observed in LWRs. Pourbaix diagrams shown in Figure 14, Figure 15 and Figure 16 represents the most thermodynamically stable CRUD oxides that are seen in LWRs [63].

Table 5. Shows the species and the thermodynamic values that are used to obtain the Pourbaix diagrams for LWRs [63].

Species	Thermodynamic values used				
	Gibbs energy at 298 K (kJ/mol)	Entropy at 298 K (J/mol K)	Heat capacity (J/mol K) $C_p = a + bT + cT^{-2}$		
			a	$b \times 10^3$	$c \times 10^{-5}$
Fe	0	27.3	12.7	31.7	2.5
FeO	−245.1	57.5	51.8	6.78	−1.6
Fe_3O_4	−1015.45	146.4	91.5	201.0	0
Fe_2O_3	−742.2	87.3	98.3	78.0	−14.8
Fe^{2+}	−78.9	−137.7	a)		
Fe^{3+}	−4.6	−315.9	a)		
$FeOH^+$	−277.4	−29.3	a)		
$Fe(OH)_2^+$	−438.1	−45.2	a)		
FeO_4^{2-}	−467.3	34.3	a)		
$HFeO_2^-$	−377.8	23.4	a)		
$FeCr_2O_4$	−1343.9	146.0	163.0	22.3	−31.9
$NiFe_2O_4$	−974.6	125.9	77.4	235.0	1.42
Cr	0	23.77	24.4	9.9	−3.68
CrO	−350.7	45.0	58.1		
CrO_2	−539.7	51.0	75.3	0.96	−18.2
Cr_2O_3	−1058.1	81.17	119.4	9.2	−15.6
Cr^{2+}	−176.1	18.0	a)		
Cr^{3+}	−215.5	−307.0	a)		
$CrOH^{2+}$	−431.0	−68.6	a)		
$Cr(OH)_2^+$	−632.7	−29.0	a)		
CrO_4^{2-}	−727.8	50.2	a)		
CrO_2^-	−536.0	96.0	a)		
$HCrO_4^-$	−764.8	184.1	a)		
$NiCr_2O_4$	−1275.7	124.26	177.4	9.2	−15.6
Ni	0	29.87	16.98	29.5	
NiO	−211.l7	38.0	−20.88	157.0	16.3
Ni_3O_4	−712.0	140.0	117.0		
Ni_2O_3	−469.7	94.0	92.0		
$NiOH^+$	−227.6	−71.0	a)		
Ni^{2+}	−45.6	−128.8	a)		
$HNiO_2^-$	−349.2	41.8	a)		

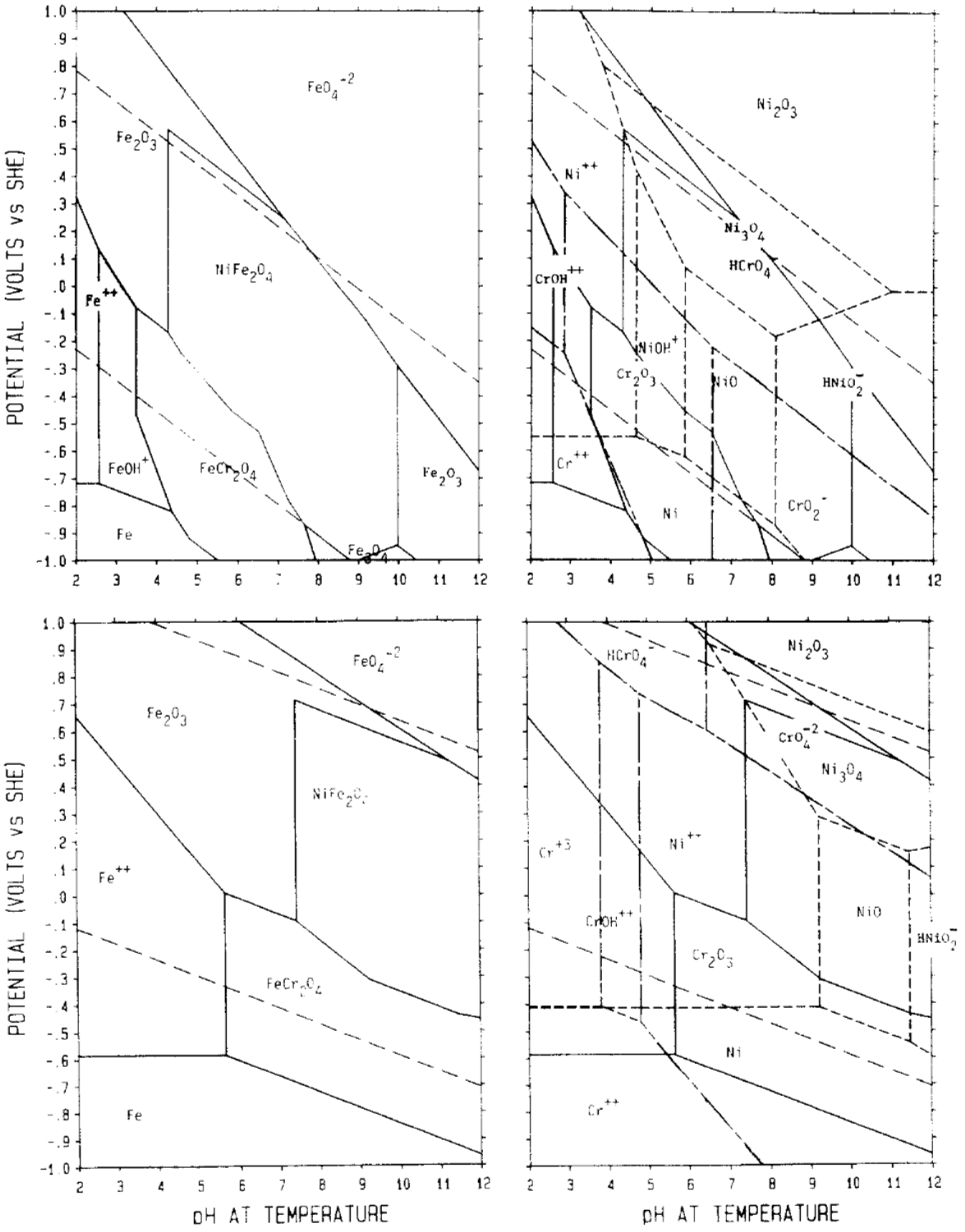

Figure 14. Diagrams for the Fe-Cr-Ni-H_2O system at 298 K (lower curves) (a,b) and 573 K (upper curves) (c,d). Predominance regions for Fe species only on the left-hand diagram. On the right are the Ni- H_2O (short dashed lines), the Cr- H_2O (long-short dashes), plus the Fe regions (full lines). The hydrogen and oxygen equilibria at 1 atm are represented by medium dash line [63].

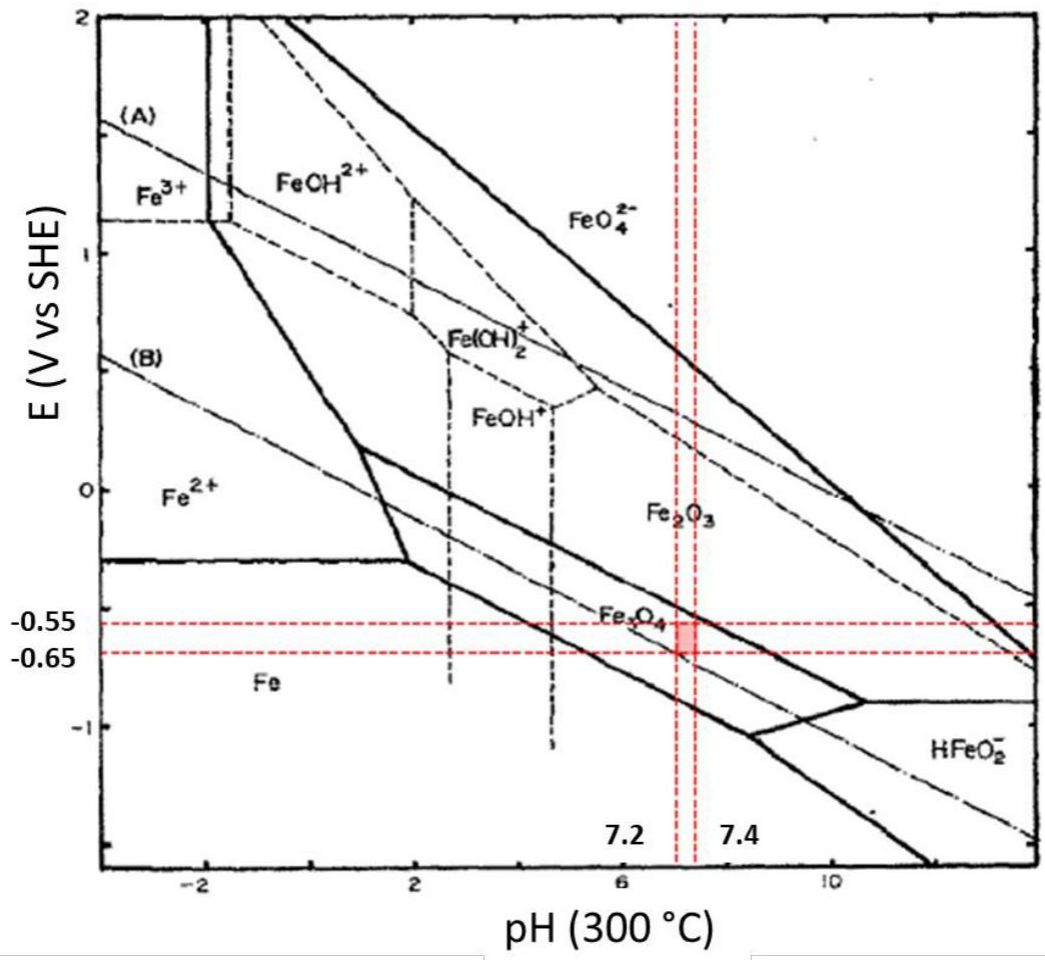

Figure 15. Pourbaix diagram of the system Fe-H_2O system at 300°C. The intersection between the red lines represents the operating conditions adopted in the PWR (primary cycle) [64].

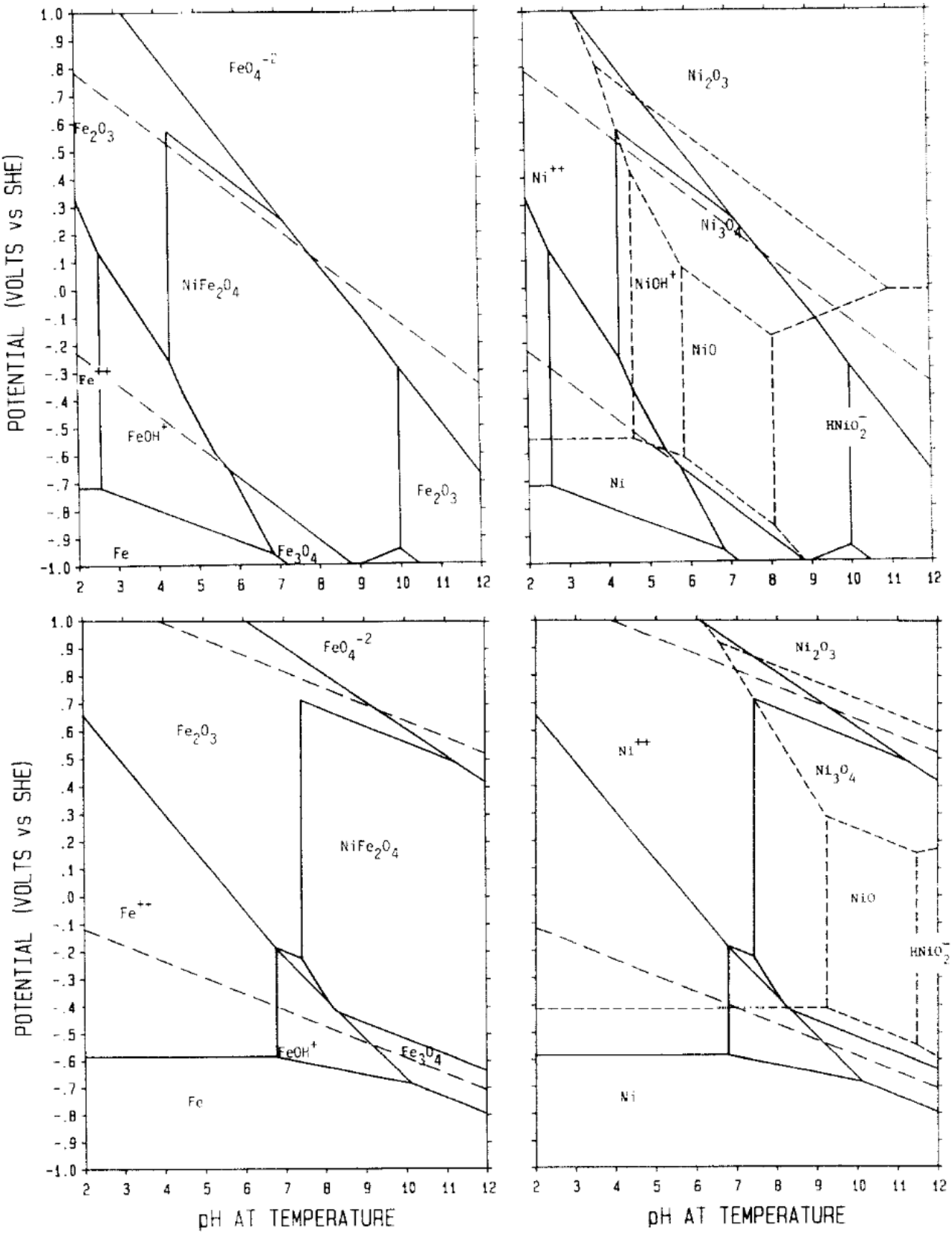

Figure 16. Diagrams for the Fe-Ni-H2O system at 298 K (lower curves) (a,b) and 573 K (upper curves) (c,d). The left hand diagrams are for Fe species, while the right hand ones are for Ni (dashed lines) plus Fe (full lines[63].

2.3. The Electrical Double Layer (EDL)

To understand how the corrosion products and the corroded surfaces are affected by and in turn affect the spatial distribution of ions in the coolant, it is useful to employ the Electrical Double Layer (EDL) model (Figure 17) [65]. It is now widely accepted that EDL is composed of a tightly bound Stern layer and a more diffuse Gouy-Chapman layer. The Stern layer is further subdivided into the inner and outer Helmholtz layers (IHL and OHL respectively). The IHL is the inner layer between the surface of the particle and the outer layer, the inner Helmholtz Plane (IHP). The OHL is the outer layer between IHP and outer Helmholtz Plane (OHP). The layer closest to the particle surface contains ions adsorbed on the surface via Coulomb interactions and chemical affinity to the particle, but these forces decrease with distance such that the outer region of the Stern layer will only have electrostatic forces acting on the charged particle. This (conceptual) boundary defines the start of the Gouy-Chapman layer or diffuse layer, which contains counter ions with opposite charge to the Stern layer. In the diffuse layer, the counterions are only loosely bound to the underlying layers, and are in random thermal motion. When flow is present, the counterion layer is sheared to produce a streaming current. The thickness of the EDL varies in the range of 10^{-9} to 10^{-6} m, and its electroneutrality is maintained according to the following equation:

$$\sigma^o + \sigma^i + \sigma^d = 0 \qquad 2.3.1$$

where σ^o is the particle surface charge density (C m^{-1}), σ^i is the charge density at the IHP (C m^{-1}) and σ^d is the charge density at the OHP (C m^{-1}).

2.3.1 Zeta Potential

Zeta potential is the term used for the electrokinetic potential of particles in colloidal dispersions. In the colloidal chemistry literature [67], it is usually denoted using the Greek letter zeta (ζ), hence

ζ-potential. The usual units are volts (V) or, more commonly, millivolts (mV). From a theoretical viewpoint, the zeta potential is the electric potential in the interfacial double layer (DL) at the location of the slipping plane relative to a point in the bulk fluid away from the interface. In other words, zeta potential is the potential difference between the dispersion medium and the stationary layer of fluid attached to the dispersed particle (Figure 17).

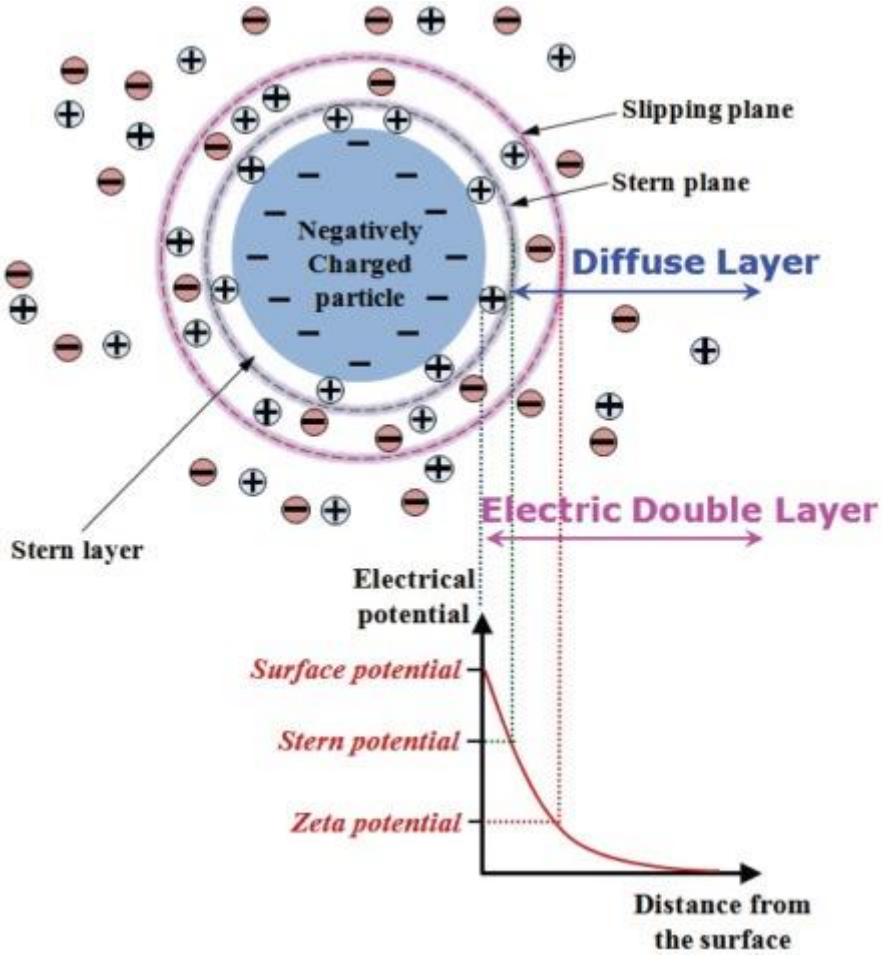

Figure 17.Schematic illustration of stern layer and the interface between the electric double layer and the bulk liquid representing the measured zeta potential l[66]

An additional variable, directly related to the zeta potential, is the Point of Zero Charge (PZC) or Isoelectric Point (IEP).

2.3.2 The Point of Zero charge (PZC) and the Isoelectric Point (IEP)

Electrokinetic reactions that are responsible for the accumulation of CRUD particles are characterized by Point of Zero Charge (PZC). PZC is the point at which a particle's net surface charge is equal to 0. This point is typically determined through mass titration. IEP (Isoelectric point) is the point for which a particle has a zeta potential equal to zero ($\zeta = 0$) [68]. This point is primarily determined through electrophoretic measurements. Colloidal particles have their lowest stability at the IEP of the electrolyte. As a result, particle flocculation and deposition are typically expected at the IEP [65]. When there are no high specific surface adsorption phenomena, the zeta potential can be used as a parameter to easily describe the surface charge of the particles in colloidal systems [67]. While the surface potential is not directly accessible, the zeta potential can be indirectly measured relatively easily and is used as a proxy for the surface charge. The main variables that influence zeta potential values include pH, operating temperature, and nature and ionic strength of the electrolyte.

2.3.3 Effect of pH on zeta potential

The pH of the solution is crucial in determining the development of a surface charge [69]. Specifically, if there are no significant specific adsorption effects, the pH will control the surface charges of the substrate. The substrate can be metal surface having an oxide layer or corrosion products in the electrolyte. In acidic conditions, there is an abundance of protons in the solution compared to hydroxide ions, and a positive surface charge builds up from proton addition. In a similar fashion, a negative surface charge builds up under basic pH due to acid dissociation. Moreover, for pH equal to the PZC, the substrate is electrically neutral as schematically shown in Figure 18.

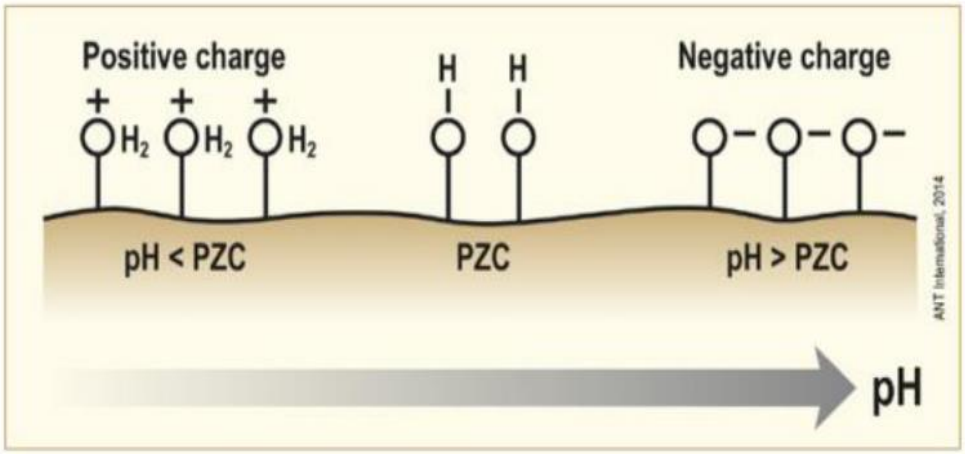

Figure 18. Evolution of the surface charges on the electrolyte's pH, showing positively and negatively charged surfaces respectively at low and high pH. Conversely, at a pH equal to the PZC, a neutral surface charge is established [68].

In real-life scenarios, the IEP may not always align with the PZC due to surface impurities or specific adsorption phenomena. This can lead to the existence of negative zeta potential in an acidic environment and vice versa. However, it is common to observe that the zeta potential decreases monotonically with pH, resulting in a positive zeta potential when the electrolyte pH is less than the IEP, and a negative zeta potential in the opposite scenario as shown in Figure 19.

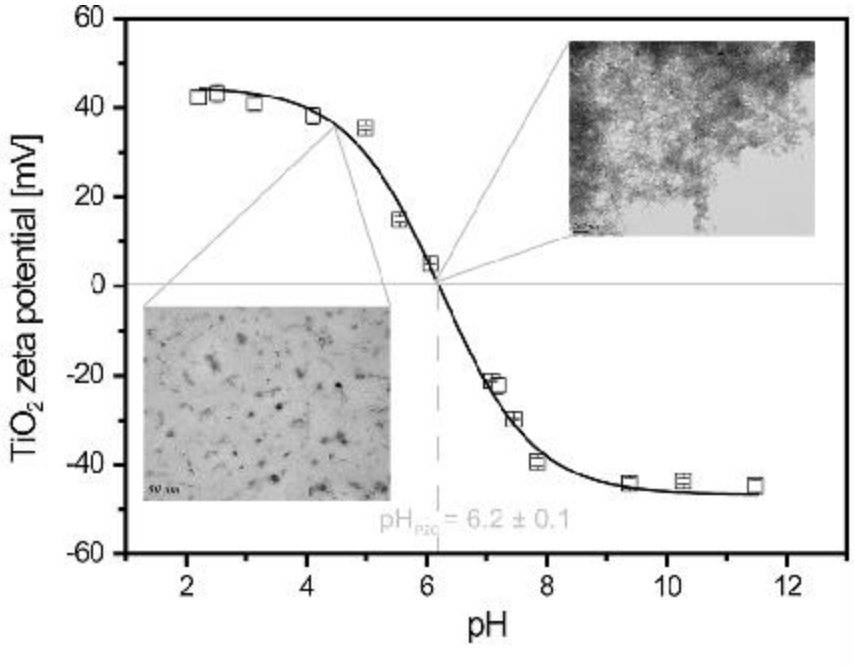

Figure 19. Variation of the zeta potential for TiO2 on pH in a KNO_3 electrolyte [70].

2.3.4. Temperature effect on zeta potential

Temperature indirectly affects zeta potential due to its impact on the density and viscosity of the electrolyte. Additionally, when it comes to particulate fouling, higher temperatures reduce the activation energy that causes particles to adhere. Overall, the effect of temperature on the IEP and zeta potential is complex. For example, magnetite showed a decrease in pH_{IEP} up to 200°C, followed by a slight increase at higher temperatures as shown in Figure 20 [69].

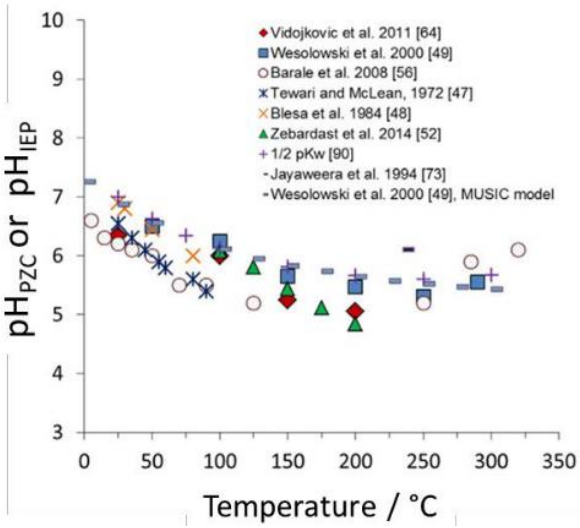

Figure 20. pH of neutrality of water corresponding to the isoelectric point or point of zero charges of magnetite on temperature [69].

Figure 20 supports the theory that the magnetite particles in typical PWR conditions are negatively charged because of the operating pH PWR (6.9-7.4 (300°C)) [69].

2.3.5 Effect of ionic strength on zeta potential

The strength of the electrolyte ions significantly impacts the magnitude of the zeta potential. Specifically, an increase in the strength of the electrolyte ions, achieved by raising the concentration of non-specifically adsorbed ions, is expected to result in a decrease in the thickness of the electrical double layer (EDL). Consequently, a decrease in the magnitude of the zeta potential is observed as shown in Figure 21.

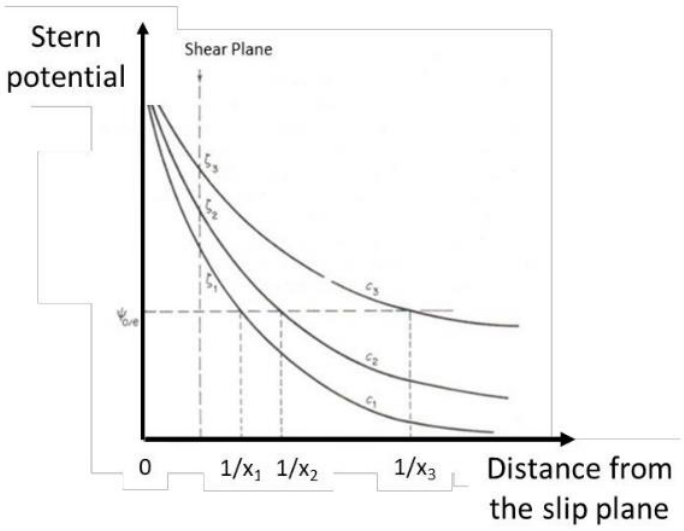

Figure 21. Stern potential on the distance from the slip plane. When the concentration (C1 > C2 > C3) of not specifically adsorbed ions is increased the zeta potential value decreases (ζ 1 < ζ 2 < ζ 3)[70].

2.4 The structure of CRUD formations in LWRs

The schematic of CRUD deposition on cladding material is show in Figure 22 [71]. The characteristics of fuel CRUD from discharged fuel rods have been extensively investigated over the last three decades. Fuel CRUD mainly consists of iron, nickel and chromium oxides depending on the structural materials used in a particular plant. Fuel CRUD is usually thin and relatively porous in the outer layer but dense in the inner layer.

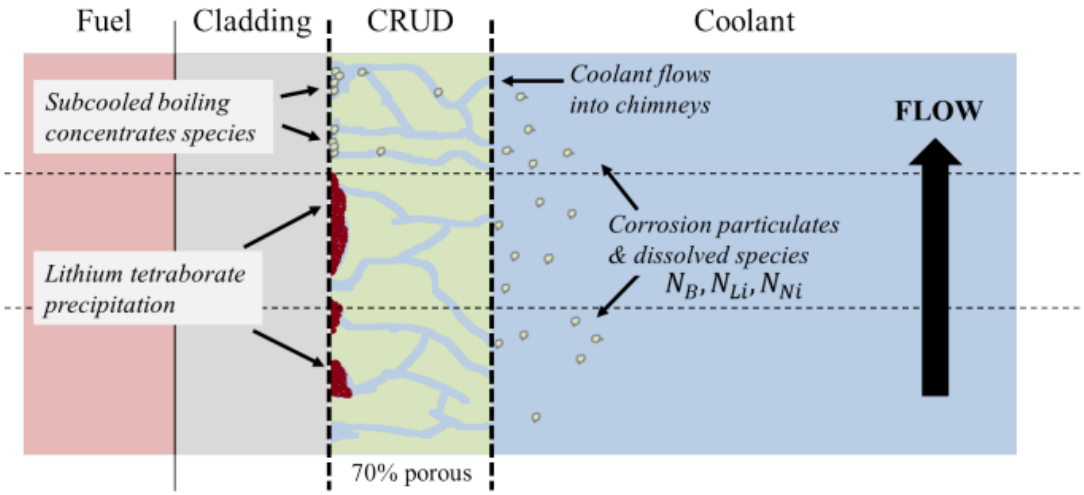

Figure 22. Schematic of CRUD deposition on fuel cladding in LWRs.

The adhesion properties of CRUD particles or agglomerates on fuel rods is still a puzzle to nuclear world. Little, if any, information is reported about the characteristics of fuel CRUD before discharging in pool due to its inaccessibility. It is uncertain if the fuel CRUD can, after pool discharge, largely preserve its characteristics appearing during reactor operation. To prevent CRUD growth, various strategies are employed, including (1) Water Chemistry Control: Proper control of water chemistry, including pH, dissolved oxygen levels, and the concentration of impurities, helps minimize CRUD formation; (2) CRUD Mitigation Additives: Additives may be introduced into the coolant to mitigate CRUD deposition. These additives can interact with CRUD precursors or modify the CRUD properties to reduce its impact; (3) Improved Cladding Materials: Ongoing research focuses on developing improved cladding materials with enhanced resistance to CRUD deposition and corrosion. Even after these mitigation strategies CRUD deposition on fuel rods is still a major concern in nuclear community. To add to this, the retention of radioactive CRUD from fuel reactors is rather difficult and expensive.

2.5 Particle Size Distributions and Physical Removal of CRUD Particles

The Chemical and Volume Control System (CVCS) typically eliminates most corrosion particles in a nuclear power plant. These particles are divided into categories based on size: colloids are substances with a size ranging from 1 to 500 nm. Conversely, substances with a diameter smaller than 1 nm and larger than 500 nm are considered soluble and suspended particles, respectively. In LWRs, only particles smaller than 200 nm are generally classified as colloids due to the filter size used. Particles smaller than the removal filter size are dispersed in the coolant and may be deposited along the cooling circuits of the reactor. However, it is also possible for particles to be deposited before being eliminated by the filters. Based on plant investigations, during undisturbed power operation, the majority of the circulating corrosion products (<90%) are in varied size distribution raining from 1- 1000 nm.

2.6 The transition to ATF fuel cladding

Over the last six decades the nuclear industry has been using varied alloyed forms of zirconium as a fuel cladding material. In the case of Zircaloy at normal operating conditions, the major factors impacting the cladding degradation are hydrogen embrittlement and radiation swelling. Under normal operating conditions, Zircaloy forms an oxide layer that impedes the corrosion of the cladding in the coolant environment. However, at elevated temperatures (above 800 ˚C), Zircaloy exhibits poor oxidation kinetics. The most crucial scenario is the loss of coolant due to breakthrough oxidation of fuel cladding material. Zircaloy cladding oxidizes rapidly in water steam and generates enormous heat due to the exothermic reaction shown below, which embrittles the fuel cladding.

$$Zr + 2H_2O = ZrO_2 + 2H_2\uparrow,\ \Delta H = -584.5\ kJ/mol\ at\ 1200\ ^\circ C \quad 2.6.1$$

The concept of Accident Tolerant Fuels (ATF) originated following a Loss Of Coolant Accident (LOCA) at Fukushima Daiichi, Japan in 2011. To prevent similar scenarios in the future, there is an urgent need to develop an ATF cladding material that enhances the robustness of LWRs in normal and possible accident conditions.

Monolithic iron-chromium-aluminum (FeCrAl) alloys are excellent candidates to replace Zircaloy as a cladding material. FeCrAl alloys exhibit excellent resistance to oxidation at high temperatures in steam up to 1300°C [74]. They also have good mechanical properties at temperatures above 400°C[75]. The hydrothermal corrosion resistance of FeCrAl alloys at temperatures in the vicinity of 300°C is excellent due to the formation of a protective passivating oxide[76]. Currently, the environmental resistance capabilities of FeCrAl as a fuel cladding material are being evaluated in the entire fuel cycle. Since FeCrAl alloys are considered leading ATF candidates it is essential to examine the CRUD deposition behavior on these alloys. Hence a part of this research work was focused on understanding the model CRUD deposition on the current (Zircaloy) and future cladding (FeCrAl) materials.

2.7 Objectives of the current study

The overarching goal of this Ph.D. thesis is to advance the nuclear community's understanding of CRUD by studying the electrokinetic behavior of model corrosion products and their deposition on cladding materials *outside* the reactor environment. First, a reliable and repeatable synthesis route was sought to closely replicate the CRUD particles found in LWRs, yielding non-stoichiometric nickel ferrites of varied sizes and compositions. Next, the synthesis process was

modified to more closely replicate the reducing environment of a reactor, and produce the full range of spinels found naturally in that environment. Finally, CRUD deposition on new ATF materials such as FeCrAl was investigated, as these are critical to future reactor design. Each of these goals is described in more detail below.

Objective 1 – Develop reliable procedure for synthesizing a range of nickel ferrite nanoparticles that closely resembles the naturally occurring CRUD particles in PWRs/BWRs to enable further experimentation.

As CRUD is mainly composed of nickel ferrites it was important to investigate the different synthesis routes through which these inverse spinel ferrites can be synthesized. According to the literature, nickel ferrite has been synthesized by sol-gel [77], solvothermal [78], co-precipitation [79], solid state reaction [80], and hydrothermal [81] synthesis processes. Many of these techniques yield nanoparticulate materials (typically seeking 10- to 50-nm particles) of uniform spherical shape and amorphous structure. In contrast, the PWR corrosion products are typically 500 to 1000 nm in size, crystalline [82], and polyhedral in shape [83]. Thus, the goal of this stage of the work was to obtain a highly crystalline CRUD at operating conditions close to LWRs using a simple, low-cost hydrothermal synthesis method without subsequent thermal annealing.

Objective 2 – Modify synthesis to achieve the (larger) range of stoichiometry found in reducing environments of PWRs/BWRs

In PWRs, the reactor is under a pressure of 160 atm, while operating at 325˚C. Whereas in BWRs, the reactor is under a pressure of 60 atm, while operating at 288˚C. Both PWRs and BWRs

are susceptible to cracking/environmental degradation in the austenitic stainless-steel components due to stress corrosion cracking (SCC). The electrochemical potential (ECP) at which the LWR reactors operate play a crucial role in SCC. Both PWR and BWR reactors operate under reducing environments to reduce the occurrence of SCC. Thus, CRUD particles were synthesized in reducing environments to more accurately reflect the reactor environment.

Objective 3 - Understand deposition of CRUD products on current and future cladding materials.

Two variants of FeCrAl, namely $Fe_{12}Cr_{5.5}Al$ [Powder Metallurgy (PM-C26M)] & $Fe_{21}Cr_{5.5}Al$ [Ferritic Alloy-Sandvik Material Technology(FA-SMT)] were explored as alternatives to Zircaloy cladding. Deposition of CRUD from dissolved ions onto these surfaces was conducted in a simulated BWR test loop at GER to develop an understanding of how thickness, composition and morphology of CRUD differed between fuel cladding materials.

3. Characterization Methods

3.1 X-ray diffraction analysis

XRD is a powerful technique through which crystallographic structural information about a material can be obtained. Incident X-rays interact with the specimen followed by the emission of fluorescent X-rays, scattered X-rays, and electrons. Scattered X-rays play a vital role in obtaining the necessary structural information of the material, since their wavelength is comparable to the interatomic spacing (~ 2-3 Å) in a crystal.

Crystallographic analysis makes use of Braggs law (Figure 23) [84] to obtain the scattered X-rays that undergo constructive interference at various angles, producing a plot of intensity vs. angle. The peak positions and intensities are determined by the crystal structure, i.e., peak position is determined by the interatomic distances while the intensity is determined by the types of atoms and their positions within the unit cell. The scattering from the specific set of parallel planes of atoms causes constructive interference in specific directions characterized by the Bragg angle, and thus provide a fingerprint for identifying and discriminating between chemically similar (but structurally distinct) phases. Furthermore, the size of nanoparticles can be estimated from the width of the XRD peaks using the Debye-Scherrer formula shown in Figure 23, where D is the crystalline size of the nanoparticles, K is the Scherrer constant (0.98), λ is the wavelength (1.54 Å in the case of this work), and β is the full width of the X-ray peak at half maximum (FWHM).

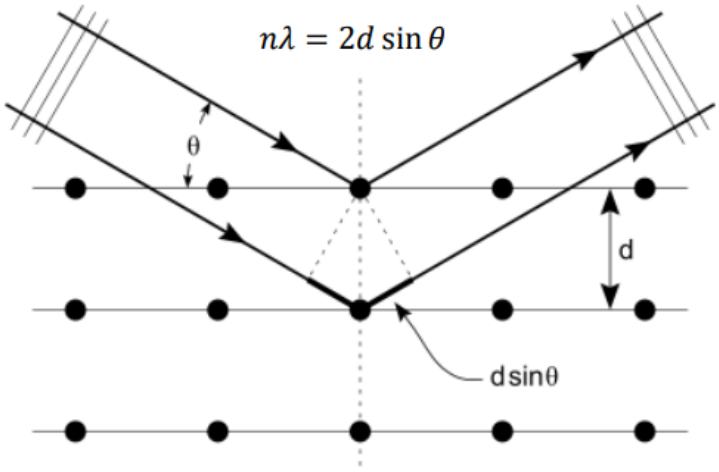

$$d_c = \frac{k\lambda}{\beta \cos\theta}$$

Figure 23. X-ray diffraction. The illustration on the left shows the generation of a Bragg reflection from a horizontal family of planes, with spacing d and incident angle q, related through the Bragg equation $n\lambda = 2d\sin\theta$. The specific set of d-spacings obtained from XRD offer structural information and phase identification. On the right is the Scherrer formula for calculating the crystal size of the particles, dc, based on the width b of a diffraction peak.

3.2 Scanning Electron Microscopy (SEM)

Scanning electron microscopy (SEM) is an imaging technique for determining the surface topography and morphology of a sample. Nominally the human eye has a resolution limit of ~ 0.1 mm, whereas an optical microscope's resolution limit is ~ 0.0002 mm. As the resolving power of a microscope is a wavelength-dependent property, by replacing the light source with electron source (λ~ 1- 10 pm) and optical lenses with electromagnetic lenses, electron microscopes were developed with a better resolution limit of ~ 5 x 10^{-6} mm.

In SEM, when the incident electrons interact with the specimen (Figure 24) [86], numerous signals are produced by both inelastic and elastic scattering. In the case of inelastic scattering where the incident electron loses some of its energy, specimen electrons can be liberated from their atoms, generating secondary electrons. Some of these low-energy (< 50 eV) secondary electrons escape

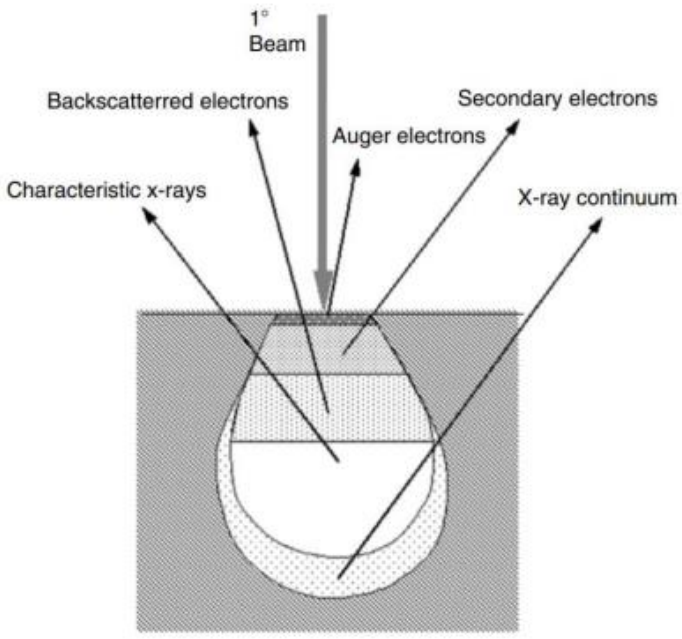

Figure 24. Schematic representation of the interaction of a high energy electron beam with a solid sample and the information that can be obtained from different depths. Typically, SEM uses secondary electrons to generate images and characteristic X-rays for elemental data[85].

the surface and can be collected to obtain the information about the texture and surface roughness of the specimen [86]. Elastic events produce backscattered electrons, where an incident electron undergoes multiple scattering events and leaves the specimen at an angle greater than 90° and with energy just slightly less than its incident value. Being higher energy than secondary electrons, these backscattered electrons can come from a greater depth (and wider area) of the specimen. As a result, the lateral resolution is much worse in this imaging mode, though it is sensitive to the atomic density of the specimen and can be used for elemental discrimination. True determination of the elemental composition of the specimen can be obtained by adding an X-ray detector to the SEM, for a technique known as Energy Dispersive X-ray Spectroscopy (EDX or EDS). Specimen atoms which are ionized by the primary beam can generate characteristic X-rays when outer shell

electrons relax to fill vacant inner shell orbits. The emitted photon has energy corresponding to the difference in orbital energies, and thus contains an elemental fingerprint.

3.3 Transmission Electron Microscopy (TEM)

TEM is one of the most powerful and versatile tools employed in soft matter, biology, and especially in material science. The basic working principle of TEM is same as a light microscopy except the source is replaced by a high energy electron beam. Electrons have much smaller wavelength (λ~ 1-10 pm) than a light source and the thickness of the specimen must be less than ~100 nm to be electron-transparent. Under those conditions, the incident electrons interact with the specimens' atoms and electrons yielding detailed information on the crystal structure, grain orientation, dislocations, and grain boundaries of the material under study.

There are three different types of imaging modes in TEM [88]. As shown in Figure 25 (a) , a bright field image is produced when the electrons are transmitted through an aperture, resulting in the background (no specimen to scatter electrons) appearing bright while specimen regions (that scatter electrons away from rather than through the aperture) are shades of darker gray based on the scattering strength of the particle. In the case of dark field imaging the opposite is true: collecting the scattered electrons while blocking the transmitted electrons results in a dark background (because scattering is negligible), while the strongly scattering regions of the specimen are very bright as shown in Figure 25 (b). Dark field images can either be produced by moving the objective aperture off-axis to exclude the unscattered beam while collecting a scattered beam (a geometry that is victim to off-axis aberrations of the imaging system), or by tilting the primary beam off-axis and centering a specific scattered beam on the axis to pass through the centered

aperture for aberration reduction. Diffraction patterns from the specimen can be obtained by adjusting the back focal plane of the objective lens for the intermediate lens to magnify and enables the identification of the crystal structure and symmetry Figure 25 (c).

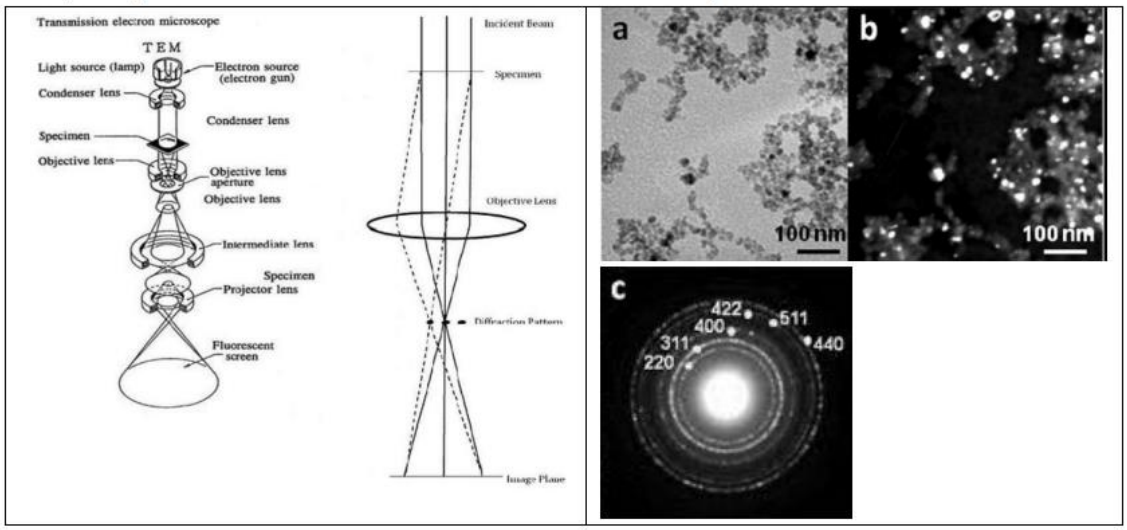

Figure 25. Working principles of TEM . The illustration on the left shows simplified diagram of a TEM and a typical ray diagram. On the right are examples of a bright field image (a), a dark field image (b), and a diffraction pattern (c)[87].

3.4 Fourier-transform infrared spectroscopy (FTIR)

FTIR is one of the versatile tools which identifies the molecular footprints of the materials [89]. In this technique, broadband infrared light is used to illuminate the specimen as shown in Figure 26. Different bonds absorb the light according to their natural frequencies, which can be correlated with known values to determine chemical bonds and composition. In practice, an interferometer to scan through the combination of IR frequencies. Then, the signal is decoded by applying Fourier transformations and a mapping of the spectral information is produced.

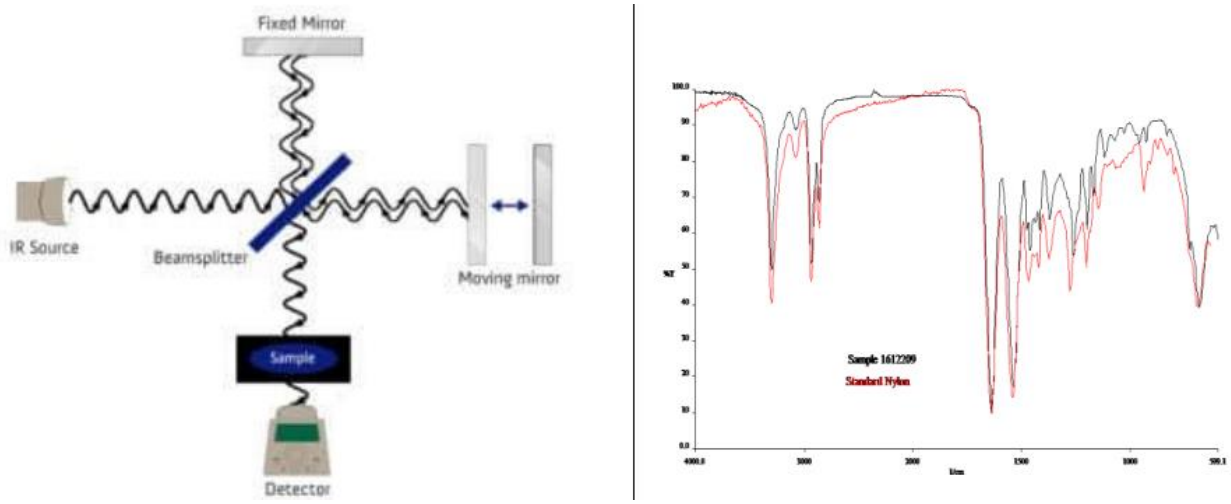

Figure 26. Cartoon illustration of the interferometer set-up for FTIR (left) along with an example of the spectral data obtained from this technique (right)[90].

From the sample point of view, especially in the case of powdered samples, there are four different measurement methods: the KBr pellet method, the Nujol method, the diffuse reflection method and the Attenuated Total Reflection (ATR) Method. In the case of the pellet method, a pellet of the sample powder is made under pressure using potassium bromide (KBr) or cesium iodide (CsI) and can be used to measure the composition of the sample. In the Nujol method, a sample powder is dispersed in a solution that has low absorption in the infrared region and the measurement is carried out. In the diffuse reflection method, as light is shone on the sample some gets absorbed and undergoes multiple scattering events in the matrix before emerging from the surface as a diffuse reflection which is collected to create the spectrum. In all the above-mentioned methods, the sample must be pretreated. However, in the case of ATR no such treatment is required as the infrared spectrum is obtained when the light undergoes total internal reflection at the interface between a high refractive index ZnSe or Ge prism and the sample.

3.5 Inductively coupled plasma mass spectrometry (ICP-MS)

ICP-MS is a method of elemental analysis, which measures elements, not molecules and compounds. ICP-MS is similar to inductively coupled plasma optical emission spectroscopy (ICP-OES), but ICP-OES uses an optical spectrometer to measure the light emitted from elements as they pass through the plasma, whereas ICP-MS measures the elements (ions) directly. While both techniques provide fast analysis of multiple elements in a sample, ICP-MS provides much lower detection limits than ICP-OES, making it a better choice for trace element analysis.

ICP-MS instruments are made up of an ion source (ICP), mass spectrometer(s) – typically a scanning Quadrupole mass filter – and detector(s). The ICP is operating under atmospheric pressure, and the MS and detector are operating in a vacuum chamber. An ICP-MS device also includes a vacuum pump, vacuum interface, and several electrostatic ion "lenses" to concentrate the ions across the system. Most modern ICP-MS systems also include some device or mechanism for resolving spectral interference as shown in Figure 27.

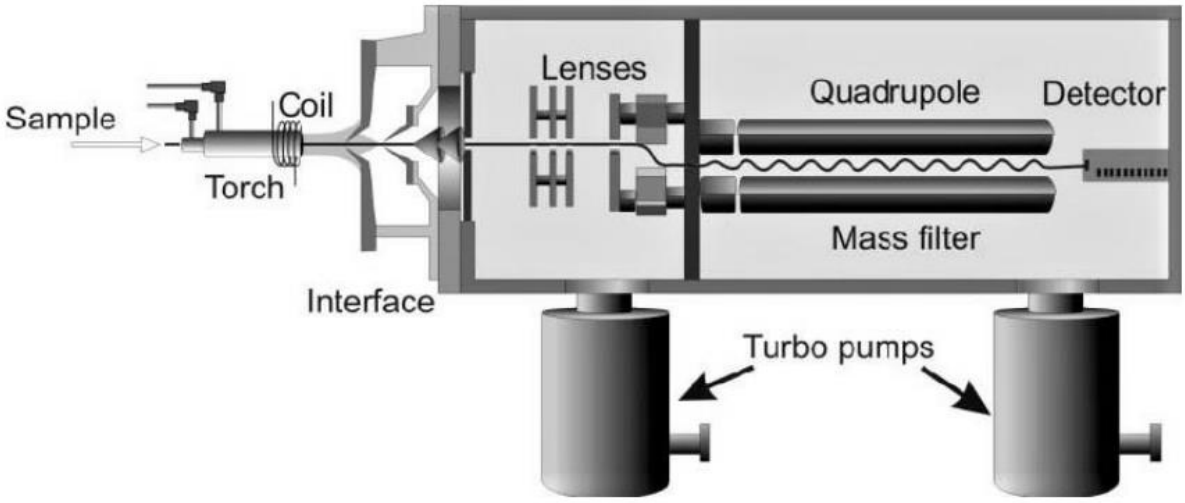

Figure 27. Cross-sectional drawing of an ICP-Mass Spectrometer showing the main components [91].

3.6 X-ray photoelectron Spectroscopy (XPS)

XPS exploits the photoelectric effect [92] where X-rays (photons) irradiate a sample and eject electrons from the surface (Figure 28, left). The XPS method is based on the principle that kinetic energy and the number of escaped electrons are measured simultaneously when the sample undergoes X-ray irradiation under high vacuum conditions. Electrons of different energies follow different paths through the detector which allows the software to differentiate the electrons and produce the spectra (Figure 28, right).

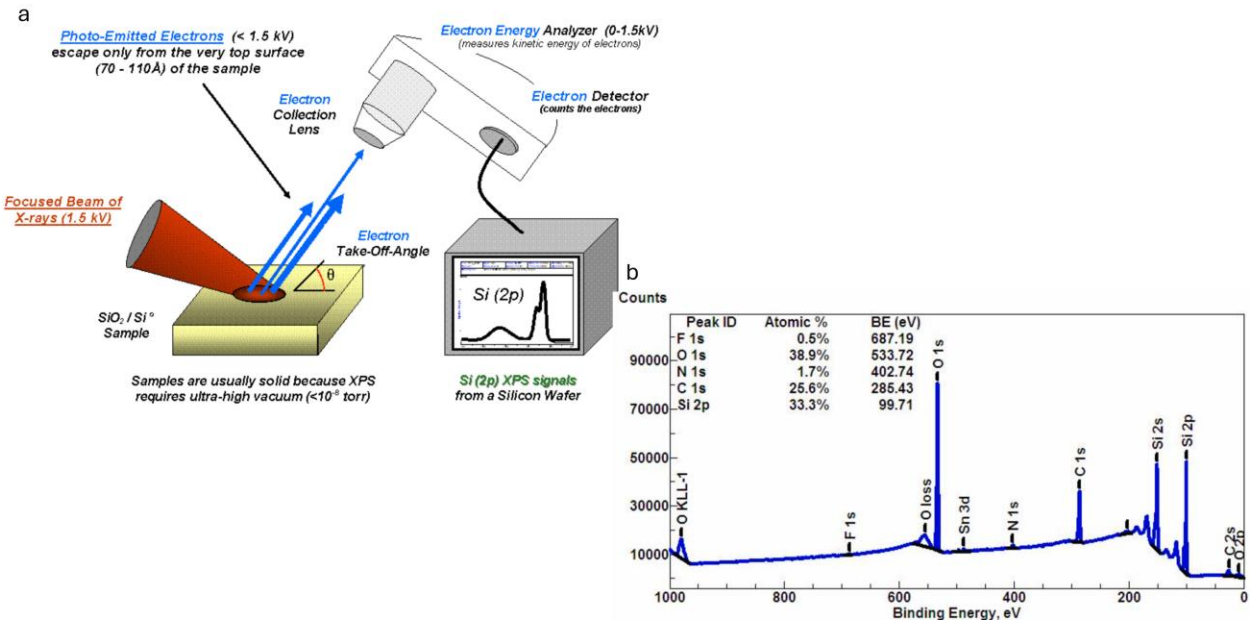

Figure 28. Diagram depicting the instrumentation of the X-ray photoelectron spectrometer along with energy spectra [93].

Atoms present in compound being tested by XPS are determined according to the equation:

$$E_{binding} = E_{photon} - (E_{kinetic} + \Phi) \quad 3.6.1$$

In here binding energy is the entanglement energy of the electron attracted to the nucleus; photon energy is the incident X-ray energy, kinetic energy is the energy of the electrons emitted from the sample; work function is also a chemical binding energy that's related to the minimum energy needed to remove an electron from an atom. The work function and the photon energy are known, and the kinetic energy is measured by the detector. Thus, the binding energy, which is element-specific, can be determined according to:

$$BE = h\nu - KE \quad 3.6.2$$

For example, electrons in orbitals closer to the nucleus have higher binding energy than electrons that are further away from the nucleus. Subshells also have different energies. For example, electrons in s, p, and d orbitals have different energies than electrons in other subshells. Because

the energy levels are atom-dependent, the list of binding energies enables determination of a sample's composition.

Furthermore, because the energy discrimination of the XPS is better than that of the EDX detector, small changes in binding energy due to chemical shifts which are not detectable via EDX can be determined using XPS.

4.Experimental Details

4.1 Materials and Methods for CRUD particle synthesis.

There are numerous methods for the synthesis of CRUD particles [77] using solid state, liquid or gas phase reactions. Control over the size of the particles and the purity of the product has always been a challenge for solid state processes as this mechanism involves the relatively slow diffusion of atoms in the solid state. On the other hand, hydrothermal synthesis makes use of the liquid for the transport and mixing of its reactants, leading to faster diffusion and more uniform distribution of components.

A typical reaction chamber for hydrothermal synthesis is shown in Figure 29, consisting of a stainless steel autoclave with a Teflon liner. This synthesis method takes advantage of high pressures generated by heating the liquid in the sealed vessel to increase the solubility of reactants at mild temperature conditions. Even materials which are not stable at elevated temperatures under ordinary atmospheric pressures can be synthesized using this method. Particles of different shapes can be synthesized by varying the solvent, and great control over the particle size and composition

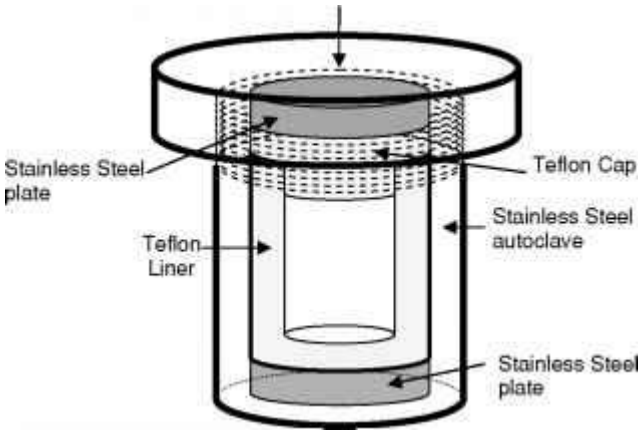

Figure 29. Cross-sectional illustration of the hydrothermal reactor. Reactants are sealed within the autoclave to generate pressure as the vessel is heated[170].

is obtained by varying the concentration of the solvent to manipulate pH, or by replacing the ambient environment with an inert or reducing gas.

The motivation for this work is to replicate the non-stochiometric nickel ferrites that are found in nuclear power reactors in a laboratory environment. A highly crystalline product needs to be obtained at relatively low temperatures using a simple, low-cost synthesis method without subsequent thermal annealing. Hydrothermal synthesis offered all of these. Since the desired iron precursor, goethite (α-FeOOH), was not available commercially, it was necessary to synthesize this compound before the ferrites could be produced.

4.1.1 Synthesis of Goethite (α-FeOOH)

In this study, both hydrothermal and co-precipitation routes were tried for the synthesis of goethite, with a goal of obtaining single phase α-FeOOH without additional phases present in the product. The XRD spectra of the obtained powders (Figure 30) show that both techniques do yield α-FeOOH (peaks labelled *).

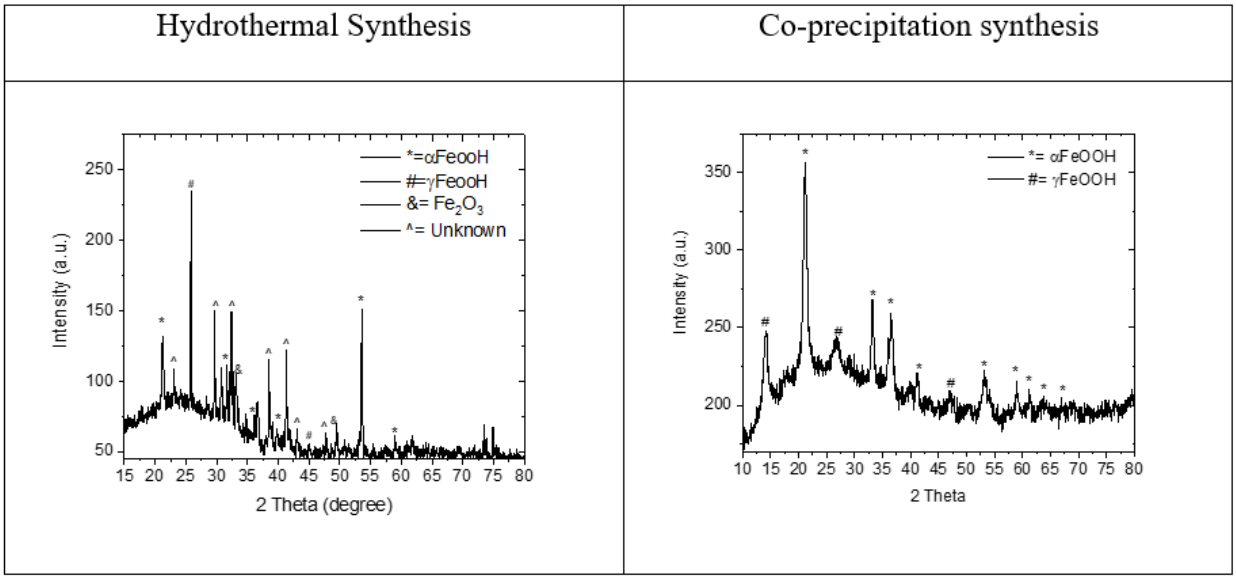

Figure 30. XRD spectra from goethite (α-FeOOH) obtained by hydrothermal (left) and co-precipitation (right) synthesis. Peaks from multiple phases are found in both samples, thought the co-precipitation yielded a better product overall.

However, the hydrothermally synthesized powder (Figure 30, left) contained a variety of other phases (#, &, ^ markers). The co-precipitation synthesis (Figure 30, right) did have a small amount of undesired g-FeOOH (labelled #), but was deemed acceptable. The recipe, adapted from [94], is summarized below.

Ferrous sulfate heptahydrate ($FeSO_4 \cdot 7H_2O$) and potassium hydroxide (KOH) were used as precursor materials. To initiate the synthesis process, 0.5M of $FeSO_4 \cdot 7H_2O$ is dissolved in 20 mL of deionized (DI) water and 0.2M of equal volume KOH stock solution is added drop by drop. Once the precursor mixture is stirred homogenously, co-precipitation synthesis was carried out at 45°C for 18 hrs. The obtained yellow powder was washed and dried at 45°C. The morphology of the obtained particles was studied by using SEM and found to be the needle shaped structures consistent with α –FeOOH, and the phase was subsequently confirmed by XRD.

4.1.2 Hydrothermal synthesis of nickel ferrites

Although co-precipitation proved preferable for the synthesis of goethite, hydrothermal synthesis, with its higher-pressure condition, was still needed for the synthesis of nickel ferrites. The recipe, adapted from [95] starts with the synthesized Goethite (α-FeOOH) from the co-precipitation synthesis described earlier, combined with nickel nitrate hexahydrate ($Ni(NO_3)_2 \cdot 6H_2O$) along with 2M NaOH solution.

A series of solutions with different concentrations were prepared from the Ni precursor to yield metal precursor ratios ([Ni]:[Fe]) between 0.25 and 0.5, this maximum corresponding to the nominal ratio found in stoichiometric $NiFe_2O_4$ [Table 6]. All synthesis reactions were conducted in a Parr 5500 compact reactor with a 100 mL Teflon liner using the Parr 4848 reactor controller in ambient atmosphere (Figure 31). The reactor was ramped at 2°C /min., held at temperature for 6 hours, and then allowed to cool radiatively to room temperature. Reaction temperatures explored the range 100°C to 250°C. The obtained brown powders were centrifuged with DI water at 9000 rpm followed by drying the particles at 60°C overnight.

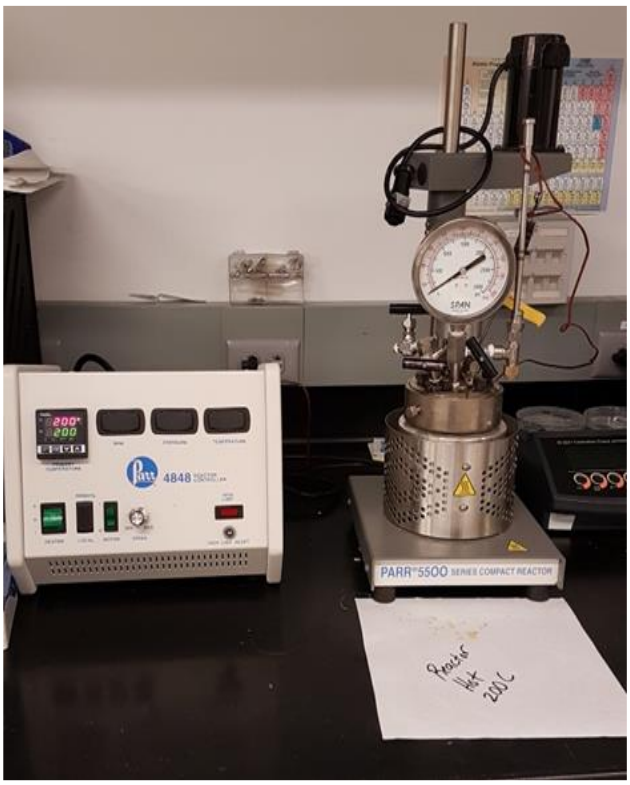

Figure 31. Photograph of the Parr reactor used for the hydrothermal synthesis of nickel ferrites, including the controller (left of image) and autoclave assembly (right of image).

Table 6. Translation table relating the molarity of the starting suspensions to the precursor concentration ratio [Ni]:[Fe]. Only when a single-phase product is obtained does this ratio correspond to the composition of the obtained nickel ferrite.

Ni suspension molarity: Fe suspension molarity	[Ni]:[Fe] Ratio of starting precursor materials
0.050M : 0.2 M	0.25
0.055M : 0.2 M	0.275
0.060M : 0.2 M	0.30
0.065M : 0.2 M	0.325
0.070M : 0.2 M	0.35
0.075M : 0.2 M	0.375
0.080M : 0.2 M	0.40
0.085M : 0.2 M	0.425
0.090M : 0.2 M	0.45
0.100M : 0.2 M	0.5

4.2 Materials and methods for CRUD ion deposition in a simulated BWR test loop

Figure 32 shows the schematic of the test loop located at GE-R. The objective of these tests was to determine the relative susceptibility of ferritic IronClad tubes (C26M and APMT) to develop surface CRUD as compared to austenitic type 304SS and bare Zircaloy-2 tubes. The nominal composition of the tube materials is listed in Table 7.

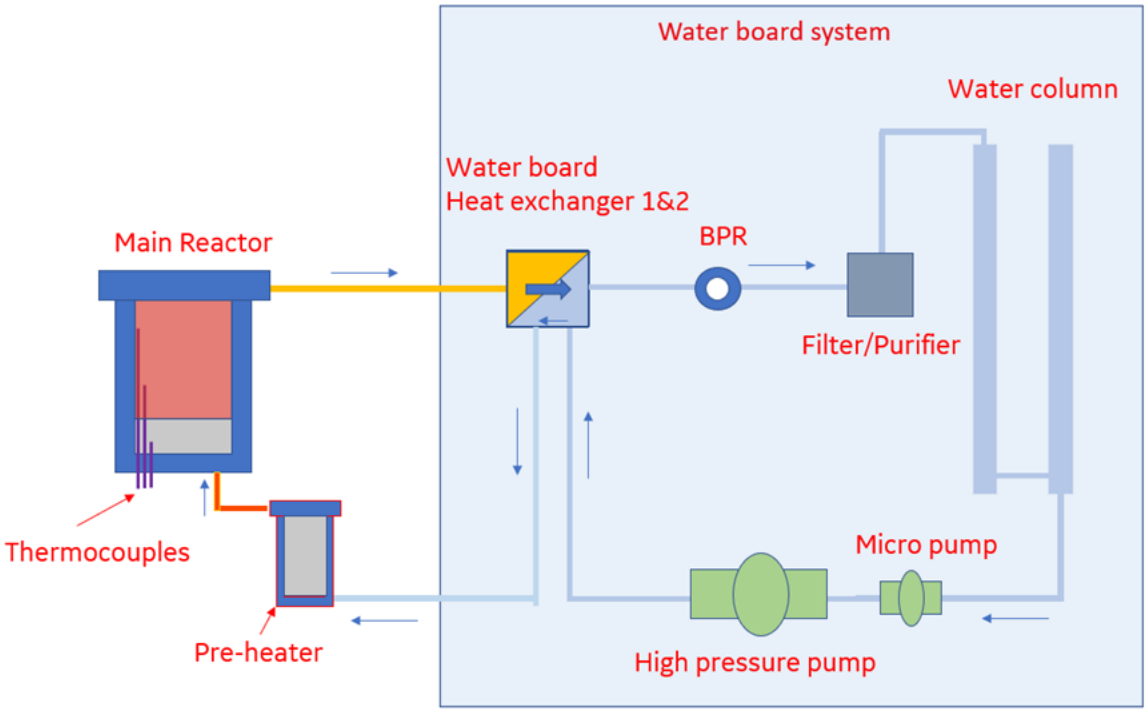

Figure 32. Schematic drawing of flowing autoclave test loop setup at GE-R that was used for this test[96].

Table 7.Chemical composition of tested tubes.

Tube designation	**Nominal composition in weight %**
Zircaloy-2	Zr + 1.5Sn + 0.15Fe+ 0.1Cr + 0.05Ni
Type 304 SS - austenitic	Fe + 18Cr + 8Ni + 2Mn
C26M - ferritic	Fe + 12 Cr + 6Al + 2Mo + 0.03Y
APMT - ferritic	Fe + 21 Cr + 5Al + 3Mo

Most tubes were heated from the inside, though some experiments proceeded without this heating. The external surfaces of the tubes were exposed to DI water simulating BWR conditions to precondition the surface of the tubes. Then a high concentration of nickel and iron salts were injected to accelerate CRUD deposition. Figure 33 shows the autoclave head with four cladding tubes that were fitted with heater rod inserts. This autoclave head was manufactured by Stern

Laboratories in Canada. Two of the rods were off-the-shelf stainless steel 304SS, one rod was APMT and one rod was C26M. The Zirc-2 tubes were tested separately under the same conditions. The wall thickness of the tubes was ~0.60 mm. Electrical power connections are on the top of the tubes, together with the thermocouples for measuring and recording the cladding surface temperature during the accelerated crud testing. Each cladding tube had two thermocouples installed on the ID (inner diameter) surface, 180° from each other. The thermocouple elevation was in the middle section of the heater rod. The length of heater rod was 175 mm and the power profile was uniform along its length. The heater rod was rated for 2.45 kW at 30 VDC, equivalent to heat flux of 40 W/cm². The total length of the heat rod/cladding assembly was ~ 1550 mm. The CRUD deposition conditions were simulated by performing a pre-conditioning step of immersion for 4 weeks in an autoclave with simulated BWR hydrogen water chemistry (HWC) (0.3 ppm hydrogen) at 288°C, followed by a rod heating stage for 2 weeks, then the injections of 25 ppm Ni^{2+} as nickel acetate and 12.5 ppm Fe^{3+} as ferric EDTA were performed for ~10 days (the injection time was generally limited by the time it took for the piping system to clear due to the injectable acetate and EDTA salts). During the testing, the cladding surface temperatures were recorded, together with the power dissipation of the heater rods. The electrochemical potential of the autoclave body against a Cu/Cu_2O reference electrode was also recorded.

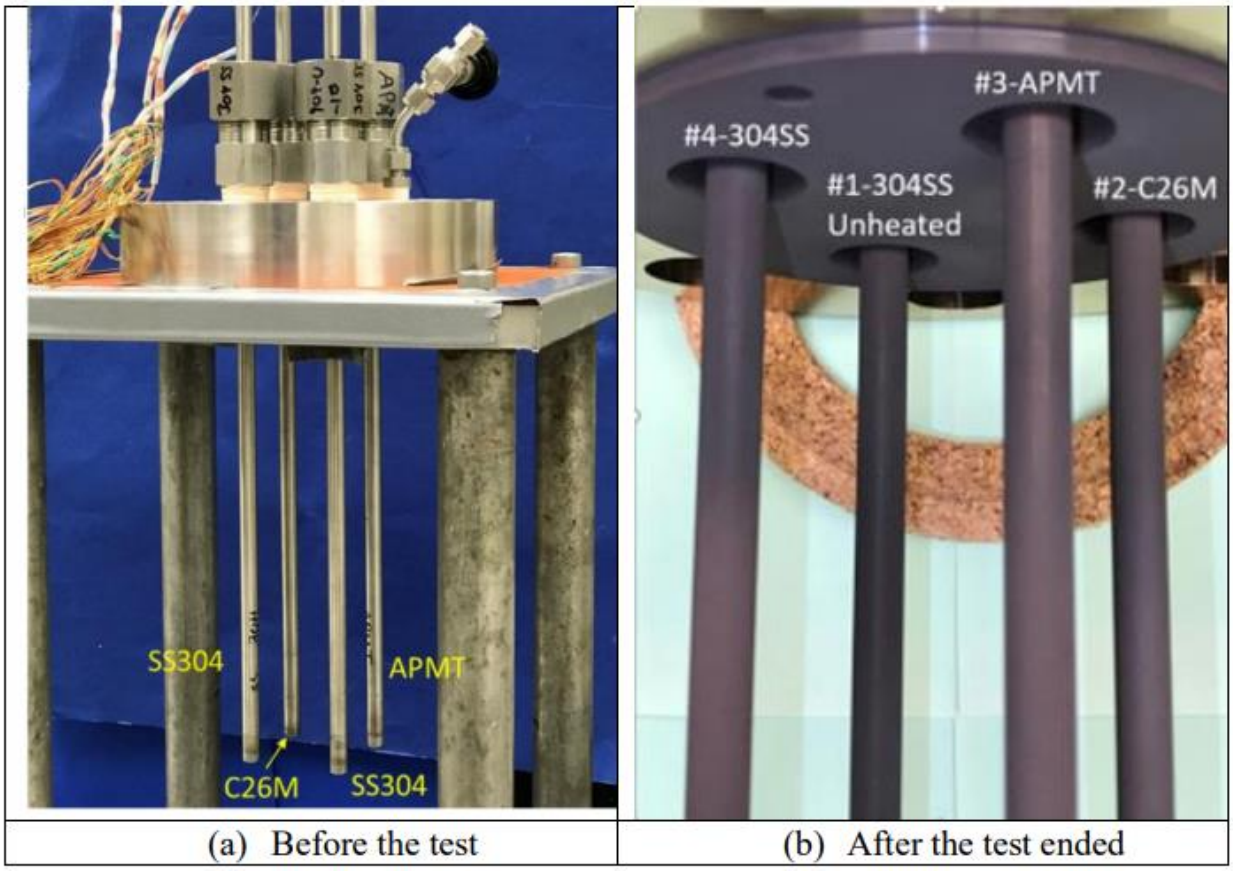

Figure 33. (a) Autoclave head built for the accelerated crud testing. (b) The four test rods after the CRUD testing.

5. Synthesis of CRUD Particles and Particle Size Evaluation

The majority of this chapter is the accepted manuscript of an article published by Taylor & Francis in the *Journal of Nuclear Technology* on 12/17/2022, available online DOI: https://doi.org/10.1080/00295450.2022.2161266 and reproduced here with the consent of the publisher. Additional figures and data have been included for sake of clarity.

5.1 Introduction

As discussed in Chapter 2, nickel ferrite ($NiFe_2O_4$) is one of the primary corrosion products formed from coolant pipes [97], tanks, and other surfaces in LWRs [82]. For example, CRUD deposition on fuel cladding may result in higher clad temperatures and may even lead to fuel failure [10]. Given the aggressive conditions in the field (irradiation), ferrite corrosion products are challenging to study *in situ*. By synthesizing nickel ferrite in a controlled laboratory setting, nonradioactive model particles can be used to study the generation, transport, deposition, and/or dissolution/crystallization of these corrosion products *ex situ*. Hence, this chapter describes the results of Objective 1, developing a reliable procedure for synthesizing a range of nickel ferrite nanoparticles that closely resembles the naturally occurring CRUD particles in PWRs/BWRs to enable further experimentation.

As LWR corrosion products are typically crystalline, and polyhedral in shape with a typical size range of 500 to 1000 nm [98]. A low-cost hydrothermal synthesis method was used to obtain the CRUD products. A process window for obtaining a single-phase product was targeted, with

(limited) control over stoichiometry within that window.

5.2 Results

At temperatures of 125°C and below, no reaction was observed in the composition range studied as shown in the photographs in Figure 34 (left, identical to starting precursors).

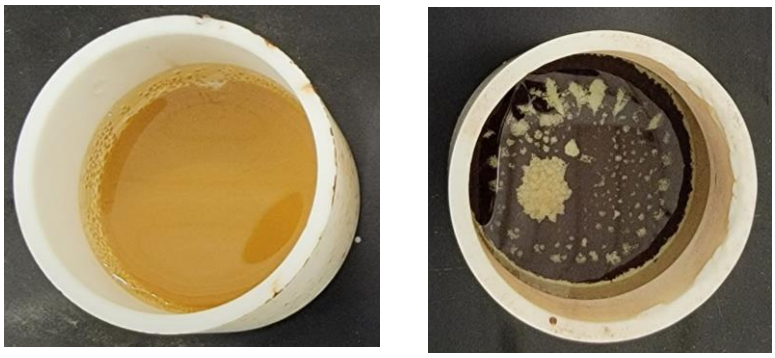

Figure 34. Powders obtained from hydrothermal synthesis at 125°C(left) & 150°C (Right) with 2M NaOH and Ni:Fe=0.35.

At temperatures of 150°C and higher, a reaction has occurred, resulting in a change in color (Figure 34, right). Figure 35 shows representative SEM images of the four distinct types of particles found in this study, obtained at different temperatures and starting compositions. The presence of octahedral particles is consistent with the expected morphology for the inverse spinel (cubic) nickel ferrite structure, Figure 35 (a). This morphology is similar to those of corrosion products found in nuclear plants [82] and thus should have bulk and surface properties that correspond with those of plant corrosion products. Additional morphologies were observed, including needle-like particles (Figure 35 (b)), large microparticles (Figure 35 (c)) and hexagonal platelets (circled, in Figure 35 (d). These different morphologies were inconsistent with the cubic nickel ferrite

structure and indicated the presence of other phases. X-ray diffraction was subsequently used to identify them.

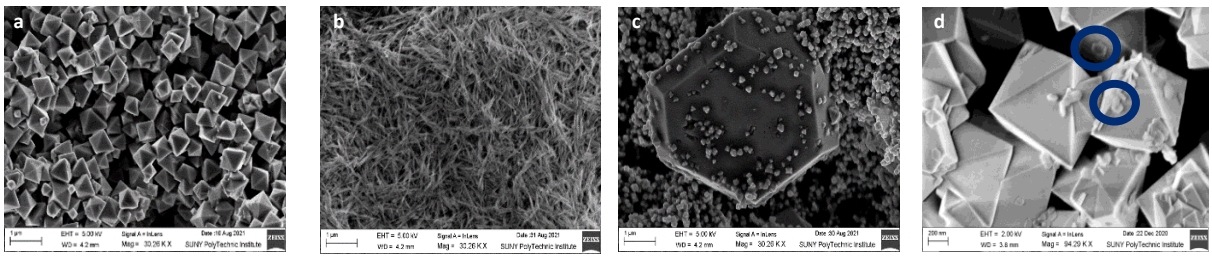

Figure 35. SEM images of the four types of particles found at different synthesis conditions. (a) Octahedral particles (~500 nm) consistent with cubic spinels; (b) needle-shaped particles; (c) large (several microns across) particles; and (d) hexagonal platelets. Images taken at different magnification in order to present salient features of each type of particle at a relevant scale.

Figure 36 shows XRD spectra for powders obtained with a starting [Ni]:[Fe] ratio of 0.30, and two different temperatures. Peaks were identified using the list of peak positions in Table 8. While nickel ferrite has no spectral interferences, goethite (α-FeOOH), hematite (α-Fe_2O_3), and theophrastite (β-$Ni(OH)_2$) have interferences, such as the peaks at 33.1°. The peak at 21.1°, is attributable only to the α-FeOOH , and thus is used as a unique marker for this phase. Similarly, the peaks at 39°, 52° and 59° are uniquely attributable to β-$Ni(OH)_2$. Therefore, in the absence of either the α-FeOOH or β-$Ni(OH)_2$ markers, the appearance a peak 33.1° was attributed to α-Fe_2O_3. In the subsequent XRD spectra, symbolic markers are used to indicate the phase identities, with "@" marking nickel ferrite peak locations, "^" used for α-FeOOH, "#" for α-Fe_2O_3, and "*" for β-$Ni(OH)_2$.

The spectra in Figure 36 indicate that powder obtained at 150°C contains nickel ferrite and α-FeOOH, while at 200°C and above, no α-FeOOH remains. At these temperatures, the product contains ferrite and α-Fe_2O_3.

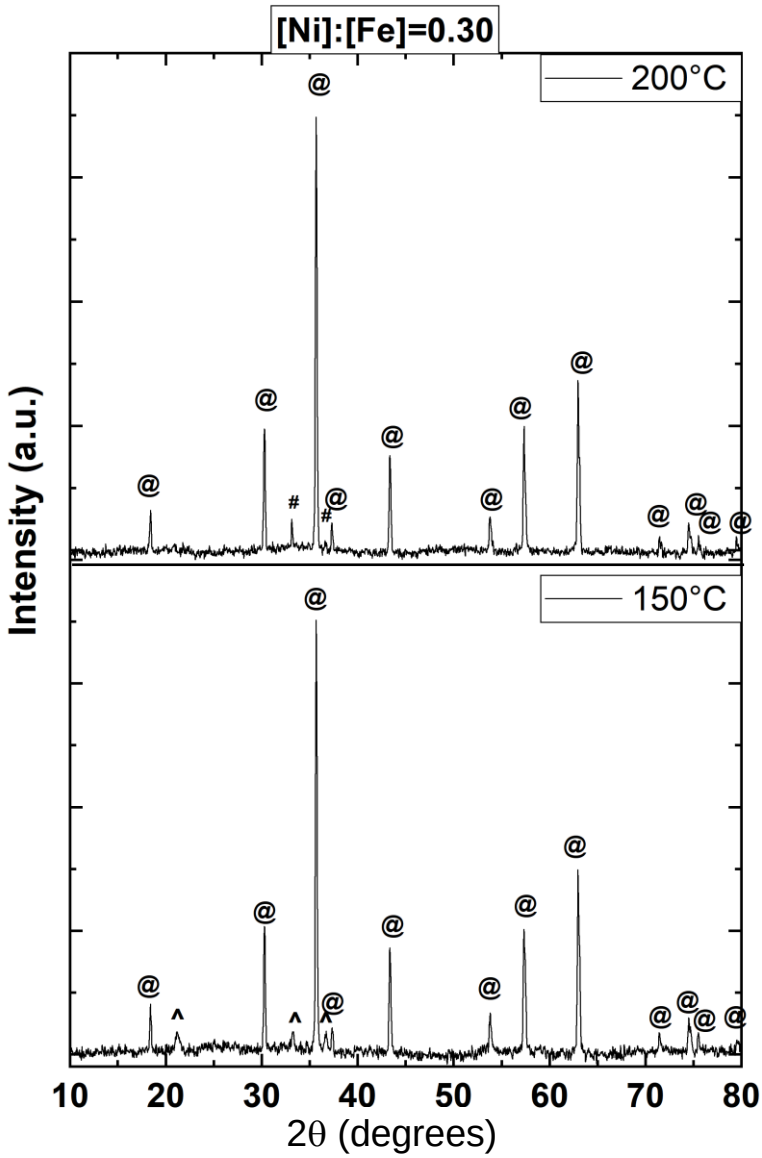

Figure 36. XRD spectra for powders obtained using [Ni]:[Fe] ratio of 0.30, at 150°C (lower) and 200°C (upper) containing nickel ferrite (@), α-FeOOH (^), and α-Fe_2O_3 (#). Several peak overlaps occur, but the presence or absence of the α-FeOOH (110) peak is definitive. At the lower temperature, some α-FeOOH remains, but at the higher temperature it has been entirely consumed to produce a mixture of nickel ferrite and α-Fe_2O_3.

Table 8.XRD Peak Positions and Miller Indices of Nickel Ferrite, α-FeOOH, α-Fe_2O_3, β-$Ni(OH)_2$.

Peak Position values, 2θ (°)	Nickel Ferrites (hkl) "**@**"	α-FeOOH (hkl) "^"	α-Fe_2O_3 (hkl) "#"	β-$Ni(OH)_2$ (hkl) "*****"
18.4	(111)			
19.3				(001)
21.1		(110)		
30.3	(220)			
33.1		(130)	(104)	(100)
35.7	(311)			
36.5		(111)	(110)	
37.3	(222)			
38.7				(101)
43.4	(400)			
52.2				(102)
53.8	(422)			
57.3	(511)			
59.2				(110)
63	(440)			
71.5	(620)			
74.5	(533)			
75.5	(622)			
79.5	(444)			

When attempting to identify β-$Ni(OH)_2$, a similar overlap occurs in 19-21° and at 33.1°, but several peaks at higher angles are well separated. As these peaks are relatively low intensity, however, additional synthesis reactions were carried out at 200°C using higher concentrations of Ni precursor to confirm their identity (Figure 37). Indeed, when [Ni]:[Fe] was increased to 0.5 (black spectrum) and even 0.75 (red spectrum), the nickel ferrite peaks remained unchanged, while the intensity of the XRD peak at 33.1° increased, as did all other distinguishable β-$Ni(OH)_2$ peaks, while no other iron-oxide peaks emerged. Therefore, under nickel-rich synthesis conditions, the

ambiguous peak at 33.1° was attributed to β-$Ni(OH)_2$ (*).With at least one marker for each of the phases of interest, then, a comprehensive analysis as a function of composition was undertaken.

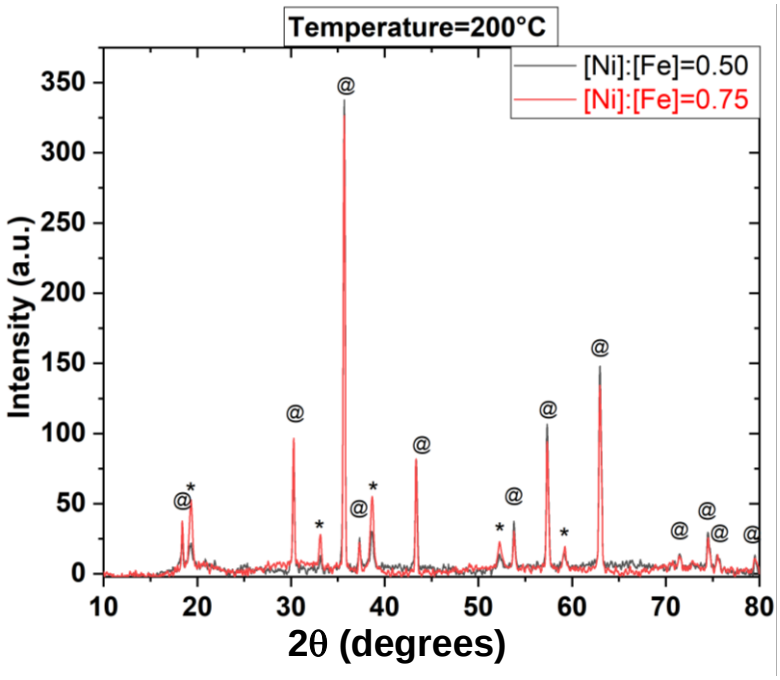

*Figure 37. XRD spectra for powders obtained at 200°C with [Ni]:[Fe] = 0.50 (black) and [Ni]:[Fe] = 0.75 (red). Nickel ferrite peaks are labelled @, β-$Ni(OH)_2$ are indicated with *. Despite the increase in Ni concentration, the height of unique ferrite peaks are unchanged, while the height of unique β-$Ni(OH)_2$ peaks increased. The increase in intensity for the 33.1° peak is therefore attributed solely to β-$Ni(OH)_2$ rather than ferrite.*

In Figure 38, three [Ni]:[Fe] starting ratios are shown. The upper spectrum is representative of the low Ni reactions, ([Ni]:[Fe] ranging from 0.25 to 0.325), which contains peaks from nickel ferrite and the precursor α-FeOOH. The middle spectrum, typical of mid-range [Ni]:[Fe] values (0.35 to 0.375), only has peaks corresponding the nickel ferrite phase, indicating a narrow window of compositions that yield a single-phase product at this temperature. Finally, the lower spectrum is representative of [Ni]:[Fe] ratios 0.4 to 0.5, containing peaks for nickel ferrite and β-$Ni(OH)_2$.

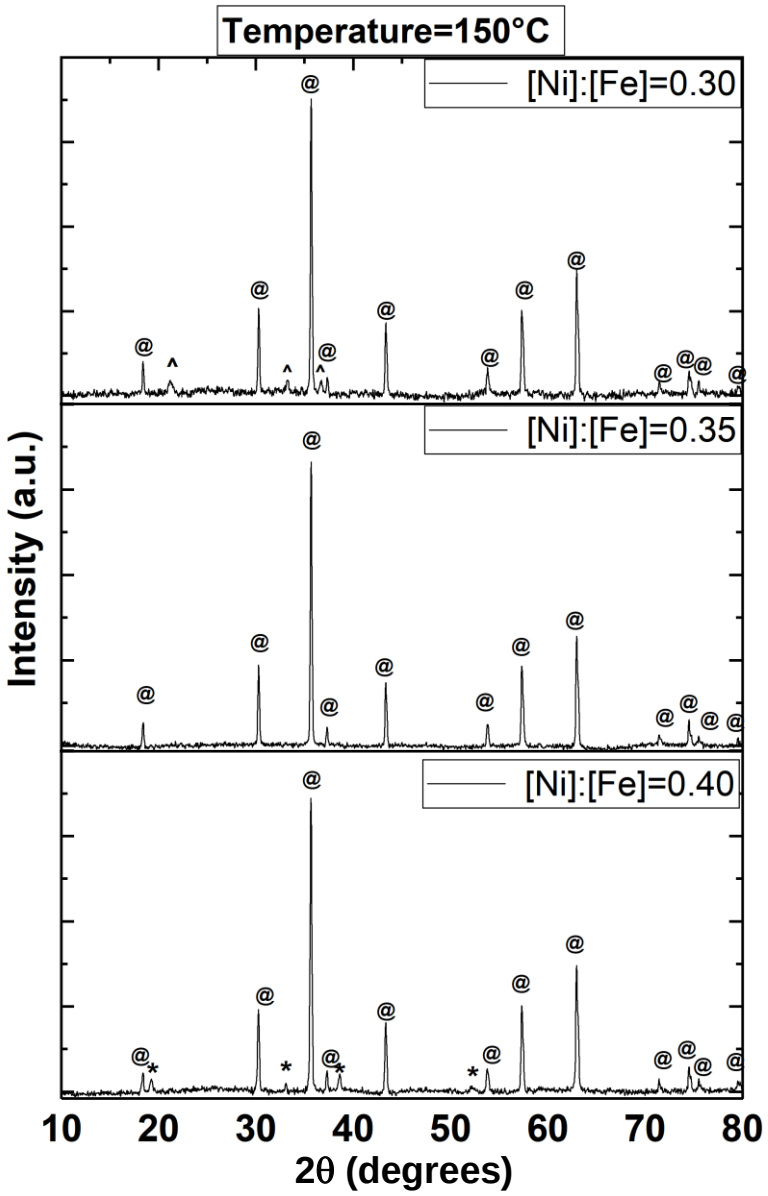

Figure 38. XRD spectra of reaction products obtained at 150°C for three representative [Ni]:[Fe] ratios containing nickel ferrite (@), α-FeOOH (^), and β-Ni(OH)$_2$ (*). While nickel ferrite is obtained for all starting compositions, the products obtained at this temperature may also contain α-FeOOH (upper spectrum), or β-Ni(OH)$_2$ (lower spectrum), depending on starting compositions.

At temperatures of 200°C-250°C, no α-FeOOH was observed for any of the syntheses. Figure 39 shows XRD spectra from the 200°C reactions as representative of this temperature range. The upper spectrum is representative of the Ni-poor reactions, which at this temperature corresponds

to [Ni]:[Fe] ranging from 0.25 to only 0.30. This spectrum contains peaks from nickel ferrite and α-Fe_2O_3. The middle spectrum, typical of mid-range [Ni]:[Fe] values (0.325 to 0.4, at this temperature), shows a single-phase nickel ferrite product. The lower spectrum contains peaks for nickel ferrite and β-$Ni(OH)_2$, occurring for [Ni]:[Fe] values of 0.425 and higher.

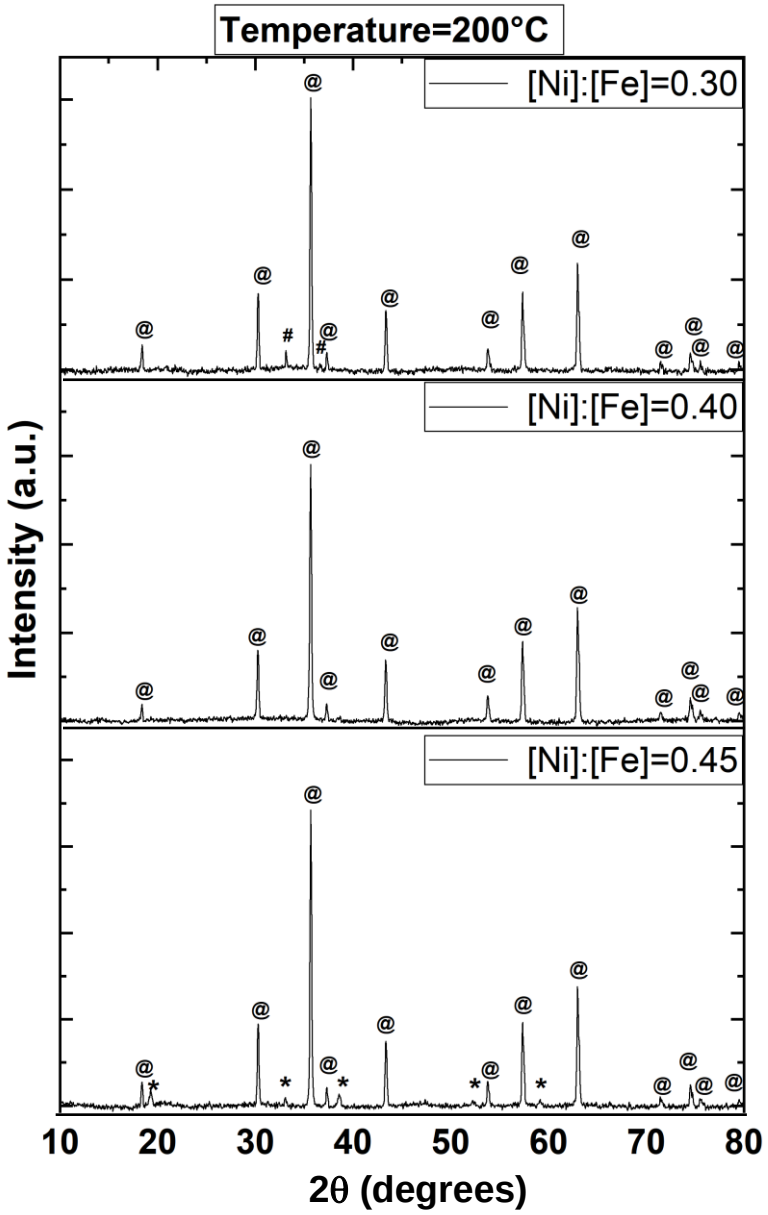

Figure 39. XRD spectra of reaction products obtained at 200°C for three representatives [Ni]:[Fe] ratios containing nickel ferrite (@), β-$Ni(OH)_2$ (*), and α-Fe_2O_3 (#). While nickel ferrite is obtained for all starting compositions the products obtained at this temperature may also contain α-Fe_2O_3 (upper spectrum), or β-$Ni(OH)_2$ (lower spectrum), depending on the starting composition.

Although the precursors were mixed in the 1:2 ratio that would be expected for stoichiometric $NiFe_2O_4$, the presence of β-$Ni(OH)_2$ in the obtained powder indicates that the ferrite cannot contain a stoichiometric amount of Ni. Since it was not possible to separate the octahedral particles from the platelets due to the range of sizes present for both populations, it was not possible to report an actual composition of the ferrite from the two-phase mixture. However, under conditions that led to a single-phase nickel ferrite product, the precursor ratio does correspond to the Ni:Fe cation ratio in the obtained powder. The 1:2 Ni:Fe ratio expected in stoichiometric $NiFe_2O_4$ was not obtained in the temperature range studied.

These procedures were then applied to syntheses using [Ni]:[Fe] ranging from 0.25 to 0.5 at six different reaction temperatures ranging from 125°C to 250°C. The results of these experiments are summarized as a phase diagram in Figure 40.

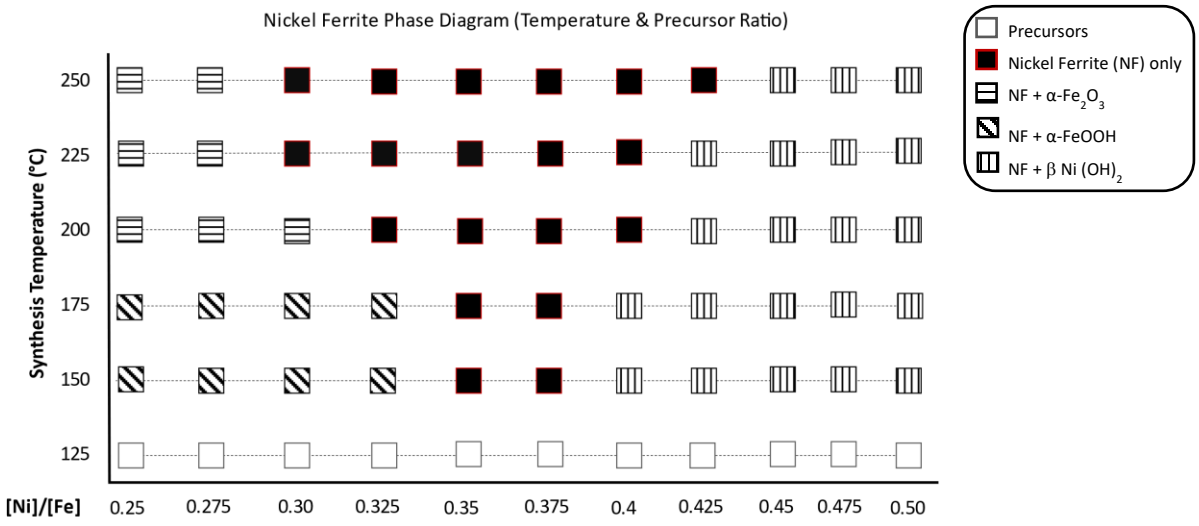

Figure 40. Phase diagram of nickel ferrite (NF) as a function of precursor concentration ratio and synthesis temperature. The shading in each block indicates the phase(s) observed. Solid white indicates unreacted precursors at 125°C. Solid black squares indicates unreacted precursors at 125°C. Solid black squares indicate single phase nickel ferrite, while the direction of the hatch marks within patterned squares indicates the identity of the additional phase appearing with the NF. In the single-phase region, the precursor concentration ratio corresponds to the Ni:Fe ratio in the non-stoichiometric nickel ferrite.

The x-axis represents the ratio of precursor solution concentrations [Ni]:[Fe], while the y-axis is the synthesis temperature. Each box represents the outcome of a synthesis at conditions given by at a pair of (x, y) coordinates, with the pattern indicating the resulting phase assembly as determined from the XRD spectra. At 100°C and 125°C, the unreacted precursors are indicated by a solid white box (the 100°C data points have been left off the diagram for simplicity). A single-phase nickel ferrite product is indicated by a solid black box. Although the stoichiometric ratio Ni:Fe = 1:2 was not obtained, the range of ferrite compositions – that is, the window over which a single phase product was obtained, widens at higher temperature to both higher and lower nickel content. Outside of this window, the identity of the two phases in the obtained powder is indicated by the striping pattern, as described in the figure legend.

ICP-OES was used to measure the composition of the synthesized powders (Table 9). Analysis of the two-phase mixture obtained for the [Ni]:[Fe]=0.50 synthesis at 200°C yields [Ni]:[Fe] ~ 0.55, consistent with the ratio of precursors introduced into the reaction chamber.

Table 9. ICP-analysis indicates no preferential loss of one type of metal cation during synthesis.

	Weight %	Fe weight %	Ni weight %
Ni:Fe:[0.5] (pure) 0.12 g	~0.5	46.4	23.8
Ni:Fe:[0.4] 0.09 g	~0.41	48.9	20.5
Ni:Fe:[0.35] 0.12 g	~0.37	50.9	19.0

Table 9 indicates that all metal atoms from the precursor were retained proportionately in the formation of the powder. While there may have been metal ions left in solution (and thus washed away during rinsing and filtering), there was not a preferential loss of one species. Thus, the starting precursor ratio is an acceptable proxy for final composition of single-phase products.

Fourier Transform Infrared (FTIR) spectroscopy was performed to study the metal occupation in octahedral and tetrahedral sites of the as-synthesized particles. FTIR was conducted using a Bruker Tensor 27 IR, scanned through a range of wavenumbers from 400 – 4000 cm^{-1}. A typical spectrum is shown in Figure 41, with two prominent absorption peaks in the 400-600 cm^{-1} region, and a small peak around 3600cm^{-1} corresponding to stretching of OH groups consistent with the presence of β-$Ni(OH)_2$. No other significant peaks were observed out to 4000 cm^{-1}. The two prominent peaks, enlarged in the inset, correspond to stretching of the bond between oxygen and metal ions, consistent with the formation of spinel ferrites. The band around 430 cm^{-1} corresponds to the bond involving Me^{2+} (either Ni^{2+} or Fe^{2+}) situated in the octahedral sites of the spinel, whereas the absorption band at 596 cm^{-1} corresponds to bond involving Fe^{3+} ions in the tetrahedral sites of the spinel. As discussed in the previous section, these ferrite particles do not contain the fully stoichiometric nickel content; thus, some of the octahedral sites are occupied by Fe^{2+}, while all of the tetrahedral sites are occupied by Fe^{3+} [99].

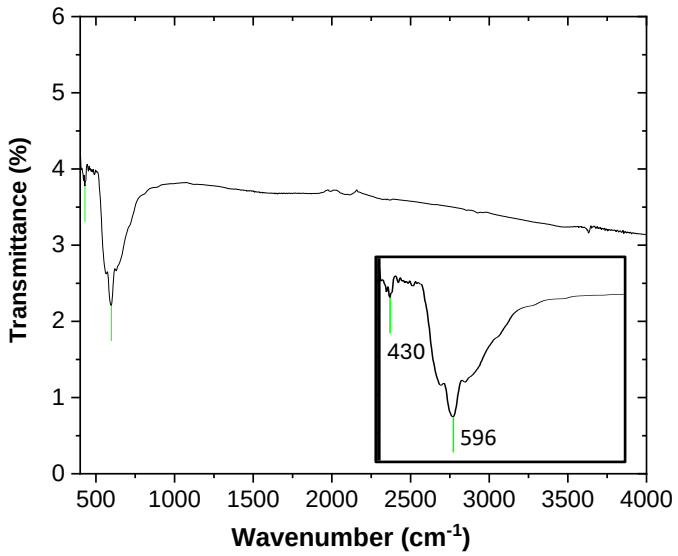

Figure 41. Representative FTIR spectrum from nickel ferrite particles. The absorption peaks at 430 and 596 cm^{-1} (expanded in inset) correspond to Me-O bonds for the Me^{2+} ion in octahedral sites and Me^{3+} ion in the tetrahedral sites, respectively. No other absorption peaks were observed in the scanned region.

Particle Size

Effect of Temperature on particle size

For studying the particle size, it was critical to select a precursor ratio that would yield a single-phase product through the entire temperature range of interest. For that reason, the precursor concentration ratio of 0.35 was selected, corresponding to Ni mole fraction 0.273 in the ferrite particles.

Since the concept of diameter is not meaningful for octahedral particles, the length of an edge was used as a measure of particle size. These lengths were measured using Image-J software. To avoid any selection bias, a modified version of the line intercept method proposed for grain size measurements in films by E. Heyn [100] was adapted. In this case, a straight line was overlaid on each image and the edge length of any octahedral particle which touched this line was measured,

excluding any that angled away (or towards) the viewer in order to avoid the geometric complications of foreshortening. The process was repeated along other arbitrary lines on other images until a total of 500 particles were measured for each synthesis condition. A histogram of these values was then plotted. Figure 42 compares the histograms for synthesis at 200°C (left) and 250°C (right). The distribution not strictly Gaussian. Nevertheless, an average particle size is a convenient metric for comparisons. Using that metric, it is clear that higher temperature resulted in a smaller average size (273 vs. 375 nm), but also a slightly broader distribution of sizes. The largest particles obtained were slightly over 500 nm in size, but their occurrence was rare.

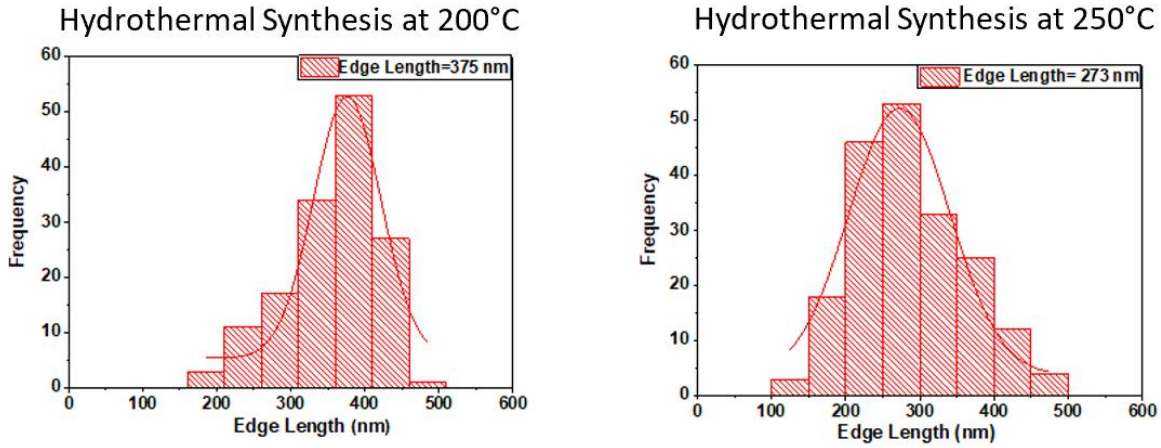

Figure 42.Histogram of particle size for two synthesis conditions, 200°(left) and 250°C (right). The cation ratio in both cases was 0.35, and the NaOH concentration was 2M. The lower temperature resulted in a higher average particle size, ~375 nm, where the higher temperature average size was 273 nm.

Effect of Ni precursor concentration on particle size at constant temperature

To isolate the effect of Ni precursor concentration on the size of the particles, a series of experiments have been conducted at 250°C where the Ni solubility is highest and no second phase anticipated. The NaOH concentration was held constant at 2M, and the Fe precursor concentration held at 0.2M. Particle sizes were measured from 500 particles at each condition, with the same

precautions taken to avoid selection bias and foreshortening. The histograms for three precursor ratios are plotted in Figure 43.

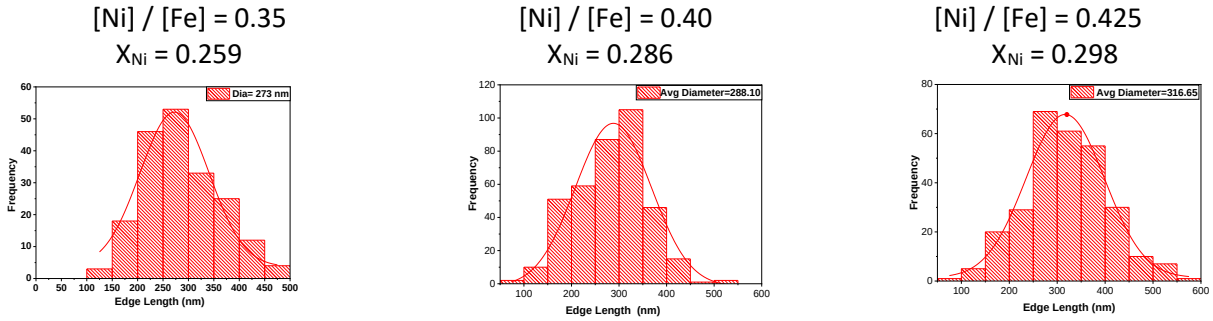

Figure 43. Particle size histograms for increasing Ni concentration (left to right). Fe concentration was held constant at 0.2M, and NaOH at 2M. Temperature was 250°C. Particle size increased from 273 nm to 320 nm. No second phase particles were observed.

The average particle size increases slightly with increasing nickel content, from 273 nm to 320 nm. The overall range of the distribution remains fairly consistent, however, from ~100 nm to 500 nm. Rarely, a particle as large as 600 nm was observed.

5.3 Discussion

Nickel ferrites were obtained under all synthesis conditions 150°C or higher, according to reaction:

$$Ni(OH)_2\,(s)+2FeOOH\,(s)\rightarrow NiFe_2O_4\,(s)+H_2O\,(l) \qquad 5.1$$

On the nickel-poor side of the diagram, all of the nickel is consumed in making the nickel ferrite. Below 200°C, any excess goethite remains unreacted, in contrast to earlier reports which found all goethite to be transformed to α-Fe_2O_3, even at such low temperatures. The phase transformation from α-FeOOH to α-Fe_2O_3 happens via α-FeOOH dissolution and reprecipitation as α-Fe_2O_3 [101]. As α-FeOOH and α-Fe_2O_3 have a good lattice match along {001} planes it is believed that initial

nucleation of α-Fe_2O_3 happens at these planes, followed by Ostwald ripening [95] in the solution, resulting in the growth of α-Fe_2O_3 as hexagonal bipyramidal platelets that achieve rather large (multi-micron) dimensions. Large α-Fe_2O_3 particles, similar to those described in [102], were observed in this study and are shown in Figure 35 (c). In this study, when no α-Fe_2O_3 was found below 200°C, it may simply be that the kinetics of the transformation were too slow for the 6-hour window that was used for the synthesis experiments. This is consistent with other findings suggesting that that the phase transformation can be thermally induced only at temperatures above 250°C [103]. The presence of Ni ions adsorbed on the surface of the goethite may also be impeding the epitaxial transformation of goethite into α-Fe_2O_3. These effects appear to be counterbalanced by the molarity of the base solution plays a role in the transformation of goethite to hematite. NaOH, being a precipitating agent, provides nucleation sites and also promotes the crystal growth along {001}, making the phase transformation at temperatures lower than the reported 250°C threshold. More detailed experiments would be needed to fully characterize the competition between these effects.

In stoichiometric $NiFe_2O_4$, Ni^{2+} ions occupy the octahedral sites, with Fe^{3+} equally distributed between octahedral and tetrahedral sites. In the case of nickel-poor ferrite, however, Fe^{2+} ions occupy some of the octahedral sites when Ni^{2+} is not available. In some instances, this is a substantial amount. For example, at 225°C, single-phase nickel ferrite is obtained from a starting ratio of [Ni]:[Fe] = 0.3, suggesting the final product can be written as $(Ni_{0.7}Fe_{0.3})^{2+}\ Fe_2{}^{3+}O_4$. The proportion of Fe^{2+} is surprising, given the starting iron precursor, goethite, contains Fe^{3+} and the experiments were not conducted under a reducing atmosphere. While XRD of the goethite precursor had no unidentified peaks corresponding to ferrous oxides or oxyhydroxides, it is

possible that a nanocrystalline or amorphous source of Fe^{2+} was present in the iron precursor material used for these syntheses. In any case, no ferrites were obtained for [Ni]:[Fe] ratios below 0.3 for any temperature studied, suggesting the redox conditions play a role in limiting the formation of the ferrite regardless of the source of the Fe^{2+}. Additional experiments using a reducing atmosphere are currently underway and will form the basis for a subsequent publication. On the nickel-rich side of the diagram, the formation of β-$Ni(OH)_2$ is governed by reaction:

$$Ni(NO_3)_2 \cdot 6H_2O\ (s) + 2NaOH\ (l) \rightarrow Ni(OH)_2\ (s) + 2NaNO_3\ (s) + 6H_2O\ (l) \qquad 5.2$$

Previous reports suggest the Ni reacts with the available OH- in the solution to form β-$Ni(OH)_2$ which then acts as an intermediate source of Ni for nickel ferrite formation. This leads to an alternative form of reaction in terms of the ionic species forming the solid precipitate β-$Ni(OH)_2$ according to reaction:

$$Ni^{2+} + 2\ (OH)^- \rightarrow\ Ni(OH)_2\ (s) \qquad 5.3$$

This form is helpful for understanding the subsequent interpretation of the phase diagrams. At 150°C, the very narrow region of single-phase nickel ferrite formation is due to a lower solubility of this intermediate phase β-$Ni(OH)_2$; when this intermediate precipitates, there is less Ni^{2+} available in solution for incorporation into the ferrite phase. At higher temperatures, the solubility of β-$Ni(OH)_2$ increases [104], making more Ni^{2+} readily available for the incorporation into nickel ferrite and a greater range of compositions for the nickel ferrite are possible. However, the stoichiometric amount of Ni is not achieved in the ferrite phase within the time frame of these experiments, resulting in two-phase mixtures of nickel ferrite and β-$Ni(OH)_2$.

5.4 Summary

A low-temperature hydrothermal synthesis method has been used to generate a series of nonstoichiometric nickel ferrites at different cation ratios and temperatures as confirmed by XRD analysis. By plotting the results as a phase diagram, the range of temperatures and starting compositions that lead to a single-phase product have been identified. This process window is quite narrow at 150°C such that a single- phase product is obtained only for starting precursor ratios [Ni]:[Fe] of 0.35 to 0.375. A broader range of starting compositions yields a single-phase powder at 250°C, from 0.3 to 0.425, although the stoichiometric ratio of 0.5 is not achieved within the synthesis time used for these experiments.

6. Iso-Electric Point Variation of Nickel Ferrite Nanoparticles as a Function of Water Chemistry

6.1 Introduction

Austenitic stainless steel is one of the main construction materials in nuclear power plants, owing to its (relatively) good corrosion resistance and its ease of manufacturing and weldability [105]. Under normal operating conditions, corrosion products from the construction materials are transported to the fuel cladding material (Zircaloy) [106]. Deposition of corrosion products on fuel cladding is one of the major problems in the nuclear industry [107]. Especially in Light Water Reactors (LWRs), CRUD deposits can inhibit the plant's ability to transfer heat. Moreover, under the plant's normal operating conditions, CRUD can become radioactive and, if later detached from the cladding, can transport the radioactivity to other locations in the plant facility [108].

Moreover, LWRs (PWRs & BWRs) usually operate under aggressive environments like Hydrogen Water Chemistry (HWC), Normal Water Chemistry (NWC), high temperatures, high pressures, and heavy irradiation. Hence it is almost impossible to study CRUD particles *in situ*. By synthesizing the nickel ferrite particles of varied sizes and compositions in a laboratory, we can study the chemical and physical parameters influencing transport and deposition. These include composition, particularly surface composition; particle size and shape; and surface charge.

In this chapter we aim to study the effect of pH on the size and composition of hydrothermally synthesized nickel ferrite particles. The pH for obtaining stoichiometric and non-stoichiometric nickel ferrites was identified. At this pH value an attempt has been made to replicate HWC of nuclear power plant by introducing the reducing agent ethylenediamine (EDA) during

hydrothermal synthesis while no such reducing agent was used to replicate the NWC. By using Malvern nano-zeta sizer the iso-electric point of the particles obtained under reducing (HWC) and non-reducing (NWC) environments was studied and correlated to water chemistry in LWRs.

6.2 Materials and Methodology

Nickel nitrate hexahydrate [Ni $(NO_3)_2$ $6H_2O$] (Sigma Aldrich), and goethite (α-FeOOH) synthesized according to [94] were used as a starting precursor materials. For all synthesis reactions a 0.2 M stock suspension of the Fe precursor was used, and the pH was controlled using sodium hydroxide solution (NaOH) (Millipore Sigma). For the pH study, a 0.1 M Ni solution prepared, while the isoelectric point experiments used a series of Ni precursors solutions with different concentrations to enable a range of +metal precursor ratios [Ni]: [Fe].

To assess the role of a reducing environment, all the experiments were conducted with (HWC) and without (NWC) of Ethylenediamine (EDA). All synthesis reactions were conducted in a Parr 5500 compact reactor with a 100-mL Teflon liner using the Parr 4848 reactor controller. The reactor was ramped at 2°C/ min, held at 200°C for 24 h, and then allowed to cool to room temperature. The obtained precipitate was centrifuged several times with ethanol and deionized water at 9000 rpm followed by drying the particles at 60°C overnight.

The phases present in the reaction product were identified by X-ray diffraction (XRD) using a Bruker D8 DISCOVER high-resolution X-ray diffractometer. Major peaks for the inverse spinel nickel ferrite ($NiFe_2O_4$) were identified using JCPDS card No. 01-086-2267. Additional peaks

were identified as hematite (α-Fe_2O_3) (JCPDS card No. 33-0664), and theophrastite [β-Ni $(OH)_2$] (JCPDS card No. 14-0117). Particles were imaged in a Zeiss/LEO 1550 scanning electron microscope (SEM). A PHI Quantes system was used to perform X-ray photoelectron spectroscopy (XPS) analysis to study the oxidation state of Fe in the samples and Zeta potential and Dynamic Light Scattering (DLS) studies were conducted using Malvern Zetasizer to understand the stability of the colloidal suspension at varied pH values.

6.3 Results

6.3.1 Effect of pH on the Synthesis of Nickel Ferrite Particles

Experiments were conducted at pH 7, pH 12 and pH 14.3 to study the effect of pH on the synthesis of nickel ferrite particles. Figure 44 shows the XRD spectra of the particles obtained using the stoichiometric precursor ratio [Ni]: [Fe] = 0.5 at these three pH conditions. At pH 7 (bottom) and pH 12 (middle), only peaks for the inverse spinel nickel ferrite ($NiFe_2O_4$) were found and labelled with @, indicating that a single-phase stoichiometric nickel ferrite product was obtained. At pH 14.3 (top), however, two phases were identified by XRD, showing peaks for both nickel ferrite and theophrastite [β-Ni (OH)2], marked with * . As some of the nickel is sequestered into this second phase, the nickel ferrite must be sub-stoichiometric despite the starting precursor ratio of [Ni]: [Fe] = 0.5.

6.3.2 Effect of pH on the Size of Nickel Ferrite Particles

Figure 45 shows representative SEM images of the two distinct types of particles found in this study, obtained at different pH conditions. In all cases, faceted octahedra consistent with the

expected morphology for the inverse spinel nickel ferrite structure were found, shown in Figure 45. This morphology is also consistent with corrosion products found in LWRs. However, the pH at which the hydrothermal synthesis was carried out had a profound impact on the size of the faceted octahedra. In Figure 45 (a,b) at pH 14.3 and pH 13, highly crystalline sub-micron octahedra

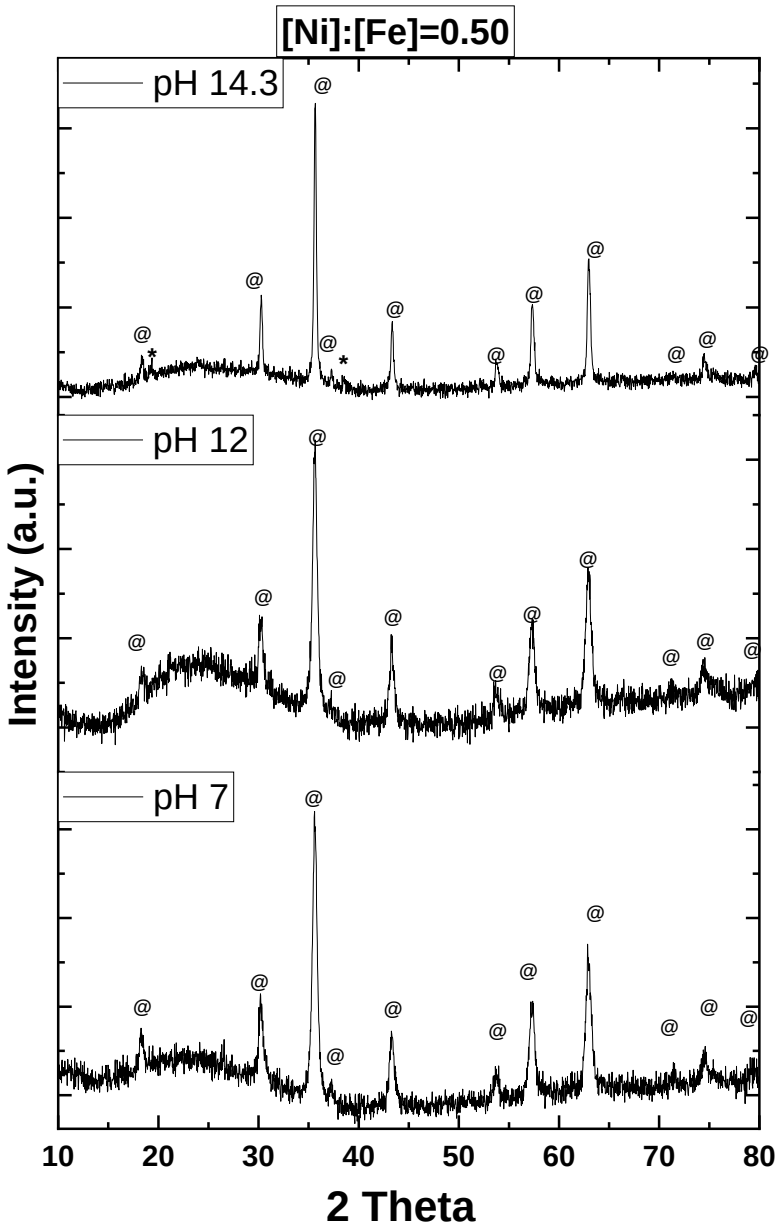

*Figure 44. XRD spectra for powders obtained using [Ni]: [Fe] ratio of 0.50 at 200°C. At pH 7 and pH 12 single phase stoichiometric nickel ferrites (@) were obtained. At pH 14.3, β-$Ni(OH)_2$ (*) was found in addition to nickel ferrite (@) as the primary phase.*

were obtained along with hexagonal platelets consistent with the theophrastite identified by XRD (circled in 38 (a), for example). At pH 7 and 12 as shown in Figure 45 (c,d), faceted nano-octahedra were observed but no platelets.

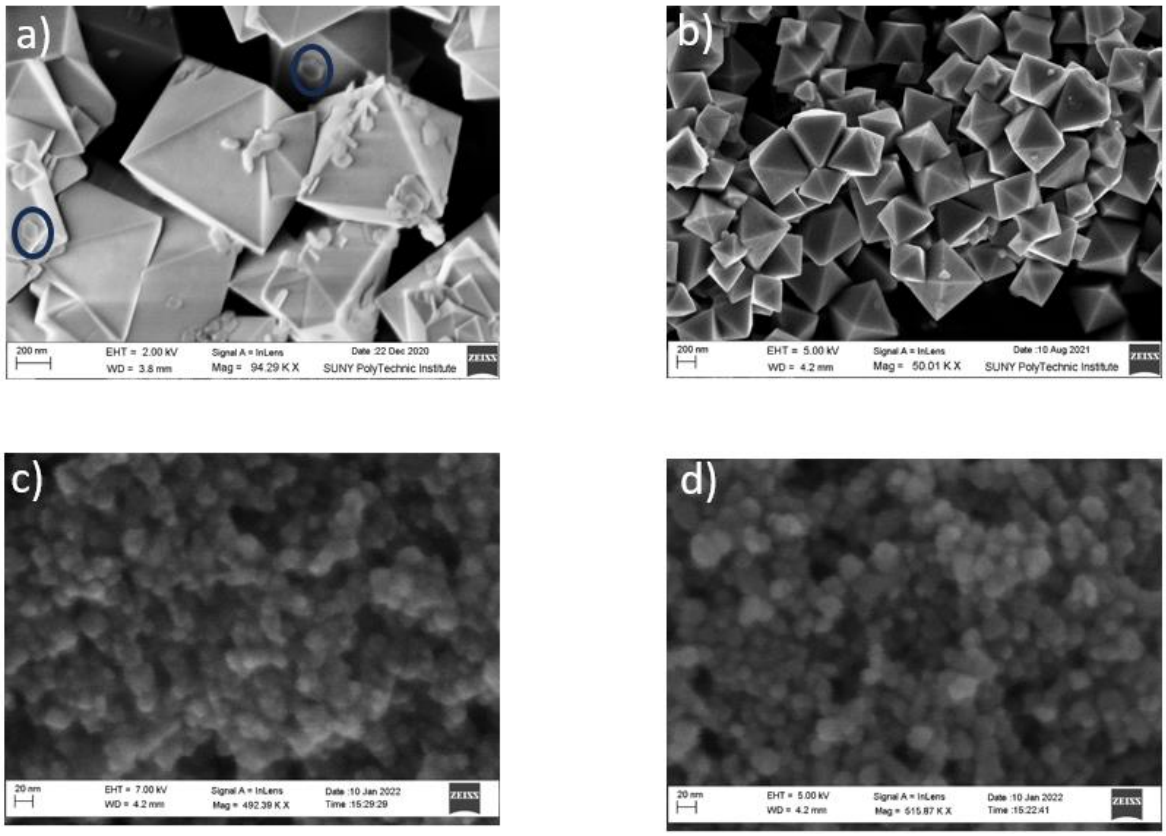

Figure 45. SEM images of the two types of particles found at different pH conditions. 38(b) shows sub-micron octahedral shaped particles along with (a) platelets at pH 14.3. 38(c) & 38(d) shows the single-phase Octahedral nano particles obtained at pH 7 and pH 12.

While SEM analysis can show the dry size of the particles, Dynamic Light Scatter (DLS) analysis of the particles suspended in water yields a measure of their hydrodynamic radii and quantifies the particle size distribution. Because the distributions for pH 7 and pH 12 were almost identical, only the data obtained for pH 12 is shown in Figure 46 (a) for comparison to pH 14.3 in Figure 46 (b). The peak of the distribution shifts from ~ 100 nm at pH 12 to ~ 500 nm at pH 14.3. Although

large particles are more representative of CRUD found in LWRs, the presence of second phase particles in the pH 14.3 and 13 syntheses made them less suitable processes for follow-on studies. Hence, pH 12 was used as a baseline to synthesize single phase nickel ferrite in order to study the effect of a reducing environment on the surface properties, particularly the isoelectric point.

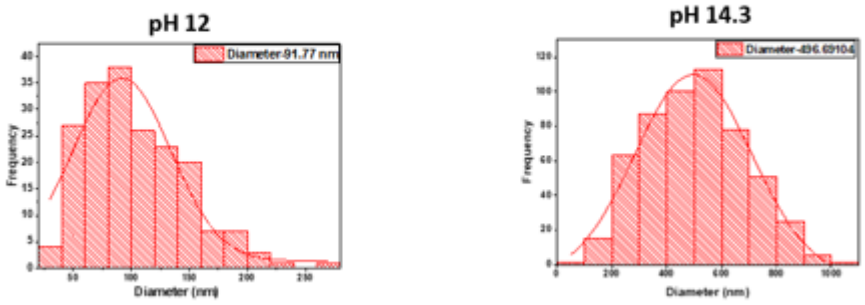

Figure 46. show the DLS analysis data as a function of pH. A fourfold increase in faceted octahedra size was observed by increasing the pH of the synthesis from 12 to 14.3..

6.3.3 Effect of EDA (Reducing Agent) on the Synthesis of Nickel Ferrite

Three precursor ratios (0.25, 0.35, and 0.5) were used to study the influence of EDA on the nickel ferrite synthesis, achieved by varying the molarity of the Ni suspension (Table 8). Figure 47 shows the XRD spectra of the particles obtained at 200°C for a reaction time of 24 hrs in the absence of EDA, representing NWC. For [Ni]:[Fe]=0.5, a hump was observed at 25 on x-axis which is coming from the amorphous glass slide and the rest all the peak reflections correspond to $NiFe_2O_4$ (@) indicating that a stoichiometric single phase product was obtained. For precursor ratios of [Ni]:[Fe]=0.35 and 0.25, hematite (^) peaks were observed along with nickel ferrite.

*Table 8. Translation Table Relating the Molarity of the Starting Suspensions to the Precursor Concentration Ratio [Ni]: [Fe]**

Nickel Suspension Molarity:Iron Suspension Molarity	[Ni]: [Fe] Ratio of StartingPrecursor Materials
0.050 *M*: 0.2 *M*	0.25
0.070 *M*: 0.2 *M*	0.35
0.100 *M*: 0.2 *M*	0.5

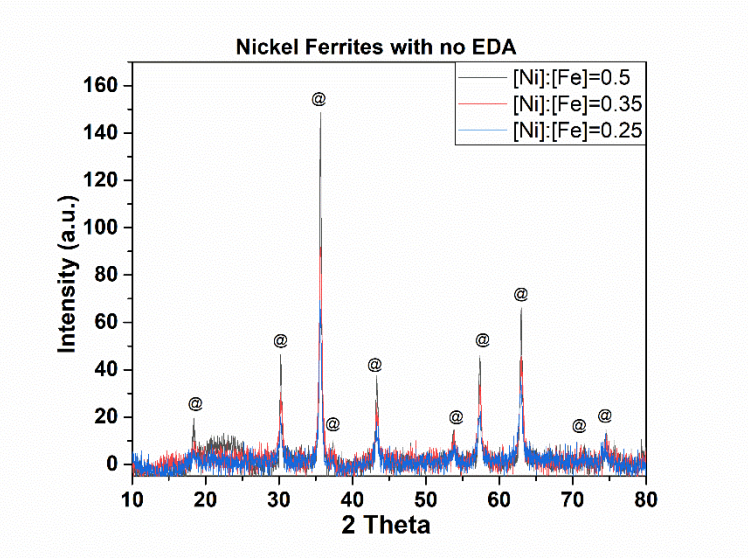

Figure 47. XRD spectra for powders synthesized without the reducing agent EDA at 200°C with [Ni]:[Fe] = 0.50 (black), [Ni]:[Fe] = 0.35 (red) and [Ni]:[Fe] = 0.25 (blue). Nickel ferrite peaks are labeled @, and hematite are labeled ^. While no traces of hematite are seen in [Ni]:[Fe] = 0.50 (black), the decrease in Ni concentration resulted in the presence of hematite for [Ni]:[Fe] = 0.35 (red) and [Ni]:[Fe] = 0.25 (blue).

Figure 48 shows the XRD spectra for the same compositions when 5 ml of EDA was used as a reducing agent during synthesis. In this case, the only phase identified in the XRD spectra was nickel ferrite (@), for all compositions.

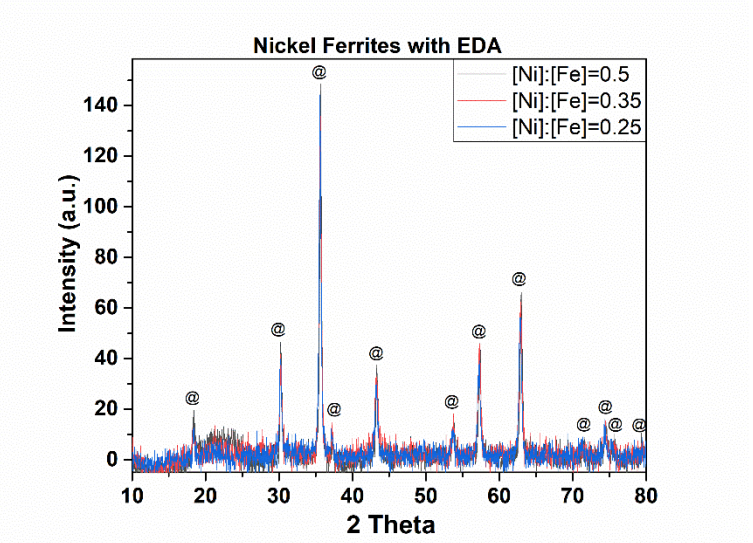

Figure 48. XRD spectra of EDA assisted synthesis obtained at 200°C with [Ni]:[Fe] = 0.50 (black), [Ni]:[Fe] = 0.35 (red) and [Ni]:[Fe] = 0.25 (blue). XRD spectra confirmed a single-phase nickel ferrite (@) and no second phase particles were observed with the decrease in Ni precursor concentration.

From these data, the lattice parameters for the nickel ferrite particles were calculated using the most intense (311) peak, enlarged to show detail in Figure 49. From the XRD spectra, particles synthesized without EDA (Figure 49 (a)) show differences in peak intensity, but similar peak position for all compositions, and thus the same lattice parameter. In (Figure 49 (b)) the peak position for particles synthesized with EDA shifts to lower 2θ values with a decrease in Ni precursor concentration, corresponding to an increase in lattice parameter. The lattice parameter results are summarized in Table 9.

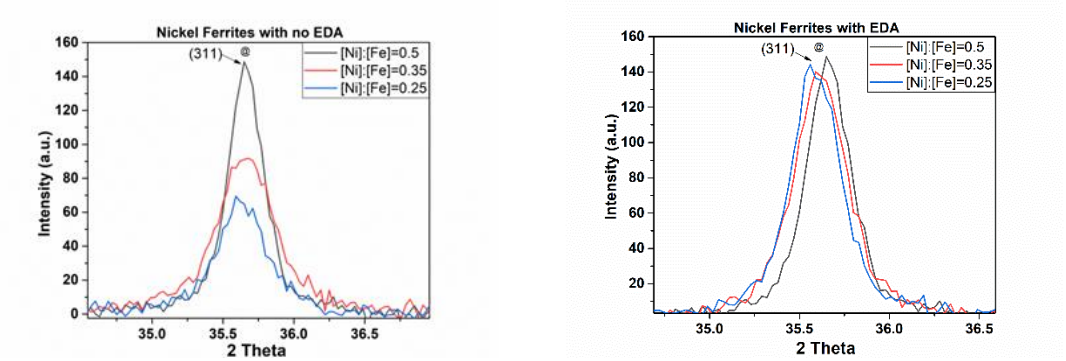

Figure 49. XRD spectra of particles obtained at 200°C with [Ni]:[Fe] = 0.50 (black), [Ni]:[Fe] = 0.35 (red) and [Ni]:[Fe] = 0.25 (blue). (a) When no EDA is used, no shift in (311) peak position was observed despite changes in the cation ratio. (b) EDA assisted synthesis results in a shift in the position of the (311) peak to lower 2q values as the Ni concentration decreases.

Table 9. Lattice parameters of nickel ferrite particles synthesized with and without EDA. In the case of EDA, the lattice parameter increases as the Ni concentration decreases.

[Ni]: [Fe] Ratio of Starting Precursor Materials	Calculated Lattice Parameters (Å) without EDA	Calculated Lattice Parameters (Å) with EDA
0.5	8.3325	8.3325
0.35	8.3328	8.3487
0.25	8.3327	8.3771

The increasing lattice parameter with decreasing Ni content suggests the substitution of the Fe^{2+} ion (0.74 Å) for the Ni^{2+} ion (0.69 Å) [109] when nickel is less available. This result means that some Fe ions appear to be incorporated into Ni site (octahedral sites) in the crystalline spinel structure, but can only occur in the presence of EDA to effect the change of Fe^{3+} to Fe^{2+}.

To confirm this conclusion, XPS analysis was performed on a single phase stoichiometric nickel ferrite powder with [Ni]:[Fe]=0.5, and with [Ni]:[Fe]=0.25 particles synthesized with and without EDA. For the ease of representation only the Fe 2p spectra are shown in Figure 50. In this energy window, Fe 2p has two split spin-orbit component, centered at Fe $2p^{3/2}$ and Fe $2p^{1/2}$ giving us a doublet spacing of 13.2 eV. The high-resolution Fe $2p^{3/2}$ peak could be deconvolved into four component peaks centered at 710.2, 711.2, 712.3, and 713.9 eV for [Ni]:[Fe]=0.5 and [Ni]:[Fe]=0.25 (No EDA). In the case of [Ni]:[Fe]=0.25 (with EDA), an additional fifth peak at 708.7 eV is also observed. This peak is primarily attributed to the existence of Fe ions in the Fe^{2+} oxidation state on the surface of the non-stochiometric nickel ferrites [110].

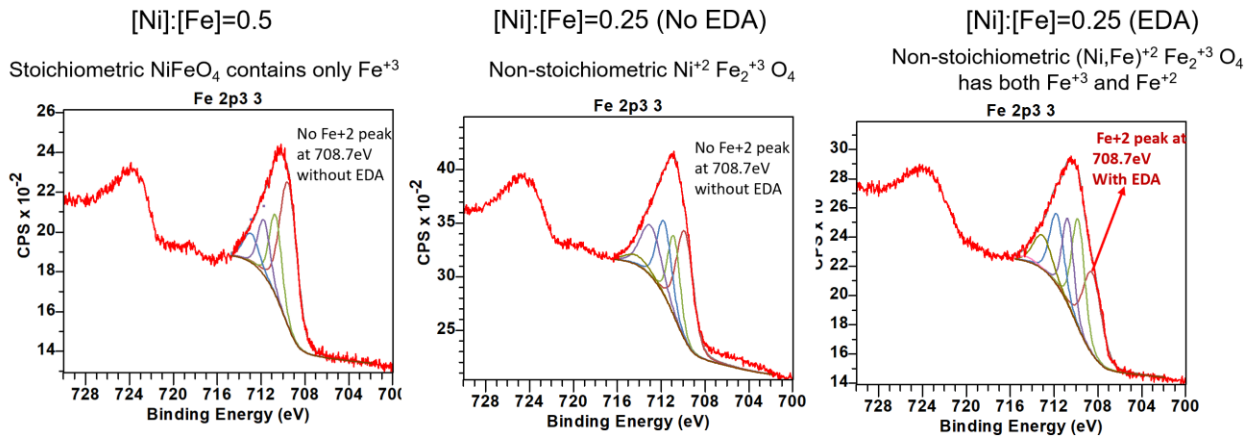

Figure 50. Shows the high resolution Fe2p$^{3/2}$ of [Ni]:[Fe]=0.5, [Ni]:[Fe]=0.25 (No EDA) and [Ni]:[Fe]=0.25 (EDA). Along with the four deconvoluted peaks, an additional photo-electron peak at 708.7 eV is observed in [Ni]:[Fe]=0.25 (EDA). This result confirms the existence of Fe^{2+} on the surface of [Ni]:[Fe]=0.25 (EDA).

6.3.4 Effect of EDA (Reducing agent) on the Iso-Electric Point (IEP) of Nickel Ferrite

For each of the batches, 2 mg of nickel ferrite powder was dispersed in 20 mL of water and sonicated for 5 minutes. The pH was adjusted using stock solutions 0.01M NaOH and 0.01M HCl to measure the zeta-potential as a function of pH. Figure 51 shows the relationship of zeta potential vs. pH for particles synthesized without EDA, with three precursor ratios, namely [Ni]:[Fe] = 0.50, [Ni]:[Fe] = 0.35, and [Ni]:[Fe] = 0.25. In the case of stoichiometric nickel ferrites ([Ni]:[Fe]=0.5) the measured IEP was close to 7.4, due to the dissociation of OH- at pKa=7 of water. For non-stoichiometric nickel ferrites ([Ni]:[Fe]=0.35 and [Ni]:[Fe]=0.25) a

slight shift of IEP to higher pH value was observed with the decrease in Ni ion concentration.

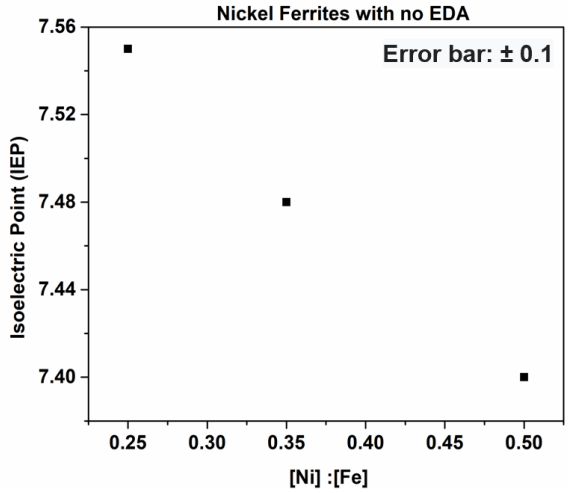

Figure 51. Shows the IEP variation as a function of Ni precursor concentration. For non-stochiometric nickel ferrites synthesized with no EDA, a decreasing Ni concentration resulted in shift of IEP towards high pH.

The zeta-potential value as a function of pH for non-stoichiometric nickel ferrite particles ([Ni]:[Fe] = 0.35 and [Ni]:[Fe] = 0.25) synthesized with EDA along with magnetite ([Ni]:[Fe] = 0) are shown in Figure 52. For this series of experiments, a decrease in Ni ion concentration resulted in a shift of IEP to lower pH value, in contrast to the particles synthesized without EDA.

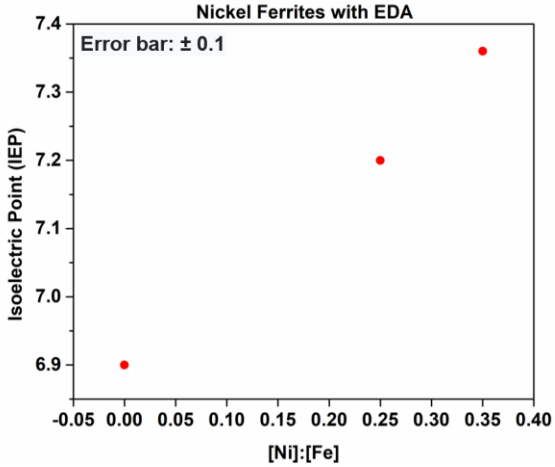

Figure 52. Shows the IEP variation as a function of Ni precursor concentration. For non-stochiometric nickel ferrites synthesized with EDA, a decreasing Ni concentration resulted in shift of IEP towards lower pH value.

6.4. Discussion

6.4.1 Effect of pH on Phase and Size of the Nickel Ferrite Particles

The effect of pH on the average size of the nickel ferrite particles is shown in Figure 45 and Figure 46. From these figures it was clear that pH plays a vital role in dictating the size of the nickel ferrite particles, consistent with other literature reports [111]. At lower pH values of 7 and 12, a finer grain size was observed which is in good agreement with the XRD results (Figure 44). All the XRD peaks of particles synthesized at pH 7 and 12 have a broader peak width indicating the low crystalline nature of the ferrites synthesized under these conditions. The particles obtained under these pH values are in nanoscale regime with a very narrow size distribution. The low concentration of OH^- at these pH values resulted in faster nucleation and slow growth rate resulting in the small particle sizes observed under these conditions. From the SEM images in Figure 45 (c,d) the average size of the particle is less than 20 nm, whereas DLS measured the average size to be around 100 nm. Since neutral pH is used to measure the hydrodynamic radius of these particles (which is close to their IEP), the larger size measured by this technique may simply reflect some degree of aggregation due to their high specific surface area [112]

Unlike the nanoparticles obtained at lower pH values, the particles synthesized at pH 14.3 are hundreds of nanometers across (Figure 45 (a)). XRD results agree with this observation displaying narrow, sharp peaks indicating that the mean crystalline size of synthesized ferrites increased as the pH increased from 12 to 14.3, suggesting that growth of existing nuclei is easier at high pH than in neutral environments [113]. Results published by Chen [114] agree with our observations where he discusses an increase in size of the final product with an increase in pH (alkali concentration).

In the case of pH 7 and 12, the nickel nitrate precursor dissociates making Ni^{+2} readily available to be incorporated into nickel ferrite, resulting in stochiometric single phase particles[115]. Hence a large range of nickel ferrite compositions were made possible at pH 12. On the other hand, at higher OH^- concentrations/ pH values, an intermediate phase is formed after the precursor dissociates, whose synthesis is governed by the reactions:

$$\text{(Ni Nitrate Precursor) } Ni^{2+} + \text{Excess (OH)} \rightarrow Ni(OH)_2 \text{ (Intermediate Precursor)} \quad 6.1$$

$$\text{(Intermediate Precursor) } Ni(OH)_2 + 2FeOOH \xrightarrow[\text{Limited}]{\text{Time \& solubility}} NiFe_2O_4 + 2H_2O + \beta Ni(OH) \quad 6.2$$

In other words, at pH 14.3, the nickel nitrate precursor dissociates and reprecipitates as $Ni(OH)_2$ which acts as an intermediate precursor source for nickel ferrite synthesis. In the presence of excess OH^- this intermediate precursor sequesters some of the Ni^{2+}, resulting in fewer ions available to be incorporated into the competing ferrite phase, resulting in two-phase mixtures of nickel ferrite and β-$Ni(OH)_2$ within the time frame of the reaction.

6.4.2 Effect of EDA on the Phase and Isoelectric Point of Nickel Ferrites

Figure 53 shows the changes in the IEP of the varied composition nickel ferrite particles synthesized with and without EDA (circles and squares, respectively), overlaying figures 8 and 9. In the case of stochiometric nickel ferrite particles, the measured IEP value was around pH 7.4 [116]. With the decrease in Ni precursor concentration, a shift of IEP to higher pH value was observed in the particles synthesized without EDA. The decrease in Ni ion concentration on the

surface of the particle may lead to a different surface composition than the bulk, causing an IEP shift toward higher pH values. Thus resulting in shift of IEP toward higher (hematite/maghemite) pH value[117]. To gain further insight XPS analysis was carried out on these samples but the evidence was inconclusive, and I can only speculate that the surface termination is on Fe3+ plane. Alongside even the presence of slight traces of second phase particles like hematite (^) in nickel ferrites ([Ni]:[Fe]=0.35 and [Ni]:[Fe]=0.25) (Figure 47) could also be the reason for this observation.

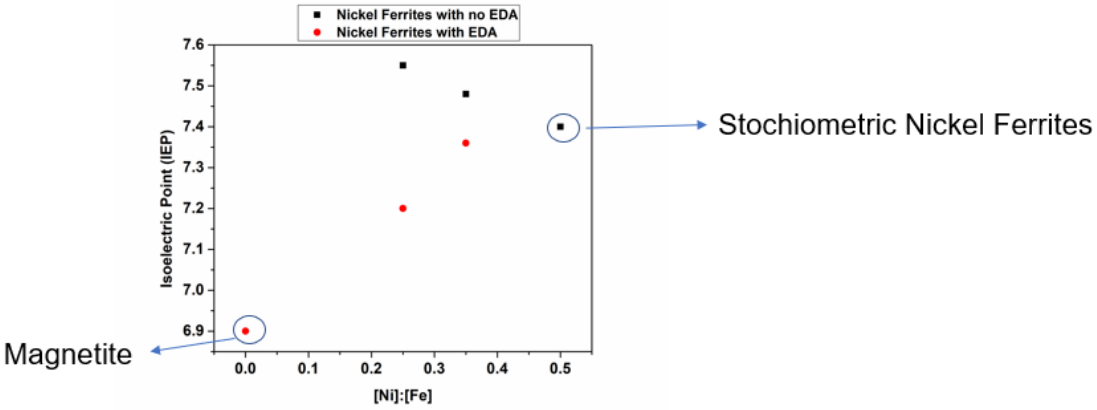

Figure 53. show the IEP variation of nickel ferrites synthesized with and without EDA. With the decrease in Ni precursor concentration a shift of IEP towards hematite was seen whereas a shift of IEP toward magnetite was observed in particles synthesized with EDA.

In the case of particles synthesized with EDA, no second phase was detected by XRD spectra, and the surface Fe ion reduction from Fe^{3+} to Fe^{2+}, consistent with the XPS data. From the zeta-potential vs pH measurements, for the [Ni]:[Fe]=0.25 case, the IEP goes from 7.55 to 7.2 with the use of EDA. For the [Ni]:[Fe]=0.35 case, it goes from 7.5 to 7.35. This finding is relevant to the reducing environment found in HWC, as the CRUD particles found there will incorporate Fe^{2+} in the absence of Ni ions. When this happens, the IEP values of the CRUD shifts lower towards that of magnetite, suggesting this phase behaves as Ni-doped magnetite.

6.5 Conclusions

In this chapter we conclude that at 200°C, Single phase nickel ferrites across a broad range of compositions can be obtained by using EDA during hydrothermal synthesis. The concentration of OH- in the solution dictates the balance between nucleation of new ferrite particles and growth of existing particles. Thus, the availability of OH- also influences the final stoichiometry of the particles, by sequestering Ni into β-$Ni(OH)_2$, such that a trade-off must be made between achieving stoichiometric particles and large size. Characterization techniques like XRD and XPS confirmed the bulk and surface Fe ions reduction in the absence of Ni ions for non-stochiometric nickel ferrites synthesized with EDA. To study the IEP values depends on the surface charge of the particle zeta potential experiments were carried out and a shift towards magnetite is observed with EDA assisted synthesis (HWC) whereas a shift towards hematite's is observed without EDA assisted synthesis (NWC).

7.Hydrothermal Corrosion of Latest Generation FeCrAl Alloys for Nuclear Fuel Cladding

The majority of this chapter is the accepted manuscript of an article published by MDPI in the *Journal of Materials* on 04/03/2024, available at https://doi.org/10.3390/ma17071633 and reproduced here with permission of the publisher. Additional figures and data have been included for sake of clarity.

7.1 Introduction

A continued demand to generate electricity while mitigating greenhouse gas emissions is possible to fulfill through nuclear power plants [118]. In all Light Water Reactors (LWRs), fuel pellets are protected in cladding tubes. Cladding material (zirconium-based alloys) plays a crucial role as a barrier by preventing the release of fuel into the coolant and by protecting the fuel from the coolant's corrosion [119]. Under normal operating conditions, using Zr-based alloys as fuel cladding material is a good choice due to their low thermal neutron absorption [120] and their acceptable mechanical properties under irradiation [121]. The problem arises in the absence of a coolant, leading to the meltdown of the core and ultimately resulting in a loss of coolant accident (LOCA) (Fukushima nuclear disaster) [122]. Thus, there is an urgent need for the development of accident tolerant fuels (ATFs).

ATF cladding designs should survive LOCA scenarios; hence, they should be resistant to oxidation at high temperatures [123] and have a good corrosion performance under normal operating

conditions [124]. Currently, materials are being explored in two different approaches to meet the ATF cladding needs. Coated zirconium alloys are being used as a short-term approach, along with monolithic FeCrAl alloys, and silicon carbide composites are being used as a mid-term approach [125, 126]. Among these concepts, FeCrAl alloys have exhibited superior corrosion resistance in operational conditions [127, 128] and LOCA conditions [129] and can even prevent detrimental fuel/cladding chemical interaction [130]. The enhanced corrosion resistance of FeCrAl alloys comes from the formation of a Cr passivation layer, which will inhibit the corrosion and act as a protective layer [76]. In the mid-term approach, FeCrAl alloys may replace Zircaloy as cladding material. Thus, it is important to expose variants of FeCrAl alloys to simulated BWR-NWC (normal water chemistry) and BWR-HWC (hydrogen water chemistry) operating conditions to investigate the formation of a protective oxide on these alloys as a function of water chemistry.

To examine the corrosion behavior of FeCrAl alloy variants under reactor operating conditions, numerous studies were performed. In the case of first-generation FeCrAl alloys [128], APMT (21Cr) was studied extensively, and it displayed excellent corrosion resistance under high temperature (~300 °C) waters but was susceptible to radiation-induced embrittlement due to α' precipitates of chromium [131,132]. Hence, for second-generation FeCrAl alloys [128], the Cr content was reduced to 12 wt%, and minor alloying elements were added (Y, Nb, Mo, and Si) to provide mechanical strengthening to these cladding tubes [133].

To study the impact of the microstructure, Umretiya et al. [134] performed a systematic study to understand the effects of the microstructure, manufacturing route, and composition on the corrosion behavior of FeCrAl alloys. They concluded that FeCrAl alloy hydrothermal corrosion

resistance has little/less sensitivity to (microstructural) the fabrication route. At the same time, Yin et al. conducted a long-term immersion test [135], where they investigated the hydrothermal corrosion behavior of FeCrAl variants of APMT (21Cr) and wrought C-26M (12Cr) for over 12 months. Their results concluded that the corrosion behavior of wrought C-26M (12 Cr) was compromised when compared to APMT (21 Cr).

Hence, in this chapter, we emphasize our findings on the hydrothermal corrosion behavior of the three latest variants of FeCrAl alloys along with Zirc-2 and SS316. APMT was slightly modified as APMT-2 (FA-SMT); unlike the traditional wrought method, powder metallurgy was used to fabricate FA-SMT and C26M alloys. Along with the modified versions of first- and second-generation FeCrAl alloys, we also tested an in-between composition space of 17 Cr alloy (Fe17Cr5.5Al) to gain insights into the corrosion performance of this variant along with standard FeCrAl alloys. The immersion test was carried out for six months in a typical BWR environment under two simulated water chemistries at 288 °C. This particular work is a continuation of our previous study where the preliminary data of this work was published by Rebak.et.al [134]. In the current chapter we are primarily focusing on the detailed characterization of the oxide layer that was developed as a function of water chemistry. via Transmission Electron Microscopy (TEM) analysis.

7.2. Experimental Conditions

As listed in Table 10, the three latest FeCrAl alloy variants along with the current nuclear cladding materials, Zirc-2 and SS316 (for reference), were tested for a time span of six months in simulated BWR environments. Apart from Fe17Cr5.5Al (flat coupon), the rest of all of the test samples were

kept in tubes. The thickness of the powdered metallurgy-processed FA-SMT and PM-C26M tube walls was targeted to be 0.3 mm. The wall thickness of the Zirc-2 specimen, including the inner diameter liner, was targeted to be around 0.675 mm. All of the tube specimens that participated in the immersion testing were nominally 12.7 mm (0.5″) long sections of actual tube claddings with an OD of 10.26 mm. By using vacuum induction melting (VIM), model alloy Fe17Cr5.5Al was cast in rod shape. Flat coupons were cut from the rod-shaped master alloy to obtain a coupon with net exposed area of 500 mm^2 with a hole to hang the coupons (1.5 mm diameter). By using 600-grit SiC paper, all samples were polished and later cleaned with Liquinox, isopropyl alcohol (IPA), and ultra-high-purity (UHP) water prior to corrosion testing.

Table 10. Nominal composition of FeCrAl alloys studied in this article.

Alloy	Geometry	chemical composition in wt%	No. of samples tested
FA-SMT	Tube	Fe + 21Cr + 5Al + 3Mo	16
Fe17Cr5.5Al	Flat coupon	Fe + 17Cr + 5.5Al	6
PM-C26M	Tube	Fe + 12Cr + 6Al + 2Mo	16
Zirc-2	Tube	Zr + 1.5Sn + 0.15Fe + 0.1Cr + 0.05Ni	16
SS316	Tube	Fe + 17Cr + 10Ni + 2Mo	16

Testing was carried out on 16 samples of each tubed alloy along with 6 samples of Fe17Cr5.5Al flat coupons. The testing conditions are shown in Table 11. By using UHP water of 18 Mega-Ohm (MΩ), testing was performed in a recirculating autoclave simulating the temperatures of BWR under two different water chemistries (HWC and NWC) with no addition of impurities. Hydrothermal corrosion testing was performed in separate autoclaves, which were circulating at a rate of 200 cm^3/min. By using the right amount of gas, high-purity water was reconditioned in a 4

L glass column followed by pumping the water to autoclave using a pressure pump (high). Later, by using a back-pressure regulator, the pressure was controlled at approximately 10 MPa. The water conductivity was measured before entering and after exiting the autoclave. Samples were taken out after six months of immersion testing, rinsed with UHP water, and dried in ambient atmosphere. The mass change of each specimen was calculated three times and reported in mg/dm^2. Mass gain during the autoclave exposure is shown in positive values, whereas negative values indicate a mass loss during the exposure.

Table 11. Autoclave testing conditions.

Autoclave	Test Conditions, Six Month Immersion
S-12	Simulated BWR, Normal Water Chemistry (BWR-NWC), 0.5 ppm O_2, 288°C
S-13	Simulated BWR, Hydrogen Water Chemistry (BWR-HWC), 0.3 ppm H_2 (<5ppbO_2), 288°C

After the water immersion, surface oxide characterization was performed using TEM. Using focused ion beam (FIB) milling, TEM lamellae were prepared for all samples. During FIB milling, a thin layer of Pt coating was applied to protect the corroded surface of the tested samples. At 300 kV, using a Thermo Scientific (Waltham, MA, USA) Themis Z aberration-corrected S/TEM, scanning transmission electron microscope (STEM), energy-dispersive X-ray spectroscopy (EDS) analysis, and bright-field (BF) TEM imaging were performed. TEM Instrument Analysis (TIA) software was used for image and composition analysis.

7.3 Results

For immersion corrosion testing, guidance was followed according to the ASTM standards G1 and G31. Although the autoclave testing conditions may differ from the actual nuclear reactor due to

the presence of oxidizing species. The experiments were designed in the vicinity of 300 °C [135] [136] to study the plausible ATF candidate FeCrAl along with nuclear alloys.

After six months of immersion test, all 16 tubes of each Zirc-2, FA-SMT, PM-C26M, SS316, along with 6 flat coupons of Fe17Cr5.5Al were taken out to determine the mass change as shown in Figure 54 . Each individual sample was measured three times. All the samples irrespective of their compositions displayed a mass gain under BWR-NWC (S-12) that contains 0.5 ppm of dissolved oxygen. Under these autoclave testing conditions, Zric-2 tube samples displayed a relatively higher mass gain (22 mg/dm²) than the FeCrAl alloys and this observation is consistent with the literature [134]. Lower mass gain of FeCrAl alloys could be due to the formation of a protective surface oxide. It is also observed that within the FeCrAl alloys, a slightly higher mass gain was observed in FA-SMT (5 mg/dm²) when compared to PM-C26M (4.5 mg/dm²) which may be due to higher Cr content. The flat coupon of Fe17Cr5.5Al recorded a mass gain of 4.9 mg/dm². However, In the BWR-HWC (S-13), PM-C26M and Fe17Cr5.5Al displayed a significant mass loss when compared to FA-SMT. Lower Cr content in Fe17Cr5.5Al and PM-C26M could be the reason for the mass loss in these alloys. The mass gain of Zric-2 tube specimens in BWR-HWC is relatively small when compared to BWR-NWC. Reducing (hydrogen) environment hindering the formation of a protective passive oxide layer could be the reason for this observation.

Optical inspection of the BWR-NWC test specimen post six months of immersion testing is shown in Figure 55. All the test specimens exposed to S-12 system (oxidizing) displayed a mass gain as shown in Figure 54. Zirc-2 tube specimens exposed to oxygenated waters developed a black oxide indicating the formation of protective ZrO_2. FA-SMT, PM-C26M and Fe17Cr5.5Al specimens visually have a distant color than the Zirc-2 tube specimens. FA-SMT specimens displayed a

slightly different appearance than the PM-C26M and Fe17Cr5.5Al specimens which could be related to the different surface corrosion products.

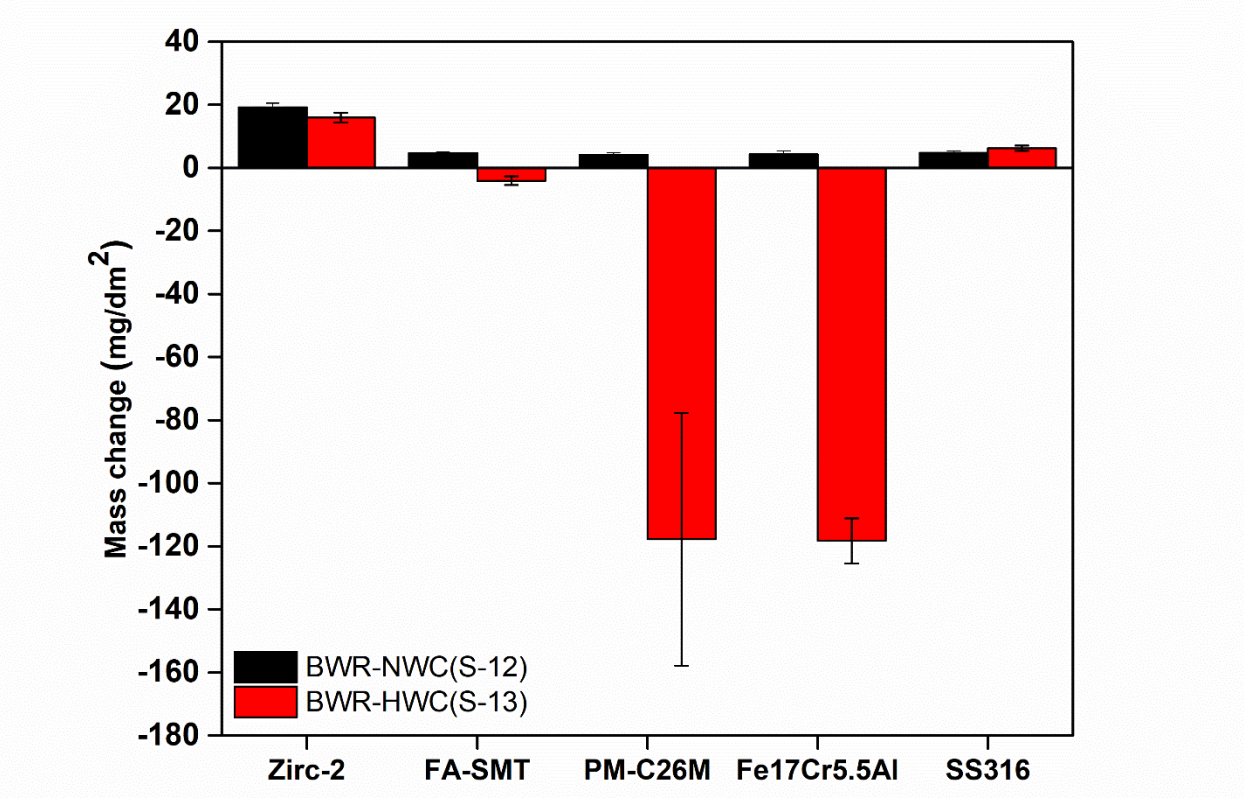

Figure 54.Mass change as a function of immersion time for FA-SMT, PM-C26M, SS316 and Zirc-2 tube specimens along with Fe17Cr5.5Al flat coupon specimens in simulated BWR-HWC, and BWR-NWC waters.

The specimens tested in BWR-HWC (S-13) are shown in Figure 56 and they displayed a distinctive visual appearance than the specimens tested in S-12. In the hydrogenated waters, apart from Zric-2 and SS316 specimens all the FeCrAl variants showcased a mass loss. Zirc-2 tubes tested in S-13 have a dull gray appearance. Unlike the FeCrAl alloy variants test in S-12, the FeCrAl specimens tested in S-13 system have a distinctive visual appearance. A shiny golden appearance for FA-SMT and a shiny gray appearance for PM-C26M was observed for tube specimens tested in S-13 could be due to higher Cr content in FA-SMT than in PM-C26M.

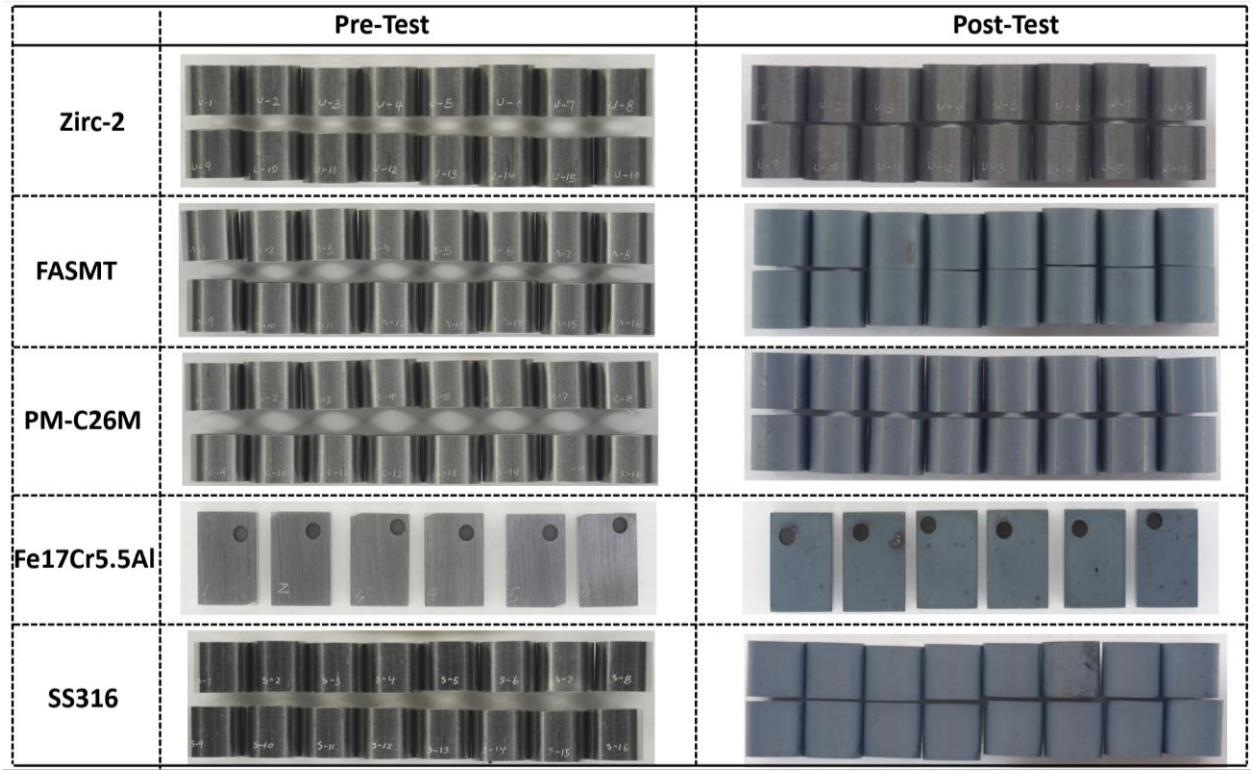

Figure 55. Visual inspection of Zirc-2, FA-SMT, PM-C26M, SS316 tubes along with Fe17Cr5.5Al flat coupons post 6 months of immersion testing in BWR-NWC (S-12).

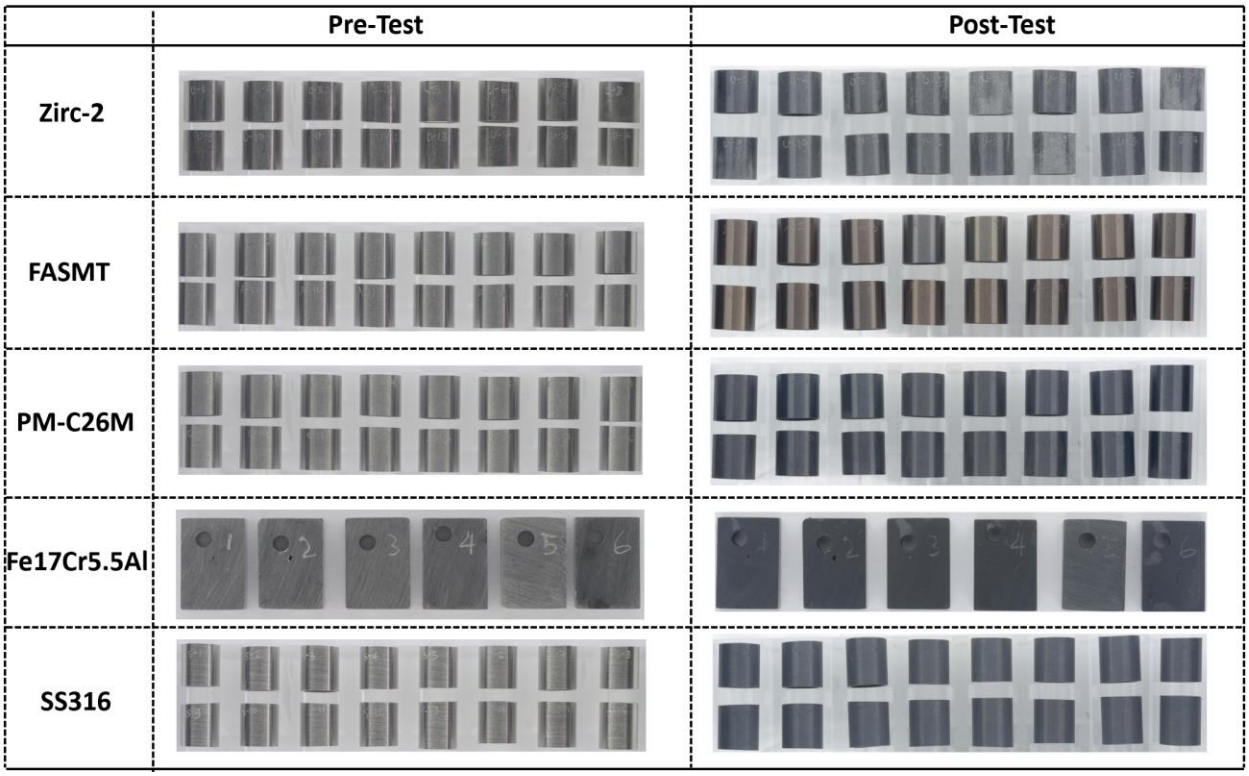

Figure 56. Visual inspection of Zirc-2, FA-SMT, PM-C26M, SS316 tubes along with Fe17Cr5.5Al flat coupons post 6 months of immersion testing in BWR-HWC (S-13).

7.3.1 TEM analysis of the alloys tested in BWR-NWC Environment

7.3.1.1 Zirc-2 Tube

TEM analysis of the Zirc-2 (tube) after 6 months of immersion in the BWR-NWC (S-12) is shown in Figure 57 . The oxide developed on the Zirc-2 tube looks almost uniform with no signs of nodular corrosion and is ~ 750 nm (Figure 58). High magnification TEM-EDS analysis confirmed the developed oxide to be ZrO_2 with second phase particles embedded in it (Fe, Cr, Ni). It is also observed that the SPPs are distributed in the Zr substrate along with the developed oxide [137]. Zirc-2 tube displayed a higher mass gain and developed a thicker external protective oxide layer when compared to all FeCrAl alloy variants under BWR-NWC.

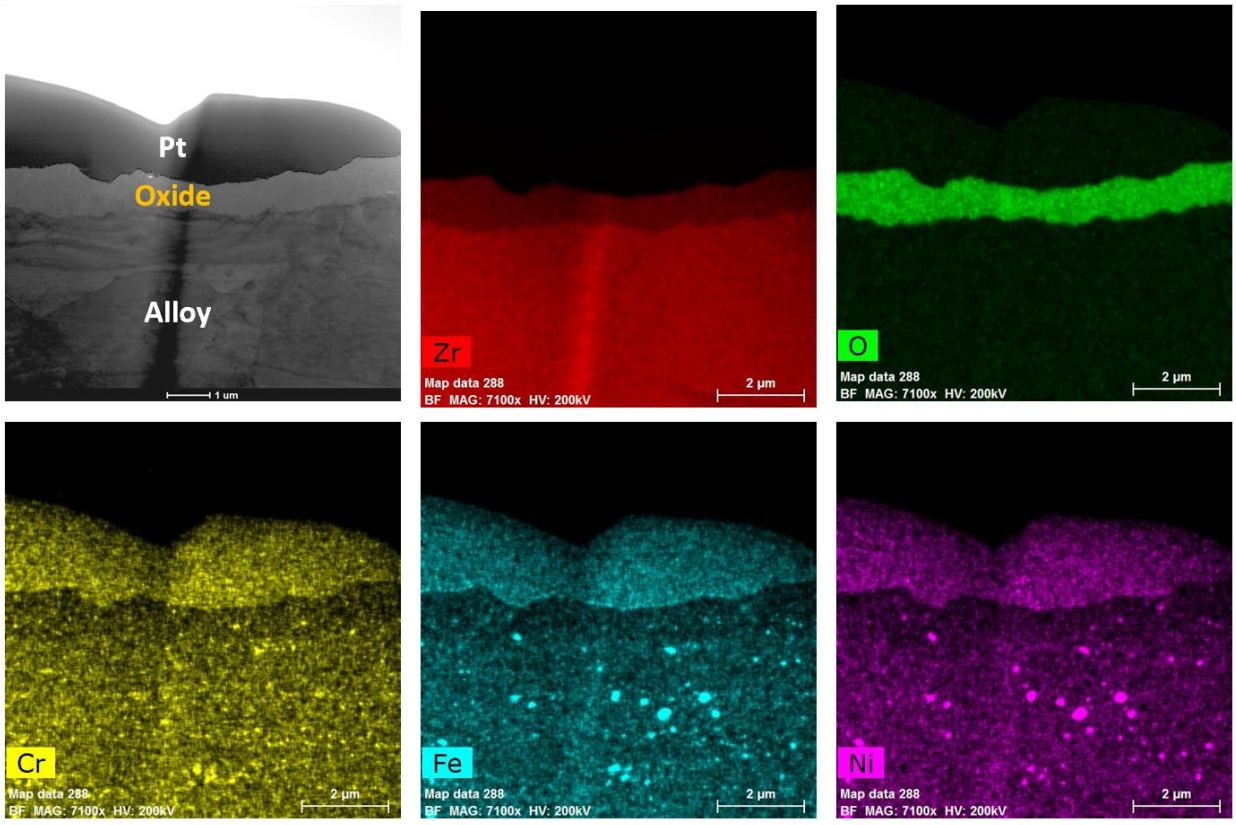

Figure 57. Low Magnification TEM-EDS for Zirc-2 (Tube) after 6 months of exposure in BWR-NWC (S-12). The marker is 2000 nm long.

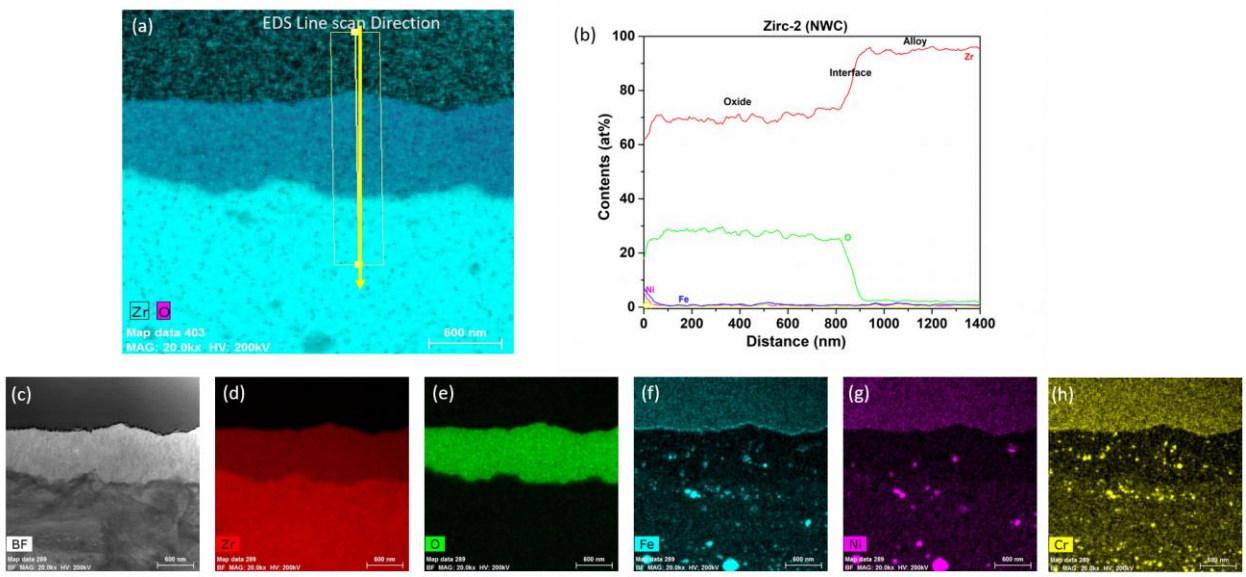

Figure 58.(a) shows the EDS line scan direction, (b)shows representative line scans of the oxide-substrate interfaces in the Zirc-2 tube after 6-months of simulated BWR-NWC exposure, and (c-h) shows the high magnification EDS mapping of Zirc-2 tube.

7.3.1.2 FA-SMT Tube

After immersion testing in the BWR-NWC (S-12) for six months, TEM analysis was conducted on one of the 16 FA-SMT tube specimens. The thickness of the oxide layer formed on FA-SMT tube was calculated to be ~500 nm using TEM bright field image (Figure 59). Low magnification TEM-EDS elemental maps showcased a fine-grained internal layer at the oxide-alloy matrix along with a continuous thick external Fe-Cr spinel oxide. Fine grained internal layer mainly composed of Fe and Cr. As shown in Figure 60 no aluminum enrichment was observed to form beneath the surface oxide layers as confirmed by line scans and high magnification TEM-EDS maps, and is contradictory to the literature [127]. Even though the Fe-Cr rich spinel oxide acts as top-layer barrier between the water and substrate to allow Cr oxide growth, the Cr oxide is non-uniform and defective. As shown in Figure 54, mass gain of FA-SMT tube under this test condition is due to the oxide formation as it limits the mass loss.

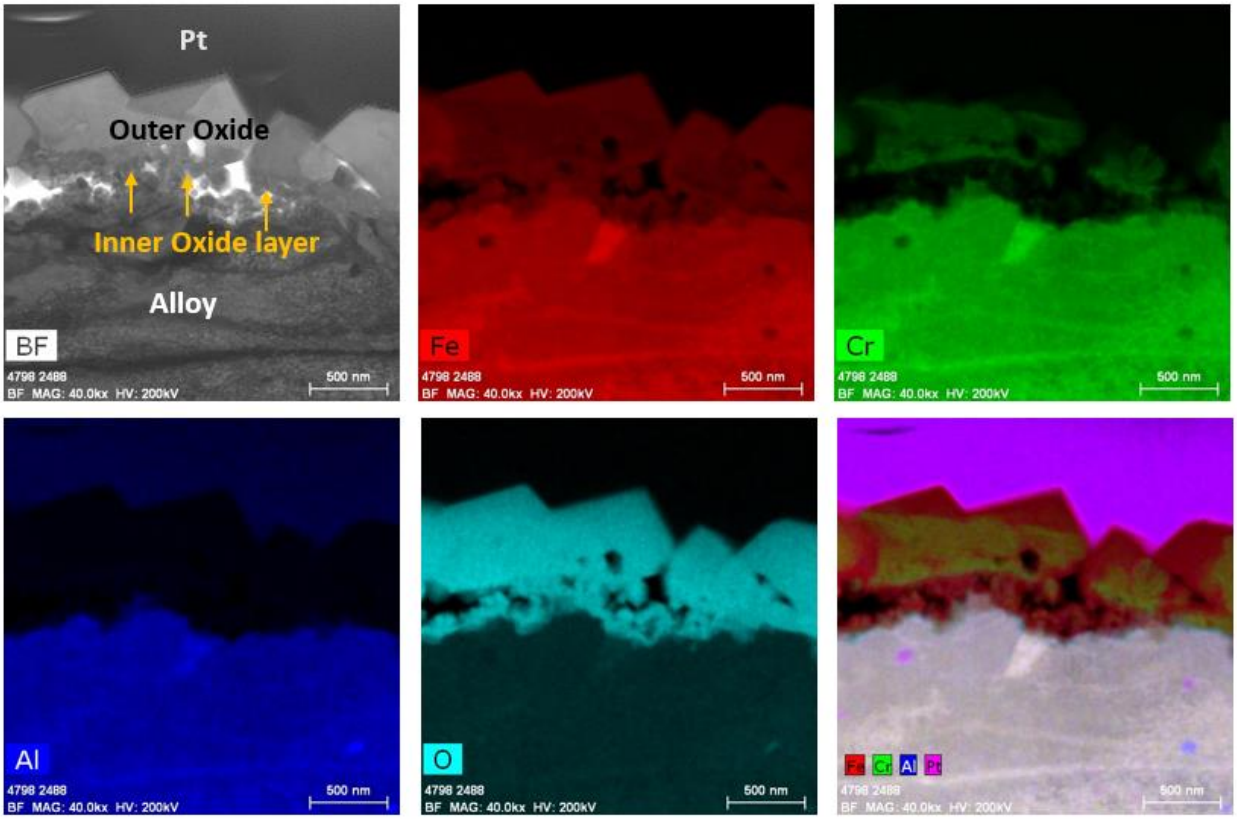

Figure 59. TEM-EDS for FA-SMT (Tube) after 6 months of exposure in BWR-NWC (S-12). The marker is 500 nm long.

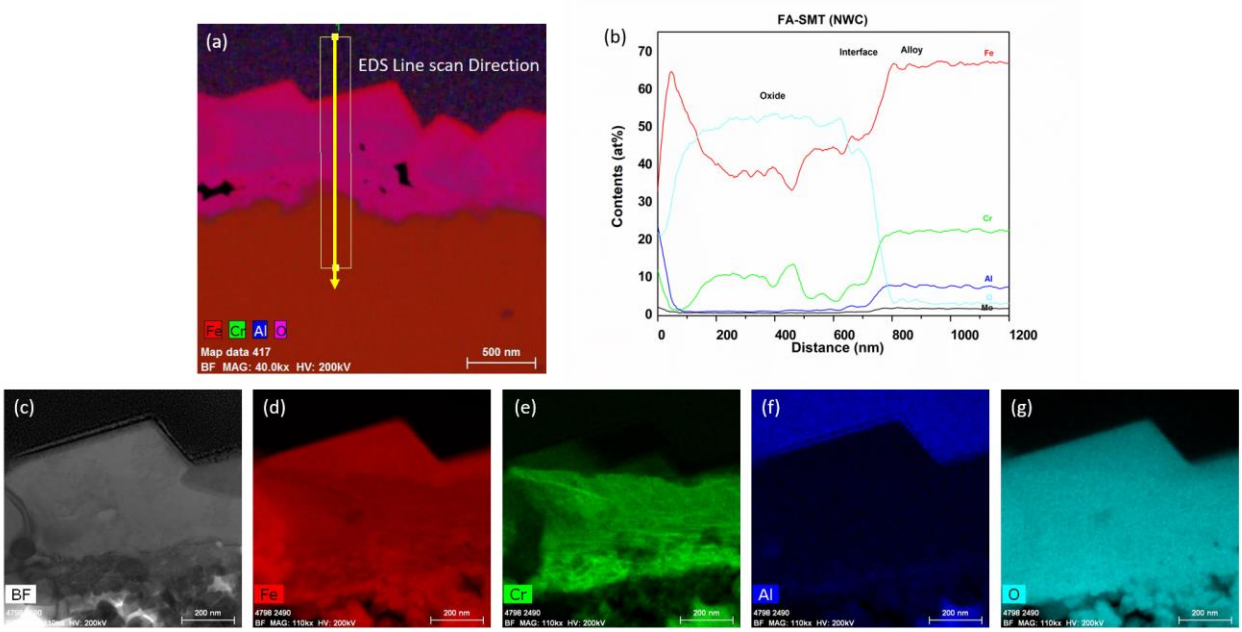

Figure 60. (a) shows the EDS line scan direction, (b)shows representative line scans of the oxide-substrate interfaces in the FA-SMT tube after 6-months of simulated BWR-NWC exposure, and (c-g) shows the high magnification EDS mapping of FA-SMT tube.

7.3.1.2 PM-C26M Tube

Figure 61 shows the oxide ~ 450 nm that was developed on PM-C26M tube after 6 months of BWR-NWC (S-12) exposure. From EDS maps in Figure 62 the external oxide layer mainly consists of Cr-oxide and Fe-oxide respectfully. The external oxide layer developed on PM-C26M is not continuous as Cr-oxide regions are embedded in surface Fe-oxide layer. Due to this non-continuous protective Cr oxide layer, no enrichment of aluminum oxide is observed at the oxide/substrate interface (Figure 62). In the current test, the weight gain of PM-C26M was slightly lower than FA-SMT.

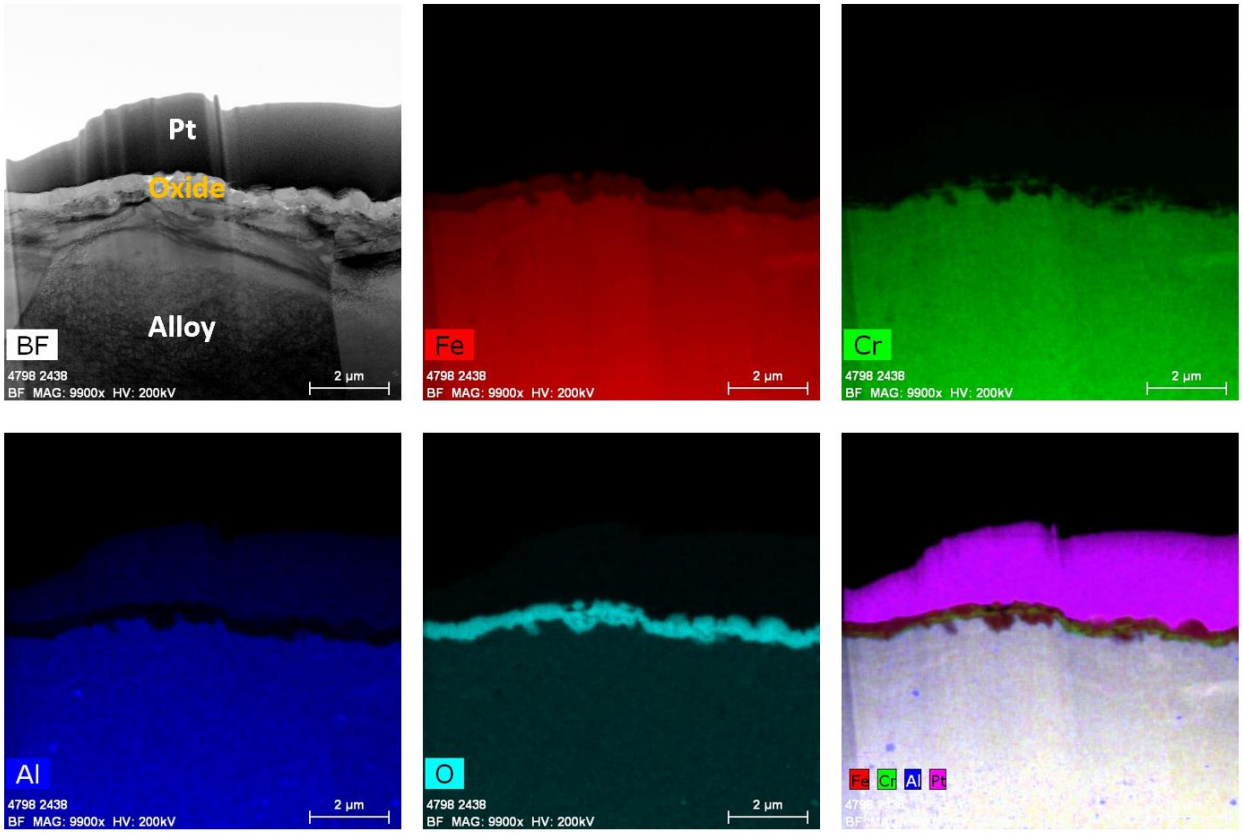

Figure 61. TEM-EDS for PM-C26M (Tube) after 6 months of exposure in BWR-NWC (S-12). The marker is 2000 nm long.

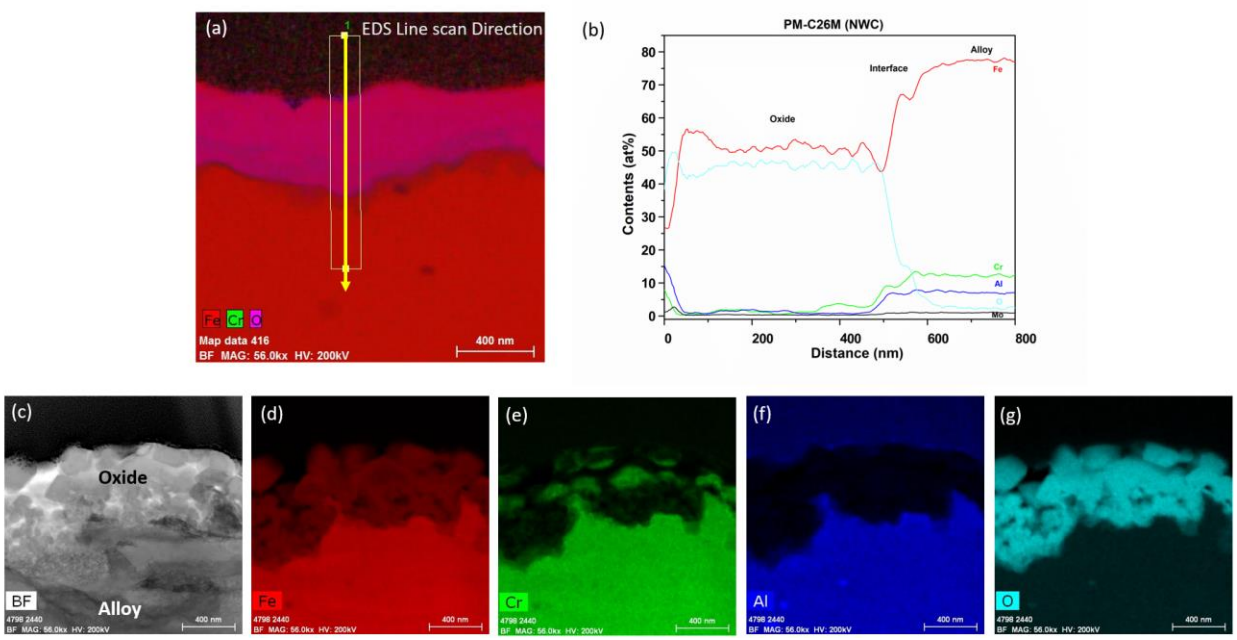

Figure 62. (a) shows the EDS line scan direction, (b)shows representative line scans of the oxide-substrate interfaces in the PM-C26M tube after 6-months of simulated BWR-NWC exposure, and (c-g) shows the high magnification EDS mapping of PM-C26M tube.

7.3.1.3 $Fe_{17}Cr_{5.5}Al$ Flat Coupon

For $Fe_{17}Cr_{5.5}Al$ (flat coupons), the oxide thickness post six months of testing is ~ 230nm (Figure 64). TEM-EDS maps show a distinct three-layered oxide structure (Figure 63). The top layer consists of a thick FeCr-rich oxide which is followed by a continuous chromium rich oxide layer. The Aluminum layer formed underneath the Cr rich oxide layer is not continuous and can be seen as an internal nodular oxide. The line scan in Figure 63 also confirms the enrichment of Al and Cr at the oxide/ substrate interface. The enrichment of Al is proposed to be due to the low oxygen partial pressure below the Cr oxide layer and above the substrate [138]. It should also be noted that the oxide developed on Fe17Cr5.5Al (Flat coupon) is thinnest of all the FeCrAl alloys tested in this study.

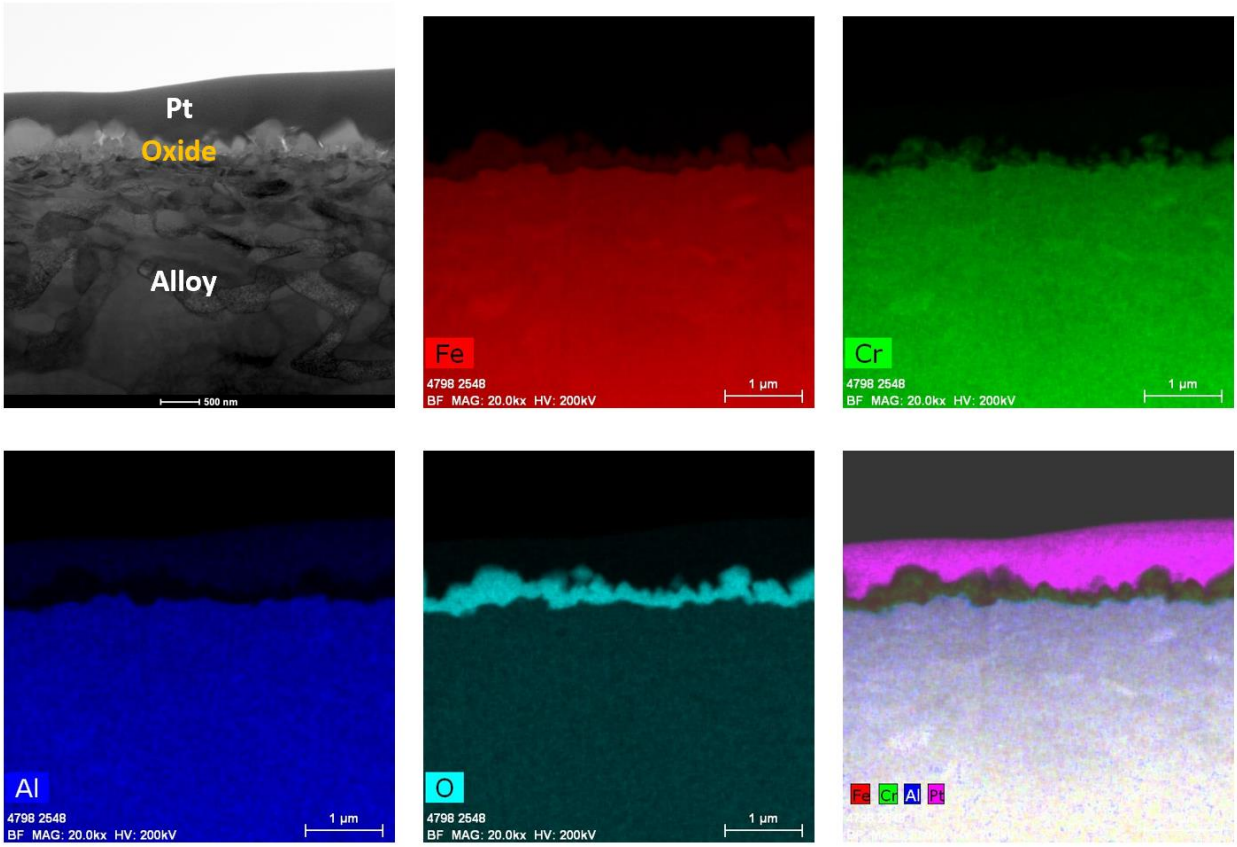

Figure 64. TEM-EDS for $Fe_{17}Cr_{5.5}Al$ flat coupon after 6 months of exposure in BWR-NWC (S-12). The marker is 1000 nm long.

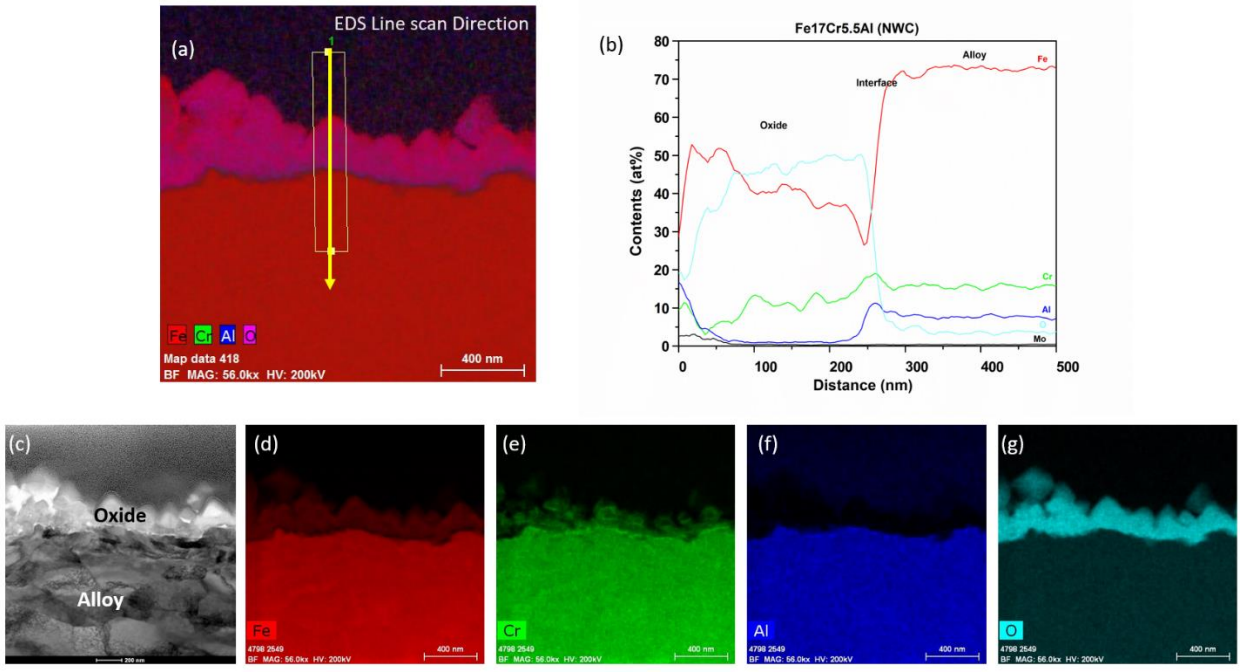

Figure 63. (a)shows the EDS line scan direction, (b)shows representative line scans of the oxide-substrate interfaces in the $Fe_{17}Cr_{5.5}Al$ flat coupon after 6-months of simulated BWR-NWC exposure, and (c-g) shows the high magnification EDS mapping of $Fe_{17}Cr_{5.5}Al$ flat coupon.

7.3.1.5 SS316 Tube

After immersion testing in the BWR-NWC (S-12) for six months, TEM analysis was conducted on SS316 tube specimens. The thickness of the oxide layer formed on SS316 tube was calculated to be ~500 nm using TEM bright field image (Figure 65). As shown in Figure 66 high magnification TEM-EDS elemental maps showcased a surface oxide spinel along with a fine-grained inner oxide layer at the oxide-alloy matrix interface. The surface oxide mainly consists of Fe-Cr spinel whereas fine grained internal layer is composed of Fe, Cr and Ni. Under oxygenated water SS316 tube specimens displayed less mass gain than the Zirc-2 tube specimens.

.

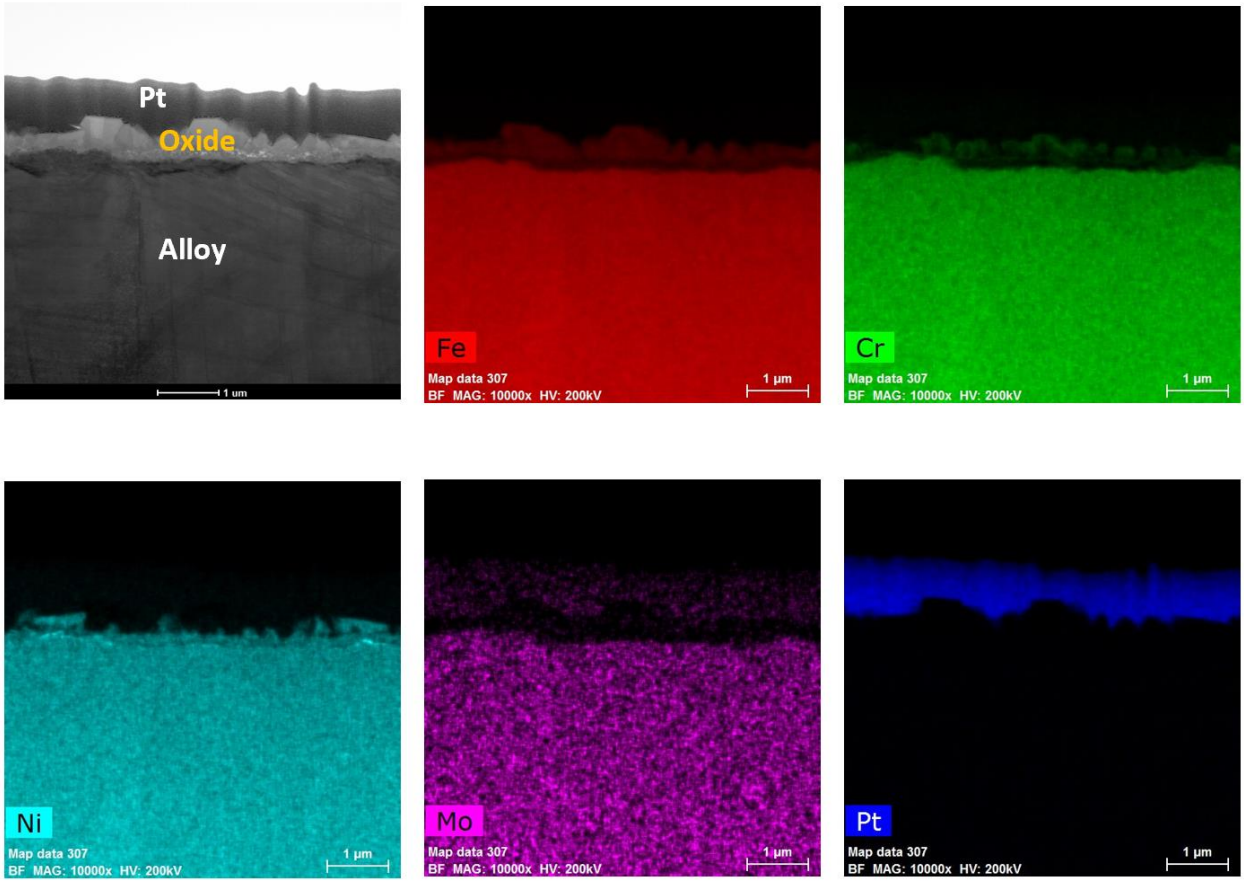

Figure 65. TEM-EDS for SS316 (Tube) after 6 months of exposure in BWR-NWC (S-12). The marker is 1000 nm long.

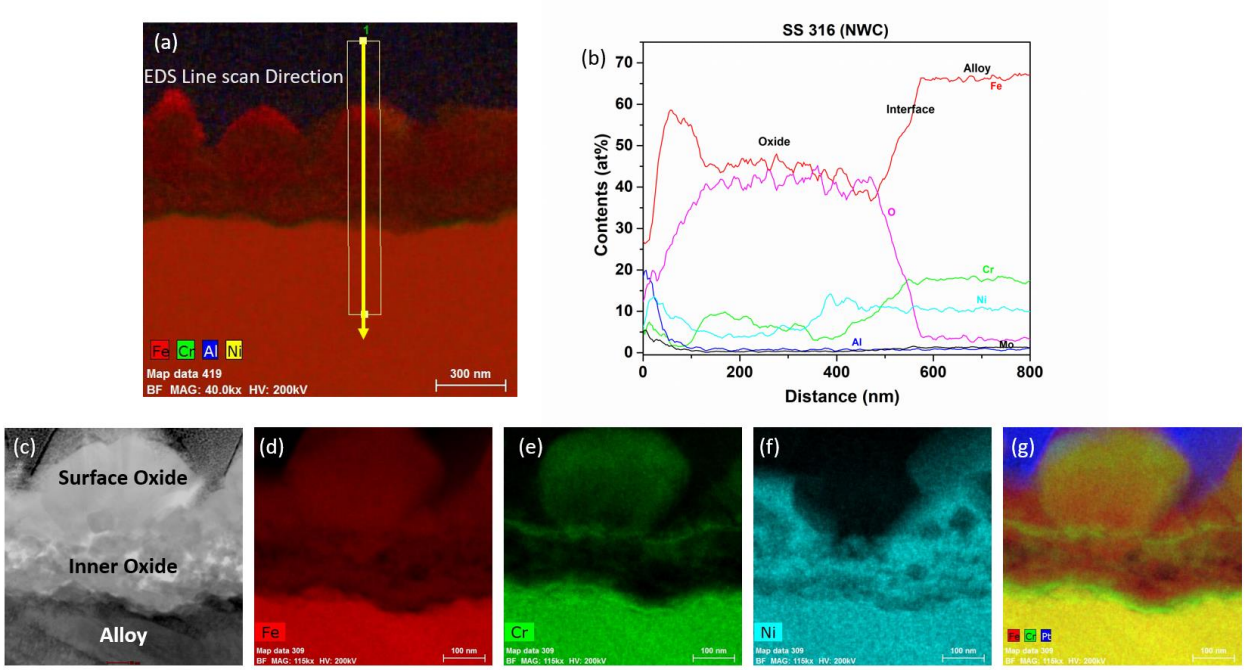

Figure 66. (a) shows the EDS line scan direction, (b)shows representative line scans of the oxide-substrate interfaces in the SS316 tube after 6-months of simulated BWR-NWC exposure, and (c-g) shows the high magnification EDS mapping of SS316 tube.

7.3.2 TEM analysis of the alloys tested in in BWR-HWC Environment

7.3.2.1 Zirc-2 tube

TEM analysis of the Zirc-2 tube after 6 months immersion in the BWR-HWC is shown in Figure 67. The oxide developed on the Zirc-2 tube looks almost uniform and is ~ 900 nm. High magnification TEM-EDS analysis (Figure 68) confirmed the developed oxide to be ZrO_2 with SPP distributed in the Zr substrate along with the oxide [63]. Even though the thickness of the oxide developed on Zirc-2 tube in BWR-HWC is slightly higher than oxide formed in BWR-NWC, weight gain is seen to be higher in BWR-NWC when compared to BWR-HWC.

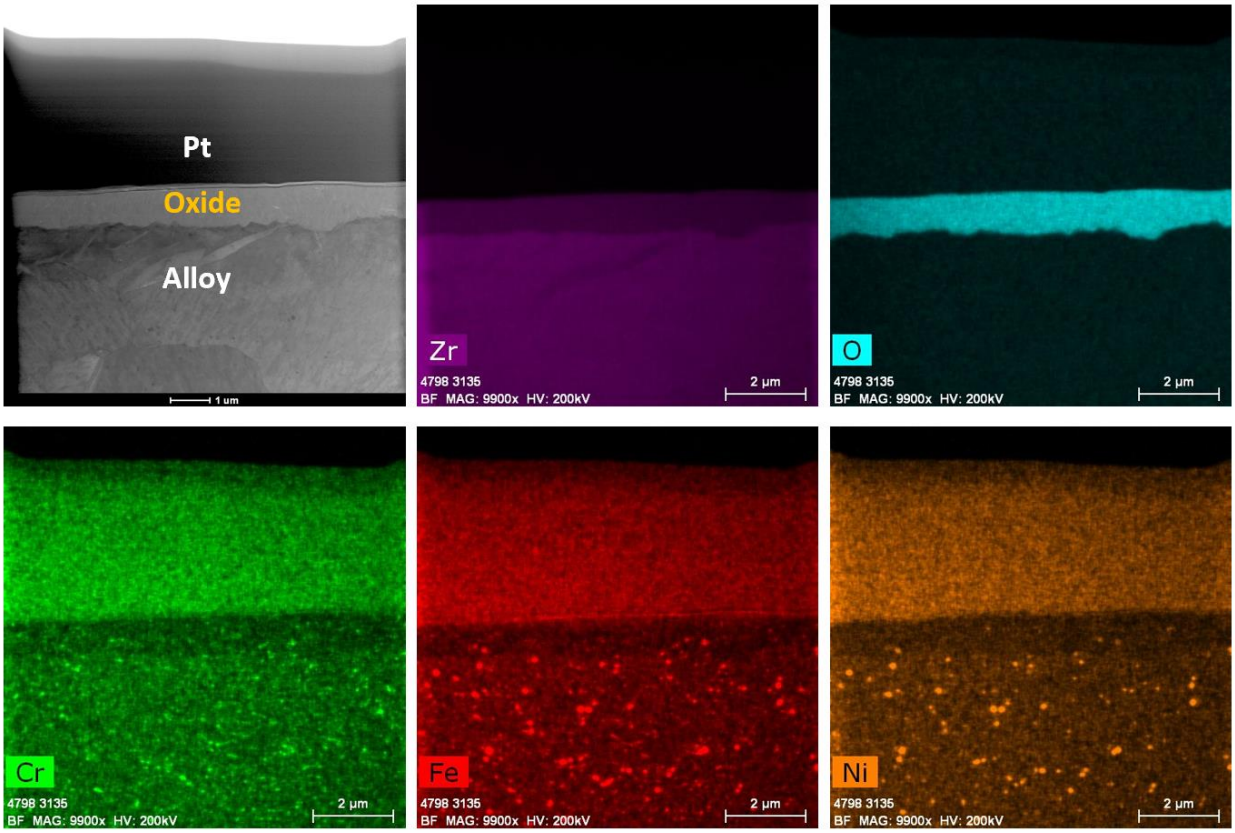

Figure 67. Low Magnification TEM-EDS for Zirc-2 (Tube) after 6 months of exposure in BWR-HWC (S-13). The marker is 2000 nm long.

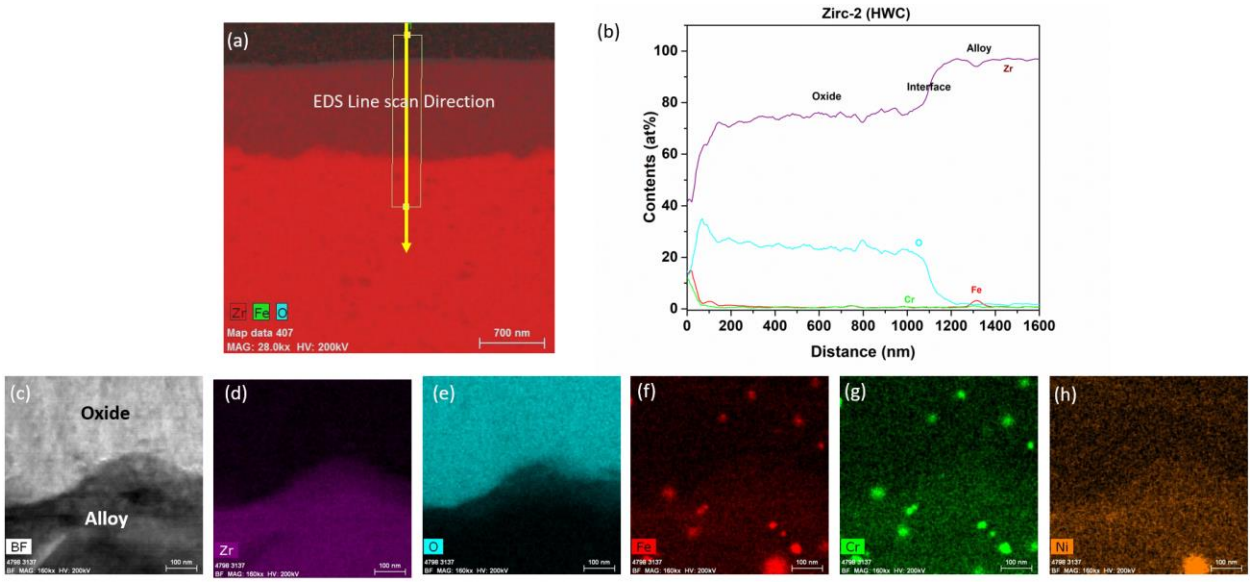

Figure 68. (a) shows the EDS line scan direction, (b)shows representative line scans of the oxide-substrate interfaces in the Zirc-2 tube after 6-months of simulated BWR-HWC exposure, and (c-h) shows the high magnification EDS mapping of Zirc-2 tube.

7.3.2.2 FA-SMT Tube

After six months of immersion testing in BWR-HWC (S-13), low magnification TEM-EDS analysis was conducted on FA-SMT tube and shown in Figure 69. TEM bright field images displayed ~ 150 nm thick oxide layer on FA-SMT tube (Figure 70). EDS elemental maps confirmed the oxide to be FeCr-oxide layer. This oxide layer is depleted of iron indicating the dissolution of Fe under BWR-HWC. At the oxide-alloy interface a slight enrichment of Al can also be observed via line scan. After 6 months of immersion testing, the mass loss on the FA-SMT tube specimen is relatively less due to higher Cr content when compared to PM-C26M (tube) and Fe17Cr5.5Al (Flat Coupon).

As Cr-oxide is stable in this environment, and the coefficient of diffusivity (D_0) of Fe cation is higher than the Cr cation, the faster Fe cation diffusion can result in mass loss. In the meantime, the formation of dense and continuous Cr-oxide layer may prevent the further diffusion of Fe from the alloy matrix thus inhibiting the dissolution of Fe from the alloy matrix.

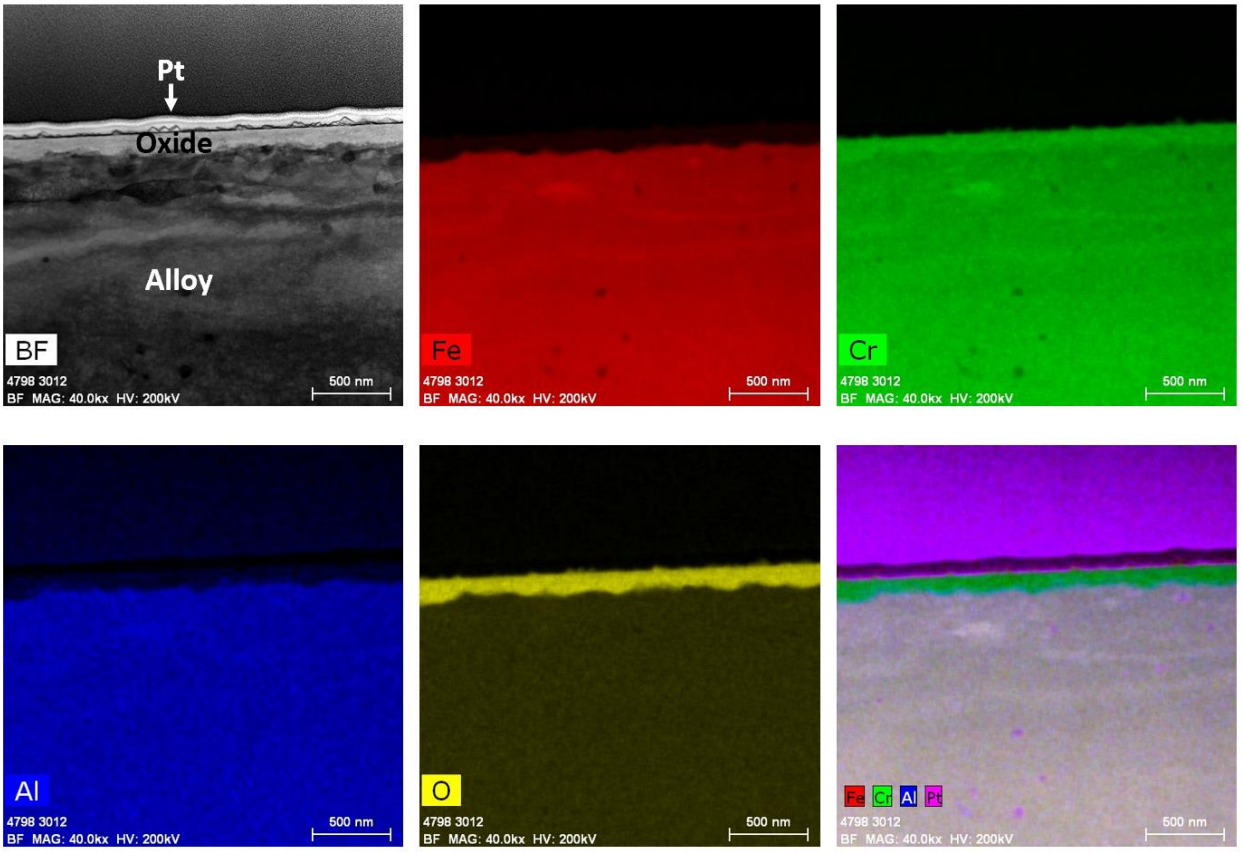

Figure 69 .TEM-EDS for FA-SMT (Tube) after 6 months of exposure in BWR-HWC (S-13). The marker is 500 nm long.

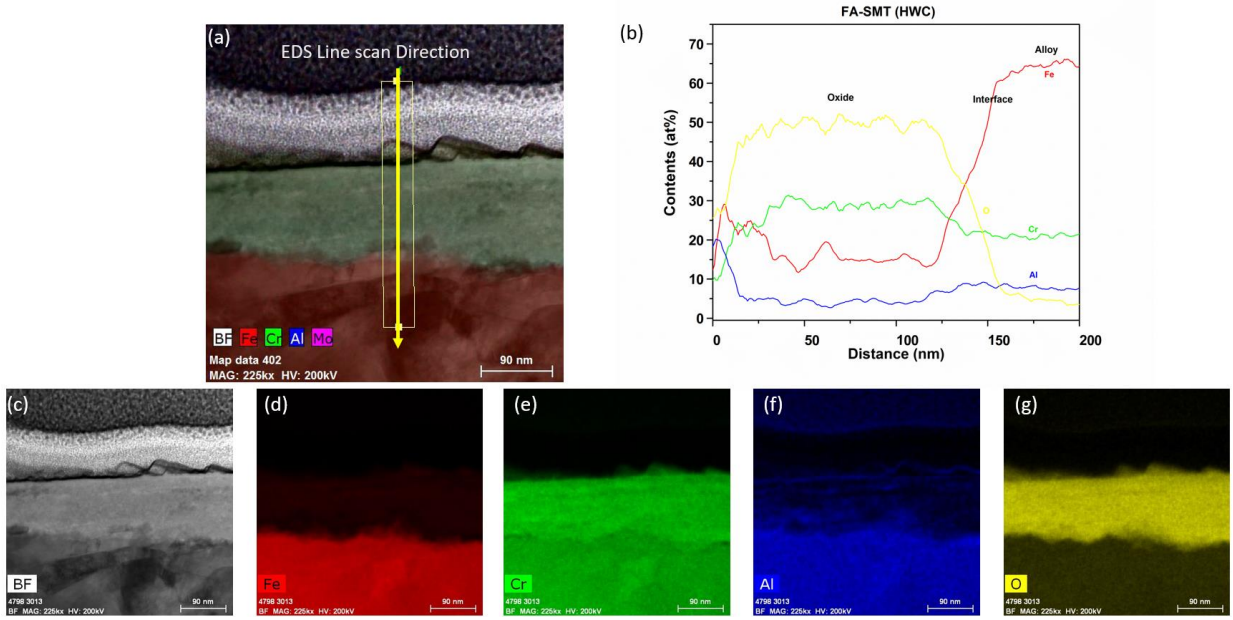

Figure 70. (a) shows the EDS line scan direction, (b)shows representative line scans of the oxide-substrate interfaces in the FA-SMT tube after 6-months of simulated BWR-HWC exposure, and (c-g) shows the high magnification EDS mapping of FA-SMT tube.

7.3.2.3 PM-C26M Tube

Figure 71 shows the low magnification TEM-EDS analysis of PM-C26M (Tube) after six months of immersion testing in BWR-HWC (S-13). Bright field images and line scans (Figure 72) confirmed the thickness of the oxide developed to be ~ 8 um. This thicker oxide layer could be primarily due to lower Cr content in alloy matrix. EDS elemental maps show external oxide layer to be a mixed Fe-Cr-Al oxide. Even though similar mass loss was observed on PM-C26M (Tube) and Fe17Cr5.5Al (Flat Coupons) the thickness of the oxide layer developed on PM-C26M (Tube) is twofold higher than the oxide developed on Fe17Cr5.5Al (Flat Coupons).

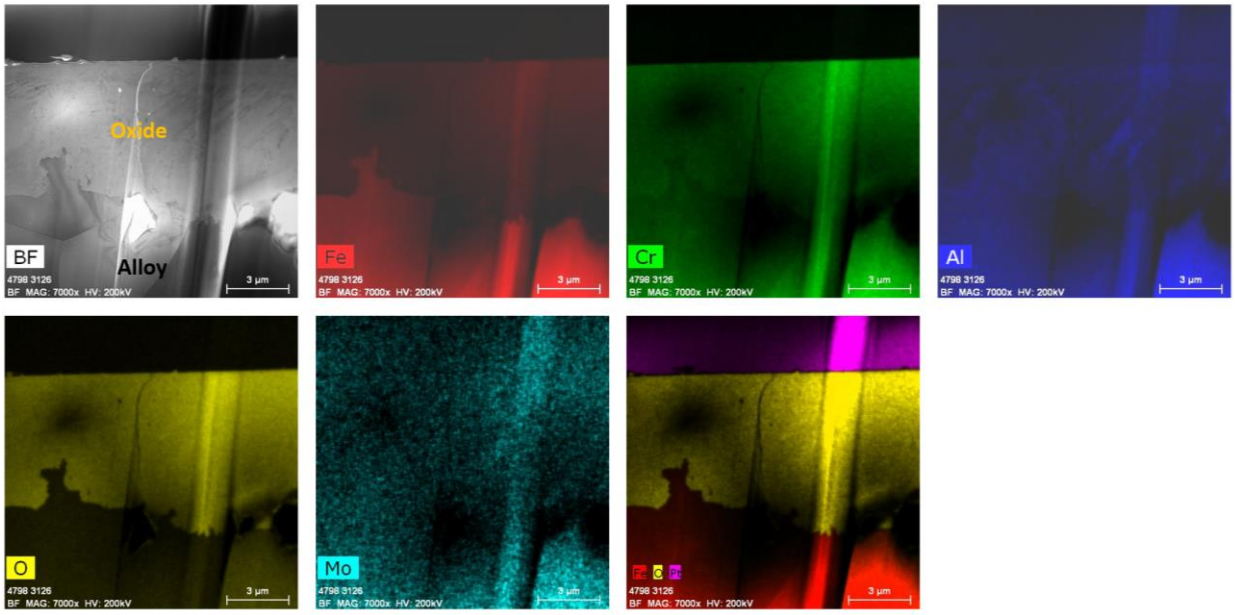

Figure 71. TEM-EDS for PM-C26M (Tube) after 6 months of exposure in BWR-HWC (S-13). The marker is 3000 nm long.

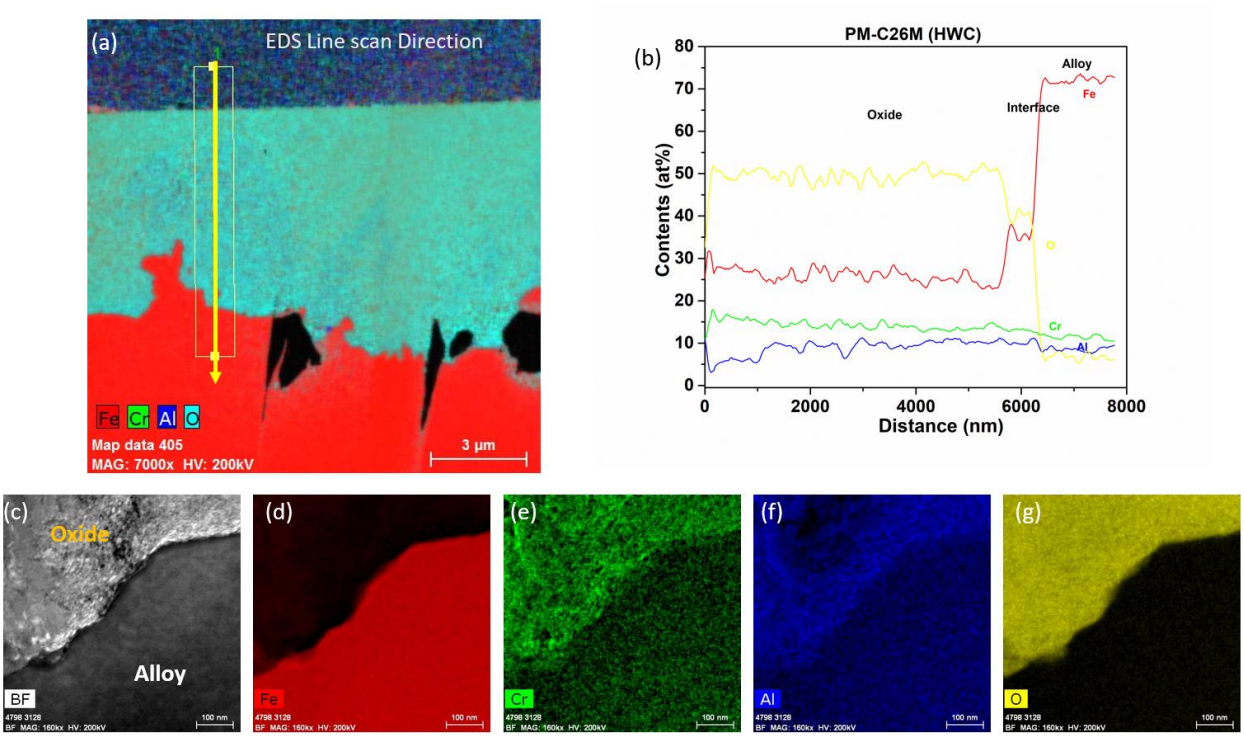

Figure 72. (a) shows the EDS line scan direction, (b)shows representative line scans of the oxide-substrate interfaces in the PM-C26M tube after 6-months of simulated BWR-HWC exposure, and (c-g) shows the high magnification EDS mapping of PM-C26M tube.

7.3.2.3 $Fe_{17}Cr_{5.5}Al$- Flat Coupon

Figure 73 shows the low magnification TEM-EDS analysis of $Fe_{17}Cr_{5.5}Al$ (Flat Coupons), after six months of immersion testing in BWR-HWC (S-13). High magnification bright field image and line scan (Figure 74) confirmed the thickness of the oxide developed to be ~ 4 um. This thicker oxide layer could be attributed to a lower Cr content in $Fe_{17}Cr_{5.5}Al$ alloy when compared to FA-SMT (tube). EDS elemental maps showcased a mixed Fe-Cr-Al oxide. The thickness of the oxide developed on $Fe_{17}Cr_{5.5}Al$ (Flat Coupon) is several orders of magnitude higher than the oxide developed on FA-SMT. It is also observed that a significant mass loss is seen in $Fe_{17}Cr_{5.5}Al$ (Flat

coupons) due to the continuous oxidation of the metal along with continuous dissolution of the Fe-oxide at the oxide-water interface.

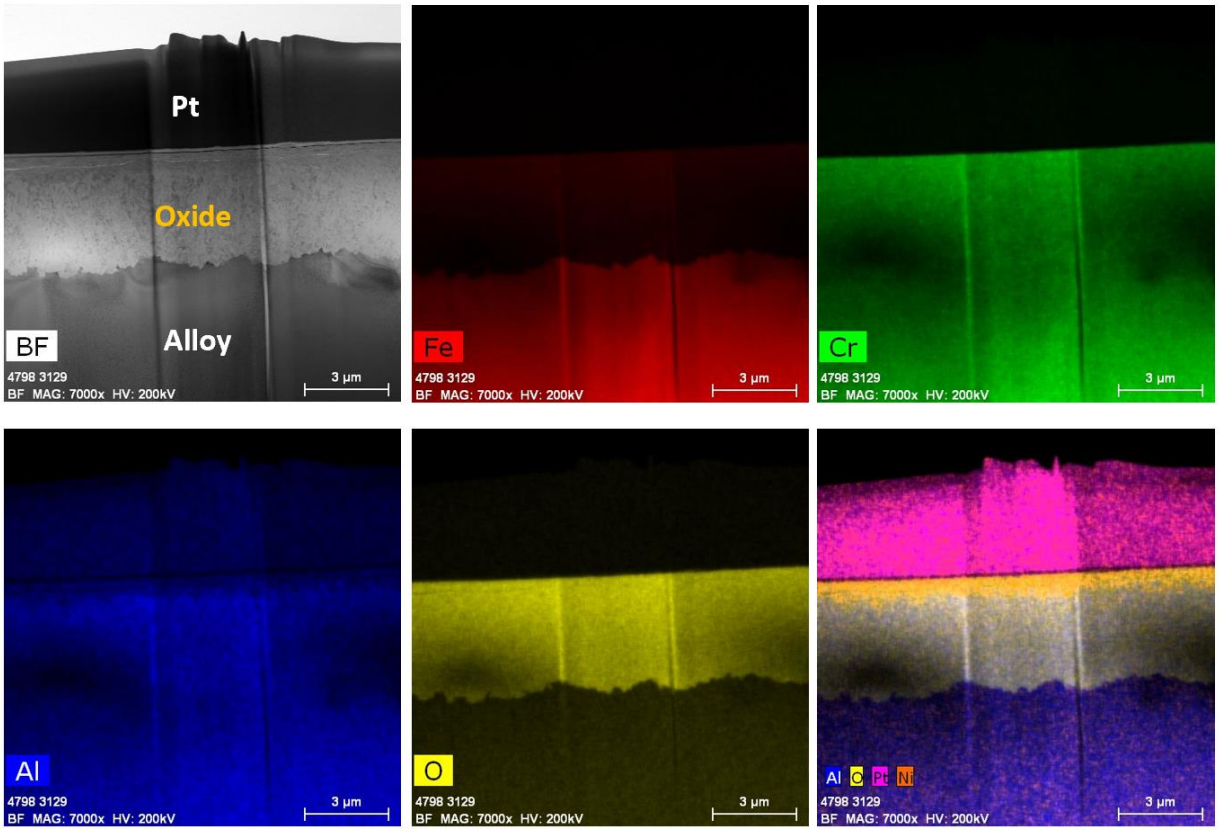

Figure 73. TEM-EDS for Fe17Cr5.5Al flat coupon after 6 months of exposure in BWR-HWC (S-13). The marker is 3000 nm long.

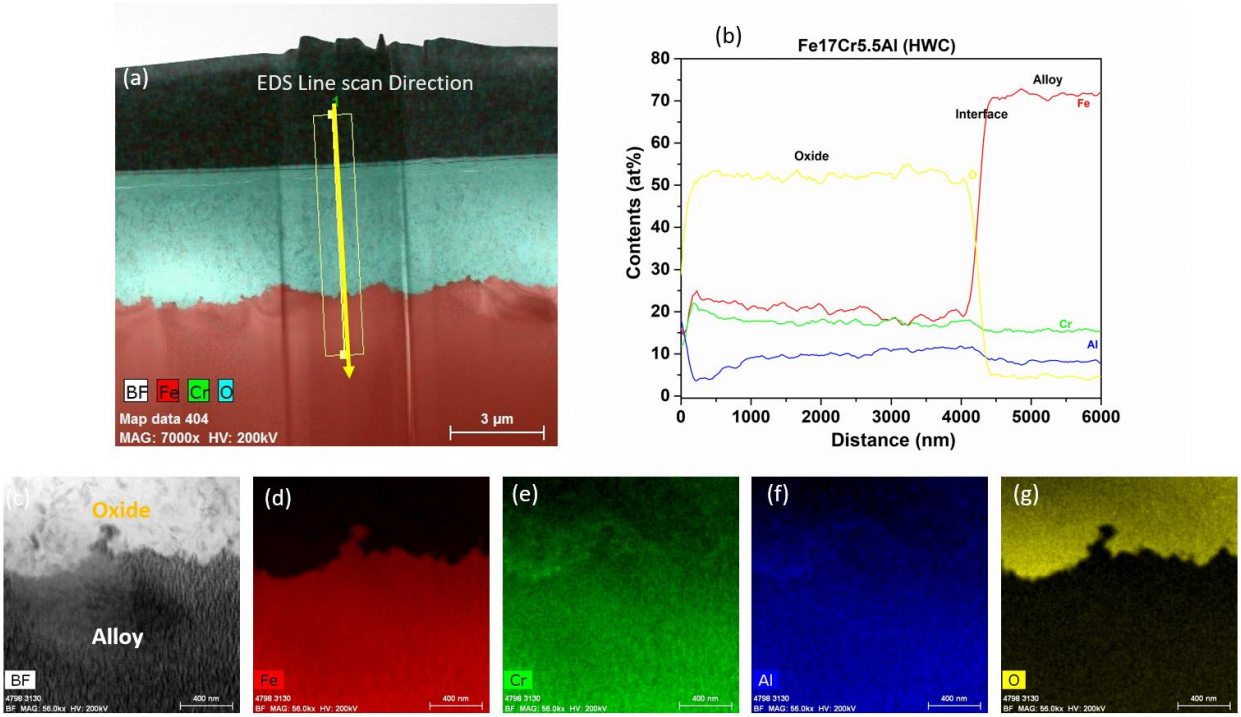

Figure 74. (a)shows the EDS line scan direction, (b)shows representative line scans of the oxide-substrate interfaces in the $Fe_{17}Cr_{5.5}Al$ flat coupon after 6-months of simulated BWR-HWC exposure, and (c-g) shows the high magnification EDS mapping of $Fe_{17}Cr_{5.5}Al$ flat coupon.

7.3.2.5 SS316 Tube

After immersion testing in the BWR-HWC (S-13) for six months, TEM analysis was conducted on SS316 tube specimens. The thickness of the oxide layer formed on SS316 tube was calculated to be ~500 nm using low magnification TEM-EDS analysis (Figure 75). As shown in Figure 76 high magnification TEM-EDS elemental maps showcased a surface oxide spinel along with an inner oxide layer at the oxide-alloy matrix interface. The surface oxide mainly consists of Fe spinel and is not continuous whereas the continuous internal layer is composed of FeCr oxide. Under hydrogenated water SS316 tube specimens displayed less mass gain than the Zirc-2 tube specimens.

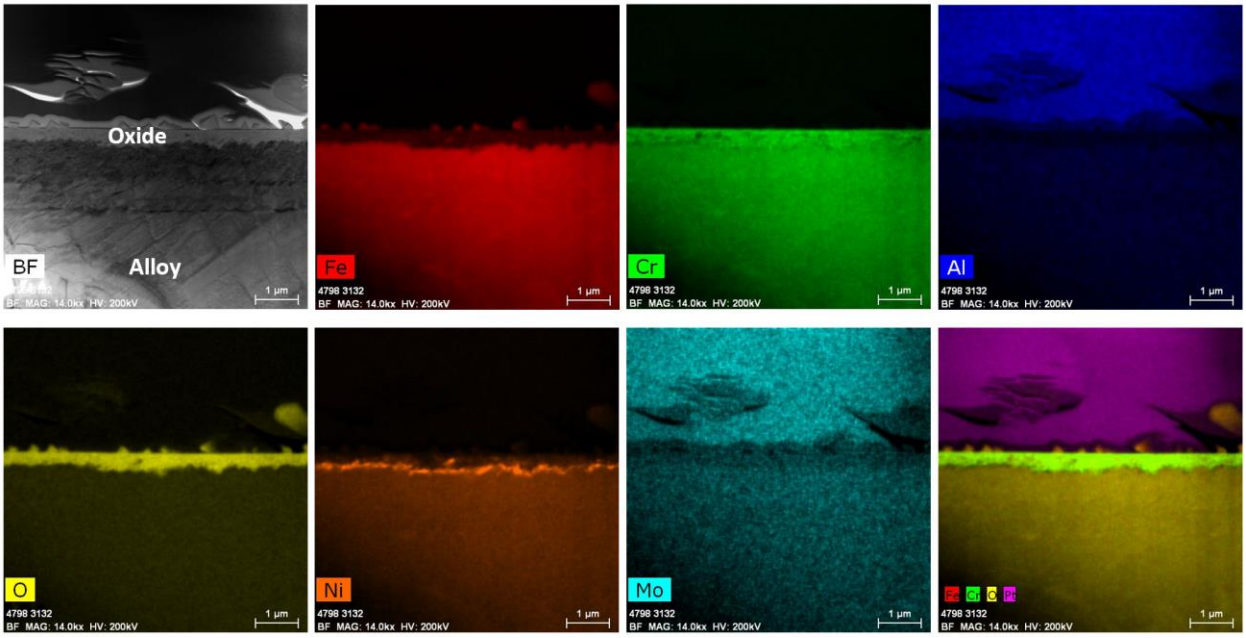

Figure 75 TEM-EDS for SS316 (Tube) after 6 months of exposure in BWR-HWC (S-13). The marker is 1000 nm long.

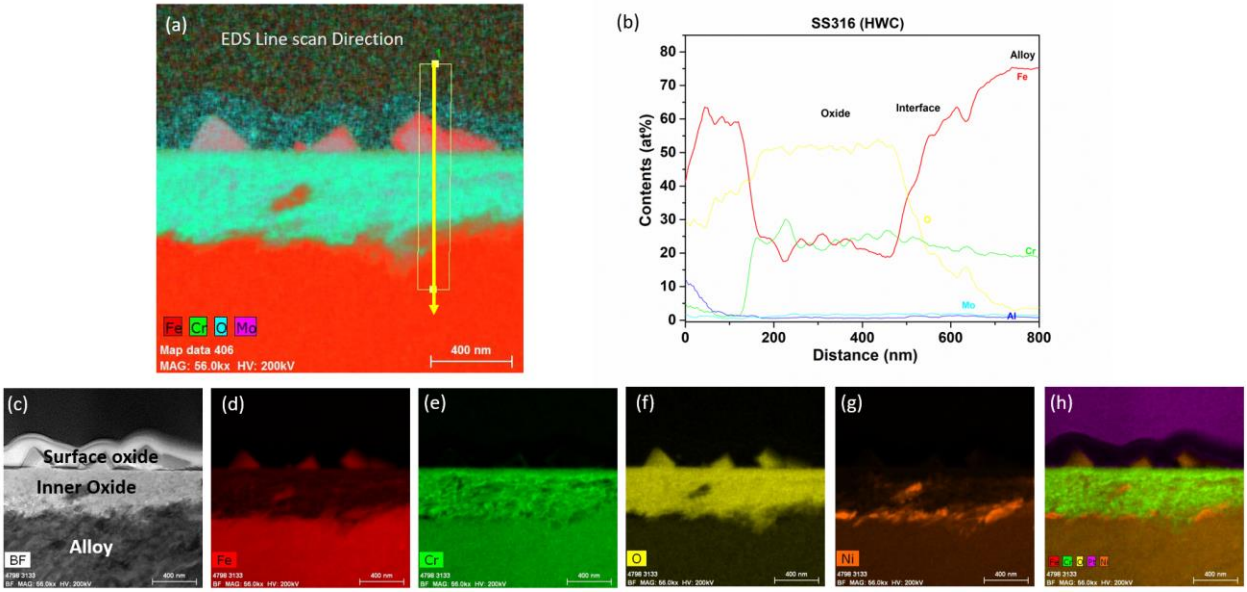

Figure 76. (a) shows the EDS line scan direction, (b)shows representative line scans of the oxide-substrate interfaces in the SS316 tube after 6-months of simulated BWR-HWC exposure, and (c-h) shows the high magnification EDS mapping of SS316 tube.

7.3.3 Oxide Thickness Comparison

In order to compare the oxide thickness of all the FeCrAl alloy variants more comprehensively, a plot is generated based on the data in Section 7.3.1 and 7.3.2.

Figure 77 shows that the oxide thickness developed on FeCrAl alloy variants tested in both water chemistries. In oxygenated water, FeCrAl alloy variants developed thinner oxides. Among the alloy variants Fe17Cr5.5Al flat coupon have the thinnest oxide than other FeCrAl alloys, FA-SMT and PM-C26M and reference material, Zirc-2 and SS316. However, in hydrogenated water the oxide developed on FA-SMT tube specimen is in nm range whereas the oxide developed on PM-C26M and Fe17Cr5.5Al are in micron range. A trend of increase in oxide thickness was observed with the decrease in Cr content.

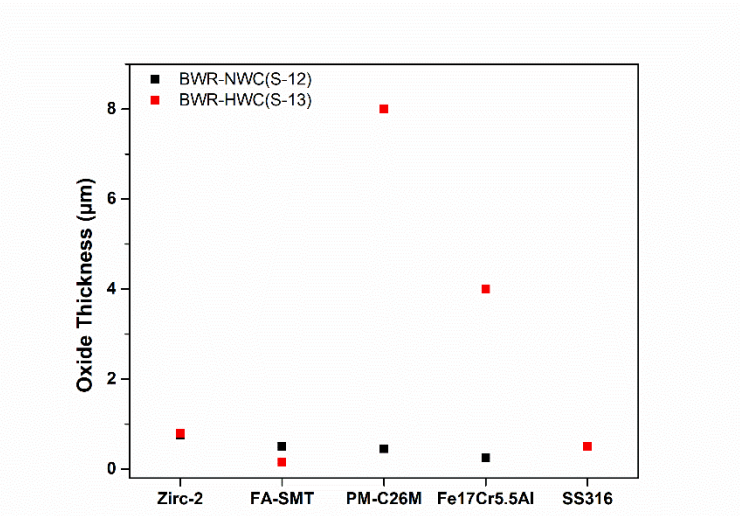

Figure 77. Oxide thickness comparison of all the alloy variants tested in simulated BWR-NWC, (S-12) and BWR-HWC (S-13) waters for six months.

7.4. Discussion

The current results show the corrosion behavior of latest generation FeCrAl alloys tested in simulated BWR water chemistries for 6-months. In Figure 54 especially for hydrogenated water, weight loss for all FeCrAl alloy variants was seen and is significantly high for PM-C26M and

Fe17Cr5.5Al specimens. In the case of BWR-NWC, weight gain was observed for FeCrAl alloy variants and is contradictory with the long-term immersion testing data of previous generation FeCrAl alloys developed at ORNL and GE [76,127,139]. This observation could be due to lower oxygen concentration (0.5 ppm) used in the current study. Long term immersion tests need to be conducted to gain further insight on the mass change of these alloys.

After immersion testing, in BWR-NWC for six months a clear enrichment of FeCr oxide spinel was observed on FA-SMT specimen. The Cr-oxide layer developed underneath the Fe-Cr oxide spinel structure is not continuous and is defective, probably because of the short testing time (Figure 59). On PM-C26M (tube), Fe-Cr oxide spinel is still growing to be an effective water barrier (Figure 61), so that it can prevent Cr oxide beneath the spinel from continuously dissolving into the water [63]. This observation can also be attributed to the lower O_2 concentration in the testing solution (0.5ppm), which did not provide sufficiently acute oxygen supply for a continuous Cr oxide layer to grow below the Fe-Cr oxide spinel. In the case of model alloy Fe17Cr5.5Al flat coupon specimens a surface Fe-Cr oxide spinel was observed followed by the enriched Cr and Al oxides (Figure 64). It is believed that the continuous Cr-oxide layer underneath the spinel provides a low partial pressure of oxygen activity [140] that is needed to stabilize Al-oxide [141]. While FA-SMT and PM-C26M tube specimens are fabricated by powder metallurgy, the model alloy flat coupons are manufactured by VIM. From our observations the different in manufacturing routes could be the reason for the enrichment of Al-oxide in Fe17Cr5.5Al flat coupon specimens [142]. Thus, the oxide layer of model Fe17Cr5.5Al specimen (~200 nm) is much thinner than PM-C26M and FA-SMT (~600 nm) tubes. The oxidation behavior of FeCrAl cladding in simulated BWR-NWC is summarized in Figure 78.

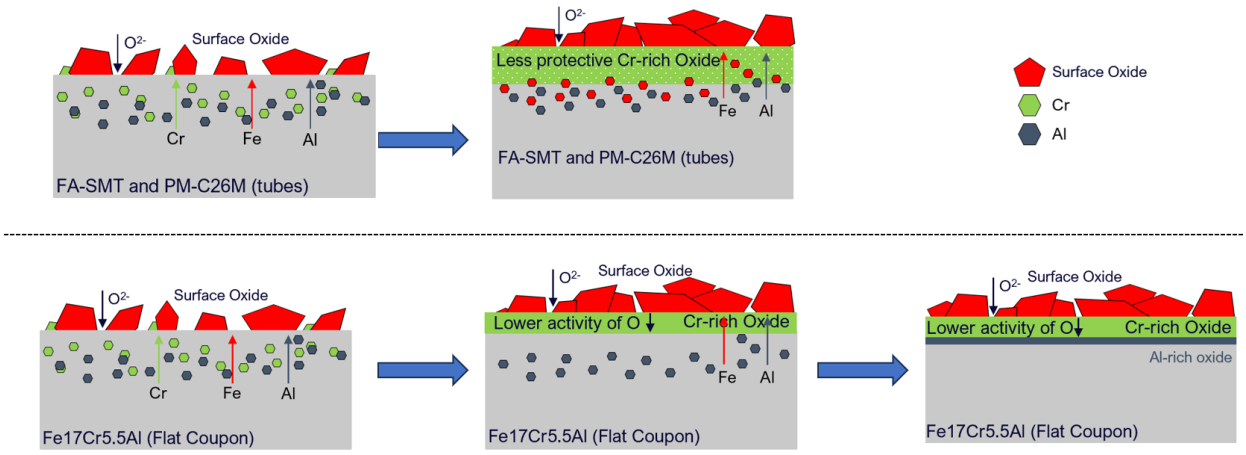

Figure 78. Illustration of the oxidation behavior of FeCrAl alloys in simulated BWR-NWC.

In the case of BWR-HWC after six months of immersion testing, a trend of increase in oxide thickness with the decrease in Cr content was observed (

Figure 77). No surface crystals were observed in hydrogenated water as compared to oxygenated water and this finding is consistent with the literature [76]. At 288˚C, even though the thickness of the oxides developed on Fe17Cr5.5Al (Flat Coupons) (Figure 73) and PM-C26M (tube) (Figure 71) alloys are much larger than FA-SMT (tube) (Figure 69), these oxide layers may not form rapid passivation by Cr-oxide due to lesser Cr content. The fact that Cr oxide is not continuous could be the reason for a huge weight loss of 120 mg/dm^2 in lower Cr containing alloys after 6 months of exposure which is consistent with the Rebak's observations [134]. Literature also hints that the presence of higher Cr content may possibly slow down the diffusion of other cations [143].

The oxygen activity in BWR-HWC is lower due to hydrogen addition [144]. The corrosion in higher Cr content (FA-SMT tube) may procced by facilitating the outward diffusion of Fe and Cr towards the electrolyte interface which enhance the formation kinetics of chromia thus preventing

the dissolved oxygen and hydrogen ingress into the high Cr content alloy. At the same time this continuous protective chromia layer may prevent the further diffusion of Fe from the alloy thus decreasing the Fe dissolution. Hence a thinner oxide layer and a lower mass loss was possible as observed for FA-SMT tube specimen under this test condition. Unlike FA-SMT specimens, the Cr content in PM-C26M (tube) and Fe17Cr5.5Al flat coupon is lower. As a result, the chances for the formation of protective chromia are less leading to a continuous dissolution of Fe from the alloys. Hence, thicker oxide layer and higher mass loss was observed for lower Cr content alloys under hydrogenated waters. The oxidation behavior of FeCrAl cladding in simulated BWR-HWC is summarized in Figure 79.

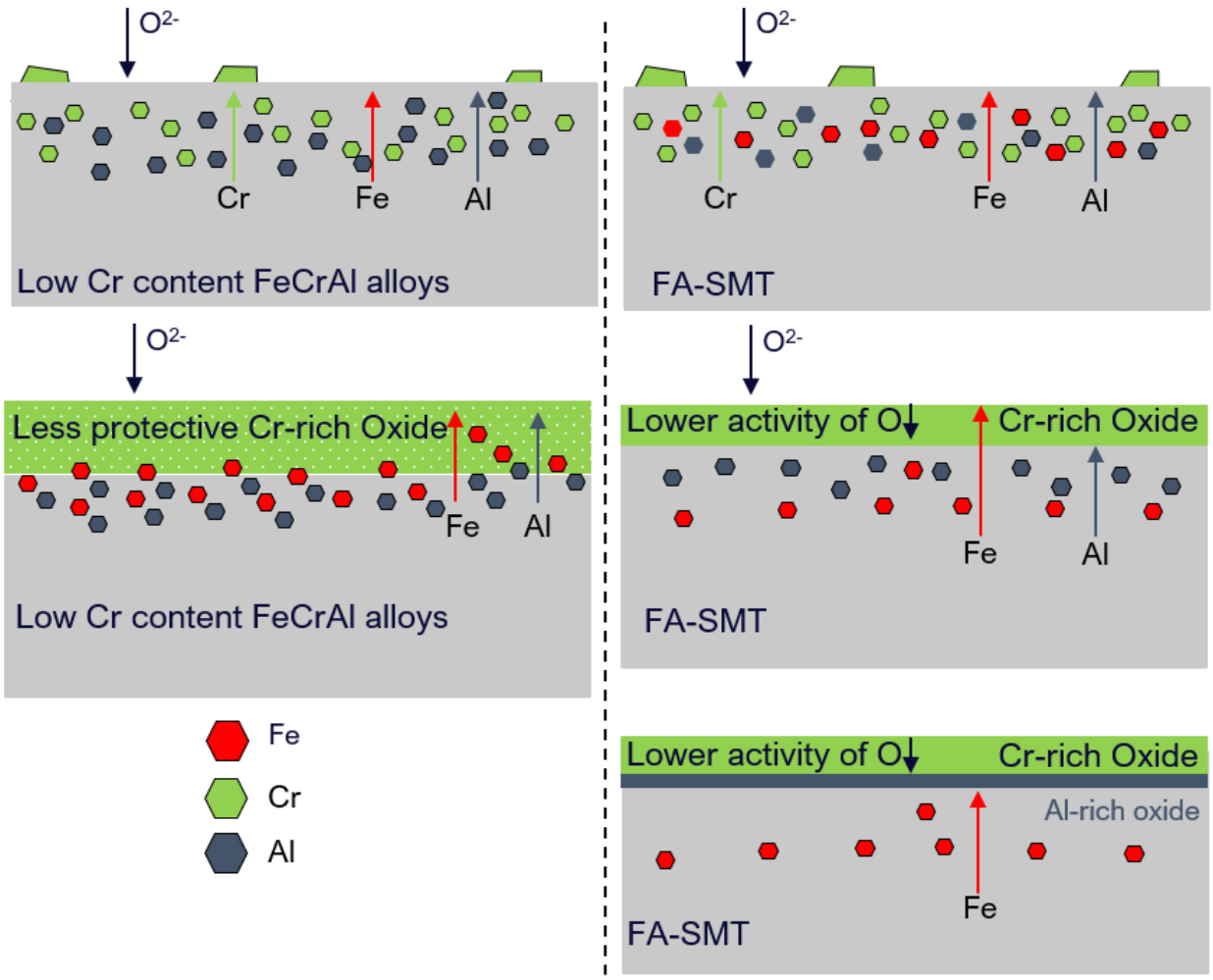

Figure 79. Illustration of the oxidation behavior of FeCrAl alloys in simulated BWR-HWC.

While all the FeCrAl alloys displayed a mass loss in BWR-HWC and a slight mass gain in BWR-NWC, Zric-2 tubes irrespective of the test conditions developed a uniform film of oxide post-test. Due to the formation of this protective oxide in both NWC and HWC, mass gain was observed on Zirc-2 tubes.

7.5.Conclusion

To design and optimize FeCrAl alloy compositions that results in next generation ATF cladding candidates, an attempt has been made to study the latest versions of FA-SMT, PM-C26M and Fe-17Cr-5.5Al specimens in BWR-HWC, and BWR-NWC autoclave systems for 6 months. The following conclusions can be drawn from the current study:

- All the three variants of FeCrAl displayed a weight gain in BWR-NWC. However, in BWR-HWC all the variants displayed a mass loss.
- For Fe17Cr 5.5Al specimen in simulated BWR-NWC, Al oxide layer forms beneath the Cr oxide layer due to the partial pressure of O_2.
- In BWR-HWC only FA-SMT specimen displayed slight enrichment of Al under the protective Cr-oxide.
- Unlike BWR-NWC specimens, no surface spinel was observed in any FeCrAl alloy variants tested in BWR-HWC.
- Overall, the latest generation FeCrAl alloys fabricated via powder metallurgy have little sensitivity to microstructural impact when compared to previous generation alloys.

8. Comparing CRUD deposition on Zircaloy-2 and FeCrAl Claddings

In the last chapter, a systematic study of the corrosion behavior of latest generation fuel cladding materials was conducted. Data obtained from this study led us to conclude that alloy composition along with water chemistry has a profound impact on the corrosion behavior of these cladding materials. In this chapter accelerated testing has been carried out, by injecting CRUD ions (Ni acetate and Ferric EDTA) into the aqueous environment after 2 weeks of pre-heating the submerged cladding materials to compare the CRUD deposition on Zirc-2 and latest generation fuel cladding.

8.1 Introduction

As stated previously, zirconium alloys are the current fuel cladding materials in the Boiling Water Reactor plants (BWRs), primarily due to their low neutron absorption cross section [145], good corrosion resistance [146] and adequate mechanical strength [147] under normal operating conditions. However, the problem arises under Loss Of Coolant Accident (LOCA) scenarios. At high temperatures in the presence of steam, zirconium alloys undergo breakaway oxidation [148] resulting in the production of hydrogen gas which can lead to explosions at nuclear power plants accidents such as the one that took place at Fukushima [149]. Following this accident, the concept of Accident Tolerant Fuels (ATF) originated to avoid the rapid oxidation of zirconium alloys under LOCA conditions. Achieving ATF may encompass changes to the cladding for the fuel and changes in the fuel itself. For the cladding, researchers have been investigating short-term approaches such as coatings on zirconium alloys [150,151], while mid-term approaches include

developing new cladding materials such as FeCrAl alloys [152], SiC coating on SiC substrates, and ceramic metal composite materials [153].

The final Aim of this dissertation focuses on the first of these mid-term approaches: replacing the Zr alloys with monolithic FeCrAl alloys, because they display good mechanical strength [75] and wear resistance [154] and have higher resistance to irradiation damages [155]. While promising, the behavior of FeCrAl alloys in light water reactor (LWR) conditions is still an active area of study [96,135,136]. Most importantly, these alloys showcase excellent oxidation resistance at high temperatures by forming an Al_2O_3 oxide layer which acts as a diffusion resistant oxide barrier thereby preventing further alloy oxidation up to 1300°C [74,156,157]. Currently, the environmental resistance capabilities of FeCrAl as a fuel cladding material are being evaluated in the entire fuel cycle.

Metal ions and oxide particles from the construction material of nuclear power plant travel through BWR primary coolant and may partially get deposited on the fuel cladding material to CRUD, described in detail previously. To summarize: CRUD deposition on the fuel cladding may result in CRUD-induced localized corrosion (CILC) [73] posing a threat to plants safety operation. Literature also suggests that the fuel rod CRUD has a large impact on plant performance and fuel economy [158,159]. As described earlier, the fuel CRUD deposited on Zr-based rods in light water reactors (LWRs) mainly consists of nickel, iron, and chrome oxides. Especially in boiling water reactors (BWRs) the CRUD mainly consists of non-stoichiometric nickel ferrites ($Ni_xFe_{3-x}O_4$) and hematite (αFe_2O_3) [9]. CRUD deposits usually have a porous outer layer with a denser inner layer. These CRUD deposits have low thermal conductivity [71] and therefore a buildup on fuel rods

could increase the surface temperature of the cladding material [19] further accelerating the environmental degradation of the cladding wall.

As the elemental composition between the zirconium alloy and FeCrAl alloys are different, it is anticipated that growth of CRUD from ions dissolved in the coolant will differ between these surfaces. Hence, in this work we have investigated the CRUD development on four candidate alloys under simulated normal operating conditions. Accelerated tests were conducted in simulated BWR hydrogen water chemistry (HWC) environments after injecting Ni^{+2} and Fe^{+3} while the cladding surface temperature was monitored. CRUD deposition characteristics, microstructure and composition was studied using characterization techniques like Raman spectroscopy, X-ray diffraction, and FIB-SEM/EDS.

8.2 Experimental Materials and Methods

The objective of these tests was to determine the relative susceptibility of ferritic FeCrAl tubes (C26M and APMT) to develop surface CRUD as compared to austenitic type 304SS and bare Zircaloy-2 tubes. The nominal composition of the tested tubes is listed in Table 12.

Table 12.Chemical composition of tested tubes.

Tube designation	**Nominal composition in weight %**
Zircaloy-2	Zr + 1.5Sn + 0.15Fe+ 0.1Cr + 0.05Ni
Type 304 SS - austenitic	Fe + 18Cr + 8Ni + 2Mn
C26M - ferritic	Fe + 12 Cr + 6Al + 2Mo + 0.03Y
APMT - ferritic	Fe + 21 Cr + 5Al + 3Mo

Figure 80 shows the autoclave head with four cladding tubes that were fitted with heater rod inserts. This autoclave head was manufactured by Stern Laboratories in Canada. Two of the rods were off-the-shelf stainless steel 304SS, one rod was APMT and one rod was C26M. The Zirc-2 tubes were tested separately under the same conditions. The wall thickness of the tubes was ~0.60 mm. Electrical power connections are on the top of the tubes, together with the thermocouples for measuring and recording the cladding surface temperature during the accelerated CRUD testing. Each cladding tube had two thermocouples installed on the ID surface, 180° from each other. The thermocouple elevation was in the middle section of the heater rod. The length of heater rod was 175 mm and the power profile was uniform along its length. The heater rod was rated for 3 2.45 kW at 30 VDC, equivalent to heat flux of 40 W/cm². The total length of the heat rod/cladding assembly was ~ 1550 mm.

The CRUD deposition conditions were simulated by performing a pre-conditioning step of immersion for 4 weeks in an autoclave with simulated BWR hydrogen water chemistry (HWC) (0.3 ppm hydrogen) at 288°C, followed by a rod heating stage for 2 weeks, then the injections of 25 ppm Ni^{2+} as Ni acetate and 12.5 ppm Fe^{3+} as ferric EDTA were performed for ~10 days (the injection time was generally limited by the time it took for the piping system to plug out due to the injectable acetate and EDTA salts). During the testing, the cladding surface temperatures were recorded, together with the power dissipation of the heater rods. The electrochemical potential of the autoclave body against a Cu/Cu_2O reference electrode was also recorded.

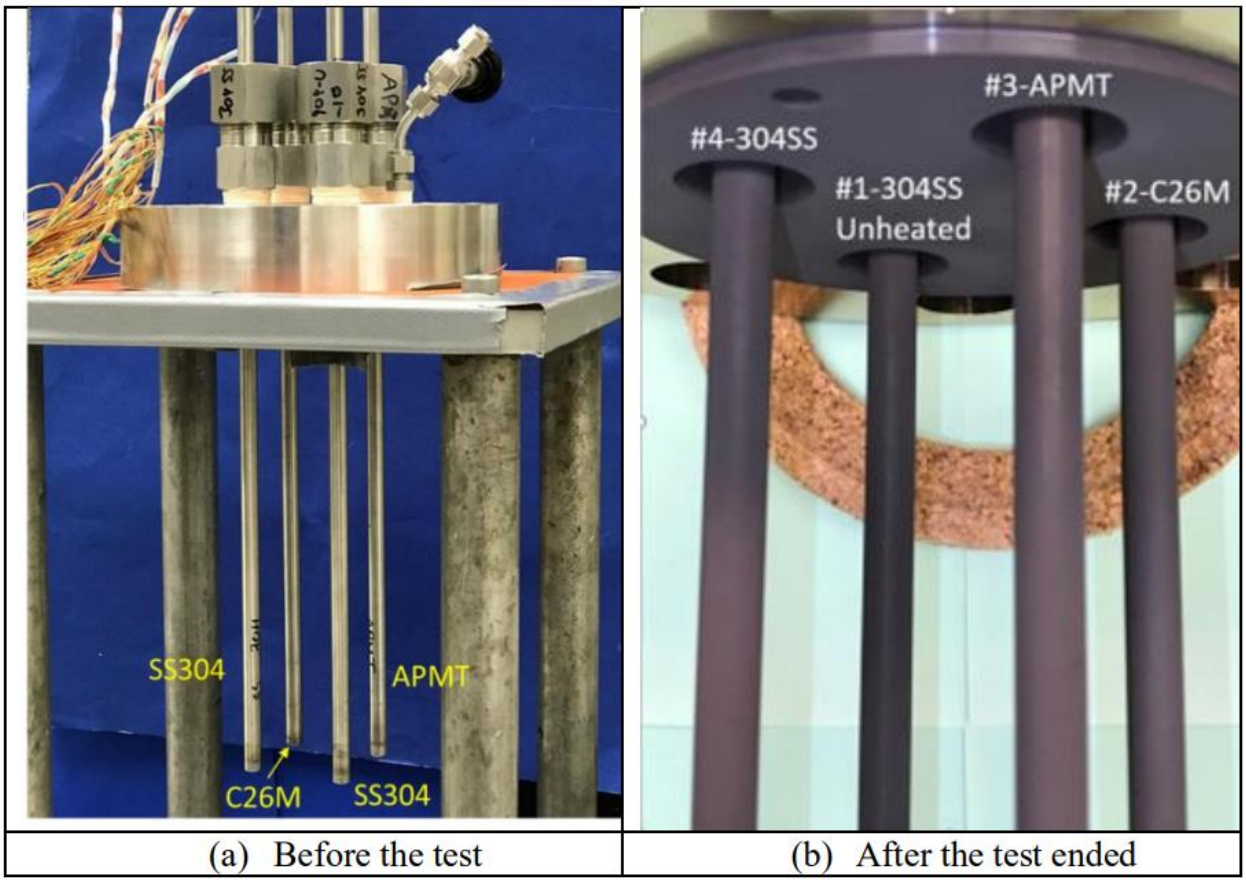

Figure 80. (a) Autoclave head built for the accelerated CRUD testing. (b) The four test rods after the CRUD testing.

8.3 Results

8.3.1 Temperature profile as a function of Ion injection

The temperature profile of the rods in pure BWR-HWC are shown in Figure 81, before the injection of the Ni and Fe salts. The electrochemical potential of the autoclave was measured (~-0.26 V) against a standard Cu/Cu_2O reference electrode and was shown in the graph as a dotted black line. Apart from one 304 SS rod, all other rods were heated from inside of the tube. The applied electrical power of 12 A in the inside of each rod led to a cladding temperature increase of ~9°C for the APMT tube, and ~12°C for the C26M and the 304SS rods. On the C26M rod, the two thermocouples read 300°C and 299°C, respectively. On the APMT and SS304 rods, the two

thermocouple readings were practically identical in both rods. After an initial increase, the cladding surface temperatures did not show significant change during the two-week heating stage prior to impurity injection.

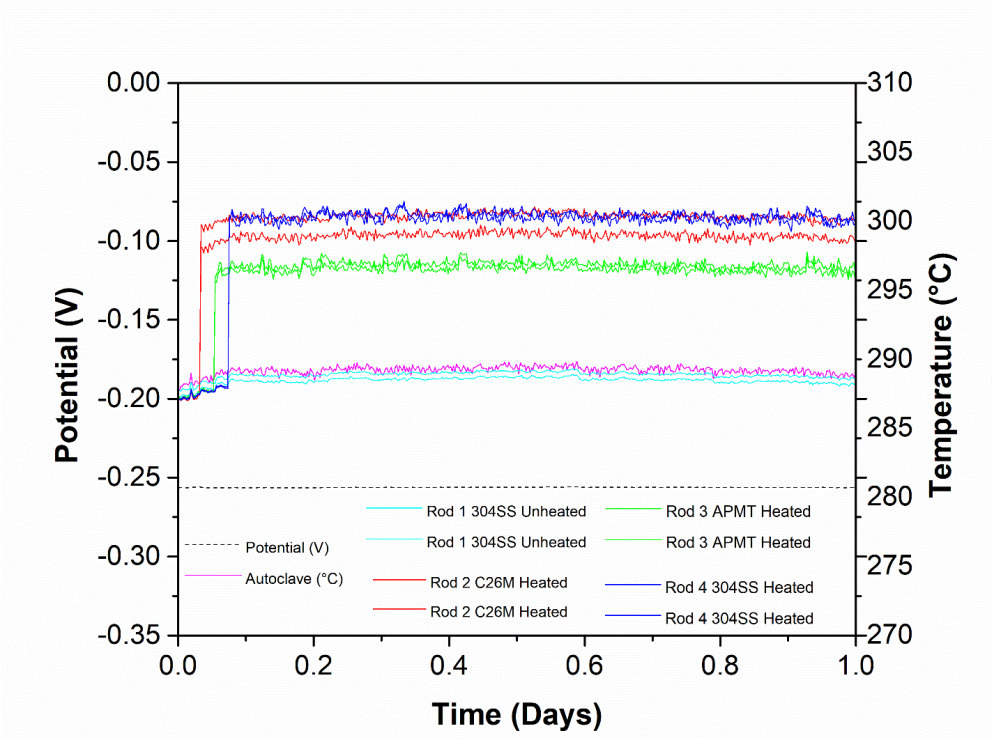

Figure 81. Temperature logging on the four test rods for the 24-h initial heating stage, without impurity injection. One SS304 rod was not powered as a reference.

After continuous heating for 15 days, injection started with 25 ppm Ni^{2+} and 12.5 ppm Fe^{3+}, resulting a decrease of ~ 50 mV of electrochemical potential. However, there was no change in the cladding temperatures (Figure 82). The lowest cladding temperature was for the APMT rod (Figure 82).

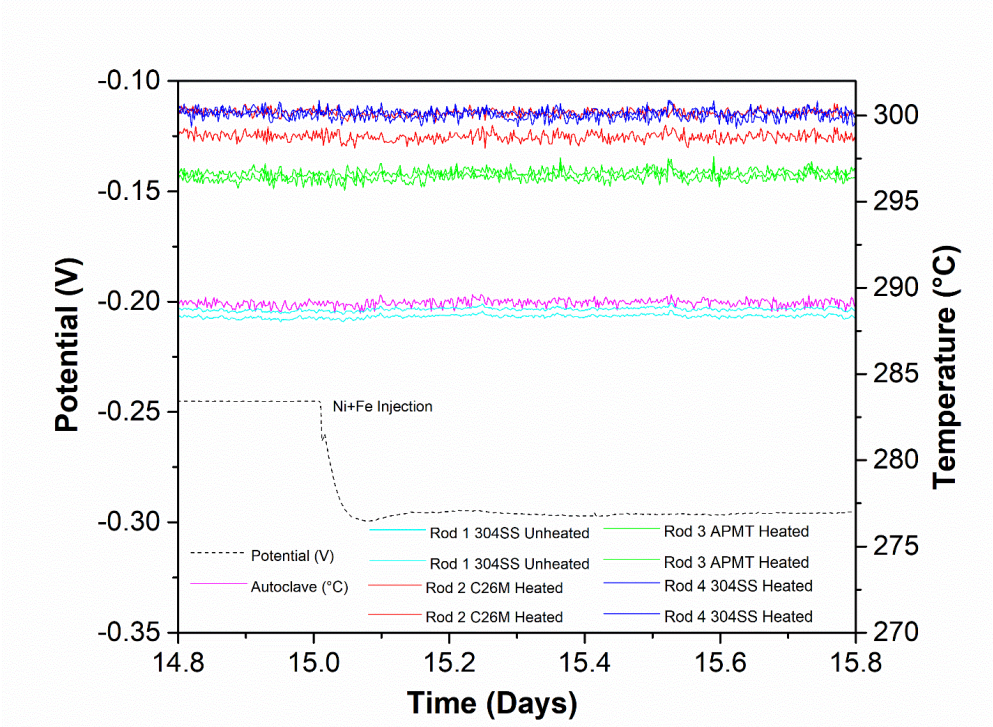

Figure 82. Temperature for the test rods at the beginning of the impurity injection stage. The injection of impurities is indicated by a dip, where the electrochemical potential shows a decrease from -0.24 V to -0.29 V.

Figure 83 show that the cladding temperature for the two FeCrAl rods was practically the same during injection of Ni and Fe ions into the system. While the water temperature was 288°C, the cladding temperature for APMT was 297°C, for Zircaloy-2 was 298°C (not shown here) and for C26M it was approximately 300°C. That is, the cladding had a temperature approximately 10°C higher than the circulating contaminated water in the autoclave.

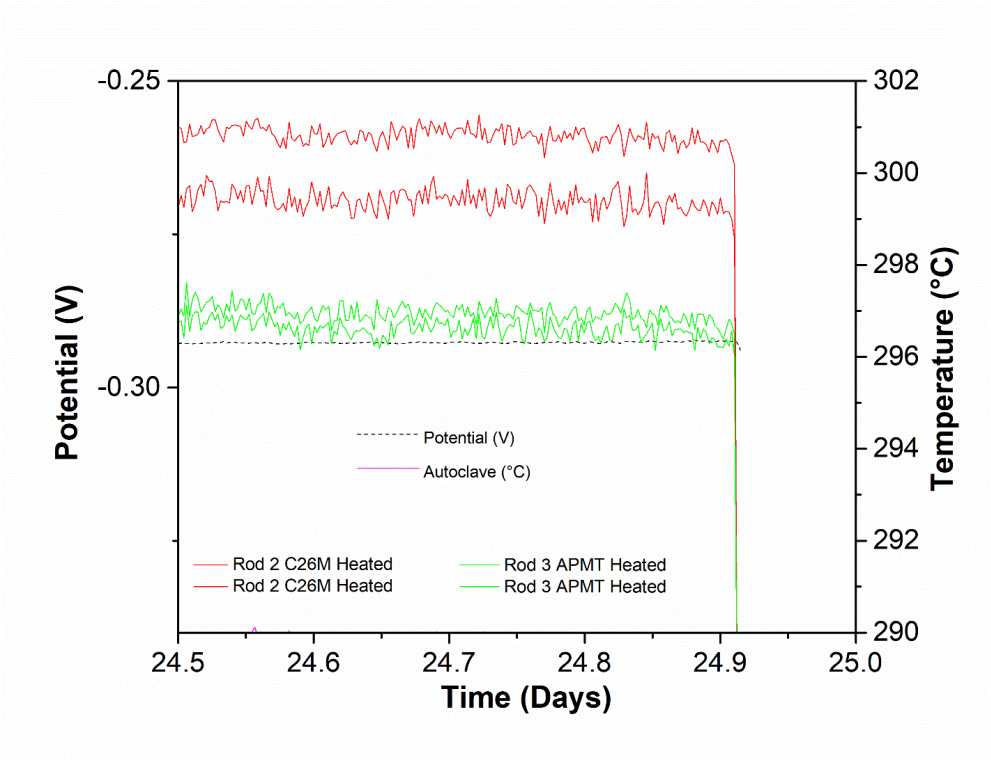

Figure 83. Similar cladding temperature for heated C26M and heated APMT.

8.3.2 XRD Phase Analysis of CRUD deposition on different cladding materials

Figure 84 shows the appearance of four rods after the autoclave tests ended (not shown are the Zirc-2 rods). They all had a similar dark appearance, with no clear visual differentiation. To analyze the phase composition, XRD was performed on these rods.

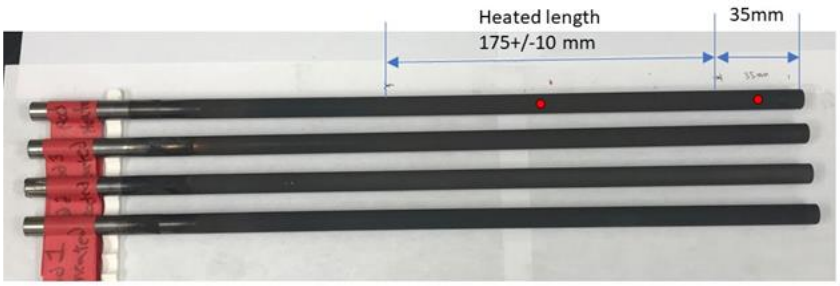

Figure 84. The four test rods (with heater inserts removed) after CRUD testing in BWR HWC with 25 ppm Ni2+ and 12.5 ppm Fe3+. From top to bottom, the rods are (a) Heated 304SS; (b) Heated C26M; (c) Heated APMT and (d) non-heated 304SS. Red dot A indicates an area of the tube where it was internally heated and red dot B an area with no internal heating.

XRD spectra for all the rods were obtained from two spots along the rod, one where internal heating was applied (spot A) and one where no internal heating was present (spot B), as shown in Figure 85 . As there were no notable differences in the phases of CRUD deposition between these two spots, only the data obtained from spot A will be shown for the remainder of this text.

Figure 85 shows XRD spectra from point A of the unheated and heated 304SS rods. Irrespective of the heating factor, the CRUD deposits found on these two rods were identical. Two major phases corresponding to the inverse spinel structure of nickel ferrites [113] and the FCC structure of stainless steel (base material) were confirmed by XRD. In the subsequent XRD spectra, symbolic markers were used to indicate the phase identities, with "@" marking nickel ferrite peak positions, and "#" used for stainless steel.

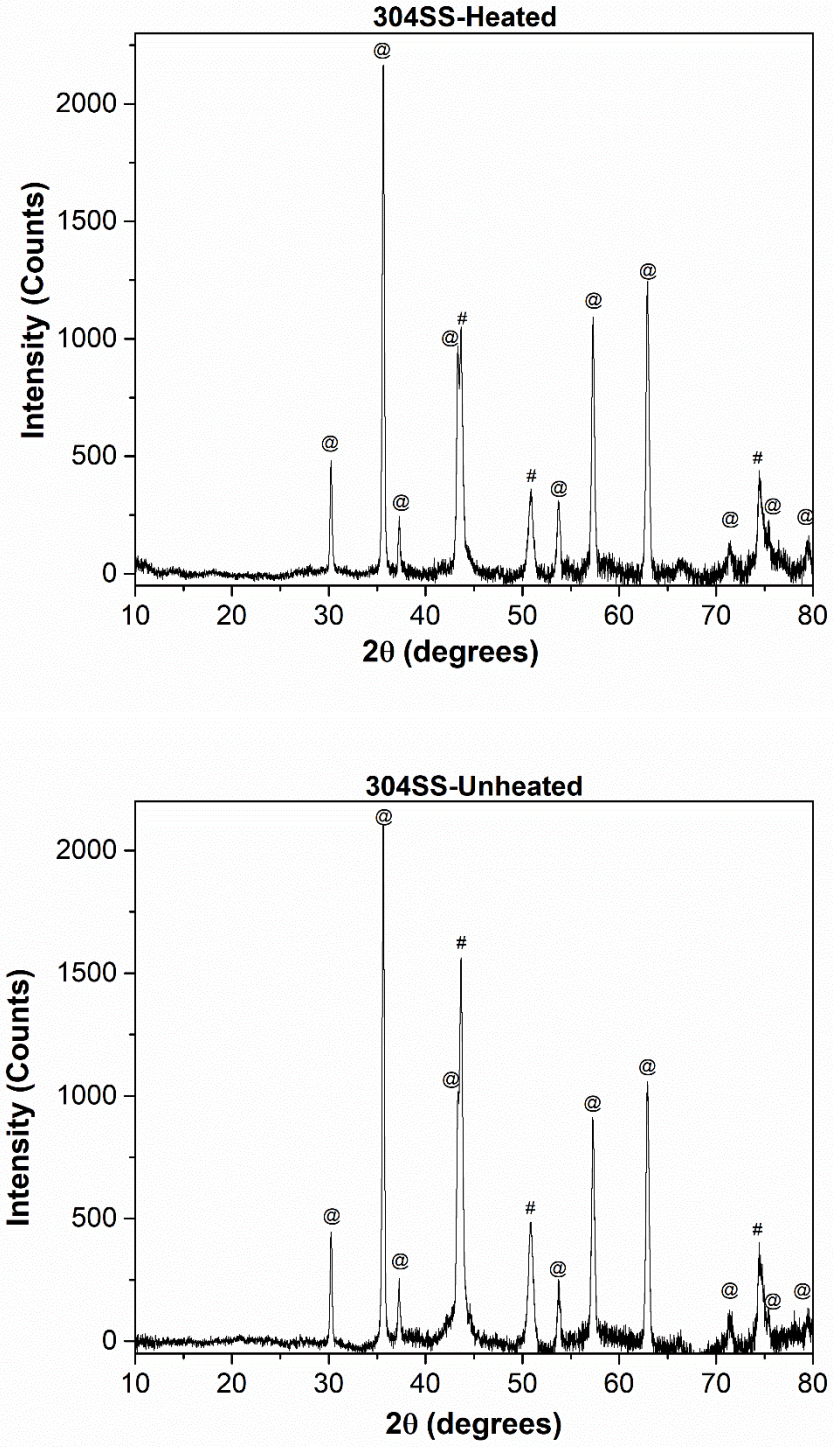

Figure 85 . XRD spectra for CRUD deposits obtained on heated and unheated 304SS containing nickel ferrite (@) and stainless steel (#).

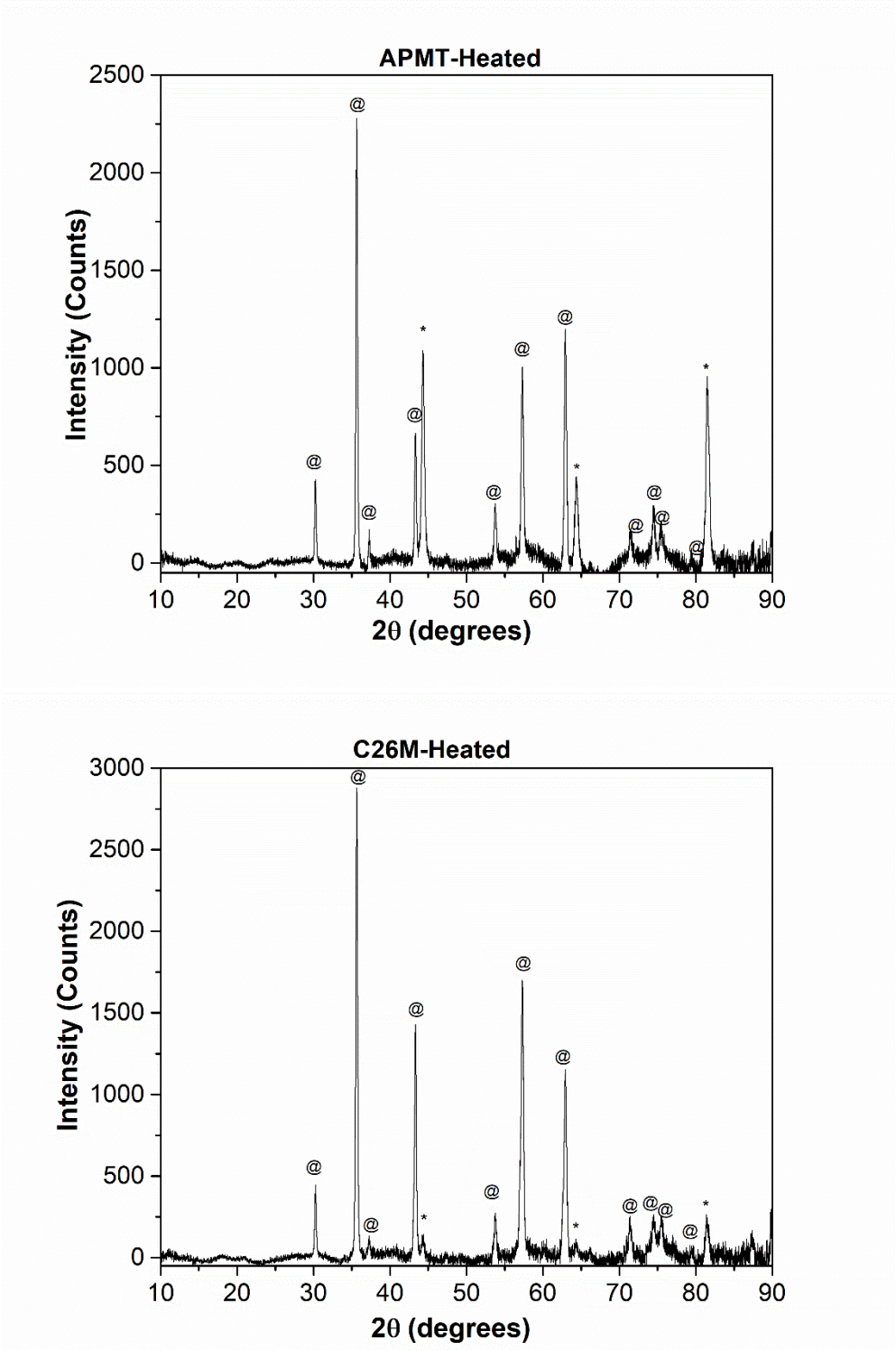

Figure 86. XRD spectra for CRUD deposits obtained on heated APMT and C26M containing nickel ferrite (@) and FeCrAl (*).

8.3.3 CRUD structure and composition

Figure 87 shows SEM images of the CRUD for heated (a-c) and non-heated (d) Zirc-2 rods after removing from the autoclaves. The CRUD on the heated Zirc-2 rod showed a more extended deposition (Figure 87a) but the CRUD was less crystalline in nature (porous). Underneath the CRUD, a layer of Zr-oxide was also be observed (Figure 87 b). The dark gray regions show the porous CRUD on Zr-oxide (Figure 87c). For the non-heated Zirc-2 rod the external CRUD had more geometric features (Figure 87d).

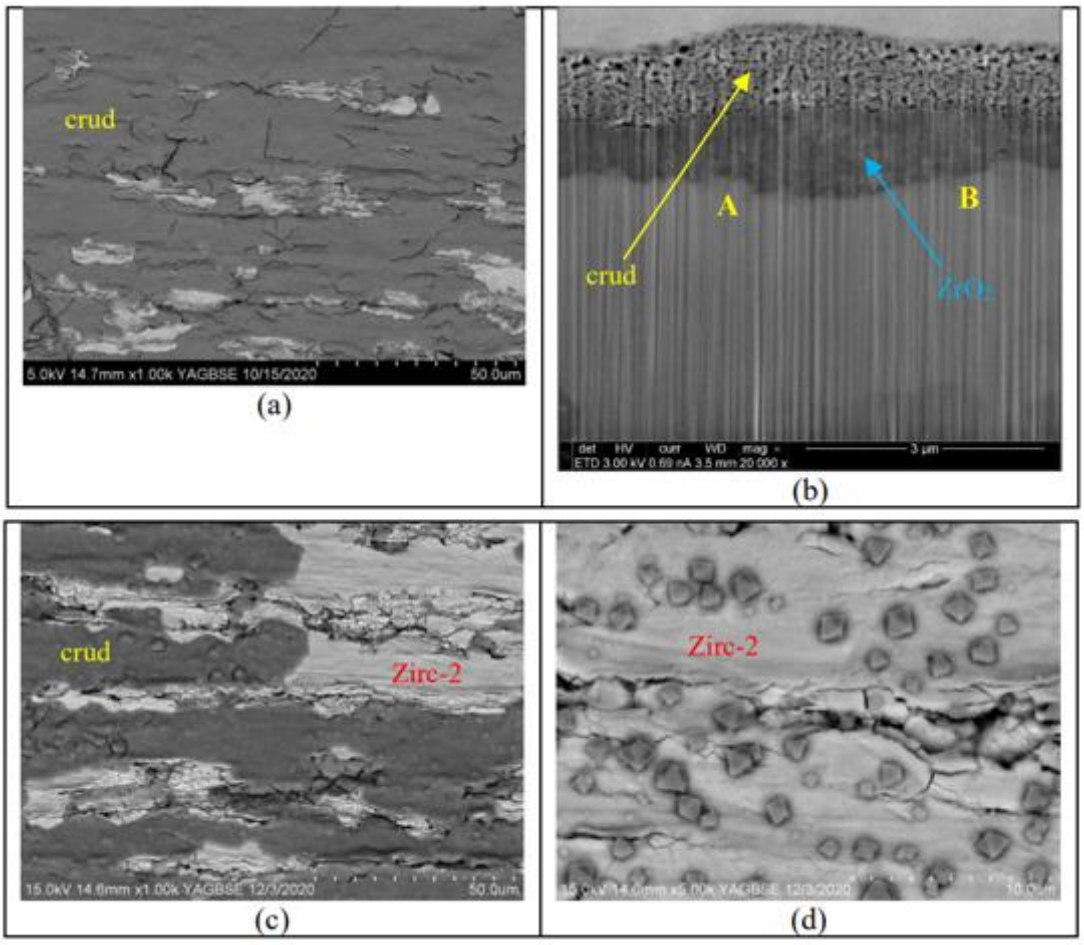

Figure 87. Appearance of the CRUD on Zirc-2 rods. (a) heated top down, (b) heated FIB cross section, (c) heated top-down BSE, (d) non-heated top-down BSE.

Figure 88 shows the elemental maps of the Zirc-2 rod after testing. The CRUD deposited on bare Zirc-2 tube was less geometric in appearance on the heated Zirc-2 rods and is rich in Ni and Fe oxide. For comparison, Figure 89 shows the surface EDS elemental maps of Zirc-2 which have not been heated, displaying geometric and crystalline octahedral CRUD particles (as obtained in objective 1&2 of this thesis) whose composition is rich in Fe and Ni oxides.

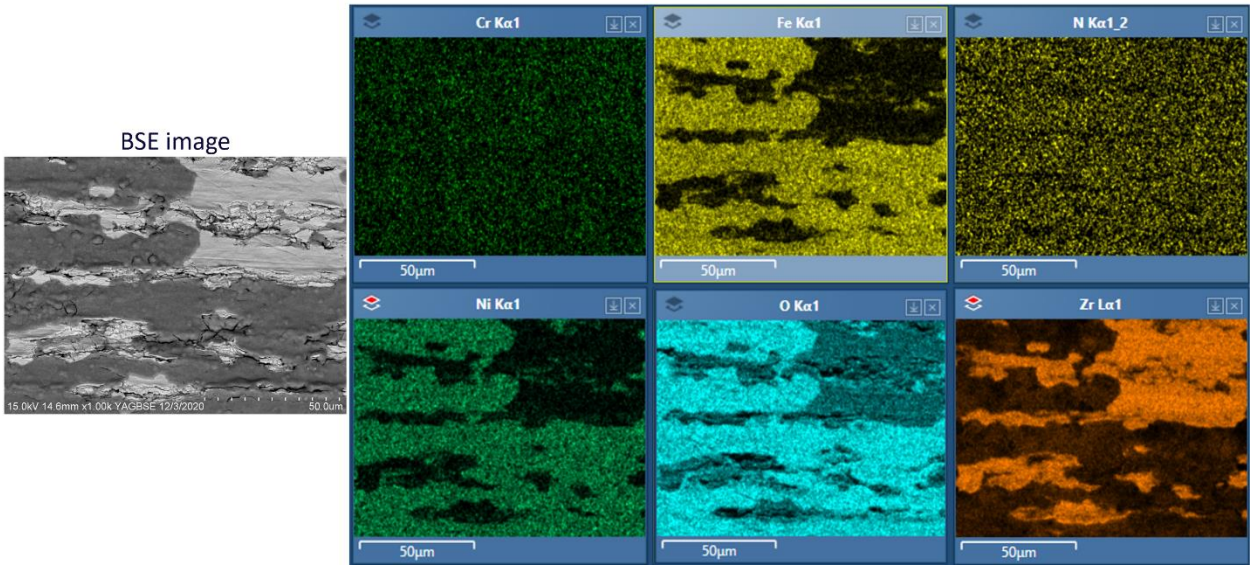

Figure 88. Surface EDS elemental maps of heated Zirc-2 rod post autoclave exposure.

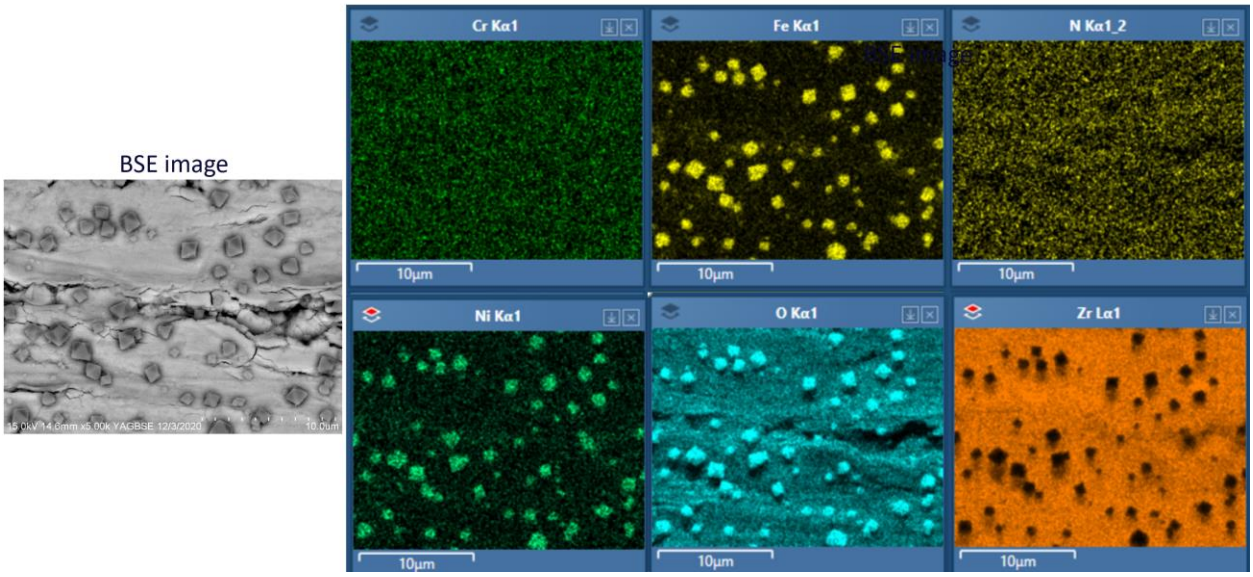

Figure 89. Surface EDS elemental maps of non-heated Zric-2 rod post autoclave exposure.

Figure 90 (b) is a FIB cross-section showing that the CRUD formed on top of the 304SS rod was thicker than the one that developed on top of the Zirc-2 rod. In between the CRUD and the 304SS substrate there was a thin layer of Cr rich oxide. The external layer of the CRUD showed highly geometric particles (Figure 90 a&c). The total thickness of the oxide including the Cr-rich layer plus the CRUD was on the order of 4.4 µm.

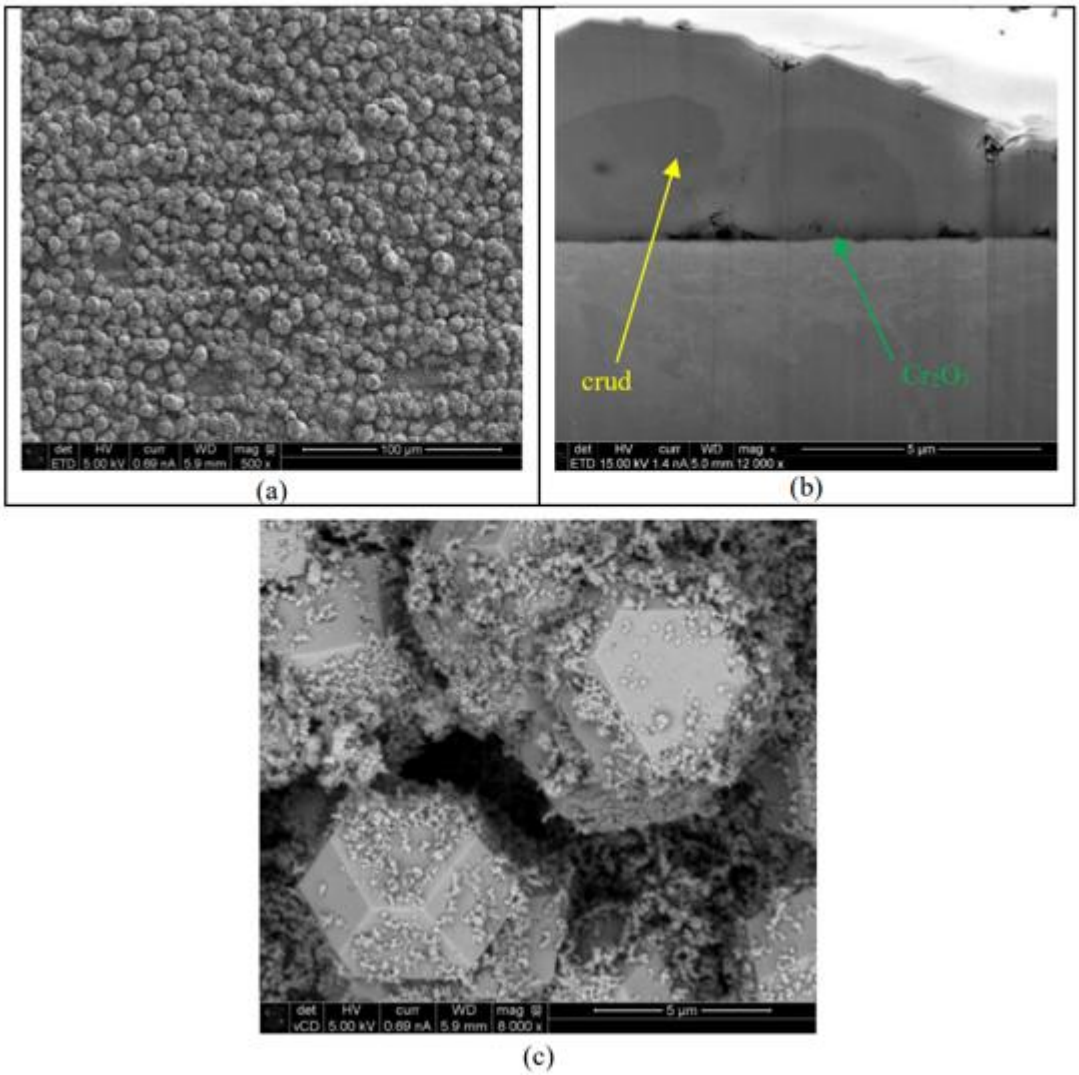

Figure 90. Appearance of the CRUD on heated 304SS rod. (a) top down SEM image, (b) FIB cross section, (c) Back Scattered Electron (BSE) image at higher magnification.

Figure 91 shows the corresponding cross-sectional SEM-EDS area maps of heated 304SS rod after autoclave testing. At the interface between the 304SS rod and CRUD particles, a thin layer of Cr_2O_3 was observed. Additionally, the EDS spectra reveal a region within the CRUD layer that is depleted in Ni but is enriched in Fe.

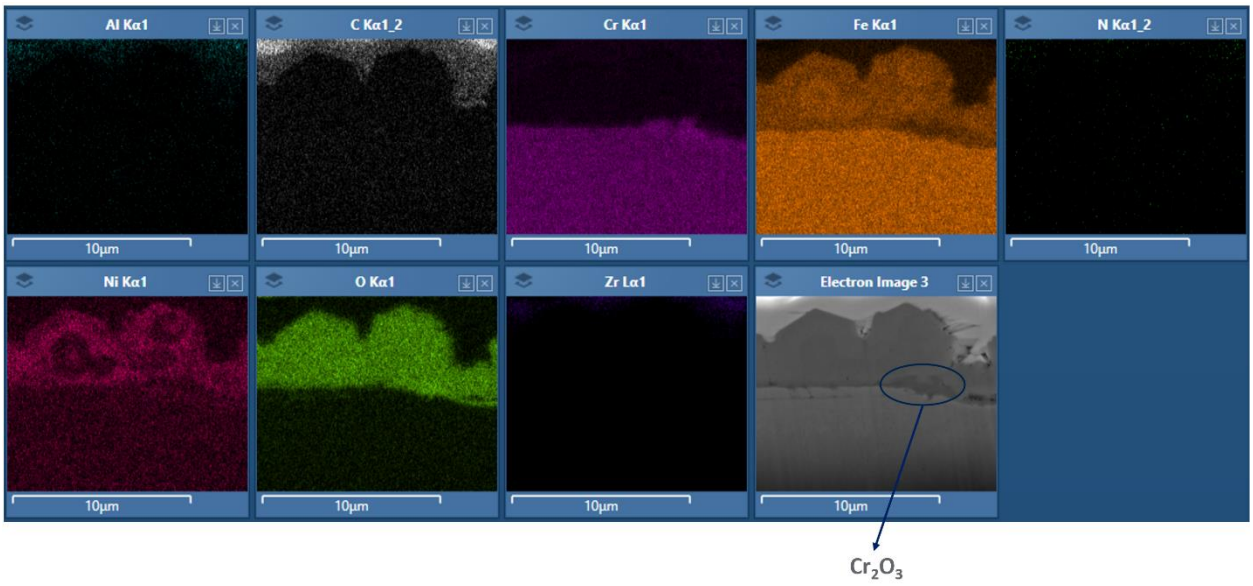

Figure 91. SEM image and cross-section EDS area maps of heated 304SS rod. The EDS maps show (Ni,Fe) oxides on top of 304SS rod.

Figure 92 shows the characteristics of the CRUD formed on top of the C26M tube, which had a thicker and more defined layer rich in Cr underneath the CRUD. It is likely that this Cr oxide layer rich in Cr was formed during the preconditioning of the rod before the Fe + Ni containing electrolyte was injected. The total thickness of the oxide including the Cr-rich layer plus the CRUD was on the order of 6 µm.

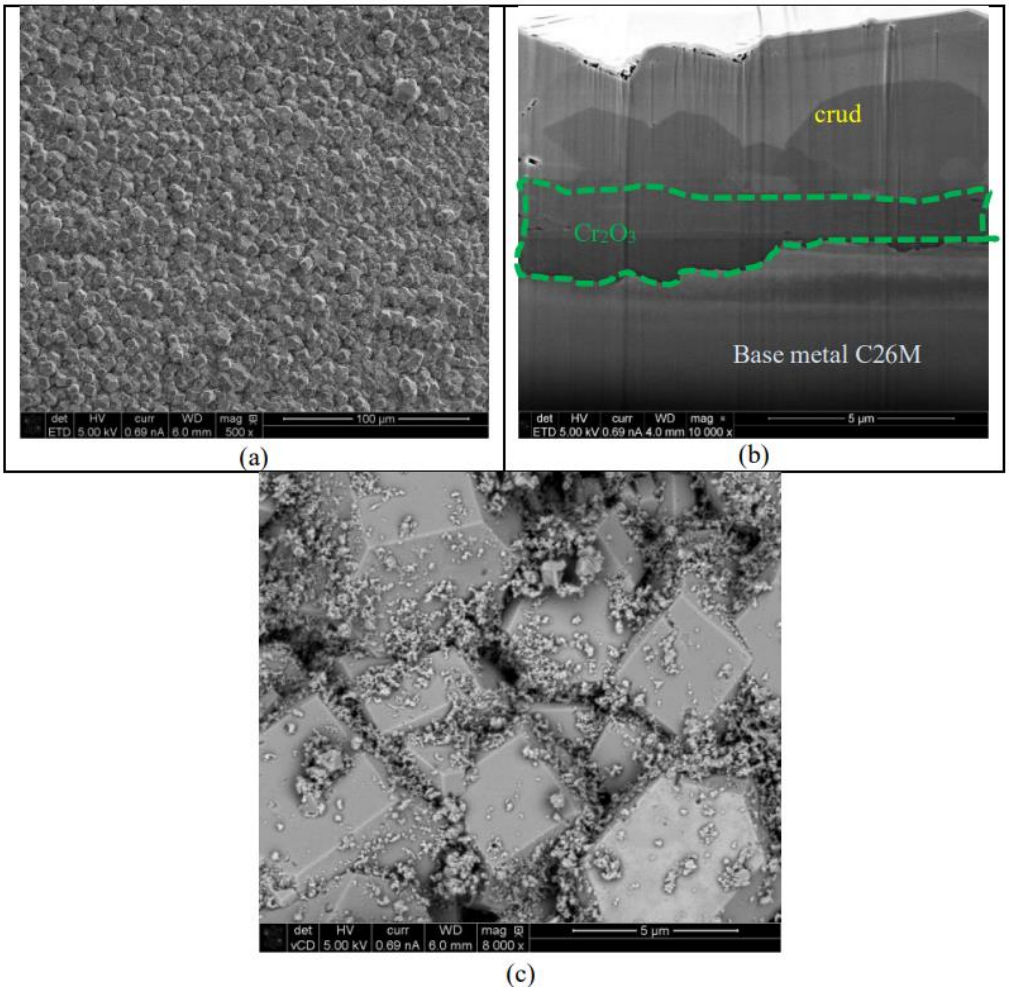

Figure 92. Appearance of the CRUD on heated C26M rod. (a) top down X500, (b) FIB cross-section, (c) Back Scattered Electron (BSE) image X8,000 mag.

Figure 93 shows the cross-section SEM-EDS area maps of heated C26M rod post autoclave testing. At the interface between the C26M rod and CRUD particles, a thick layer of Cr_2O_3 was observed. Similar to the 304SS case, the EDS spectra reveal a region within the CRUD layer that is depleted in Ni but is enriched in Fe.

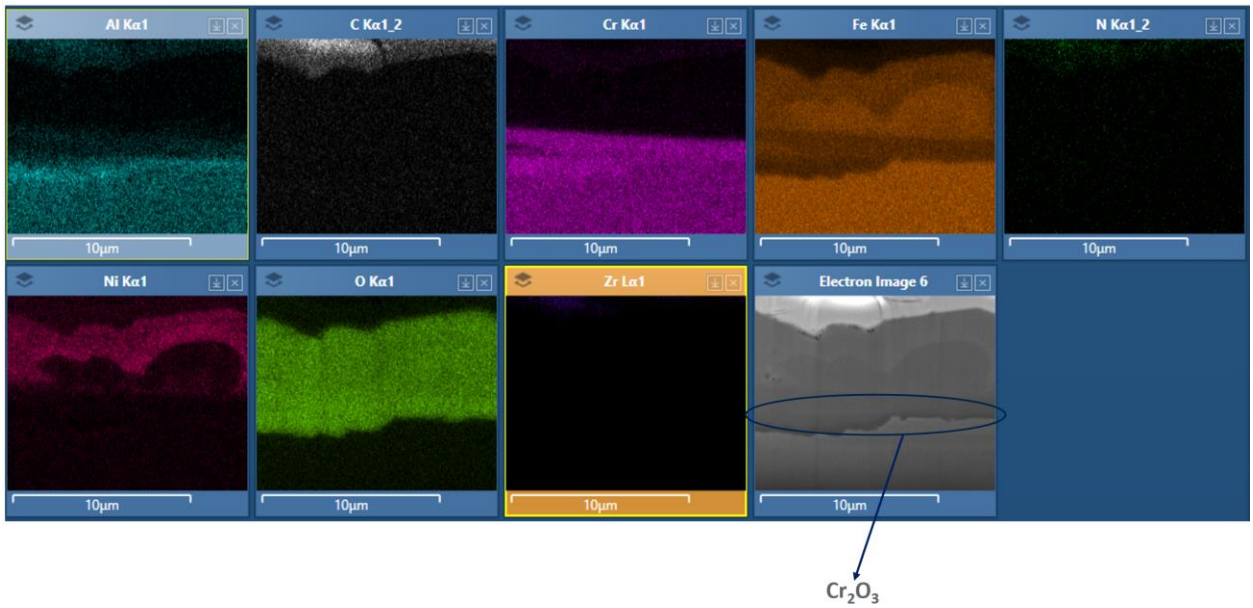

Figure 93.SEM image and cross-section EDS area maps of heated C26M rod. The EDS maps show (Ni,Fe) oxides on top of C26M rod.

Figure 94 shows the CRUD characteristics formed on top of the heated rod of APMT. The structure was like that of C26M and 304SS. The Cr-rich oxide thickness was like that of type 304SS, probably because of the higher Cr content in APMT compared to C26M. The total thickness (CRUD + Cr rich oxide) was 4.3 µm, on the same order as the layers on 304SS.

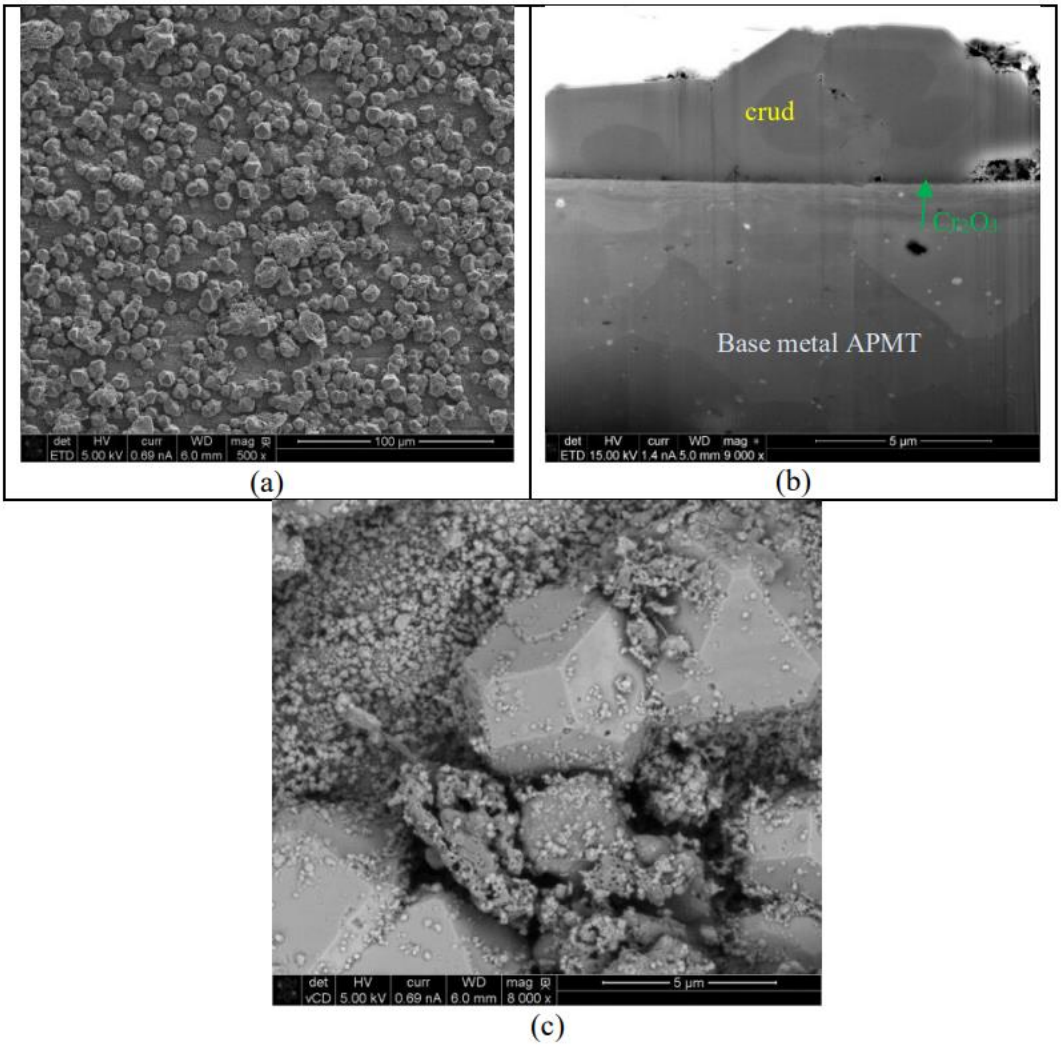

Figure 94. Appearance of the CRUD on heated APMT rod. (a) top down 500X, (b) FIB cross section, (c) Back Scattered Electron (BSE) image 8,000X mag.

Figure 95 shows the cross-section SEM-EDS area maps of heated APMT rod after autoclave testing. At the interface between the APMT rod and CRUD particles, only a thin layer of Cr_2O_3 was observed. Similar to the previous two cases, the EDS spectra reveal a region within the CRUD layer that is depleted in Ni but is enriched in Fe.

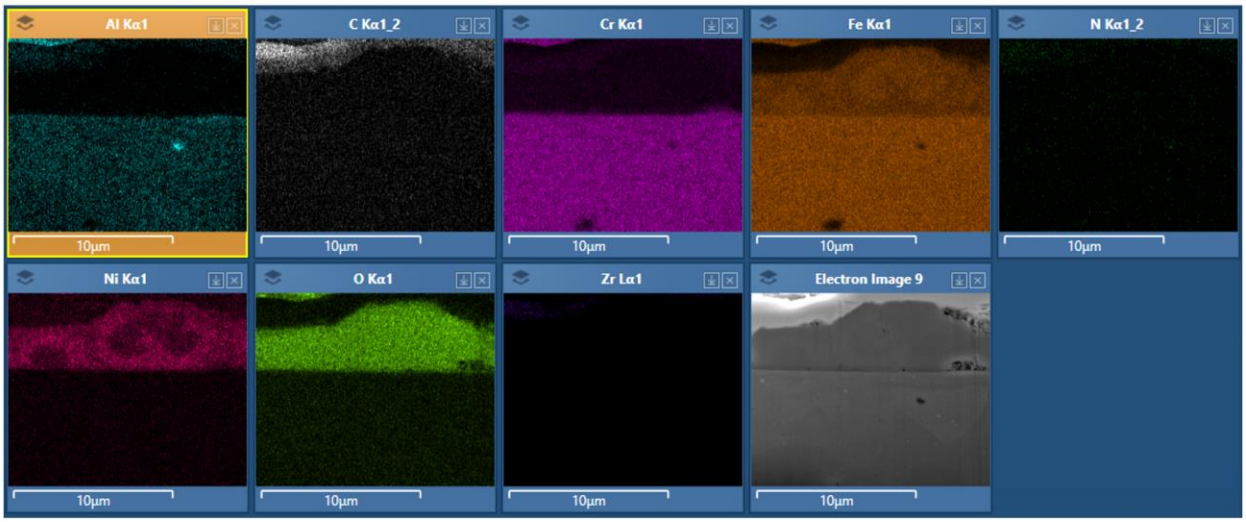

Figure 95.SEM image and cross-section EDS area maps of heated APMT rod. The EDS maps show (Ni,Fe) oxides on top of APMT rod.

Figure 96 shows the Raman spectra obtained from the OD deposits on 304SS (both heated and un-heated), C26M, APMT, along with two reference spectra from nickel ferrite (trevorite) and magnetite The spectral signatures match well to the Raman features of the nickel ferrite $NiFe_2O_4$ standard including strong bands at 700, 570, and 484 cm^{-1}. The shoulders in the measured spectra at ~665 cm^{-1} could indicate that magnetite was present as a minor phase. In actual BWR plants, the CRUD composition may vary from plant to plant [160][159][44][161]. Under normal water chemistry (NWC) the CRUD may be composed of hematite and non-stoichiometric nickel ferrite spinels whereas in HWC the CRUD may be composed of magnetite and nickel ferrites. The CRUD in some US BWR plants had a smaller fraction of Ni than plants in Sweden or Japan [159].

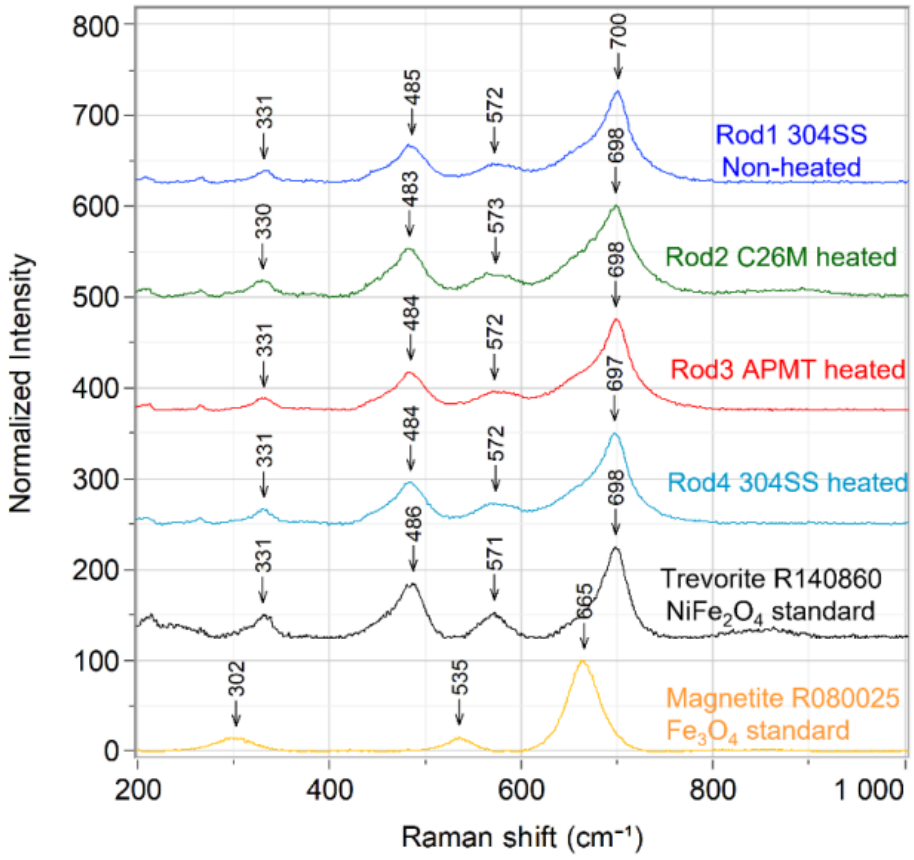

Figure 96. Average Raman spectra from the outer diameter of the tested rods showing similar CRUD products independently of the type of cladding tube.

8.4 Discussion

According to the literature, CRUD deposition can reduce the heat transfer efficiency [10]. This phenomenon is due to the porous, thermally non-conducive CRUD being deposited on the fuel cladding material increasing the fuel cladding temperature [162]. To test this hypothesis, temperature profiles of the cladding materials were monitored pre- and post- CRUD ion injection. Contradictory to expectations, no increase in temperature was observed post-test as shown in Figure 83. This deviation from expectation may be because the autoclave does not fully replicate the subcooled nuclear boiling (SNB) conditions [163] usually found in BWRs. This condition is

commonly observed in BWRs as most of the liquid is below the saturation temperature. As a result, bubbles from the boiling water condenses on top of the fuel rods creating boiling chimneys, and further increasing fuel cladding temperature. For our experiments, the autoclave in which the fuel cladding materials were tested is not equipped to create those SNB conditions that lead to local variations in thermal resistance, and as a result no rise in cladding temperature was observed even after CRUD deposition.

Figure 86 shows the XRD spectra of the heated APMT and C26M fuel claddings post-test. The spectra confirm the existence of nickel ferrites on top of the fuel cladding materials. Due to the larger penetration depth of X-ray signal, peaks from the underlying base fuel cladding material were also observed along with nickel ferrite peaks. This phenomenon can be used to estimate the relative thickness of the CRUD based on the X-ray penetration depth. That is, a thicker oxide layer will attenuate the X-ray beam more, leading to less signal from the from the underlying fuel cladding. Comparing the ratio of cladding peak height to nickel ferrite peak height, more signal is found from the APMT than the C26M. This suggests that the oxide developed on C26M is thicker than the oxide developed on APMT and is confirmed by direct visualization shown in Figure 93 and Figure 95. Although no changes in cladding temperatures were observed in our testings, in actual nuclear reactors CRUD deposits increase the cladding temperatures by reducing the efficiency of heat transfer. In this case, the reduction is significant enough that boiling is no longer an effective form of heat transfer from the solid surface to the coolant liquid, resulting in enhanced Critical Heat Flux (CHF) [164]. Hence a thicker CRUD oxide deposit on APMT and C26M may increase the fuel cladding temperature in actual LWRs, and remains a concern.

As discussed in chapter 7, the corrosion behavior of Zirc-2 cladding rod is different from the FeCrAl cladding tubes. Usually under the operating conditions of the reactor Zirc-2 cladding rod undergoes uniform corrosion (Figure 58) [165]. In this scenario, the dissolved oxygen reacts with the metallic Zirc-2 alloy to produce ZrO_2. Unlike Zirc-2, the FeCrAl cladding rods develop a bilayer oxide structure (Figure 60). During the formation of the inner oxide, metal ions from the cladding rods dissolve and re-precipitate on top of the inner oxide layer to form the outer oxide resulting in a bilayer structure [166]. Thus, this different oxide film formation mechanism on FeCrAl cladding may also lead to a chemical interaction between the outer oxide layer of FeCrAl claddings and the injected CRUD ions.

To remove CRUD deposits from fuel cladding assemblies, ultrasonic cleaning has been established as a standard procedure in LWRs [167]. Ultrasonication removes the CRUD deposits (not the ZrO_2) on zirconium-based cladding materials, and it can even reduce the total mass of CRUD within the reactor [168]. Because FeCrAl-based claddings materials have different oxide formation mechanisms than the standard Zirc-2, it is unknown whether this simple physical removal technique will be sufficient. It was therefore important to investigate the interaction between CRUD deposits and the bilayer oxides developed on the FeCrAl cladding materials to determine whether CRUD particles are more or less firmly attached than they are to the standard cladding material.

Two sections (1/2” long) were cut out of each 7” tested APMT and C26M alloy tubes. To understand the adhesion between the CRUD deposits and the oxide films developed on these FeCrAl claddings, cross-sectional SEM was performed on 1 piece from each APMT and C26M

alloy, while the other sample from each alloy underwent ultrasonication for 30 minutes before imaging with cross-sectional SEM. For both of the FeCrAl alloys, the combined thickness of oxide films and the CRUD deposits was unchanged by ultrasonication (Figure 97). This observation indicates that the adhesion between the fuel cladding, oxide film and CRUD deposits on FeCrAl cladding is stronger than the purely physical adhesion found in the case of CRUD on the zirconium-based cladding materials. Further, this suggests that the formation of the outer oxide layer on FeCrAl and CRUD growth on this oxide layer happened simultaneously [169]. Hence if the mid-term approach to accident tolerant design were to mean replacing zirconium alloys with FeCrAl-based cladding materials, the removal of CRUD deposits from the fuel cladding tube would need to be more aggressive than simple ultrasonication. This is an unfortunate impediment to the adoption of FeCrAl-based alloys, if more complicated or time-consuming maintenance procedures are required. In addition, the FeCrAl alloys have a second impediment – the thicker non-thermally conductive layer (bilayer oxides combined with CRUD deposits) which may reduce the overall reactor performance if FeCrAl based cladding tubes were used as fuel rods. In a real system, SNB conditions exist and the thicker oxide found on FeCrAl alloys along with CRUD deposition could enhance the CHF thus increasing the overall cladding temperature beyond acceptable tolerances.

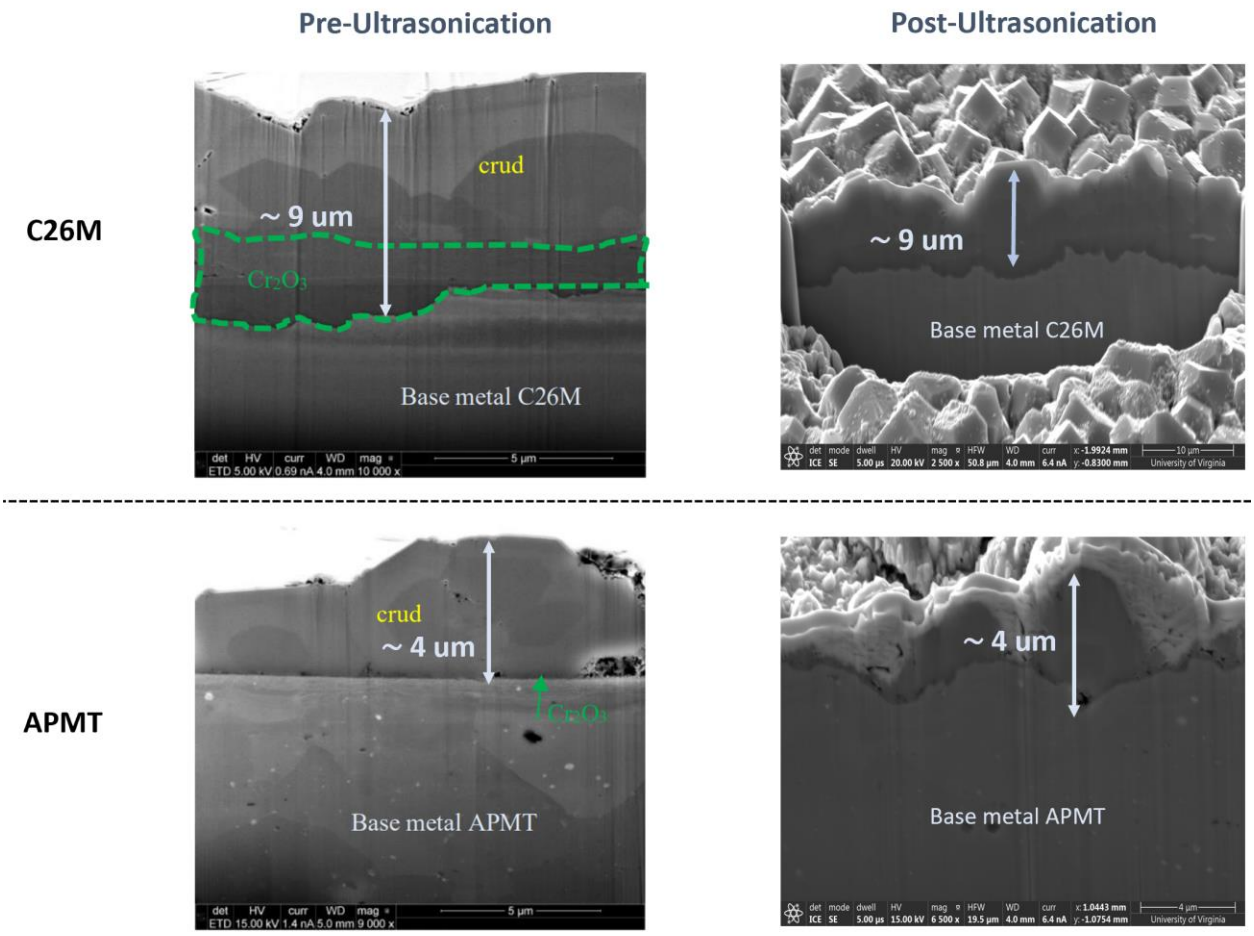

Figure 97. Combined thickness of FeCrAl Cladding rods pre- and post-ultrasonication.

8.5 Conclusion

To study the CRUD deposition on latest generation of FeCrAl cladding materials, cladding rods were submerged and heated, followed by CRUD ion injection. Contrary to expectations based on literature reports, no increase in cladding temperature was observed after CRUD deposition, which could be due to the absence of Subcooled Nuclear Boiling conditions in the autoclave used for testing, resulting in no enhanced CHF. The combined thickness of the CRUD layer and oxide layer of C26M cladding material is higher than those found on APMT as confirmed by cross-section SEM images which could result in increased cladding temperature in actual nuclear reactor. Unlike

Zirconium cladding where most of the CRUD layer is removed by ultrasonication, the oxide and CRUD on FeCrAl claddings showed no change in thickness after ultrasonification. This apparently stronger adhesion between FeCrAl claddings, oxide layers, and CRUD on these cladding rods could prove to be an impediment to the implementation of next-generation accident-tolerant fuel materials.

9. Final Summary

Even though each chapter has been summarized with conclusions, to emphasize the wholeness of this dissertation, the key findings of this work and future perspectives are laid out below.

To remedy gaps in the understanding of corrosion product behavior in the nuclear field, I directly synthesized my own CRUD particles, investigated the role of water chemistry (particularly pH) in particle nucleation and growth, measured the resulting particles' surface properties, and studied the growth CRUD products on current (Zircaloy) and future cladding (FeCrAl) materials. By combining my results with the current available literature on the genesis and surface properties of CRUD in LWRs, a more complete understanding was reached.

This work began by synthesizing nickel ferrite particles that resemble the corrosion products in LWRs by a hydrothermal route to enable *ex situ* characterization. By varying the starting ratio of metal precursors and analyzing the resultant particles, a composition and temperature field for obtaining single phase nickel ferrites was identified and plotted as a phase-diagram. The window was widest at 250°C, the highest temperature studied, but even at that temperature the end member compositions (i.e., [Ni]:[Fe] = 0 and [Ni]:[Fe] = 0.5) did not did yield a single phase product. On the Ni-poor side of the window, this was attributed to the limited availability of Fe^{2+} from an Fe^{3+} precursor under oxidizing conditions. On the Ni-rich side of the window, the availability an intermediate compound $Ni(OH)_2$ in solution was key to incorporating nickel into the ferrite crystals.

The knowledge obtained from these synthesis experiments was used to determine the mechanism and growth rate of the CRUD particles. By controlling the concentration of the nucleating agent (NaOH), I controlled the availability of the intermediate $Ni(OH)_2$, and I was able to control particle size in addition to composition. At 2M NaOH, octahedral CRUD particles of 300 nm were obtained whereas at 0.01M NaOH, the particles were only 100 nm. This also controlled the phases obtained, due to the excess availability of OH^- ions. At 2M NaOH, single phase stoichiometric nickel ferrites were not obtained due to the stability of the intermediate whereas at 0.01M stoichiometric single-phase particles were obtained. Thus, by controlling the pH at which experiments were carried out we were able to control both the phase and size of the CRUD particles.

In LWRs, there is a limited range of pH that can be tolerated due to other failure modes like stress corrosion cracking. Thus some CRUD growth, detachment and transport is to be expected. It is therefore critical to understand how the surface properties of these CRUD particles in LWRs dictate the adhesion of these particles onto the cladding materials and other surfaces. My initial synthesis experiments were all conducted in an oxidizing environment, but real LWRs may operate under HWC (reducing) conditions. I therefore simulated HWC chemistry using EDA (a reducing agent) for comparison to NWC. The surface properties – in particular the surface potential – of the particle synthesized in a reducing environment were very different from those synthesized in NWC. In NWC, the IEP increased with decreasing Ni content of the particles, while in HWC synthesis the opposite trend is observed: decreasing Ni content shifted the IEP downward, approaching that of magnetite. Thus I conclude that the water chemistry in a particular LWR will have a profound effect on CRUD surface properties and deposition behavior.

Knowing the behavior of the particles is only part of the corrosion story, as the growth surface matters as well. Thus for the final part of this dissertation with the help of GE-R, I designed and conducted experiments to study the corrosion behavior of current and future cladding tubes. Very little has been published on the process of CRUD deposition on FeCrAl cladding, but such questions must be addressed before alternative cladding materials can be deployed. With over 6 months of testing in HWC and NWC of BWR environment, I was able to conclude that a uniform native oxide was developed on Zirc-2 whereas a bilayer oxide structure was observed on FeCrAl cladding tubes. To further understand how ions in solution would interact with existing oxide layers on the cladding, I injected CRUD ions in the realistic BWR test loop at GE-R and analyzed the resulting layers. Unlike Zirc-2 cladding tube where most of the CRUD particles can be removed by ultrasonication, this purely physical removal mechanism caused no change in the combined thickness of native oxide + CRUD deposits on FeCrAl cladding tubes. I therefore deduce the existence of a chemical interaction between the native oxide of FeCrAl cladding tubes with injected CRUD ions. These experiments imply a significant hurdle for FeCrAl as an alternative cladding materials, because a thick, non-uniform, thermally non-conductive layer that is difficult to remove cause local increases in the cladding temperature, deteriorating its performance over time.

Curiously, no increase in cladding temperature due to this thicker oxide was observed in our experiments. This departure from expectations could be due to the absence of SNB conditions in our test loop. Usually, BWRs have a SNB condition where water is converted into steam which may impact cladding temperature due a different thermal conductance. Additional testing would

be needed in SNB conditions to fully explore the interaction between the native oxide + CRUD deposits on FeCrAl cladding tubes before they can be implemented in real reactors.

Many questions remain, of course. For example, real CRUD is not exclusively nickel ferrite, suggesting other metal oxides should be studied. Other analysis techniques could be used to study the surface charge of individual particles rather than the ensemble measurements offered by zeta potential used in this dissertation. Also, the detachment of CRUD particles from corroded surfaces has not been addressed at all in this work. The interaction of these suspended particles with cladding materials has not been addressed either, only dissolved ions. Such questions could be aided by fluid mechanical modeling that took into account the attraction or repulsion of particles based on surface charges, which my work suggests is composition dependent as well as pH-dependent. As intriguing as these questions may sound, they are beyond the scope of this dissertation and will be an interesting field of research to be explored by future students.

10. References

[1] W. Report, DEVELOPMENT AND COOPERATION ON NUCLEAR RESEARCH AND ENERGY IN THE MIDDLE EAST WORKSHOP REPORT MIDDLE EAST WEAPONS OF MASS, (n.d.).

[2] D. Stevenson, The Role of Coal Gasification in the Global Energy Transition, 2022.

[3] W.D. Magwood, H. Paillere, Looking ahead at reactor development, Prog. Nucl. Energy 102 (2018) 58–67. https://doi.org/10.1016/j.pnucene.2017.07.001.

[4] M.D. Mathew, Nuclear energy: A pathway towards mitigation of global warming, Prog. Nucl. Energy 143 (2022) 104080. https://doi.org/10.1016/j.pnucene.2021.104080.

[5] H. Lodge, B.S. Edmunds, A Brief Introduction to Light and Sound, 44 (n.d.).

[6] L. Varro, B. Wanner, C.A. Hernández Alva, A. Herzog, P. Fraser, Nuclear power in a clean energy system, Int. Energy Agency. Https//Webstore. Iea. Org/Nuclear-Power-in-a-Clean-Energy-System (2019).

[7] WNA, World Nuclear Performance Report 2020 Produced by: World Nuclear Association, (2020) 1–68.

[8] C.F. Baes Jr, T.H. Handley, Maritime Reactor Program Annual Progress Report, Water Chem. Stud. 43 (1961).

[9] J. Chen, SKi 3 1/21, (2000).

[10] N. Cinosi, I. Haq, M. Bluck, S.P. Walker, The effective thermal conductivity of crud and heat transfer from crud-coated PWR fuel, Nucl. Eng. Des. 241 (2011) 792–798. https://doi.org/10.1016/j.nucengdes.2010.12.015.

[11] C.W. Turner, Fouling Of Nuclear Steam Generators: Fundamental Studies, Operating Experience and Remedial Measures Using Chemical Additives, AECL Nucl. Rev. 2

(2013) 61–88. https://doi.org/10.12943/anr.2013.00007.

[12] A.F. Cea, F.D. Cea, B.G.I. Uds, G.R.E.D.F. Septen, G.R.A. Np, Modelling of crud growth phenomena on PWR fuel rods under nucleate boiling conditions, Nucl. Plant Chem. (2012).

[13] J. Deshon, D. Hussey, B. Kendrick, J. McGurk, J. Secker, M. Short, Pressurized water reactor fuel crud and corrosion modeling, Jom 63 (2011) 64–72. https://doi.org/10.1007/s11837-011-0141-z.

[14] S.H. Jung, K.J. Daub, J.W. Yeon, K.S. Choi, J. Choi, H. Yang, D.H. Lee, K. Song, Investigation on exceptional fuel CRUD samples by using radioactivity ratios of cobalt isotopes, Appl. Radiat. Isot. 81 (2013) 307–309. https://doi.org/10.1016/j.apradiso.2013.03.062.

[15] S. Uchida, Y. Asakura, H. Suzuki, Deposition of boron on fuel rod surface under sub-cooled boiling conditions - An approach toward understanding AOA occurrence, Nucl. Eng. Des. 241 (2011) 2398–2410. https://doi.org/10.1016/j.nucengdes.2011.04.009.

[16] P. Bennett, Effects of water chemistry and thermal-hydraulic conditions on crud formation on PWR fuel in the Halden reactor, in: Int. Conf. Water Chem. Nucl. React. Syst., 2008.

[17] J. Chen, J. Eskhult, C. Marks, J. Dingee, B. Bengtsson, D. Wells, Characteristics of fuel CRUD from Ringhals Unit 4. A comparison of CRUD samples from ultrasonic fuel cleaning and fuel scrape, (2014).

[18] P.L. Frattini, J. Blok, S. Chauffriat, J. Sawicki, J. Riddle, Axial offset anomaly: Coupling PWR primary chemistry with core design, Nucl. Energy 40 (2001) 123–135. https://doi.org/10.1680/nuen.40.2.123.39952.

[19] M. Barale, M. Guillodo, C. Brun, M.H. Clinard, G. Corredera, O. De Bouvier, Preliminary

laboratory tests of investigation on the blockage phenomena observed on TSP of French SGs, in: Proc. Int. Conf. Water Chem. Nucl. React. Syst. Berlin, Ger. Pap. P2-41, 2008.

[20] A.W. Peakman, Development of a Long-Life Core for Commercial Marine Propulsion, (2014).

[21] NRC.GOV, Coated Cladding | NRC.gov, (2024). https://www.nrc.gov/reactors/power/atf/technologies/chrom-clad.html (accessed June 15, 2024).

[22] T. Murakami, A historical review and analysis on the selection of nuclear reactor types and implications to development programs for advanced reactors; A Japanese study, Energy Reports 7 (2021) 3428–3436. https://doi.org/10.1016/j.egyr.2021.05.049.

[23] NRC.GOV, The Pressurized Water Reactor (PWR) | NRC.gov, (2017). https://www.nrc.gov/reading-rm/basic-ref/students/animated-pwr.html (accessed June 15, 2024).

[24] nrc.gov, The Boiling Water Reactor (BWR) | NRC.gov, (2017). https://www.nrc.gov/reading-rm/basic-ref/students/animated-bwr.html (accessed June 15, 2024).

[25] Q. Bignon, F. Martin, Q. Auzoux, F. Miserque, M. Tabarant, L. Latu-Romain, Y. Wouters, Oxide formation on titanium alloys in primary water of nuclear pressurised water reactor, Corros. Sci. 150 (2019) 32–41. https://doi.org/10.1016/j.corsci.2019.01.020.

[26] P.G. Garzarolli, F.; Jorde, D.; Manzel, R.; Parry, G. W.; Smerd, Review of PWR fuel rod waterside corrosion behavior, (1980).

[27] M.S. Park, H.S. Shim, S.H. Baek, J.G. Kim, D.H. Hur, Effects of oxidation states of fuel cladding surface on crud deposition in simulated primary water of PWRs, Ann. Nucl.

Energy 103 (2017) 275–281. https://doi.org/10.1016/j.anucene.2017.01.014.

[28] W. Zhang, A. Sun, X. Zhao, N. Suo, L. Yu, Z. Zuo, Structural and magnetic properties of La 3+ ion doped Ni–Cu–Co nano ferrites prepared by sol–gel auto-combustion method, J. Sol-Gel Sci. Technol. 90 (2019) 599–610. https://doi.org/10.1007/s10971-019-04941-4.

[29] P. Loganthurai, S. Parthasarathy, S. Selvakumaran, V. Rajasekaran, Energy conservation measures in a technical institutional building in Tamilnadu in India, Energy Procedia 14 (2012) 1181–1186. https://doi.org/10.1016/j.egypro.2011.12.1025.

[30] IAEA, Stress Corrosion Cracking in Light Water Reactors: Good Practices and Lessons Learned, IAEA Nucl. Energy Ser. No. NP-T-3.13 (2011) 115. https://www-pub.iaea.org/MTCD/publications/PDF/P1522_web.pdf.

[31] H. Margareth, No Title طرق تدريس اللغة العربية, Экономика Региона (2017) 32.

[32] G.C.W. Comley, The significance of corrosion products in water reactor coolant circuits, Prog. Nucl. Energy 16 (1985) 41–72. https://doi.org/10.1016/0149-1970(85)90005-8.

[33] D. Lister, S. Uchida, Determining water chemistry conditions in nuclear reactor coolants, J. Nucl. Sci. Technol. 52 (2015) 451–466. https://doi.org/10.1080/00223131.2014.973460.

[34] M.S. Yim, H. Ocken, Radiation dose management in nuclear power plants, Prog. Nucl. Energy 39 (2001) 31–51. https://doi.org/10.1016/S0149-1970(01)00002-6.

[35] G. Saji, ICONE22-30990, (2016) 1–14.

[36] A. Molander, On line electrochemical monitoring in light water reactor (LWR) systems, Nucl. Corros. Sci. Eng. (2012) 408–437. https://doi.org/10.1533/9780857095343.4.408.

[37] O.K. Chopra, A.S. Rao, A review of irradiation effects on LWR core internal materials - IASCC susceptibility and crack growth rates of austenitic stainless steels, J. Nucl. Mater. 409 (2011) 235–256. https://doi.org/10.1016/j.jnucmat.2010.12.001.

[38] P.L. Andresen, Stress corrosion cracking (SCC) of austenitic stainless steels in high temperature light water reactor (LWR) environments, Underst. Mitigating Ageing Nucl. Power Plants Mater. Oper. Asp. Plant Life Manag. (2010) 236–307. https://doi.org/10.1533/9781845699956.2.236.

[39] P.L. Andresen, C.L. Briant, Environmentally assisted cracking of types 304L/316L/316NG stainless steel in 288°C water, Corrosion 45 (1989) 448–463. https://doi.org/10.5006/1.3582044.

[40] L.W. Niedrach, Effect of palladium coatings on the corrosion potential of stainless steel in high-temperature water containing dissolved hydrogen and oxygen, Corrosion 47 (1991) 162–169. https://doi.org/10.5006/1.3585237.

[41] C. Park, N.Y. Us, Y. Jin, C. Park, N.Y. Us, P. Diaz, S. Martin, C.A. Us, (12) United States Patent, 2 (2004).

[42] A. Bruggeman, E. Dubost, M. Ekenved, E.W. Hooper, E.B. Houbetsov, I. Kallonen, M. Lucas, S. Luo, S.K. Sen Gupta, J. Timulak, A.F. Tsarenko, M. Ojovan, J. Viszlay, Processing of nuclear power plant waste streams containing boric acid - TECDOC-911, Iaea-Tecdoc-911 2 (1996) 1–67.

[43] S. Cassineri, J. Duff, A. Cioncolini, M. Curioni, A. Banks, F. Scenini, Deposition of corrosion products under pressurised water nuclear reactor conditions: The effect of flow velocity and dissolved hydrogen, Corros. Sci. 159 (2019). https://doi.org/10.1016/j.corsci.2019.108113.

[44] I. Betova, M. Bojinov, T. Saario, Start-up and Shut-down Water Chemistries in Pressurized Water Reactors, VTT Res. Rep. VTT-R-00699-12 (2012) 1–81.

[45] X. Wu, X. Liu, Z. Zhang, J. Tan, E.H. Han, W. Ke, Some fundamental understandings of

Zn-injection water chemistry on material corrosion in pressurized water reactor primary circuit, Corros. Commun. 6 (2022) 52–61. https://doi.org/10.1016/j.corcom.2021.12.004.

[46] Y. Ma, C. Qin, J. Chen, X. Li, Z. Zhang, L. Zhang, Influence of zinc injection on deposition of corrosion products on inner wall of heat transfer tube, Int. J. Adv. Nucl. React. Des. Technol. 3 (2021) 139–144. https://doi.org/10.1016/j.jandt.2021.07.003.

[47] K. Hisamune, T. Nambu, D. Akutagawa, N. Nagata, Y. Shimizu, K. Nagamine, N. Kogawa, Study on a Corrosion Products Behavior With Zinc Injection in Pwr Primary, 18th Int. Conf. Water Chem. Nucl. React. Syst. (2012) 1–11.

[48] A. Pardo, M.C. Merino, A.E. Coy, F. Viejo, R. Arrabal, E. Matykina, Pitting corrosion behaviour of austenitic stainless steels - combining effects of Mn and Mo additions, Corros. Sci. 50 (2008) 1796–1806. https://doi.org/10.1016/j.corsci.2008.04.005.

[49] J. Robertson, The mechanism of high temperature aqueous corrosion of stainless steels, Corros. Sci. 32 (1991) 443–465. https://doi.org/10.1016/0010-938X(91)90125-9.

[50] S. Odar, P. Rudling, Crud in PWR/VVER Coolant Volume I – Sources, Transportation in Coolant, Fuel Deposition and Radiation Build-up, ANT Int. I (2014).

[51] A. Machet, A. Galtayries, P. Marcus, P. Combrade, P. Jolivet, P. Scott, XPS study of oxides formed on nickel-base alloys in high-temperature and high-pressure water, Surf. Interface Anal. 34 (2002) 197–200. https://doi.org/10.1002/sia.1282.

[52] M. Griffiths, Ni-based alloys for reactor internals and steam generator applications, Elsevier Inc., 2019. https://doi.org/10.1016/B978-0-12-397046-6.00009-5.

[53] T. Terachi, N. Totsuka, T. Yamada, T. Nakagawa, H. Deguchi, M. Horiuchi, M. Oshitani, Influence of dissolved hydrogen on structure of oxide film on alloy 600 formed in primary water of pressurized water reactors, J. Nucl. Sci. Technol. 40 (2003) 509–516.

https://doi.org/10.1080/18811248.2003.9715385.

[54] H. Takiishi, J.H. Duvaizen, I.M. Sato, J.L. Rossi, L.A.T. Pereira, L.G. Martinez, Recycling of zircaloy machining chips by VAR remelting and powder metallurgy techniques, Mater. Sci. Forum 727–728 (2012) 356–361. https://doi.org/10.4028/www.scientific.net/MSF.727-728.356.

[55] B. Cox, J.P. Pemsler, Diffusion of oxygen in growing zirconia films, J. Nucl. Mater. 28 (1968) 73–78. https://doi.org/10.1016/0022-3115(68)90058-5.

[56] S.B. Narang, K. Pubby, Nickel Spinel Ferrites: A review, J. Magn. Magn. Mater. 519 (2021) 167163. https://doi.org/10.1016/j.jmmm.2020.167163.

[57] 1-s2.0-S266652392100091X-main.pdf, (n.d.).

[58] J. Guo, G. Li, H. Zhang, X. Jia, Q. Meng, W. Liu, Coupling of capillary electrophoresis with electrospray ionization multiplexing ion mobility spectrometry, Electrophoresis 40 (2019) 1639–1647. https://doi.org/10.1002/elps.201800462.

[59] P.R. Tremaine, A CALCULATION AND THE SOLLJBILUY OF MAGNETITE IN Hz0 AND DzO TO 300°C OF GIBBS FREE ENERGIES FOR FERROUS IONS, Thermochmic Acata 19 (1977) 287–300.

[60] F.H. Sweeton, C.F. Baes, The solubility of magnetite and hydrolysis of ferrous ion in aqueous solutions at elevated temperatures, J. Chem. Thermodyn. 2 (1970) 479–500. https://doi.org/10.1016/0021-9614(70)90098-4.

[61] S. Zhang, R. Shi, Y. Tan, Comparison of the Solubility of ZnFe2O4, Fe3O4 and Fe2O3 in High Temperature Water, J. Solution Chem. 47 (2018) 1112–1126. https://doi.org/10.1007/s10953-018-0779-z.

[62] M.H. Kim, U.C. Kim, C.W. Won, W.Y. Maeng, Experimental evaluation of primary water

chemistry for prevention of axial offset anomaly, Thermochim. Acta 542 (2012) 80–88. https://doi.org/10.1016/j.tca.2011.12.011.

[63] D. Cubicciotti, jourual of uialerlals systems fluulm under LWR conditions, 201 (1993) 176–183.

[64] R.J. Biernat, R.G. Robins, High-temperature potential/pH diagrams for the iron-water and iron-water-sulphur systems, Electrochim. Acta 17 (1972) 1261–1283. https://doi.org/10.1016/0013-4686(72)80013-6.

[65] Z. Stojek, The electrical double layer and its structure, Electroanal. Methods Guid. to Exp. Appl. (2010) 3–9. https://doi.org/10.1007/978-3-642-02915-8_1.

[66] S. V. Sujith, H. Kim, J. Lee, A Review on Thermophysical Property Assessment of Metal Oxide-Based Nanofluids: Industrial Perspectives, Metals (Basel). 12 (2022) 1–21. https://doi.org/10.3390/met12010165.

[67] S.E. McNeil, Characterization of Nanoparticles Intended for Drug Delivery (Humana Press, 2010), 2010.

[68] Y.P. Sun, X. qin Li, J. Cao, W. xian Zhang, H.P. Wang, Characterization of zero-valent iron nanoparticles, Adv. Colloid Interface Sci. 120 (2006) 47–56. https://doi.org/10.1016/j.cis.2006.03.001.

[69] J.M. Berg, A. Romoser, N. Banerjee, R. Zebda, C.M. Sayes, The relationship between pH and zeta potential of ∼ 30 nm metal oxide nanoparticle suspensions relevant to in vitro toxicological evaluations, Nanotoxicology 3 (2009) 276–283. https://doi.org/10.3109/17435390903276941.

[70] S.T. Hunter, Preface, 2014. https://doi.org/10.4159/harvard.9780674499171.prf.

[71] M.P. Short, D. Hussey, B.K. Kendrick, T.M. Besmann, C.R. Stanek, S. Yip, Multiphysics

modeling of porous CRUD deposits in nuclear reactors, J. Nucl. Mater. 443 (2013) 579–587. https://doi.org/10.1016/j.jnucmat.2013.08.014.

[72] T. Kim, A. Couet, S. Kim, Y. Lee, S.C. Yoo, J.H. Kim, In-situ electrochemical study of zirconium alloy in high temperature hydrogenated Water conditions, Corros. Sci. 173 (2020) 108745. https://doi.org/10.1016/j.corsci.2020.108745.

[73] S.H. Baek, H.S. Shim, J.G. Kim, D.H. Hur, Effects of dissolved hydrogen on fuel crud deposition and subcooled nucleate boiling in PWR primary water at 328 °C, Nucl. Eng. Des. 345 (2019) 85–93. https://doi.org/10.1016/j.nucengdes.2019.02.010.

[74] A.K. Hoffman, R. V. Umretiya, V.K. Gupta, M. Larsen, C. Graff, C. Perlee, P. Brennan, R. Rebak, Oxidation Resistance in 1200°C Steam of a FeCrAl Alloy Fabricated by Three Metallurgical Processes, Jom 74 (2022) 1690–1697. https://doi.org/10.1007/s11837-022-05209-z.

[75] E. Aydogan, J.S. Weaver, S.A. Maloy, O. El-Atwani, Y.Q. Wang, N.A. Mara, Microstructure and mechanical properties of FeCrAl alloys under heavy ion irradiations, J. Nucl. Mater. 503 (2018) 250–262. https://doi.org/10.1016/j.jnucmat.2018.03.002.

[76] R.B. Rebak, M. Larsen, Y.J. Kim, Characterization of oxides formed on iron-chromium-Aluminum alloy in simulated light water reactor environments, Corros. Rev. 35 (2017) 177–188. https://doi.org/10.1515/corrrev-2017-0011.

[77] P.K. Roy, J. Bera, Characterization of nanocrystalline NiCuZn ferrite powders synthesized by sol-gel auto-combustion method, J. Mater. Process. Technol. 197 (2008) 279–283. https://doi.org/10.1016/j.jmatprotec.2007.06.027.

[78] X. Wang, Z. Zhao, J. Qu, Z. Wang, J. Qiu, Shape-control and characterization of magnetite prepared via a one-step solvothermal route, Cryst. Growth Des. 10 (2010)

2863–2869. https://doi.org/10.1021/cg900472d.

[79] W.E. Pottker, R. Ono, M. Angel, A. Hernando, Annealing temperature effect upon nickel ferrites nanoparticles : Structural , morphological and magnetic properties In fl uence of order-disorder e ff ects on the magnetic and optical properties of, (2017). https://doi.org/10.1016/j.ceramint.2018.06.190.

[80] V.K. Mittal, S. Bera, R. Nithya, M.P. Srinivasan, S. Velmurugan, S. V. Narasimhan, Solid state synthesis of Mg-Ni ferrite and characterization by XRD and XPS, J. Nucl. Mater. 335 (2004) 302–310. https://doi.org/10.1016/j.jnucmat.2004.05.010.

[81] G.M. Alzoubi, Probing the structural and magnetic properties of small crystalline nickel ferrite nanoparticles near the upper size limit of the single-domain regime, 6753 (2020). https://doi.org/10.1080/17436753.2020.1759923.

[82] J.W. Yeon, I.K. Choi, K.K. Park, H.M. Kwon, K. Song, Chemical analysis of fuel crud obtained from Korean nuclear power plants, J. Nucl. Mater. 404 (2010) 160–164. https://doi.org/10.1016/j.jnucmat.2010.07.024.

[83] W.L. CLARKE, G.M. GORDON, Investigation of Stress Corrosion Cracking Susceptibility of Fe-Ni-Cr Alloys in Nuclear Reactor Water Environments, Corrosion 29 (1973) 1–12. https://doi.org/10.5006/0010-9312-29.1.1.

[84] J. Epp, X-Ray Diffraction (XRD) Techniques for Materials Characterization, Elsevier Ltd, 2016. https://doi.org/10.1016/B978-0-08-100040-3.00004-3.

[85] K. Akhtar, S.A. Khan, S.B. Khan, A.M. Asiri, Scanning electron microscopy: Principle and applications in nanomaterials characterization, 2018. https://doi.org/10.1007/978-3-319-92955-2_4.

[86] A. Mohammed, A. Abdullah, Scanning Electron Microscopy (Sem): a Review, Int. Conf.

OnHydraulics Pneum. (2018) 77–85.

[87] W. Zhou, Transmission Electron Microscopy, Met. Oxide Catal. 1 (2009) 443–485. https://doi.org/10.1002/9783527626113.ch10.

[88] C.Y. Tang, Z. Yang, Transmission Electron Microscopy (TEM), Elsevier B.V., 2017. https://doi.org/10.1016/B978-0-444-63776-5.00008-5.

[89] W. Herres, J. Gronholz, Understanding FT-IR Data Processing, J. Comput. Appl. Lab. 2 (1984) 216–220.

[90] Fourier Transform Infrared Spectroscopy Published by : American Association for the Advancement of Science Stable URL : https://www.jstor.org/stable/1741844, 191 (1976) 31–37.

[91] S.C. Wilschefski, M.R. Baxter, Inductively Coupled Plasma Mass Spectrometry: Introduction to Analytical Aspects, Clin. Biochem. Rev. 40 (2019) 115–133. https://doi.org/10.33176/AACB-19-00024.

[92] A.A. Sorokin, S. V. Bobashev, T. Feigl, K. Tiedtke, H. Wabnitz, M. Richter, Photoelectric effect at ultrahigh intensities, Phys. Rev. Lett. 99 (2007) 1–4. https://doi.org/10.1103/PhysRevLett.99.213002.

[93] G. Greczynski, L. Hultman, X-ray photoelectron spectroscopy: Towards reliable binding energy referencing, Prog. Mater. Sci. 107 (2020) 100591. https://doi.org/10.1016/j.pmatsci.2019.100591.

[94] F. Gilbert, P. Refait, F. Lévêque, C. Remazeilles, E. Conforto, Synthesis of goethite from Fe(OH)2 precipitates: Influence of Fe(II) concentration and stirring speed, J. Phys. Chem. Solids 69 (2008) 2124–2130. https://doi.org/10.1016/j.jpcs.2008.03.010.

[95] Y. Cheng, Y. Zheng, Y. Wang, F. Bao, Y. Qin, Synthesis and magnetic properties of

nickel ferrite nano-octahedra, 178 (2005) 2394–2397. https://doi.org/10.1016/j.jssc.2005.05.006.

[96] H.J. Qu, H. Abouelella, A.S. Chikhalikar, R. Rajendran, I. Roy, J. Priedeman, R. Umretiya, A. Hoffman, J.P. Wharry, R. Rebak, Effect of nickel on the oxidation behavior of FeCrAl alloy in simulated PWR and BWR conditions, Corros. Sci. 216 (2023) 111093. https://doi.org/10.1016/j.corsci.2023.111093.

[97] J.A. Sawicki, Nuclear chemistry model of borated fuel crud, Int. Conf. Water Chem. Nucl. React. Syst. (2002) 5–7. http://inis.iaea.org/Search/search.aspx?orig_q=RN:34057649.

[98] H.P. Hermansson, G. Persson, A. Reinvall, Corrosion product particles in boiling water reactor condensates, Nucl. Technol. 103 (1993) 101–112. https://doi.org/10.13182/nt93-a34833.

[99] P. Sivakumar, R. Ramesh, A. Ramanand, S. Ponnusamy, C. Muthamizhchelvan, Synthesis and characterization of nickel ferrite magnetic nanoparticles, Mater. Res. Bull. 46 (2011) 2208–2211. https://doi.org/10.1016/j.materresbull.2011.09.009.

[100] Heyn, Emil, (n.d.).

[101] Y. Cudennec, A. Lecerf, The transformation of ferrihydrite into goethite or hematite, revisited, J. Solid State Chem. 179 (2006) 716–722. https://doi.org/10.1016/j.jssc.2005.11.030.

[102] S. Gialanella, F. Girardi, G. Ischia, I. Lonardelli, M. Mattarelli, M. Montagna, On the goethite to hematite phase transformation, J. Therm. Anal. Calorim. 102 (2010) 867–873. https://doi.org/10.1007/s10973-010-0756-2.

[103] V.P. Ponomar, Thermomagnetic properties of the goethite transformation during high-temperature treatment, Miner. Eng. 127 (2018) 143–152.

https://doi.org/10.1016/j.mineng.2018.08.016.

[104] Surianti, A.N. Utami, M.A. Permatasari, I.M. Bendiyasa, W. Astuti, H.T.B.M. Petrus, Valuable Metals Precipitation of Low Grade Nickel Ore Leachate Using Sodium Hydroxide, IOP Conf. Ser. Mater. Sci. Eng. 742 (2020) 6–13. https://doi.org/10.1088/1757-899X/742/1/012043.

[105] W. Karlsen, G. Diego, B. Devrient, Localized deformation as a key precursor to initiation of intergranular stress corrosion cracking of austenitic stainless steels employed in nuclear power plants, J. Nucl. Mater. 406 (2010) 138–151. https://doi.org/10.1016/j.jnucmat.2010.01.029.

[106] S. Cassineri, J. Duff, M. Curioni, A. Banks, F. Scenini, CRUD deposition in accelerated high-temperature water: Investigation on the effect of substrate material and water chemistry, J. Nucl. Mater. 529 (2020) 151915. https://doi.org/10.1016/j.jnucmat.2019.151915.

[107] J. Yang, J. Wang, J. Liu, S. Wang, D. Yun, D. Ma, Y. Li, D. Xu, Microstructural understanding on the fouling behavior of crud on PWR fuel cladding surface, J. Nucl. Mater. 582 (2023). https://doi.org/10.1016/j.jnucmat.2023.154500.

[108] J.H. Park, S.Y. Cho, J.J. Kim, C.B. Lee, S.H. Lee, M.H. Lee, J.S. Song, Study of the radioactivity inventory deposited in the reactor coolant system during the decommissioning of Kori Unit 1, Ann. Nucl. Energy 190 (2023) 109860. https://doi.org/10.1016/j.anucene.2023.109860.

[109] J. feng Lu, C.J. Tsai, Hydrothermal phase transformation of hematite to magnetite, Nanoscale Res. Lett. 9 (2014) 1–8. https://doi.org/10.1186/1556-276X-9-230.

[110] M.C. Biesinger, B.P. Payne, A.P. Grosvenor, L.W.M. Lau, A.R. Gerson, R.S.C. Smart,

Resolving surface chemical states in XPS analysis of first row transition metals, oxides and hydroxides: Cr, Mn, Fe, Co and Ni, Appl. Surf. Sci. 257 (2011) 2717–2730. https://doi.org/10.1016/j.apsusc.2010.10.051.

[111] S.H. Lafta, Effect of pH on Structural, Magnetic and FMR Properties of Hydrothermally Prepared Nano Ni Ferrite, Open Chem. 15 (2017) 53–60. https://doi.org/10.1515/chem-2017-0007.

[112] T. Zheng, S. Bott, Q. Huo, Techniques for Accurate Sizing of Gold Nanoparticles Using Dynamic Light Scattering with Particular Application to Chemical and Biological Sensing Based on Aggregate Formation, ACS Appl. Mater. Interfaces 8 (2016) 21585–21594. https://doi.org/10.1021/acsami.6b06903.

[113] B.S. Nagothi, J. Arnason, K. Dunn, A Hydrothermal Phase Diagram for the Low-Temperature Synthesis of Nonstoichiometric Nickel Ferrite Nanoparticles, Nucl. Technol. 209 (2023) 887–894. https://doi.org/10.1080/00295450.2022.2161266.

[114] D. Chen, D. Chen, X. Jiao, Y. Zhao, M. He, Hydrothermal synthesis and characterization of octahedral nickel ferrite particles, Powder Technol. 133 (2003) 247–250. https://doi.org/10.1016/S0032-5910(03)00079-2.

[115] B. Baruwati, R.K. Rana, S. V. Manorama, Further insights in the conductivity behavior of nanocrystalline Ni Fe2 O4, J. Appl. Phys. 101 (2007). https://doi.org/10.1063/1.2404772.

[116] M. Barale, G. Lefèvre, F. Carrette, H. Catalette, M. Fédoroff, G. Cote, Journal of Colloid and Interface Science Effect of the adsorption of lithium and borate species on the zeta potential of particles of cobalt ferrite , nickel ferrite , and magnetite, 328 (2008) 34–40. https://doi.org/10.1016/j.jcis.2008.09.007.

[117] J.J. Carlson, S.K. Kawatra, Factors affecting zeta potential of iron oxides, Miner. Process.

Extr. Metall. Rev. 34 (2013) 269–303. https://doi.org/10.1080/08827508.2011.604697.

[118] X. Rabilloud, Comments on “prevented mortality and greenhouse gas emissions from historical and projected nuclear power,” Environ. Sci. Technol. 47 (2013) 13896–13899. https://doi.org/10.1021/es404245a.

[119] A.T. Motta, A. Couet, R.J. Comstock, Corrosion of Zirconium Alloys Used for Nuclear Fuel Cladding, Annu. Rev. Mater. Res. 45 (2015) 311–343. https://doi.org/10.1146/annurev-matsci-070214-020951.

[120] J.R. Santisteban, M.A. Vicente-Alvarez, P. Vizcaino, A.D. Banchik, S.C. Vogel, A.S. Tremsin, J. V. Vallerga, J.B. McPhate, E. Lehmann, W. Kockelmann, Texture imaging of zirconium based components by total neutron cross-section experiments, J. Nucl. Mater. 425 (2012) 218–227. https://doi.org/10.1016/j.jnucmat.2011.06.043.

[121] Y. Katoh, G. Vasudevamurthy, T. Nozawa, L.L. Snead, Properties of zirconium carbide for nuclear fuel applications, J. Nucl. Mater. 441 (2013) 718–742. https://doi.org/10.1016/j.jnucmat.2013.05.037.

[122] S.I. Tanaka, Accident at the Fukushima Dai-ichi nuclear power stations of TEPCO - outline & lessons learned, Proc. Japan Acad. Ser. B Phys. Biol. Sci. 88 (2012) 471–484. https://doi.org/10.2183/pjab.88.471.

[123] K.A. Terrani, S.J. Zinkle, L.L. Snead, Advanced oxidation-resistant iron-based alloys for LWR fuel cladding, J. Nucl. Mater. 448 (2014) 420–435. https://doi.org/10.1016/j.jnucmat.2013.06.041.

[124] G.E. Global, N. Fuels, G.E. Power, R. Fawcett, R. Augi, C. Paone, P. Davis, D. Lutz, M. Powers, D. Keck, B. Eber, K. Ledford, P. Cantonwine, R. Stachowski, Y. Lin, S. Desilva, J. Harrison, R. Rand, M. Yilmaz, B. Frew, B. Moore, J. Head, B. Schulz, L. Schichlein, P.

Davis, R. Higgins, K. Martin, J. Banfield, J. Reynolds, M. Short, P. Mccumbee, S. Nuclear, J.B. Williams, J. Chavers, N.A. Satterlee, I. National, M. Pi, G. Hoggard, J. Harp, G. Povirk, G. Core, B. Durtschi, C. Woolum, R.O. Brien, DE-NE0008221 GE Final Technical and Scientific Report, (2018) 1–47.

[125] A. FAZI, Development and performance evaluation of accidenttolerant coated fuel claddings for light water reactors, 2023. https://research.chalmers.se/publication/533922%0Ahttps://research.chalmers.se/publication/533922/file/533922_Fulltext.pdf.

[126] D. Mandal, P.A. Dabhade, B.K. Chougule, Thin film coating of silicon carbide on zircaloy-4 tube by FCVD process and a study on its kinetics, J. Nucl. Mater. 552 (2021) 152996. https://doi.org/10.1016/j.jnucmat.2021.152996.

[127] S.S. Raiman, K.G. Field, R.B. Rebak, Y. Yamamoto, K.A. Terrani, Hydrothermal corrosion of 2nd generation FeCrAl alloys for accident tolerant fuel cladding *, J. Nucl. Mater. 536 (2020) 152221. https://doi.org/10.1016/j.jnucmat.2020.152221.

[128] K. Terrani, Y.J. Kim, B. Pint, Uniform corrosion of model FeCrAl alloys in LWR coolants, Trans. Am. Nucl. Soc. 112 (2015) 274–275.

[129] R. Rajendran, A.S. Chikhalikar, I. Roy, H. Abouelella, H.J. Qu, R. V. Umretiya, A.K. Hoffman, R.B. Rebak, Effect of aging and α' segregation on oxidation and electrochemical behavior of FeCrAl alloys, J. Nucl. Mater. 588 (2024) 154751. https://doi.org/10.1016/j.jnucmat.2023.154751.

[130] C. Guéneau, J. Piron, J. Dumas, V. Bouineau, F.C. Iglesias, B.J. Lewis, Fuel-cladding chemical interaction, Nea/Nsc/R(2015)5 (2015) 80–90.

[131] S.A. Briggs, P.D. Edmondson, K.C. Littrell, Y. Yamamoto, R.H. Howard, C.R. Daily,

K.A. Terrani, K. Sridharan, K.G. Field, A combined APT and SANS investigation of α′ phase precipitation in neutron-irradiated model FeCrAl alloys, Acta Mater. 129 (2017) 217–228. https://doi.org/10.1016/j.actamat.2017.02.077.

[132] K.G. Field, K.C. Littrell, S.A. Briggs, Precipitation of α′ in neutron irradiated commercial FeCrAl alloys, Scr. Mater. 142 (2018) 41–45. https://doi.org/10.1016/j.scriptamat.2017.08.022.

[133] Version of Record: https://www.sciencedirect.com/science/article/pii/S0022311515302658, (n.d.) 1–39.

[134] R.B. Rebak, L. Yin, W. Zhang, R. V Umretiya, Effect of the redox potential on the general corrosion behavior of industrial nuclear alloys, J. Nucl. Mater. 576 (2023) 154257. https://doi.org/10.1016/j.jnucmat.2023.154257.

[135] L. Yin, T.B. Jurewicz, M. Larsen, M. Drobnjak, C.C. Graff, D.R. Lutz, R.B. Rebak, Uniform corrosion of FeCrAl cladding tubing for accident tolerant fuels in light water reactors, J. Nucl. Mater. 554 (2021) 153090. https://doi.org/10.1016/j.jnucmat.2021.153090.

[136] K.A. Terrani, B.A. Pint, Y.J. Kim, K.A. Unocic, Y. Yang, C.M. Silva, H.M. Meyer, R.B. Rebak, Uniform corrosion of FeCrAl alloys in LWR coolant environments, J. Nucl. Mater. 479 (2016) 36–47. https://doi.org/10.1016/j.jnucmat.2016.06.047.

[137] R.B. Rebak, R.J. Blair, D.R. Lutz, Localized corrosion behavior of FeCrAl nuclear fuel cladding in pool storage, Am. Nucl. Soc. Glob. (2019) 1056–1062.

[138] A. Chikhalikar, I. Roy, H. Abouelella, R. Umretiya, A. Hoffman, M. Larsen, R.B. Rebak, Effect of aluminum on the FeCr(Al) alloy oxidation resistance in steam environment at low temperature (400 °C) and high temperature (1200 °C), Corros. Sci. 209 (2022)

110765. https://doi.org/10.1016/j.corsci.2022.110765.

[139] R.B. Rebak, Alloy Selection for Accident Tolerant Fuel Cladding in Commercial Light Water Reactors, Metall. Mater. Trans. E 2 (2015) 197–207. https://doi.org/10.1007/s40553-015-0057-6.

[140] J. Wang, Y. Ling, Z. Lu, Q. Zhou, R. Wang, Z. Zhang, Enhanced formation of α-Al2O3 at low temperature on Cr/Al coating by controlling oxygen partial pressure, Appl. Surf. Sci. 515 (2020) 146053. https://doi.org/10.1016/j.apsusc.2020.146053.

[141] W. Wu, G. Ran, Y. Li, S. Cong, C. Ye, R. Zhang, Y. Sun, Early corrosion behaviour of irradiated FeCrAl alloy in a simulated pressurized water reactor environment, Corros. Sci. 174 (2020) 108824. https://doi.org/10.1016/j.corsci.2020.108824.

[142] A. Hoffman, R. V Umretiya, W. Zhang, R. Motyl, R. Blair, L. Yin, A.K. Hoffman, V. Gupta, R.B. Rebak, E. Dolley, Effect of Microstructure, Manufacturing Method and Composition on Corrosion Behavior of FeCrAl alloys Accident Tolerant Fuels Claddings and the Evolution of their Surface Characteristics under Critical Heat Flux View project FeCrAl for Accident Tolerant F, (n.d.). https://doi.org/10.13182/TopFuel22-39013.

[143] T. Terachi, T. Yamada, T. Miyamoto, K. Arioka, K. Fukuya, Corrosion behavior of stainless steels in simulated PWR primary water—effect of chromium content in alloys and dissolved hydrogen—, J. Nucl. Sci. Technol. 45 (2008) 975–984. https://doi.org/10.1080/18811248.2008.9711883.

[144] D.D. Macdonald, G.R. Engelhardt, A Critical Review of Radiolysis Issues in Water-Cooled Fission and Fusion Reactors: Part II, Prediction of Corrosion Damage in Operating Reactors, Corros. Mater. Degrad. 3 (2022) 694–758. https://doi.org/10.3390/cmd3040038.

[145] J. Liu, K. Li, J. Sayers, T. Aarholt, G. He, H. Hulme, A. Garner, M. Preuss, H. Nordin,

J.M. Partezana, M. Limbäck, S. Lozano-Perez, S. Ortner, C.R.M. Grovenor, Characterisation of deuterium distributions in corroded zirconium alloys using high-resolution SIMS imaging, Acta Mater. 200 (2020) 581–596. https://doi.org/10.1016/j.actamat.2020.09.040.

[146] T. Kim, K.J. Choi, S.C. Yoo, Y. Lee, J.H. Kim, Influence of dissolved hydrogen on the early stage corrosion behavior of zirconium alloys in simulated light water reactor coolant conditions, Corros. Sci. 131 (2018) 235–244. https://doi.org/10.1016/j.corsci.2017.11.026.

[147] R.B. Adamson, P. Rudling, Properties of zirconium alloys and their applications in light water reactors (LWRs), Woodhead Publishing Limited, 2013. https://doi.org/10.1533/9780857097453.2.151.

[148] A. Zieliński, S. Sobieszczyk, Hydrogen-enhanced degradation and oxide effects in zirconium alloys for nuclear applications, Int. J. Hydrogen Energy 36 (2011) 8619–8629. https://doi.org/10.1016/j.ijhydene.2011.04.002.

[149] Shannon Bragg-Sitton, Development of advanced accident-tolerant fules for commercial LWRs, Nucl. News (2014) 83–91.

[150] C. Tang, M. Stueber, H.J. Seifert, M. Steinbrueck, Protective coatings on zirconium-based alloys as accident-Tolerant fuel (ATF) claddings, Corros. Rev. 35 (2017) 141–165. https://doi.org/10.1515/corrrev-2017-0010.

[151] E. Kashkarov, B. Afornu, D. Sidelev, M. Krinitcyn, V. Gouws, A. Lider, Recent advances in protective coatings for accident tolerant zr-based fuel claddings, Coatings 11 (2021) 1–32. https://doi.org/10.3390/coatings11050557.

[152] R.B. Rebak, FeCrAl—iron–chromium–aluminum monolithic alloys, 2020. https://doi.org/10.1016/b978-0-12-817503-3.00005-5.

[153] R.B. Rebak, Silicon carbide and ceramics metal composite, Accid. Toler. Mater. Light Water React. Fuels (2020) 143–156. https://doi.org/10.1016/b978-0-12-817503-3.00006-7.

[154] T.C. Winter, R.W. Neu, P.M. Singh, L.E. Kolaya, C.S. Deo, Fretting wear comparison of cladding materials for reactor fuel cladding application, J. Nucl. Mater. 508 (2018) 505–515. https://doi.org/10.1016/j.jnucmat.2018.05.069.

[155] J. Haley, S.A. Briggs, P.D. Edmondson, K. Sridharan, S. Lozano-perez, K.G. Field, AC SC, Acta Mater. (2017). https://doi.org/10.1016/j.actamat.2017.07.011.

[156] A. Chikhalikar, I. Roy, H. Abouelella, R. Umretiya, A. Hoffman, M. Larsen, R.B. Rebak, Effect of aluminum on the FeCr(Al) alloy oxidation resistance in steam environment at low temperature (400 °C) and high temperature (1200 °C), Corros. Sci. 209 (2022) 110765. https://doi.org/10.1016/j.corsci.2022.110765.

[157] R.B. Rebak, V.K. Gupta, M. Larsen, Oxidation Characteristics of Two FeCrAl Alloys in Air and Steam from 800 ° C to 1300 ° C, JOM 70 (2018) 1484–1492. https://doi.org/10.1007/s11837-018-2979-9.

[158] S.E. Garcia, P. Tran, J.F. Giannelli, A.J. Jarvis, M.L. Jarvis, BWR Source Term Management--Strategies and Results at General Electric-designed BWRs, in: ISOE Int. Symp. Cambridge, United Kingdom, 2010: pp. 17–19.

[159] J.A. Sawicki, Analyses of fuel crud and coolant-borne corrosion products in normal water chemistry BWRs, J. Nucl. Mater. 419 (2011) 85–96. https://doi.org/10.1016/j.jnucmat.2011.08.032.

[160] S. Uchida, Y. Asakura, K. Ohsumi, M. Miki, M. Aizawa, Y. Matsushima, K. Yonezawa, Chemical composition of crud depositing on BWR fuel surfaces, J. Nucl. Sci. Technol. 24

(1987) 385–392. https://doi.org/10.1080/18811248.1987.9735818.

[161] C.C. Lin, A review of corrosion product transport and radiation field buildup in boiling water reactors, Prog. Nucl. Energy 51 (2009) 207–224. https://doi.org/10.1016/j.pnucene.2008.05.005.

[162] L. Oliver, W. Electric, CHANGE IN CRUD DEPOSITION , WATER CHEMISTRY AND ECP RESPONSE AFTER THE TRANSITION TO HWC / OLNC AT KKL – AN UPDATE, (n.d.).

[163] C.P. Coyle, Synthesis of CRUD and its Effects on Pool and Subcooled Flow Boiling by, (2016).

[164] C. Coyle, J. Buongiorno, T. Mckrell, R. Cohen, M. Ave, Synthesis of CRUD and its Effects On Pool and Subcooled Flow Boiling Department of Nuclear Science and Engineering Department of Chemical Engineering Massachusetts Institute of Technology, Nureth-16 (2015) 7143–7153.

[165] T.R. Allen, Author ' s personal copy Corrosion of Zirconium Alloys, 1st ed., Elsevier Inc., 2012. https://doi.org/10.1016/B978-0-08-056033-5.00063-X.

[166] B.S. Nagothi, H. Qu, W. Zhang, R. V Umretiya, E. Dolley, R.B. Rebak, Hydrothermal Corrosion of Latest Generation of FeCrAl Alloys for Nuclear Fuel Cladding, (2024).

[167] B. Andersen, J. Hou, A. Godfrey, A Novel Method for Controlling Crud Deposition in Nuclear Reactors Using Optimization Algorithms and Deep Neural Network Based Surrogate Models †, (2022) 504–522.

[168] D.O.F. Philosophy, J. Wu, Finite Element Modelling of CRUD Deposition in PWRs A thesis submitted to the University of Manchester for the degree of Table of Content, (2019).

[169] C. Xue, Z. Zhang, J. Tan, X. Wu, E. Han, W. Ke, Effects of Zn injection on corrosion behavior and crud deposition of FeCrAl fuel cladding under subcooled nuclear boiling condition in high-temperature pressurized water, Corros. Sci. 211 (2023) 110909. https://doi.org/10.1016/j.corsci.2022.110909.

[170] W. Jia, J. Li, Z. Lu, Y. Juan, Y. Jiang, Synthesis of honeycomb-like Co3O4 nanosheets with excellent supercapacitive performance by morphological controlling derived from the alkaline source ratio, Materials (Basel). 11 (2018). https://doi.org/10.3390/ma11091560.